Salt Weathering in Humidity-Change or Freeze-Thaw Environments: A Series of Laboratory Experiments

January 2019

Masato SATO

Salt Weathering in Humidity-Change or Freeze-Thaw Environments: A Series of Laboratory Experiments

A Dissertation Submitted to

the Graduate School of Life and Environmental Sciences,

the University of Tsukuba

in Partial Fulfillment of the Requirements

for the Degree of Doctor of Philosophy in Science

(Doctoral Program in Geoenvironmental Sciences)

Masato SATO

Abstract

A series of laboratory weathering experiments were carried out to examine salt weathering in humidity-change and freeze-thaw environments.

In first series of experiments simulating under changing humidity conditions, five types of rocks (porous tuff, porous sandstone, dense sandstone, and two porous mudstones) with three types of salts (sodium chloride, sodium sulfate, or magnesium sulfate) were subjected to humidity oscillations in a climatic cabinet where air humidity ranged from 20%RH to 98%RH during 6-hour periods at 10°C or 20°C. Prior to the weathering experiment, the rock specimens were oven-dried, and the water supply was restricted only from air humidity during the experiment.

Humidity oscillation induced cycles of repeated of salt deliquescence-recrystallization and hydration-dehydration. Salts on rock surface deliquesced and hydrated in a high-humidity period, while they crystallized in a low-humidity period. The degrees of damage were correlated with the moisture amount absorbed to the rock specimens in the high-humidity period.

Sodium chloride which deliquesces at humidity of more than 80%RH caused the most intensive weathering. Porous sandstone with sodium chloride was completely broken down after 100 cycles of humidity changes. Dense sandstone and porous tuff showed flaking or swelling on their surfaces. The Equotip rebound value dense sandstone with sodium chloride decreased with increasing number of humidity cycles. Sodium chloride can easily deliquesce and recrystallize in environment with cycles

of air humidity in a short time interval, such as the surfaces of rock cliff in coastal spray zones.

Magnesium sulfate induced a weight loss in porous sandstone, through flaking from the surface of porous tuff, and through swelling and cracking on the surface of dense sandstone. Sodium sulfate was not effective in the humidity-change experiment, although salt efflorescence was extensively produced. Slow hydration rate of sodium sulfate can cause the ineffectiveness of sodium sulfate. In addition, volumetric expansion with hydration of sodium sulfate may result in pore clogging, and hinder infiltration of moisture into the rock. The restricted activity of sodium sulfate suggests that sodium sulfate rarely induces salt decay by daily humidity fluctuation. Magnesium sulfate might influence rock decay more than sodium sulfate when air humidity fluctuates in a short period.

The second series of experiments were carried out simulating a combination of salt and ice crystallization using saturated salt solution. Four types of rocks (porous tuff, dense tuff, dense sandstone, and porous andesite) saturated with salt solutions (sodium chloride, sodium sulfate, or magnesium sulfate) were subjected to freeze-thaw cycles in the climatic cabinet where air temperature ranged from −30˚C to 10˚C within 24 hours. Prior to the freeze-thaw experiment, rock specimens were immersed in saturated salt solutions at 10°C or distilled water for 72 hours, and covered with foil for preventing the specimens from drying.

Saturated solution of magnesium sulfate induced the greatest damage on rock specimens, although magnesium sulfate has been regarded as an inactive salt in the previous freeze-thaw experiments in which rock specimen were partly immersed in salt solution with dilute or mild

concentration. Sodium sulfate induced rock damages comparable with sodium chloride.

Specimens immersed in saturated salt solutions showed greater freezing strain, weight losses and reductions in Equotip rebound value and longitudinal wave velocity than those immersed in distilled water. The reduction rates of Equotip rebound value were comparable with those of specimens subjected to cycles of total immersion in salt solution and subsequent drying. These results imply that salt crystallization significantly contributes to rock breakdown due to freezing of saturated salt solution.

Sodium and magnesium sulfate crystallized from saturated solution and induced rock expansion prior to freezing. These salt crystals may fill micro-pores in rock and facilitates rock expansion and breakdown due to freezing. Magnesium sulfate solution can induce intensive weathering in a freeze-thaw condition with saturated salt solutions, although the previous studies reported that magnesium sulfate was ineffective in freeze-thaw experiment.

Key words: *salt weathering, humidity change, frost shattering, sodium chloride, sodium sulfate, magnesium sulfate, surface hardness*

Contents

List of Tables

List of Figures

Chapter. I Introduction

I-1. Salt weathering in natural conditions

I-1-1. Principles of salt weathering

Salt weathering is one of the major processes of stone decay that causes serious damage to brick walls (Goudie, 1977; Kuchitsu *et al*., 2000; Oguchi *et al*., 2002; Matsukura *et al.*, 2004), structural foundations (Mottershead, 1994; Takahashi *et al*., 1994), and historical buildings (Gauri, 1990; Gauri *et al*., 1990; Kamh, 2005; Thomachot-Schneider *et al*., 2011). In natural environments, salt weathering occurs in coastal areas (Mottershead, 1982; Matsukura and Matsuoka, 1991, 1996), deserts (Cook, 1981; Goudie and Cook, 1984; Viles and Goudie, 2013), and the Antarctic inlands (Selby and Wilson, 1971; Miotke, 1982; Marchant and Head, 2007). Field observations undertaken globally in a wide range of environments have suggested that stone decay is affected by microclimatic conditions, including temperature (Hœrlé, 2006), insolation (McFadden *et al*., 2005; Gunzburger and Merrien-Soukatchoff, 2011), moisture (Cooke, 1994; Moreno *et al*., 2006; Takaya *et al*., 2011; Mol and Viles, 2012; Mol, 2014), and humidity (Viles, 2005; López-Arce *et al*., 2010; Benavente *et al*., 2011; Schnepfleinter *et al*., 2016).

Three mechanisms have been proposed for rock breakage by salt weathering; (1) stress of salt crystallization from solution, (2) stress by hydration and (3) thermal expansion of salt crystals in rock pores and cracks. Winkler and Singer (1972)

calculated the crystallization pressure of some common salts. The pressure is described as a function of temperature where salt crystals grow and increases with increasing temperature. In addition to temperature, air humidity also affects the effectiveness of salt crystallization. Goudie and Viles (1997) emphasized that salt crystallization can occur only when the relative humidity is lower than the equilibrium relative humidity of saturated solution of the salt. Arnold and Zehnder (1989) reviewed the equilibrium relative humidity of common salts.

Both temperature and humidity control salt hydration and dehydration processes. Salt crystal can hydrate, and volume of the crystal increases when ambient humidity exceeds the equilibrium humidity at the temperature. Winkler and Wilhelm (1970) calculated and reviewed the hydration pressures of some common salts in various combinations of temperature and humidity conditions. Cooke and Smalley (1968) pointed out a possibility that thermal expansion of salt induces pressure in rock pores. Cooke and Smalley (1968) and Goudie and Viles (1997) revealed that some common salts have larger coefficients of thermal expansion than granite and common rock minerals.

Rodriguez-Navarro and Doehne (1999) revealed that the location of crystallization is a key factor for the degree of salt damages. In their studies, sodium sulfate tended to form subflorescence in highly localized areas, although halite tended to grow on the stone surface as efflorescence or fill homogeneously the small pores of the stone.

They assumed that salt crystallization as subflorescence within the rock pores induces greater crystallization pressure than salt efflorescence on rock surface. Doehne (2002) assumed evaporation (solution transport) rate, surface tension and viscosity of solution, and pore-size distribution of rock as important controls on the location of crystallization.

I-1-2. Salt weathering in dry or cold environments

Frost shattering is a major process of debris production and crack development in cold regions. Many laboratory experiments on frost shattering (e.g., McGreevy, 1981; Murton *et al*., 2006) and field observations (e.g., Hall, 1987; Anderson, 1998) have been carried out. Matsuoka (2001) classified the frost shattering in rocks or soil into two types; (1) diurnal cycle of in-situ freezing and expansion which requires the degree of saturation more than 80%, and (2) seasonal cycle of freezing which requires the presence of a nearby moisture source such as groundwater or seasonal melting layer. In any condition, a large amount of moisture is required for frost shattering.

Meanwhile, Hall *et al*. (2002) pointed out the importance of other weathering processes such as thermal shattering (Ishimaru and Yoshikawa, 2000; French and Guglielmin, 2002; Hall and Andrè, 2001; Hall *et al*., 2008), salt weathering (Selby and Wilson, 1971; Miotke, 1982; Marchant and Head, 2007), chemical weathering (Allen *et al*., 2002), and biological weathering (Friedman, 1982) in cold regions. In

Antarctica, the separation of rock surfaces referred to as "granular disintegration" (French and Guglielmin, 2002), salt accumulation (Selby and Wilson, 1971; Matsuoka *et al*., 2006), and tafoni (Andrè and Hall, 2005; Marchant and Head, 2007; Strini *et al*., 2008) were observed. These features are often associated with salt weathering. Parsons *et al*. (2005) reported the presence of white and yellow precipitation at the bottom of a tafone-like hole in the McMurdo Dry Valleys.

Matsuoka *et al*. (1996) performed a field experiment in which specimens of Oya tuff saturated with each of aqueous solution of sodium chloride, sodium sulfate, calcium sulfate or distilled water were placed on a talus slope in the Sør Rondane mountains, Antarctica. After four to five-year exposure, the specimen saturated with distilled water was not weathered, therefore frost shattering hardly occurs in their site; cracks were generated in the specimen saturated with sodium sulfate solution; and the specimen saturated with sodium chloride solution was completely destroyed. The rock breakdown implied that salt weathering can be induced by dairy or seasonal changes of temperature and humidity in cold and dry regions.

Malin (1974) and Clark and Van Hart (1981) pointed out a possibility that frost shattering and salt weathering also occur on Martian surface. Characteristic topography in the terrestrial cold region such as polygonal soil and pingo (Burr *et al*., 2009; Mellon *et al*., 2009) is also found on the Martian surface. The presence of frozen layer has also been confirmed by Phoenix Mars Lander (Smith *et al*., 2009).

Weathering features such as tafoni (Mutch *et al*., 1976a, 1976b; Rodriguez-Navarro, 1998), puzzled rock (Bell *et al*., 2004; Jagoutz, 2006; Levy *et al*., 2009), and a large amount of angular gravel and coarse sand in soil layer (Smith *et al*., 1997; Bell *et al*., 2004; Squyres *et al.*, 2004a, 2004b) have been confirmed from images of Martian surface taken by on-site cameras mounted on Mars landers and rovers.

Salt weathering and frost shattering might occur by freezing of salt solution or salt deliquescence-crystallization on the present Martian surface. Malin (1974) also pointed out a possibility of unfrozen water with a high content of salt. Recurring slope lineae (RSL), which are narrow, dark and liquid flow-like features, were found by the High Resolution Imaging Science Experiment (HiRISE) on the Mars Reconnaissance Orbiter (McEwen *et al*., 2011, 2013). RSL appeared during spring and summer on rock outcrop and crater wall, particularly south-facing slope (Ohja *et al*., 2014). These authors pointed out that distribution of RSL is similar to that of chloride, and associated RSL with highly concentrated salt water. Magnesium sulfate and calcium chloride are common on the Martian surface. A large amount of Na, Mg, S, Cl and Ca were detected in rocks and soils by the alpha particle X-ray spectroscopic analyzer installed on the Mars Exploration Rover (MER), Opportunity (e.g., Gellert *et al*., 2004; Rieder *et al*., 2004). Another MER, Spirit, also detected a large amount of sulfate from wheel track excavated by the probe (Campbell *et al*., 2008). It is also pointed out that perchloride and chloride of potassium and magnesium could

deliquesce and precipitate with fluctuation of humidity and temperature on Martian surface (e.g., Chevrier and Rivera-Valetin, 2012; Buenestado *et al*., 2015).

Air humidity is one of the important water sources affecting stone heritages. Arnold and Zehnder (1989) pointed out the importance of monitoring air humidity and temperature for preservation of heritages, as air humidity and temperature control salt crystallization and hydration. Goudie and Viles (1997) assumed that air humidity affects salt crystallization from solution, change of phase (hydration/dehydration), and crystallization pressure. Seasonal salt deliquescence and precipitation have occurred on stone heritages in the presence of air humidity changes (Goudie, 1977; Matsukura *et al*., 2004; Takaya and Oguchi, 2011). In natural conditions, air humidity is also a major source of water. Tafoni, which are often associated with salt weathering, are common in coastal areas (e.g., Mottershead, 1982; Matsukura and Matsuoka, 1991, 1996; Mottershead and Pye, 1994). They occasionally appear hundreds of meters away from coastal lines. In supratidal zones, sea spray would provide salts on rock surfaces. Tafoni also developed on rock wall in mountain areas on which rainwater and/or ground water provide salts to rock surfaces (e.g., Matsukura and Tanaka, 2000; McBride and Picard, 2000; Brandmeier *et al.*, 2011; Mol and Viles, 2012). In these conditions, salt supplied and precipitated on the rock surface and subsurface may induced salt weathering by cyclic humidity-changes (Wellman and Wilson, 1965; Campbell and Claridge, 1987; Yen *et al*., 2005; Martín-Torres *et al*., 2015; Heinz *et*

al., 2016; Gough *et al*., 2016, 2017).

I-2. Experimental studies

I-2-1. Salt weathering experiments with humidity change

The influence of humidity on salt hydration/dehydration, particularly those of sulfates has been thoroughly examined (Rodriguez-Navarro and Doehne, 1999; Benavente *et al*., 2004; Steiger and Asmussen, 2008), although these studies mainly focused on the micro-scale behavior of salts. This section introduces some previous experimental studies in which significant damage was generated in macro-scale by humidity fluctuation.

Fahey (1985) subjected rock specimens to daily freeze-thaw or humidity-change environments. The temperature ranged from –20°C to +15°C during a freeze-thaw cycle. The humidity oscillated between 30% and 100% in RH, and temperature ranged from –1°C to +20°C during a humidity cycle. The specimens were immersed in mild (0.2 mol/L) solution of sodium sulfate or magnesium sulfate prior to the experiments. Dolomite specimens subjected to humidity change showed comparable or minor weight losses to those in a freeze-thaw experiment. Sodium sulfate induced greater weight losses to rock specimens than magnesium sulfate. Goudie (1993) subjected the rock specimens to six daily climatic conditions, which simulated the temperature and the humidity in different desert areas. The rock specimens were once

immersed in salt solution of sodium sulfate, magnesium sulfate, sodium chloride, sodium carbonate, or sodium nitrate. Sodium sulfate and sodium nitrate induced distinct weight losses to rock specimens. The "Negev" cycle in which the maximum air humidity was close to 100%RH showed larger weight losses than the "Wadi Digla" cycle of which the temperature range was widest (from 22°C to 72°C) in six climatic conditions. The specimens subjected to other four climatic conditions showed negligible weight losses.

I-2-2. Freeze-thaw experiments using salt solution

Frost shattering and salt weathering are individually intensive weathering processes. Several laboratory studies on the combined effects of frost shattering and salt crystallization were carried out, although the results are conflicting. An early work by Goudie (1974) subjected rock specimens saturated with sodium sulfate solution to a freeze-thaw environment in which air temperature oscillated from –10°C to +18°C in 24 h. The weight losses in the freeze-thaw condition were greater than the weight losses when the specimens were dried at room temperature. Williams and Robinson (1981) conducted a freeze-thaw experiment using distilled water and two saturated salt solutions of sodium chloride and sodium sulfate. The ambient temperature oscillated from –30°C to +20°C in 5 days. The weight losses of the rock specimens saturated with a solution of sodium chloride or sodium sulfate were greater

than the weight losses of the specimens saturated with distilled water. McGreevy (1982) conducted a freeze-thaw experiment using dilute salt solutions (0.25, 0.50 and 1.00 mol/L) of sodium chloride, sodium sulfate, and magnesium sulfate. The weight losses of rock specimens immersed in salt solutions were smaller than the case using distilled water. Jerwood *et al*. (1990a) explained the difference between the results of Williams and Robinson (1981) and McGreevy (1982) by using a phase equilibrium diagram of a salt solution. Trenhaile and Rudakas (1981) estimated effectiveness of sea water on frost shattering. Saline water with half concentration of seawater induced more rock breakdown than solutions with normal and higher concentrations of sea water or deionized water.

Jerwood *et al*. (1990a, b) suggested the complicated behavior of rock specimen to frost shattering and salt crystallization in combination as described below. Jerwood *et al*. (1990a) subjected rock specimens immersed in salt solutions to four environmental conditions with different cooling rate and minimum temperature. The weight losses of the specimens were greater in conditions with high cooling rate or low minimum ambient temperature. Jerwood *et al*. (1990b) carried out freeze-thaw experiment using salt solutions in two ways. A group of specimens were saturated with salt solution at the beginning of each freeze-thaw cycle, and another group of specimens were saturated only once before the experiment. They reported that the frost shattering was dominant in high moisture conditions, whereas salt weathering

was promoted in low moisture environments. Williams and Robinson (1991) reviewed mechanisms of weathering in a combined condition of frost shattering and salt crystallization. They described that degree of contribution of the two mechanisms varies according to freezing regime (cooling rate and temperature range), concentration of salts (freezing point, supersaturation ratio, viscosity of the solution, osmotic pressure and mobility of solution), the way and amount of moisture supply, and the physical properties of the rock. They also pointed out characteristic behavior of salt solution such as precipitation of cryohydrate, pore clogging and surface sealing by precipitated salts.

I-2.3. Experimental procedure employed in previous studies

Many laboratory experiments have simulated salt weathering under the conditions of "cyclic total immersion" or "continuous partial immersion". In cyclic total immersion experiment, rock specimens are repeatedly subjected to total immersion in a saturated salt solution followed by drying (Goudie *et al*., 1970; Robinson and Williams, 1982; Williams and Robinson, 1998). In continuous partial immersion experiment, specimens partly immersed in saturated solutions are subjected to cyclic temperature and/or humidity changes (Goudie, 1986; Robinson and Williams, 2000; Oguchi and Yuasa, 2010). However, these conditions, in which abundant salt water is supplied to the rock specimen, are not likely to occur in natural conditions, with

exception of intertidal zones and places close to groundwater. In addition, high temperature drying, which is often adopted in the previous studies, also affects salt crystallization processes (Aly *et al*., 2015). The disjuncture between field environments and laboratory experiments has often been pointed out (McGreevy and Smith, 1982; Smith *et al*., 2005).

I-3. Objective of this study

As described in the section I-2-1, the past experimental studies suggested that humidity fluctuation could cause visible rock breakdown (Fahey, 1985; Goudie, 1993). However, in their studies, rock specimens were partly immersed in salt solution, or fully saturated to salt solution prior to weathering experiment. They also subjected specimens to humidity changes along with temperature fluctuations. Salt weathering process in dry conditions in which the water source was restricted, particularly the effectiveness of humidity fluctuation on salt decay, has not yet been investigated in detail.

The effect of dissolved salts on freezing behaviors is still unclear, as described in the section I-2-2, because weathering processes of salt crystallization with ice formation were affected by various factors. The previous studies employed salt solutions with dilute or mild concentrations (e.g., Trenhaile and Rudakas, 1981; Jerwood *et al*., 1990a, b; McGreevy, 1982). Freeze-thaw experiments using

concentrated salt solution have rarely been carried out.

This study entailed a series of laboratory experiments on salt damage in rock specimens under humidity fluctuation at a constant temperature. The weathering processes due to salt crystallization with ice formation were also investigated under a condition with abundant salt.

Chapter II. Materials and methods

II-1. Rock and salt selection

Seven types of rocks (two tuffs, two sandstones, two mudstones, and one andesite) were used for a series of weathering experiments (Figure 2.1). Table 2.1 shows combinations of rocks used for each experimental procedure. Oya tuff and Aoshima sandstone was used for all of three experimental procedures. For the humidity-change experiments, Ubara sandstone, Taitozaki mudstone, and Miiri mudstone were employed, in addition to Oya tuff and Aoshima sandstone. For freeze-thaw experiments, Shirakawa tuff and Andesite were also employed. For total immersion experiments, Shirakawa tuff was also used in addition to Oya tuff and Aoshima sandstone. Four types of rocks (Oya tuff, Aoshima sandstone, Shirakawa tuff, and Andesite) were shaped into cubic specimens with a side of 5 cm. The other three types of rocks (Ubara sandstone, Taitozaki mudstone and Miiri mudstone) were shaped into cylindrical specimens with a diameter and a height of 3.5 cm, because of difficulties in shaping the material into cubes.

Oya tuff is dacitic or rhyolitic marine pumice tuff of the Miocene age. The pumice part was often altered to a block of Fe-rich montmorillonite which is referred to as “Miso”. The samples were quarried in Utsunomiya, Tochigi Prefecture, central Japan. In Japan, a variety of buildings and stone statues are made from Oya tuff, which is often damaged by salt weathering (Oguchi and Yuasa, 2010). Aoshima sandstone is

very fine-grained, well-cemented sandstone of the Pliocene age. The samples were collected in the Nichinan Coast, Miyazaki Prefecture, southwest Japan (Figure 2.2). Tafoni and honeycomb weathering features are well developed on Type-B shore platforms (Tsujimoto, 1985) in coastal area where Aoshima sandstone is exposed (Takahashi *et al*., 1994) (Figure 2.3). Ubara sandstone, Taitozaki mudstone, and Miiri mudstone were collected on the southeast coast of Chiba Prefecture, central Japan (Figure 2.4). Ubara sandstone is fine-grained, weakly cemented, porous sandstone of the Miocene age. Taitozaki mudstone is weakly cemented, porous mudstone of Pleistocene age. Miiri mudstone is cemented, porous mudstone of Miocene age. Type-A shore platforms are developed in coastal areas where Taitozaki mudstone is exposed. Type-B shore platforms are often developed in coastal areas where Ubara sandstone and Miiri mudstone are exposed. Tafoni-like features are well developed on coastal cliffs composed of Ubara sandstone (Figure 2.5). Shirakawa tuff is dacitic welded tuff of Pleistocene age. The samples were quarried from pyroclastic-flow deposit in Shirakawa area, Fukushima Prefecture, central Japan. In the area, a variety of buildings are made from Shirakawa tuff. Andesite is porous, porphyritic andesite composed of quartz, hornblende, and pyroxene. The sampling site of Andesite was unknown.

Table 2.2 shows physical properties of rocks. Bulk density ρ_{bulk} was calculated by diving dry weight by volume of rock specimen. The dry weight of each specimen

was measured after oven drying at 110°C for 48 hours. The volume of each specimen was evaluated with a vernier caliper. True density ρ_{true} was measured by using powdered specimens and a pycnometer according to Japanese Industrial Standards (JIS) A1202, and it was calculated by:

$$\rho_{true} = \frac{m_2 - m_1}{(m_4 - m_1) - (m_3 - m_2)} \times \rho_w \tag{1}$$

where m_1 is weight of the empty pycnometer, m_2 is weight of the pycnometer with dry specimen, m_3 is weight of the pycnometer filled with specimen and water, m_4 is weight of the pycnometer filled only with water, and ρ_w is density of water. Effective porosity n_e was evaluated using a vacuum desiccator. Rock specimens were immersed in distilled water for 72 hours in the vacuum desiccator where air pressure was reduced to 0.1 Pa by a vacuum pump. After immersion in vacuumed condition, the specimens were taken out from distilled water, lightly wiped with paper cloth, and weighed to measure vacuum saturated weight. The effective porosity n_e was calculated by:

$$n_e = \frac{(w_{sat} - w_{dry})}{\rho_w V} \times 100 \tag{2}$$

where w_{sat} is vacuum saturated weight of the specimen, w_{dry} is dry weight of the specimen, V is bulk volume of the specimen. Tensile strength S_t was measured by indirect tensile strength test using cylindrical specimen with a diameter and a height of 5.0 cm according to Japanese Industrial Standards (JIS) M0303. Tensile strength S_t was calculated by:

$$S_t = \frac{2P}{\pi dl} \tag{3}$$

where P is maximum pressure when the specimen broke, d and l are the diameter and the height of the cylindrical specimen, respectively. The tensile strength was measured with three specimens for each rock type. The specimens were oven dried at 110°C for 48 hours before the test. The tensile strength data were based on Yamada *et al*. (2005) for Shirakawa tuff, and Tsujimoto (1985) for Taitozaki and Miiri mudstone, respectively. Equotip rebound value (L-value) L was evaluated with a Type-D Equotip hardness tester (Proceq) as an index of rock surface hardness. The rebound value L is defined by:

$$L = \frac{V_r}{V_i} \times 1000 \tag{4}$$

where V_r and V_i are rebound and impact velocities of impact tip, respectively. This study applied the single impact method, which is one of two methodologies for hardness tests with Equotip (Aoki and Matsukura, 2007). This method measures the mean L-value of single impacts at ten different points. The mean L-value represents hardness of surficial portion of rock. Longitudinal wave velocity (P-wave velocity) Vp was measured with an ultrasonic tester (Pundit Plus, CNS Farnell), and it is defined by:

$$Vp = \frac{l}{t} \tag{5}$$

where l is a distance from one surface to the opposite surface of a rock specimen on which transducers are attached with grease, t is transit time of a pulse of ultrasonic longitudinal stress waves in the rock specimen. P-wave velocity was employed for evaluating conditions of pores and cracks for interior rock.

Pore-size distribution and specific surface area SSA of rock specimen were measured with a mercury intrusion porosimeter (AutoPore IV, Micromeritics). The pore-size distributions of each rock type were represented as an averaged value of two or three specimens. Table 2.3 shows specific surface area and average pore volumes of a range of pores, where V_{total} is total volume of pores with a range of

diameter from $10^{-2.5}$ to 200 μm, V_1, V_2, V_3, and V_4 are total volumes of pores with a range of diameters of $10^{1.5}$–$10^{0.5}$ μm (large pores), $10^{0.5}$–$10^{-0.5}$ μm (median pores), $10^{-0.5}$–$10^{-1.5}$ μm (small pores), and less than $10^{-1.5}$ μm (very small pores), respectively. Oya tuff has pores with wider ranges of diameter. Aoshima sandstone and Shirakawa tuff is characterized by a large proportion of V_2. Ubara sandstone has pores with wider ranges of diameter and a large proportion of V_1. Taitozaki mudstone is characterized by a large proportion of V_2 and V_3. Miri mudstone is characterized by a large proportion of V_3. V_{total} of Andesite is lower than half that of Shirakawa tuff, although Andesite has a comparable effective porosity with Shirakawa tuff. Andesite has a large proportion of very large pores which are larger than 200 μm in diameter. Volume of very small pores V_4 for Andesite is represented as "N.A." in Table 2.3, because the measured value was negative.

Three types of salts (sodium chloride, sodium sulfate, and magnesium sulfate, referred to as NaCl, Na_2SO_4, and $MgSO_4$, respectively) were used for a series of experiments. NaCl existing abundantly in sea water is major agent of salt weathering in coastal areas (Bradley *et al*., 1978; Mottershead, 1982; Mustoe, 1982; Young, 1987; Matsukura and Matsuoka, 1991, 1996; Mottershead, 1994; Mottershead and Pye, 1994). Two sulfates are commonly present in inlands (Goudie and Day, 1980; Matsukura and Kanai, 1988; Goudie and Viles, 1997; Goudie *et al*., 1997; Brandmeier *et al*., 2011; Schnepfleitner *et al*., 2016), particularly in Antarctica (Keys

and Williams, 1981; Goudie and Cooke, 1984; Gore *et al*., 1996; Matsuoka *et al*., 2006). These salts were also detected in building materials and historical heritages (Goudie, 1977; Winkler, 1987; Kamh, 2005; López-Arce *et al*., 2009, 2011; Benavente *et al*., 2011; Thomachot-Schneider *et al.*, 2011; Lubelli *et al*., 2018), and destruction by these salts has been recognized as a problem. Table 2.4 shows solubilities of each salt at 10°C and 20°C. The solubility of NaCl is almost constant with temperature, while Na_2SO_4 is relatively insoluble at low temperature.

II-2. Humidity-change weathering experiment

Figure 2.6 shows an outline of the humidity-change experiment. Five types of rocks (Oya tuff, Aoshima sandstone, Ubara sandstone, Taitozaki mudstone, and Miiri mudstone) were used for the experiment. For Oya tuff and Aoshima sandstone, the humidity-change experiments were carried out at 10°C and 20°C. For Ubara sandstone, Taitozaki mudstone, and Miiri mudstone, the humidity-change experiment was carried out only at 20°C. Saturated solutions of NaCl, Na_2SO_4, or $MgSO_4$ were prepared at each temperature. Twelve specimens were prepared for Oya tuff and Aoshima sandstone. Four specimens were used for measuring weight, other four were used for measuring L-value and P-wave velocity, and the remaining four were used for measuring surface strain and temperature. Eight specimens were prepared for Ubara sandstone, Taitozaki mudstone, and Miiri mudstone. Four specimens were

used for measuring weight, the other four specimens were used for measuring L-value and P-wave velocity. The surface strain and temperature were not measured for Ubara sandstone, Taitozaki mudstone, and Miiri mudstone.

The initial values of the weight, L-value and P-wave velocity ($W_{initial}$, $L_{initial}$, $Vp_{initial}$, respectively) of the specimens were measured after oven drying at 110°C for 48 hours. Prior to the humidity-change experiment, the rock specimens were immersed in one of the three salt solutions or distilled water for 72 hours. After immersion, the specimens were oven dried again at 110°C for 48 hours. The weight or L-value and P-wave velocity were measured again after the oven drying, and the values are referred to as cycle-0 values (W_0, L_0, Vp_0, respectively). A strain gauge and thermocouple were installed on surface of the specimens before the humidity-change experiment. Linear strain gauge (KFW-2, Kyowa) was bounded to the surface of the specimens with dedicated epoxy adhesive. A strain gauge was used for humidity-change experiment at 10°C, and two strain gauges were adhered to different faces of a specimen for humidity-change experiment at 20°C. A T-type thermocouple was installed in a 5-mm deep pit with a diameter of 3.2 mm. The thermocouple was bonded with silicone sealant mixed with powdered rock specimens.

The specimens were placed in an ambient chamber (PL-3K, ESPEC). Each specimen for measuring weight was placed on a sieve with 2-mm opening. All the specimens were subjected to humidity changes in the chamber, in which air humidity

oscillated from 18%RH to 98%RH every 6 hours (Figure 2.7). Air temperature in the chamber was kept at 10°C or 20°C during the experiment with an accuracy of ±2°C. Air temperature and relative humidity in the chamber were recorded every 5 minutes with a data logger (TR-72wf, T&D) with accuracies of ±0.5% for temperature and ±5% for RH. The sensor required 7 minutes to reach a 90% response. The strain and the temperature were recorded with data loggers (DA100, Yokokawa; D1-007A-8P1, Log Electronics; NR-600 series, Keyence) at 5-minute intervals. Weight, L-value, and P-wave velocity of the specimens were measured every 20 cycles. All fragments remaining on the sieve were weighed. In addition, the specimens of Oya tuff and Aoshima sandstone were weighed at the end of high humidity period in the first humidity cycle in order to estimate the amount of water that absorbed from the air on the specimens in the high-humidity period.

II-3. Freeze-thaw weathering experiment

Figure 2.8 shows an outline of the freeze-thaw experiment. Saturated solutions of NaCl, Na_2SO_4, or $MgSO_4$ were prepared at 10°C. Four types of rocks (Oya tuff, Aoshima sandstone, Shirakawa tuff, and Miiri mudstone) were used for the experiment. Twelve specimens were prepared for each type of rocks. As same as the humidity-change experiment, four specimens were used for measuring weight, other four were used for measuring L-value and P-wave velocity, and the remaining four

were used for surface strain and temperature.

W_0, L_0, and Vp_0 were measured after oven drying at 110°C for 48 hours. Strain gauges were installed on surface of the specimens prior to the freeze-thaw experiment (Figure 2.9). The specimens and the strain gauges were pretreated as below to prevent the gauge from wetting. A face of the specimen on which the strain gauge was attached was coated with dedicated epoxy adhesive prior to adhering the strain gauge. The strain gauge adhered on the specimen was coated with silicone sealant. T-type thermocouples were installed in pits at depths of 10 mm and 25 mm. The diameter of the pit was 3.2 mm. The thermocouples were bonded with silicone sealant mixed with powdered rock specimens. After these treatments, the specimens were immersed in one of the three salt solutions or distilled water for 72 hours. The saturated specimens were covered with foil for preventing the specimens from drying.

All the specimens were placed in the chamber and subjected to freeze-thaw cycles, in which air temperature oscillated from –30°C to 10°C every 24 hours with cooling and thawing rates of ±4°C/h. (Figure 2.10). The strain and the temperature were recorded using the data loggers at 5-minute intervals. Weight, L-value, and P-wave velocity of the specimens were measured after every cycle during the first 20 cycles. These measurements were carried out every 10 cycles after 20 cycles. The specimens were picked up from the chamber and the foil were removed before every measurement. All fragments remaining on the sieve with 2-mm opening were

weighed. After every measurement, one gram of salt solution or distilled water was supplied to the specimens, and the specimens were covered with foil again for preventing the specimens from drying.

In addition to the specimens saturated with salt solutions, oven-dried specimens prior to the freeze-thaw experiment were also subjected to freeze-thaw cycles only for Oya tuff. Damage induced by temperature fluctuation in dry condition, i.e., effect of thermal expansion/contraction of rock and salt crystal, was evaluated by using another twelve Oya tuff specimens. Four specimens were used for measuring weight, other four were used for measuring L-value and P-wave velocity, and the remaining four were used for measuring surface strain and temperature. $W_{initial}$, $L_{initial}$, and $Vp_{initial}$ were measured after oven drying at 110°C for 48 hours. Strain gauges and thermocouples were installed in the same way as described above. The thermocouple was installed only in a pit at a depth of 10 mm. The specimens were immersed in one of the three salt solutions or distilled water for 72 hours. After immersion, the specimens were oven dried again at 110°C for 48 hours. The weight, L-value and P-wave velocity of the specimens were measured again after the oven drying, which are referred to as W_0, L_0, and Vp_0, respectively. All the specimens were subjected to freeze-thaw cycles in the same way as described above. The specimens were not covered with foil, and any extra moisture was not supplied to the specimens during the freeze-thaw experiment. Weight, L-value, and P-wave velocity of the specimens

were measured every cycle during the first 20 cycles. These measurements were carried out approximately every 5 cycles after 20 cycles to 101 cycles, approximately every 10 cycles after 101 cycles to 232 cycles. The experiment was carried out up to 301 cycles.

II-4. Total immersion weathering experiment

Weathering experiment on repeated wetting-drying with a salt solution, referred to as "total immersion experiment", was carried out in order to compare its results with other two experiments. Figure 2.11 shows an outline of the total immersion experiment. The total immersion experiments were carried out at 10°C and 20°C. Saturated solutions of NaCl, Na_2SO_4, or $MgSO_4$ were prepared at each temperature in the same way as in the humidity-change experiment. Eight cubic specimens for each of three type of rocks (Oya tuff, Aoshima sandstone, and Shirakawa tuff) were prepared. Four cubes were used for measuring the weight, the other four cubes were used for measuring the L-value and P-wave velocity.

After measuring the initial weight, L-value and P-wave velocity, the specimens were subjected to cycles of wetting and drying, each of which was composed of the following treatment steps. The specimens were (1) immersed in one of the three salt solutions or distilled water for 24 hours at 20°C, (2) oven dried at 110°C for 48 hours, and (3) immersed in distilled water for 24 hours to remove salt that had crystallized in

the specimens. After cooling, they were (4) oven dried again at 110°C for 48 hours, and (5) weighed, and their L-value and P-wave velocity were measured. All fragments remaining on the sieve with 2-mm opening were weighed.

Chapter III. Results

III-1. Results of humidity-change experiments

III-1-1. Amount of salt in rock specimens

Table 3.1 shows amounts of salt contained in the rock specimens for each combination of rock and salt solution. Porous Oya tuff contained larger amount of salt than Aoshima sandstone with lower porosity (Table 2.2). The amounts of Na_2SO_4 were smaller than those of NaCl and $MgSO_4$, because of lower solubility of Na_2SO_4 (Table 2.4). The specimens immersed in saturated salt solutions at 20°C tended to contain larger amount of salts than the specimens immersed in saturated salt solutions at 10°C.

III-1-2. L-value and P-wave velocity changes prior to humidity-change experiment

Table 3.2 shows initial salt-free and the cycle-0 values of L-value and P-wave velocity. Figures 3.1–3.2 show pictures of rock specimens during humidity-change experiments for Oya tuff, Figures 3.3–3.4 for Aoshima sandstone, Figures 3.5–3.8 for Ubara sandstone, Figures 3.9–3.12 for Taitozaki mudstone, and Figures 3.13–3.16 for Miiri mudstone, respectively.

Most specimens showed decreases in L-value after immersion and subsequent drying (Table 3.2). The specimens of Oya tuff, Aoshima sandstone, and Ubara

sandstone did not show any obvious crack propagation, flaking, or swelling at the beginning of the humidity-change experiment (0 cycle in Figures 3.1–3.8).

Regardless of temperature at which the saturated salt solutions were prepared, NaCl induced larger decreases in L-value than Na_2SO_4 and $MgSO_4$ (Table 3.2). Change ratios of L-values after the pre-treatment to the initial L-values, i.e., $L_0/L_{initial}$ of Oya tuff pre-treated with saturated salt solutions of NaCl at 10°C, kept more than 90%. $L_0/L_{initial}$ of Oya tuff pre-treated with the solution of Na_2SO_4 and $MgSO_4$ at 10°C, was 95.3% and 102.3%, respectively. For Aoshima sandstone, $L_0/L_{initial}$ of the specimens pre-treated with NaCl, Na_2SO_4, and $MgSO_4$ at 10°C, was 90.8%, 99.2%, and 100.6% of $L_{initial}$, respectively. The L-value changes for the specimens pre-treated with saturated salt solutions at 20°C were larger than those at 10°C. $L_0/L_{initial}$ of Oya tuff at 20°C was 71.7% for NaCl, 93.0% for Na_2SO_4, and 141.3% for $MgSO_4$. For Aoshima sandstone, $L_0/L_{initial}$ at 20°C (10°C), was 89.7% (90.8%) for NaCl, 93.1% (99.2%) for Na_2SO_4, and 84.8% (100.6%) for $MgSO_4$.

The L-values of Ubara sandstone considerably decreased after the pre-treatment. The decreases were larger than the cases of Oya tuff and Aoshima sandstone (Table 3.2). $L_0/L_{initial}$ of the specimens pre-treated with solution of NaCl, Na_2SO_4, and $MgSO_4$ was 65.5%, 68.1%, and 74.9%, respectively. All specimens of two mudstones showed crack propagation over the whole area of the specimen, and they were separated into a couple of fragments (Figures 3.9–3.16). The crack propagation

would be induced by slaking, because the cracking occurred during immersion in the salt solution or distilled water. L-values of Taitozaki mudstone largely decreased due to the crack propagation (Figures 3.9–3.16), $L_0/L_{initial}$ of Taitozaki mudstone was 64.6% for NaCl, 89.6% for Na_2SO_4, and 84.3% for $MgSO_4$. For Miiri mudstone, the L-value of the specimen pre-treated with the solution of $MgSO_4$ largely decreased, although the L-values of the specimens pre-treated with other salt solutions increased. $L_0/L_{initial}$ was 107.8% for NaCl, 105.4% for Na_2SO_4, and 44.2% for $MgSO_4$.

The P-wave velocity of the pre-treated specimen tended to increase (Table 3.2), because salt crystals filled the pores in rock specimen. P-wave velocity increased for all the specimens immersed in the solutions of $MgSO_4$. In contrast, P-wave velocity slightly decreased for Oya tuff immersed in the solutions of NaCl or Na_2SO_4 at 10°C and Aoshima sandstone at 20°C.

III-1-3. Weight changes in a humidity cycle

The weights of the rock specimens increased in the high-humidity period and decreased in the low-humidity period. The weight oscillation means that the rock specimens absorbed water from air in the high-humidity period, and they dried in the low-humidity period. During the high-humidity period, all the three salts appears to have formed a solution by dissolving into the water absorbed from air. In the low-humidity period, salts crystallized on the surface of specimens. Table 3.3 shows

difference in weight between beginning and end of the first high-humidity period, i.e., the amount of moisture absorbed into specimens during the first high-humidity period. The specimens with NaCl significantly increased their weights during the high-humidity period regardless of temperature. The specimens with $MgSO_4$ also showed larger increases than the specimens with Na_2SO_4 or the controlled specimens at 20°C. The weight increases of the specimens with Na_2SO_4 were comparable to the values of the controlled specimens at 20°C. The weight increases of the specimens with Na_2SO_4 or $MgSO_4$ were comparable to the values of the controlled specimens at 10°C.

III-1-4. Weight, L-value, and P-wave velocity in humidity-change experiment at 20°C

III-1-4-1. Temporal variations in weight in humidity-change experiment at 20°C

Figures 3.17–3.21 show the temporal variations in the weight, L-value, and P-wave velocity during the humidity experiments at 20°C. The weight of some specimens (e.g., Oya tuff with NaCl, Figure 3.17a; Taitozaki mudstone with $MgSO_4$, Figure 3.20a) slightly increased during the first 20 cycles, because of the absorption of water from the air.

The weights of Ubara sandstone and Taitozaki mudstone with NaCl significantly decreased (Figures 3.19a, and 3.20a). Ubara sandstone with NaCl showed flaking of

mm-scale fragments and sand particles from surface of the specimen (Figure 3.5). The flaking phenomenon is known as granular disintegration (Goudie and Viles, 1997). The shape of the specimen gradually became rounder with an increase in the number of humidity cycles. The specimen split into cm-scale large fragments controlled by a bedding plane at 40 cycles, and was completely broken into sand particles at 100 cycles (Figures 3.5 and 3.19a). Taitozaki mudstone with NaCl was separated into a couple of angular fragments by slaking during the pre-treatment prior to the humidity-change experiment (Figure 3.9). Though the crack propagation continued through the humidity-change experiment, granular disintegration appears to have been dominant (Figure 3.9). There were more powder-like particles in the fragments deposited under the sieve than angular fragments which would be induced by slaking. The weight of Taitozaki mudstone with NaCl decreased to 9.8% of W_0 at 300 cycles of humidity fluctuation (Figure 3.20a).

The specimens of Ubara sandstone and Taitozaki mudstone with $MgSO_4$ also showed decreases in their weight (Figures 3.19a and 3.20a). The weights of specimens with $MgSO_4$ at 300 cycles were 20.0% of W_0 for Ubara sandstone and 52.8% for Taitozaki mudstone. Ubara sandstone with $MgSO_4$ showed granular disintegration (Figure 3.19a), the shape became gradually rounder (Figure 3.7). Though Taitozaki mudstone with $MgSO_4$ showed granular disintegration and crack propagation simultaneously (Figure 3.11), crack propagation was more obvious than

the case of NaCl (Figure 3.9).

The weights of Ubara sandstone and Taitozaki mudstone with Na_2SO_4 slightly decreased during the experiment (Figures 3.19a and 3.20a). The weight of Ubara sandstone and Taitozaki mudstone with Na_2SO_4 were 18.8% and 26.3% of W_0 at 300 cycles. Sand particles gradually flaked from the upper edge of the Ubara sandstone with Na_2SO_4 (Figure 3.6). Taitozaki mudstone with Na_2SO_4 showed granular disintegration, though cracking by slaking was relatively indistinct (Figure 3.10).

The controlled specimens of Ubara sandstone and Taitozaki mudstone did not show any change in their appearance and weight (Figures 3.8, 3.12, 3.19a, and 3.20a). The controlled specimen of Taitozaki mudstone did not show any crack propagation through the humidity-change experiment (Figure 3.12), although the specimens with salts showed crack propagation (Figures 3.9–3.11).

Miiri mudstone with $MgSO_4$ was split into a lot of cm-scale fragments in the first 100 humidity cycles, though the specimen did not show any obvious change in the later 200 cycles (Figure 3.15). Miiri mudstone with $MgSO_4$ showed weight loss, and the weight at 300 cycles was 84.1% of W_0 (Figure 3.21a). The other specimens of Miiri mudstone did not show any crack propagation through the humidity-change experiment (Figures 3.13, 3.14, and 3.16). These specimens did not show obvious weight losses with the exception of increase during the first 20 cycles (Figure 3.21a). Miiri mudstone with NaCl or Na_2SO_4 only showed minor granular disintegration

through the humidity-change experiment (Figures 3.13 and 3.14).

Oya tuff and Aoshima sandstone did not show any significant weight losses (Figures 3.1, 3.3, 3.17a, and 3.18a), although a few granular fragments were deposited under the sieve in the cases of Oya tuff with NaCl at 20°C. The weight of Oya tuff with NaCl slightly decreased through the experiment, the final weight at 200 cycles was 94.8% of W_0 (Figure 3.17a). The specimens of Oya tuff with NaCl or $MgSO_4$ showed flaking on their surfaces (Figures 3.22a and b), while Aoshima sandstone with NaCl showed swelling on the surface (Figure 3.22c). Cracking parallel to the rock surface occurred in the Aoshima sandstone with $MgSO_4$ (Figure 3.22d). Aoshima sandstone with Na_2SO_4 did not show any obvious crack, flaking, or swelling during the experiment (Figure 3.23a), although tabular fragments flaked from the surface of the Oya tuff with Na_2SO_4 when the specimen was immersed in distilled water after humidity-change experiment (Figure 3.23b).

III-1-4-2. Temporal variations in L-value and P-wave velocity in humidity-change experiment at 20°C

The L-values of the Oya tuff, Aoshima sandstone, and Ubara sandstone specimens with NaCl decreased as the number of humidity cycles increased (Figures3.17b, 3.18b and 3.19b). The L-value of these specimens with NaCl could not be measured when their surfaces became rough. The final L-value at 120 cycles was 60.4% of L_0

for Oya tuff (Figure 3.17b) and 32.7% at 160 cycles for Aoshima sandstone (Figure 3.18b). The final L-value of Ubara sandstone at 60 cycles was 53.8% of L_0 (Figure 3.19b). The L-values of Aoshima sandstone with NaCl from 160 to 200 cycles were measured after a treatment that loose particles on the surface were removed with paper cloth (Figure 3.18b).

Oya tuff with $MgSO_4$ showed a reduction in L-value, although 49.8% decrease (from 100% to 50.2% of L_0) during the first 20 cycles was greater than the change in the subsequent 180 cycles (from 50.2% to 32.4% of L_0) (Figure 3.18b). For Ubara sandstone with $MgSO_4$, decrease during the first 20 cycles (from 100% to 84.1% of L_0) was distinct compared with the change in the subsequent 260 cycles (from 84.1% to 41.9% of L_0) (Figure 3.19b).

The L-value of Oya tuff with Na_2SO_4 fluctuated between 90.9% and 109.2% of L_0 (Figure 3.17b). The L-value changes of Aoshima sandstone with Na_2SO_4 was indistinct, except for the decrease during the first 20 cycles (Figure 3.18b). The L-value of Ubara sandstone with Na_2SO_4 decreased until 160 cycles (from 100% to 62.1%), although the value increased after 160 cycles (81.6% at 300 cycles) (Figure 3.19b).

The L-value changes of Taitozaki mudstone and Miiri mudstone were unclear (Figures 3.20b and 3.21b). The L-value of these mudstones could not be measured in the earlier stages of the experiments, due to crack development and split of specimens

by slaking (Figures 3.9–3.16). The periods in which L-values could be measured were relatively longer for the specimens with Na_2SO_4. The final L-value of Taitozaki mudstone at 60 cycles was 58.6% of L_0, and the final L-value of Miiri mudstone at 160 cycles was 87.9% of L_0 (Figures 3.20b and 3.21b).

The P-wave velocities of Oya tuff and Aoshima sandstone were constant or slightly increased throughout the experiment (Figures 3.17c and 3.18c) with exceptions of decrease during the first 20 humidity cycles. The P-wave velocities of Oya tuff with NaCl could not be measured after 80 cycle (Figure 3.17c), because the surface of the specimen became loose and the transducer of Pundit Plus could not be fixed on the surface.

III-1-5. Weight, L-value, and P-wave velocity in humidity-change experiment at 10°C

Figures 3.24 and 3.25 show the temporal variations in the weight, L-value, and P-wave velocity during the humidity experiments at 10°C. As same as the result of the experiments at 20°C, the weight of Oya tuff and Aoshima sandstone did not show any obvious weight loss (Figures 3.24a and 3.25a), and increased slightly by water absorption from the air in early stage of the experiment. Oya tuff which has a higher porosity (Table 2.2) absorbed more water than the Aoshima sandstone.

The L-values of Oya tuff with NaCl or Na_2SO_4 fluctuated between approximately 80% and 110% of L_0 (Figure 3.24b). The L-values of Oya tuff with $MgSO_4$ fluctuated between approximately 60% and 70% of L_0, after decrease of 34.0% (from 100% to 66.0% of L_0) during the first 20 cycles. The L-values of Aoshima sandstone with $MgSO_4$ were constant during the experiment with the exception of decrease during the first 20 cycles (Figure 3.25b).

The P-wave velocities of all the specimens were constant or slightly decreased during the experiment with the exception of Aoshima sandstone with NaCl (Figures 3.24c and 3.25c). The P-wave velocity of the Aoshima sandstone with NaCl slightly increased through the experiment, with the exception of decrease from 103.1% of Vp_0 at 60 cycles to 87.0% at 80 cycles (Figure 3.25c).

III-1-6. Surface temperature and strain in humidity-change experiments

Figures 3.26–3.29 show typical temperature and humidity, and surface strain changes during two humidity cycles. The increase of strain represents expansion. Air temperature in the ambient chamber temporarily rose at the beginning of the high-humidity period (e.g., Figure 3.26a), and was kept about 1–2°C lower than setting temperature during the high-humidity period. In the low-humidity period, air temperature was kept lower than the high-humidity period. Both the temporary rising in the high-humidity period and the low temperature in the low-humidity period

would be caused by characteristics of the chamber. The temporary rising in air temperature would be caused by heating for humidification. Humidify controller is equipped at a lower part of the chamber, and humidifies air in the chamber by heating water in a tray on a convection heater. This equipment would also heat the air in the chamber, and would result in the temporary rising in air temperature. The heating for humidifying only occurred in the initial tens of minutes of the high-humidity period, because air humidity in the chamber reached almost 100%RH within a first few minutes of the high-humidity period. An air compressor for cooling would cause the low air temperature in the low-humidity period. The compressor also works for dehumidification through the low-humidity period, and lowers the air temperature. The temporary rising of air temperature was distinct in the experiment at 10°C (Figures 3.28a and 3.29a), though the rising was indistinct in the experiment at 20°C (Figures 3.26a and 3.27a). Conversely, cooling in the low-humidity period was more distinct on the experiment at 20°C than the case at 10°C.

As same as air temperature, the surface temperature of the specimens rose at the beginning of the high-humidity period, and lowered in the low-humidity period (e.g., Figure 3.26a). The surface temperatures of most specimens were higher than air temperature, although the patterns of temperature changes through a humidity cycle were analogous. The patterns of the temperature changes varied with a combination of rock type, salt, and temperature. The surface temperatures of specimens with NaCl

or Na_2SO_4 were lower than the specimens with $MgSO_4$ in the low-humidity period (Figures 3.26a, 3.28a and 3.29a), with the exception of Aoshima sandstone at 20°C. In case of Aoshima sandstone at 20°C (Figure 3.27a), the specimen with NaCl showed the higher temperature than the other specimens in the low-humidity period. The specimens with NaCl showed the highest temperature in the high-humidity period (Figures 3.26a–3.28a) with an exception of Aoshima sandstone at 10°C (Figure 3.29a). The specimens with $MgSO_4$ showed similar temperature changes to the controlled specimens (Figures 3.26a, 3.27a and 3.29a), with the exception of Oya tuff at 10°C. Oya tuff at 10°C (Figure 3.28a) showed lower temperature than the controlled specimen during the high-humidity period.

The specimens showed surface expansion in the high-humidity period and contraction in the low-humidity period, although some specimens showed indistinctive changes. Some specimens showed expansion through a humidity cycle (e.g., Oya tuff with NaCl or Na_2SO_4 at 10°C, Figure 3.28b). Two strain gauges were adhered to different faces of a cubic specimen in the humidity-change experiment at 20°C. The two strain gauges adhered to some specimens showed different patterns of change even for the same specimen (e.g., controlled specimen of Oya tuff and Oya tuff with Na_2SO_4, Figure 3.26b). However, these strain changes in a humidity cycle would be insignificant, because that the strain changes of most specimens ranged within ±0.1‰.

Figures 3.30–3.33 show cumulative surface strain changes through 200 humidity cycles. The surface strain of Aoshima sandstone with $MgSO_4$ in humidity-change experiment at 20°C, was lacked due to mechanical trouble during 101–120 cycles (Figure 3.31). The experiment at 10°C had two interruptions for a week in the first and twelve days in the second (Figures 3.32 and 3.33). There are gaps in strain value before and after the interruptions. The surface strains of the specimens with NaCl at 20°C, accumulated through the experiments (Figures 3.30 and 3.31). The specimens with NaCl also showed strain accumulation at 10°C, although the strains were relieved during the interruptions (Figures 3.32 and 3.33). Na_2SO_4 induced strain accumulation on the specimens at 10°C (Figures 3.32 and 3.33), although the specimens with Na_2SO_4 slightly contracted at 20°C (Figures 3.30 and 3.31). The specimens with $MgSO_4$ at 20°C also contracted through the whole experiment (Figures 3.31–3.33), with the exception of expansion in the first 16 cycles of Oya tuff (Figure 3.30). At 10°C, the strain of the specimens with $MgSO_4$ was once accumulated, and relieved in the later stage of the experiment (Figures 3.32 and 3.33). The controlled specimens at 20°C showed minor strain accumulation (Figures 3.30 and 3.31). The strain of controlled specimen of Oya tuff at 10°C (Figure 3.32) was once accumulated from the start of experiment until 14 cycles, and relieved after 14 cycles until the first interruption. Although the strain relieved during interruptions, strain was accumulated again. In case of controlled specimen of Aoshima sandstone

at 10°C (Figure 3.33), the strain did not show distinctive change and the gauge was detached at 10 cycles.

III-2. Results of freeze-thaw experiment

III-2-1. Rock temperature and strain in freeze-thaw experiment

Figures 3.34–3.38 represent typical changes in the temperature of the surface and center of each rock specimen in a freeze-thaw cycle. The increase of strain represents expansion. The air temperature in the ambient chamber occasionally rose in a short period due to auto-defrosting function of the chamber (Figure 2.10). The temperatures and surface strains of specimens were also slightly increased due to the defrosting (e.g., oven dried specimens of Oya tuff, Figure 3.38). The temperatures of rock specimens with salt solutions or distilled water decreased with decreasing air temperature. Once freezing of salt solutions in rock pores began, rock temperature rapidly rose. The temperature was kept constant until solution in rock pores mostly froze (e.g., Oya tuff with Na_2SO_4 solution or distilled water, Figure 3.34a), and decreased once again. In some cases, the surface temperature continued to decrease, although the surface temperature rose when freezing occur (e.g., Shirakawa tuff with NaCl or $MgSO_4$ solution, Figure 3.36a). The rock temperature rose slowly during thawing and rose at a greater rate after termination of thawing (e.g., Oya tuff with NaCl, Figure 3.34a).

Freezing points of salt solutions were lowered by dissolved salts. Table 3.4 summarizes freezing points and turning points measured in this study. A freezing point was defined as a constant temperature after a sudden rise of temperature. A turning point was also defined as temperature immediately before the sudden rise of temperature. Both freezing points and turning point at 1.0 cm depth were comparable or slightly lower than those at 2.5 cm depth. Freezing at 1.0 mm and 2.5 mm occurred almost simultaneously, difference in time was less than 4 minutes.

Theoretical freezing points of each saturated solution are –21.4°C for NaCl, –3.3°C for Na_2SO_4, and –6.7°C for $MgSO_4$ (Jerwood *et al*., 1990a). All solutions and distilled water in specimens were overcooled prior to freezing, because all the turning points were lower than the theoretical freezing point (Table 3.4). The turning point differed with rock types, Andesite showed lower turning point.

The freezing points of NaCl and Na_2SO_4 solutions in the present study were approximately –25°C and –2°C, respectively (Table 3.4). The freezing points of $MgSO_4$ solution and distilled water ranged from –8.1°C to –5.6°C and from –1.5°C to –0.3°C, respectively. The freezing points of NaCl solution or distilled water were lower than the theoretical value as described above, while the values of Na_2SO_4 solution were higher than the theoretical value. For $MgSO_4$, Oya tuff and Aoshima sandstone showed lower freezing points than the theoretical value, while Shirakawa tuff and Andesite showed higher freezing points.

The surface strain of the specimens with salt solution overall decreased with decreasing rock temperature (e.g., Figure 3.34b), which indicates thermal contraction of rock specimens and thermocouples due to cooling. Any strain increase was not observed from 10°C to the freezing points of each solution (Table 3.4). The surface strains rapidly increased when freezing began. The increase in surface strain represents expansion of rock specimen due to ice formation. In case of salt solutions, salt crystallization should simultaneously occur. The rock specimens with salt solutions continued to expand after pore water mostly froze (e.g., Oya tuff with Na_2SO_4 solution, Figure 3.34), and more than 30 later the surface strain reached a local maximum. The surface strain decreased after reaching a peak.

In the thawing period, surface strain basically increased with temperature rise due to thermal expansion (e.g., 3.34). The expansion was temporary moderated due to melting of ice crystal and salt dissolution. The freezing expansion was almost relieved during thawing period.

The right column of Table 3.4 summarizes average freezing strain for each condition. The freezing strain was defined as a difference in strain at the start of expansion and the peak. Table 3.4 also shows ranges of the freezing strain in each cycle. Magnitude of the freezing strain irregularly changed from cycle to cycle. The freezing strains of Andesite were represented as “0”, because that Andesite did not show distinguishable increases in surface strain (Figure 3.37b). Most freezing strains

induced by salt solutions were greater than the strain induced by distilled water (Table 3.4). The solution of two sulfates induced distinct and greater freezing strains than NaCl solution. The freezing strains of NaCl was comparable or lower than the value of distilled water for Oya tuff, while the values of NaCl were greater than the values of distilled water for Aoshima sandstone and Shirakawa tuff.

Figures 3.39–3.43 represent the cumulative strain changes. The recording of temperature and strain were ceased by the end of 20 freeze-thaw cycles, because of the limitation of channel number of data loggers. The recording of strain was also discontinued when the gauge removed from the surface of specimen. Some specimens such as Oya tuff saturated with Na_2SO_4 or distilled water showed distinct accumulation of strain (Figure 3.39). The accumulation indicates generation of cracks or pore expansion in the rock specimens. In contrast, Oya tuff saturated with NaCl contracted. Aoshima sandstone saturated with $MgSO_4$ showed accumulated expansion (Figure 3.40), while the other specimens of Aoshima sandstone showed a trend of contracting. Shirakawa tuff and Andesite did not show any accumulation of strain (Figures 3.41 and 3.42). Shirakawa tuff saturated with distilled water (Figure 3.41) showed gradual contraction with a sudden decrease in strain at the end of 16 cycles. It might be resulted from partial detachment of the strain gauge.

The oven-dried specimens of Oya tuff (Figure 3.38b) showed only thermal contraction and expansion according to temperature oscillation without strain change

due to ice formation and salt phase change (crystallization and hydration). The cumulative strain also did not show significant change (Figure 3.43). The cumulative strains of specimens with salts were less than ±0.3‰ even after 301 freeze-thaw cycles. The cumulative strain of controlled specimen was 2.2‰ after 301 freeze-thaw cycles, although more than 30% of the cumulative strain was due to sudden increase during 293 cycles (from 1.2‰ at 292 cycles to 1.9‰ at 293 cycles).

III-2-2. Weight, L-value, and P-wave velocity in freeze-thaw experiment

III-2-2-1. Temporal variations in weight, L-value and P-wave velocity of oven-dried specimens in freeze-thaw experiment

Figure 3.44 shows the temporal variations in the weight, L-value, and P-wave velocity of specimens oven dried prior to the freeze-thaw experiment. Figure 3.45 shows pictures of the specimens during the freeze-thaw experiment.

Oya tuff specimens (the additional series) oven dried prior to the freeze-thaw experiment showed a mild weight change in the early stage of the experiment (Figure 3.44a). Weight of Oya tuff with NaCl decreased 91.0% of W_0 at 301 cycles, although L-value and P-wave velocity of the specimen slightly increased over 301 freeze-thaw cycles (Figures 3.44b and c). The final values were 124.7% of L_0 for L-value and 124.9% of Vp_0 for P-wave velocity. Any visible sign of breakdown was not observed on the specimen (Figure 3.45).

The weights of the other Oya tuff specimens increased. These weight changes became unclear as the number of freeze-thaw cycle increased, and the weight of the specimens did not change after 100 cycles. The other Oya tuff specimens did not show any distinct change in L-value and P-wave velocity.

III-2-2-2. Temporal variations in weight of specimens with salt solutions in freeze-thaw experiment

Figures 3.46–3.49 show the temporal variations in the weight, L-value, and P-wave velocity of specimens immersed in saturated salt solutions. Figures 3.50–3.53 show pictures of rock specimens during the freeze-thaw experiment for Oya tuff, Figures 3.54–3.57 for Aoshima sandstone, Figures 3.58–3.61 for Shirakawa tuff, and Figure 3.62 for Andesite, respectively.

The specimens with salt solutions showed greater decreases in weight. Oya tuff saturated in salt solutions completely broke down in the early stage of the experiment (Figures 3.50–3.52). The weights of the specimens suddenly decreased at 7 cycles for $MgSO_4$, and 20 cycles for NaCl and Na_2SO_4 (Figure 3.45a). Oya tuff with salt solutions disintegrated into a lot of mm-scale fragments during weighing procedure (when the specimens were picked up from the chamber or the foil covers were removed before weighing). The size of all fragments was smaller than opening of the sieve on which specimens were placed. The specimens with NaCl or $MgSO_4$ showed

minor crack propagation prior to the sudden breakdown (Figures 3.50 and 3.52). The specimens could not resist treatment for weighing, because the specimens weaken by salt crystallization and ice formation prior to the measurement. Oya tuff with distilled water showed moderate crack propagation (Figure 3.53), although the weight of the specimen was constant through the experiment.

The weight of Aoshima sandstone rapidly decreased (Figure 3.47a). Aoshima sandstone saturated in NaCl and Na_2SO_4 solution was completely disintegrated into sand particles at 30 and 20 cycles, respectively. A couple of cm-scale cracks were observed on Aoshima sandstone saturated in NaCl solution at 7 freeze-thaw cycles, and the cracks extended with increasing number of freeze-thaw cycles (Figure 3.54). Aoshima sandstone immersed in Na_2SO_4 solution was suddenly disintegrated into sand particles without any visible crack propagation, although a mm-scale fragment split from edge of the specimen at 19 cycles (Figure 3.55). The weight of specimen saturated in $MgSO_4$ solution suddenly decreased after 40 cycles (Figure 3.47a). A cm-scale cracks was observed on Aoshima sandstone saturated in $MgSO_4$ solution at 5 freeze-thaw cycles (Figure 3.56). The number of cracks increased with increasing number of freeze-thaw cycles, and the cracks gradually connected. The specimen was disintegrated into a lot of fragments and sand particles at 30 cycles. Aoshima sandstone with distilled water did not show any change in its weight and appearance (Figure 3.57).

Shirakawa tuff saturated in NaCl solution showed crack propagation (Figure 3.58), although the weight of the specimen did not decrease (Figure 3.48a). A cm-scale crack was observed lower part of the specimen at 50 cycles, and the crack extended with increasing number of freeze-thaw cycles (Figure 3.58). Shirakawa tuff saturated in Na_2SO_4 solution showed minor disintegration of mm-scale fragments from surface of the specimen (Figure 3.59). Shirakawa tuff did not show any weight loss with the exception of the specimen saturated in $MgSO_4$ solution (Figure 3.48a). The weight of Shirakawa tuff saturated in $MgSO_4$ solution decreased after 30 cycles, and the final weight was 5.4% of W_0 at 301 cycles. The specimen was disintegrated into a couple of fragments and small particles at 40 cycles, and only mm-scale fragments remained on sieve at 100 cycles (Figure 3.60). Andesite did not show any change in their weight and appearance (Figures 3.49a and 3.62).

III-2-2-3. Temporal variations in L-value and P-wave velocity of specimens with salt solutions in freeze-thaw experiment

Table 3.5 shows the reduction rates of L-value, and P-wave velocity, calculated by dividing the final measured value by both the cycle-0 value and the number of freeze-thaw cycles. L-value and P-wave velocity of the specimens decreased with increasing number of freeze-thaw cycles with exception of Andesite (Figures 3.46–3.49). All measurements of these values of Oya tuff with salt solutions were

discontinued by rock breakdown after 9 cycles, particularly the values of specimens saturated in $MgSO_4$ could not be measured after 3 cycles (Figures 3.45b and c). The final L-value at 2 cycles was 56.2% of L_0, and the final P-wave velocity at one cycle was 62.6% of Vp_0. For NaCl, the measurements of L-value and P-wave velocity were discontinued at 5 cycles and 4 cycles, respectively. The final L-value was 57.4% of L_0 and the final P-wave velocity was 13.2% of Vp_0. For Na_2SO_4, the measurements of L-value and P-wave velocity were discontinued at 8 cycles and 7 cycles, respectively. The final L-value was 48.1% of L_0 and the final P-wave velocity was 10.9% of Vp_0. The decreases in L-value and P-wave velocity were also observed on Oya tuff saturated in distilled water. The final values of L-value and P-wave velocity were 60.8% of L_0 and 17.3% of Vp_0, respectively.

All measurements of these values of Aoshima sandstone with salt solution were discontinued by rock breakdown. As same as Oya tuff, these values distinctly decreased in the case of $MgSO_4$ (Figures 3.47b and c). The final L-value at 30 cycles was 35.8% of L_0, and the final P-wave velocity at 17 cycles was 30.1% of Vp_0. For NaCl, the measurements of L-value and P-wave velocity were discontinued at 50 cycles and 40 cycles, respectively. The final L-value was 50.3% of L_0 and the final P-wave velocity was 23.0% of Vp_0. For Na_2SO_4, the measurements of L-value and P-wave velocity were discontinued at 30 cycles and 20 cycles, respectively. The final L-value was 35.8% of L_0 and the final P-wave velocity was 47.2% of Vp_0. Aoshima

sandstone saturated in distilled water moderately decreased. The final L-value at 80 cycles was 77.3% of L_0. P-wave velocity of the specimen did not show any distinct change.

Shirakawa tuff saturated in each of two sulfate solutions showed distinct decreases in their L-value and P-wave velocity (Figures 3.48b and c). For Na_2SO_4, the measurement of P-wave velocity was discontinued at 110 cycles. The final L-value at 120 cycles was 49.4% of L_0, and the final P-wave velocity at 110 cycles was 15.0% of Vp_0. For $MgSO_4$, the measurements of L-value and P-wave velocity were discontinued at 40 cycles. The final L-value was 67.9% of L_0, and the final P-wave velocity was 28.0% of Vp_0. The L-values of specimens saturated in NaCl solution or distilled water did not change distinctly. The P-wave velocities of these specimens were almost constant over 120 freeze-thaw cycles. An aberrant high P-wave velocity was observed on the specimen saturated with NaCl at 12 cycles. The specimen did not show any distinct cracking or other sign of breakdown and the P-wave velocity measured after 13 cycles was comparable with the value measured before 11 cycles. Andesite did not show any distinct change in L-value and P-wave velocity (Figures 3.49b and c).

III-3. Results of total immersion experiment

III-3-1. Weight, L-value, and P-wave velocity in total immersion experiment using saturated solution at 20°C

Figures 3.63–3.65 show the temporal variations in the weight, L-value measured during the total immersion experiment at 20°C. Figures 3.66–3.68 show pictures of rock specimens subjected to total immersion cycles for Oya tuff, Figures 3.69–3.71 for Aoshima sandstone, Figures 3.72–3.74 for Shirakawa tuff, and Figure 3.75 for controlled specimens, respectively. The reduction rates of weight, L-value, and P-wave velocity are summarized in Table 3.6. These reduction rates were calculated by dividing final value by both the cycle-0 value and the number of total immersion cycles. The weights of some specimens could not be measured when the sieve openings became clogged with rock fragments and sieving the fragments was difficult without breakdown of the fragments. In addition, the L-values could not be measured when surface of the specimen became rough.

Although the effect of NaCl was comparable to that of Na_2SO_4 for Oya tuff, NaCl was relatively inactive for Aoshima sandstone. A lot of cracks occurred in Oya tuff with NaCl, and the specimen split into a lot of fragments after 5 cycles (Figure 3.66). The final weight at 13 cycles was 53.8% of W_0 and the final L-value at 9 cycles was 32.0% of L_0 for Oya tuff (Figure 3.63). Aoshima sandstone with NaCl did not show distinct change in neither weight nor L-value (Figure 3.64), although the specimen

split into two cm-scale large fragments controlled by a bedding plane at 7 cycles (Figure 3.69). Shirakawa tuff immersed in NaCl did not showed any distinct change in weight and L-value (Figure 3.65). The surface of the specimen became rough with an increase of the number of total immersion cycles, and mm-scale fragments split from surface of the specimen (Figure 3.72).

Na_2SO_4 substantially damaged Oya tuff and Aoshima sandstone. Oya tuff with Na_2SO_4 split into a lot of fragments at 7 cycles and the final weight at 13 cycles was 43.8% of W_0 (Figures 3.63a and 3.67). The L-value of the specimen rapidly decreased and the final L-value at 9 cycles was 44.8% of L_0 (Figure 3.63b). A cm-scale crack occurred in Aoshima sandstone with Na_2SO_4 at 4 cycles, the specimen disintegrated rapidly after 5 cycles. The final weight at 13 cycles was 15.4% of W_0 and the final L-value at 9 cycles was 24.1% of L_0 (Figure 3.64). Shirakawa tuff with Na_2SO_4 also showed weight loss and L-value reduction (Figure 3.65). A cm-scale crack occurred at 8 cycles, and the specimen split into various sizes of fragments at 13 cycles. The final weight at 20 cycles was 71.0% of W_0 and the final L-value at 12 cycles was 57.1% of L_0.

Among in the three salts, $MgSO_4$ induced the largest damage to Oya tuff and Shirakawa tuff. Oya tuff immersed in $MgSO_4$ split into a lot of fragments after 5 cycles, and almost no fragments remained on the sieve at 16 cycles (Figures 3.63a and 3.68) The L-value of the specimen could not be measured after 2 cycles (Figure

3.63b). Shirakawa tuff immersed in $MgSO_4$ split into various sizes of fragments after 6 cycles (Figure 3.74). The final weight at 20 cycles was 26.6% of W_0 and the final L-value at 5 cycles was 59.1% of L_0 (Figure 3.65). For Aoshima sandstone specimens, $MgSO_4$ induced substantial weight loss and reduction in L-value (Figures 3.64). The shape of the specimen gradually became rounder with an increase of the number of total immersion cycles (Figure 3.71). The final weight at 20 cycles was 21.7% of W_0 and the final L-value at 9 cycles was 44.8% of L_0.

The controlled specimens immersed in distilled water did not show distinct changes in weight (Figures 3.63–65). The specimen did not show any sign of weathering (Figure 3.75). The L-values of Oya tuff and Shirakawa sandstone increased with increasing number of total immersion cycles (Figures 3.63b and 3.65b), and the L-values of Aoshima sandstone fluctuated between 80.8% and 101.2% of L_0 (Figure 3.64b).

III-3-2. Weight, L-value, and P-wave velocity in total immersion experiment using saturated solution at 10°C

Figures 3.76–3.78 show the temporal variations in the weight, L-value measured during the total immersion experiment at 10°C. Figures 3.79–3.81 show pictures of rock specimens subjected to the total immersion experiment for Oya tuff, Figures 3.82–3.84 for Aoshima sandstone, Figures 3.85–3.87 for Shirakawa tuff, and Figure

3.88 for controlled specimens, respectively. The reduction rates of weight, L-value, and P-wave velocity are summarized in Table 3.6. The weights of some specimens could not be measured after the sieve openings became clogged with rock fragments. In addition, the L-values could not be measured after their surfaces became rough.

Oya tuff immersed in NaCl showed weight losses and L-value reductions (Figures 3.76 and 3.79). The specimen split into a lot of fragments after 3 cycles. The L-value of Oya tuff could not be measured at 3 cycles. The final weight at 10 cycles was 4.8% of the W_0 and the final L-value was 60.9% of L_0 at 2 cycles. Aoshima sandstone immersed in NaCl also showed weight loss in the later stage of the experiment (Figures 3.77 and 3.82). The final weight was 42.3% at 20 cycles. The L-value of Aoshima sandstone moderately decreased, and the final L-value at 20 cycles was 49.0% of L_0. Shirakawa tuff immersed in NaCl did not showed distinct changes in its weight and L-value (Figure 3.78), although some mm- and cm- scale fragments split from surface of the specimen (Figure 3.85).

Oya tuff immersed in Na_2SO_4 showed weight loss in the later stage of the experiment (Figures 3.76 and 3.80). The weight of specimen decreased from 91.3% of W_0 at 15 cycles to 60.2% at 20 cycles. A lot of cracks occurred in the specimen, and the specimen split into a lot of fragments after 10 cycles. Aoshima sandstone and Shirakawa tuff immersed in Na_2SO_4 kept more than 95% of W_0 at 20 cycles (Figures 3.77 and 3.78). Cracks occurred in Aoshima sandstone after 4 cycles (Figure 3.83).

Some mm-scale tabular fragments split from surface of Shirakawa tuff (Figure 3.86). The L-values of Oya tuff and Aoshima sandstone also decreased. The final L-values were 45.2% of L_0 at 10 cycles for Oya tuff, and 41.4% at 6 cycles for Aoshima sandstone.

Oya tuff immersed in $MgSO_4$ rapidly disintegrated (Figures 3.76 and 3.81). The specimen split into a lot of fragments after 2 cycles, and any fragment did not remain on the sieve at 15 cycles (Figure 3.81). The L-value of the specimen could not be measured after 2 cycles. The final L-value at one cycle was 83.9% of L_0. $MgSO_4$ caused the greatest weight loss and the second greatest reduction in L-value to Aoshima sandstone (Figures 3.77 and 3.84). Cracks occurred in the specimen at 13 cycles. Tabular fragments split from the surface after 15 cycles, and shape of the specimen gradually became rounder as an increase with the number of total immersion cycles. The final weight at 20 cycles was 39.3% of W_0 and the final L-value at 9 cycles was 37.6% of L_0. $MgSO_4$ also caused the greatest weight loss and L-value reduction to Shirakawa tuff (Figures 3.78 and 3.87). Cracks occurred in the specimen, and the specimen split into various sizes of fragments after 9 cycles. The final weight at 20 cycles was 35.1% of W_0 and the final L-value at 10 cycles was 51.5% of L_0.

The controlled specimens immersed in distilled water did not show distinct changes in weight and L-value with an exception of L-value of Aoshima sandstone

(Figures 3.76–3.78 and 3.88). The L-value of Aoshima sandstone decreased with increasing number of total immersion cycles (Figure 3.77). The specimen did not show any sign of weathering (Figure 3.88).

Chapter IV. Discussion

IV-1. Interpretation of humidity-change experiment

IV-1-1. Salt crystallization processes in humidity-change experiment

IV-1-1-1. Salt deliquescence in high-humidity period

During the high-humidity period, all three salts appeared to form a solution by dissolving into the water absorbed from the air, indicating occurrence of salt deliquescence. Salt deliquescence occurs when the vapor pressure of a saturated salt solution on salt crystals is less than the vapor pressure of water in the air. The relative humidity rapidly increased and reached almost 100%RH within a first few minutes in the high-humidity period (Figure 2.7).

Apelblat and Korin (1998, 2002) and Apelblat and Manzurola (2003) summarized the relative humidity when salt deliquescence occurs, referred to as deliquescence relative humidity (DRH). The practical DRHs of the three salts are 75.0–79.0%RH for NaCl, 83.3–95.1%RH for Na_2SO_4 and 92.7%RH for $MgSO_4$ at 20°C. The practical DRHs at 10°C are 75.5–85.0%RH for NaCl, 74.4–75.1%RH for Na_2SO_4 and 87.0–96.4%RH for $MgSO_4$.

The DRH of two sulfates differ with type of hydrated form. Na_2SO_4 exists in two stable phases: thenardite (anhydrate) and mirabilite (decahydrate). Theoretical DRH at 20°C of thenardite and mirabilite is 86.6%RH and 95.6%RH, respectively (Steiger and Asmussen, 2008). $MgSO_4$ has three stable hydrated forms: kieserite

(monohydrate), hexahydrate and epsomite (heptahydrate) (Chou and Seal, 2003; Vaniman *et al*., 2004; Balboni *et al*., 2011). Though a large number of metastable forms of $MgSO_4$ have been identified, the behavior of these metastable forms is still unclear (Chipera and Vaniman, 2007). An amorphous hydrate phase was also detected (Vaniman *et al*., 2004). Theoretical DRH at 20°C of kieserite, hexahydrate and epsomite is approximately 58%RH, 86%RH and 91%RH, respectively.

The high salt content of the specimens (Table 3.1) and the low DRH of NaCl (75.0–79.0%RH at 20°C) caused the largest weight gain of specimens, i.e., the greatest moisture absorption from air in the high-humidity period (Table 3.3). As described in section IV-1-1-2, the high absorption capacity would also have been affected by the fact that NaCl does not hydrate substantially. The specimens with NaCl could absorb greater amounts of water because NaCl only dissolved and made a solution with deliquescence.

The amount of moisture absorption is attributed to both the salt content in the specimens and the DRH of salts. At 20°C, the amount of moisture absorption of the specimens with Na_2SO_4 were lower than those with $MgSO_4$ (Table3.3). The smaller moisture absorption at 20°C would be triggered by the smaller salt content of the rock specimens (Table 3.1), while the DRH of Na_2SO_4 is comparable with the DRH of $MgSO_4$. At 10°C, the moisture absorption of the specimens with Na_2SO_4 was comparable to that with $MgSO_4$. The DRH of Na_2SO_4 at 10°C (74.4–75.1%RH) was

significantly lower than the value of $MgSO_4$ (87.0–96.4%RH), while the salt content of rock specimens with Na_2SO_4 were lower than the values of the specimens with $MgSO_4$.

IV-1-1-2. Salt hydration processes in high-humidity period

Hydration processes would also occur in the high-humidity period. Salt recrystallization of two sulfates occurred on the specimens approximately 30 minutes after the high-humidity period started, although saturated solution was formed by deliquescence at the beginning of the high-humidity period.

Steiger *et al*. (2008) described detailed hydration-dehydration system of $MgSO_4$. They suggested that hydration of kieserite (monohydrate) and formation of hexahydrate occur rapidly when the relative humidity exceeds the DRH of kieserite (60%RH at 25°C), although the reaction proceeds above the equilibrium relative humidity between kieserite and hexahydrate (42%RH at 25°C). The rapid reaction occurs as a two-step process of deliquescence and subsequent crystallization. Because the saturated solution of low-order hydrated form is supersaturated to high-order hydrated form, the high-order hydrated form crystallizes from the saturated solution (Flatt, 2002).

Steiger *et al*. (2008) also reported that epsomite (heptahydrate) did not form above the equilibrium RH between hexahydrate and epsomite (51%RH at 25°C). However,

they did not confirm which kind of hydrated crystals form at relative humidity above the DRH of hexahydrate (81%RH at 25°C). Epsomite when form when the relative humidity exceeds the DRH of hexahydrate. Their experimental results implied that the two-step hydration process is significantly faster than direct hydration (from crystal to crystal).

At the beginning of the present humidity-change experiment, kieserite should crystallize on the surface of oven-dried specimens at 110°C. The two-step hydration process of deliquescence of kieserite and the subsequent crystallization of hexahydrate would have occurred rapidly above the DRH of hexahydrate (approximately 86%RH at 10–20°C), while the direct hydration (crystal to crystal) would also have occurred above the equilibrium RH of kieserite (39%RH at 20°C and 35%RH at 10°C). The crystallization of epsomite may have occurred above the DRH of epsomite (91–93%RH at 10–20°C), although the formation of solution and subsequent recrystallization appeared only once during a high-humidity period. The RH values are derived from Steiger *et al*. (2008).

For the specimens with Na_2SO_4, the two-step hydration process of deliquescence and the subsequent crystallization of hydrated salt have also occurred. At the beginning of the experiments, thenardite should crystallize on the surface of oven-dried specimens at 110°C (Flatt, 2002). Thenardite deliquescence and subsequent crystallization of mirabilite would have occurred above the DRH of

thenardite (85–87%RH at 10–20°C), while direct hydration from thenardite to mirabilite would have occurred above the equilibrium RH (76.4%RH at 20°C and 68%RH at 10°C). The RH values are derived from Steiger and Asmussen (2008).

The sequence of deliquescence and hydration of thenardite should occur at the beginning of every high-humidity period. However, the deliquescence and phase changes of Na_2SO_4 were most distinct in the first high-humidity period. These changes became unclear with increasing number of humidity cycles, and the rock surface became covered with efflorescence of Na_2SO_4 (e.g., Figure 3.2). The pores of Oya tuff were filled by the efflorescence at the end of the experiment (Figure 3.23a), although most efflorescence on rock surface was gradually detached.

The hydration-dehydration of Na_2SO_4 would hardly have occurred during the present experiments, in which the air humidity oscillated over a short interval. Kwaad (1970) emphasized that the hydration rate of Na_2SO_4 is much slower than that of $MgSO_4$. They placed some kinds of salt crystals oven-dried at 105°C under the condition with 90%RH for humidity and 20°C for temperature. Na_2SO_4 did not adsorb any water during the 12-hour period of the experiment. Goudie and Viles (1997) also revealed the slow hydration of Na_2SO_4. York Stone specimens were immersed in some salt solutions, oven dried at 105°C and subjected to the condition with 25°C in temperature and 90%RH in humidity. Weight gain of rock specimen with Na_2SO_4 was less than half of that of specimen with $MgSO_4$.

The accumulated efflorescence of Na_2SO_4 would occur due to the following reasons. Thenardite deliquescence and subsequent crystallization of mirabilite would have occurred in the early stage of the humidity-change experiment. The deliquescence of mirabilite hardly occurred due to the high DRH of mirabilite (95.6% at 20°C and 97.8%RH at 10°C). The dehydration to thenardite also have been hindered by the slow hydration-dehydration rate. As a result, the efflorescence of mirabilite accumulated in the later stage of the humidity-change experiment (Figure 3.23a).

The hydrated salt might hinder further hydration of anhydrate salt due to pore clogging of rock specimen (Steiger and Asmussen, 2008). Yu and Oguchi (2010a) suggested that Na_2SO_4 occasionally crystallized in rock pores and filled the pore. The hydration of the two sulfates involves volume expansion of salt crystals. The hydrated crystals might have filled pores in the rock and hindered infiltration of water (Steiger and Asmussen, 2008). In fact, the pores of Oya tuff subjected to 200 humidity cycles were filled by the efflorescence of Na_2SO_4 (Figure 3.23a).

The specimens with NaCl or $MgSO_4$ did not show such behavior in the present experiments, although Espinosa-Marzal and Scherer (2013) revealed that these three salts could induce pore clogging. They also revealed that the occurrence of pore clogging was affected by type of salts and pore structure. Charola *et al*. (2006) attributed slow crystallization of gypsum to accumulation of salt and results in pore

clogging on the surface and subsurface of porous material. The slow hydration rate of Na_2SO_4 might have resulted in the salt accumulation in rock pores in the present experiments (Figure 3.23a).

IV-1-1-3. Salt crystallization and dehydration processes in low-humidity period

Salt crystallized from solution at the beginning of the low-humidity period. NaCl only crystallized as halite. Mirabilite should start to crystallize from the solution at the DRH of mirabilite (95.6%RH) and dehydrate to thenardite below the equilibrium RH for mirabilite to thenardite (76.4%RH) (Steiger and Asmussen, 2008). The crystallization of thenardite is dominant below the DRH of thenardite (86.6%RH at 20°C), while both mirabilite and thenardite crystallize directly from solution (Steiger and Asmussen, 2008). At 10°C, the DRH of mirabilite and thenardite are 97.8%RH and 85.6%RH, and the equilibrium RH for mirabilite to thenardite is 68.2%RH.

The epsomite and hexahydrate would have crystallized in the low-humidity period. The kieserite would rarely have crystallized under the humidity conditions of the present study, because the kieserite formation is limited by the low equilibrium humidity (39%RH at 20°C and 35%RH at 10°C) between hexahydrate and kieserite (Balboni *et al*., 2011).

IV-1-2. Effect of pre-treatment prior to humidity experiment

The damage caused by the initial immersion in a salt solution and oven drying were relatively weak with exceptions of slaking for mudstones (Table 3.2). The specimens of Oya tuff, Aoshima sandstone, and Ubara sandstone did not show any obvious crack propagation, flaking, or swelling after the pre-treatment (at 0 cycles) (Figures 3.1–3.8). The changes in the L-value (Table 3.2) would be mainly induced by changes in surface micro topology due to salt efflorescence. Except for two mudstone specimens affected by slaking (Figures 3.9–3.16), the damage caused by the pre-treatments is negligible in comparison with the damage induced by the subsequent humidity cycles.

Weights of the specimens slightly increased during the first 20 humidity cycles due to rapid moisture absorption, because the pre-treated specimens were almost totally dry. Increase of surface roughness due to salt deliquescence and hydration would cause the decrease in L-value during the first 20 humidity cycles (Figures 3.17–3.19 and 3.24–3.25). Salt hydration and crystallization of the hydrated crystals would cause changes in the surface micro morphology, which cause the reduction in the L-value.

IV-1-3. Effect of salt type on weathering in humidity-change experiment

The specimens subjected to the humidity oscillation showed concentrated damage

on their surfaces (Figure 3.22). Among the three kinds of salt, NaCl caused the largest damage to all types of rock in the humidity-change experiment at 20°C (Figures 3.17–3.21), whereas NaCl was relatively inactive as a weathering agent in the other experiments. $MgSO_4$ caused the second largest damage to the specimens. Na_2SO_4 was mostly inactive as a weathering agent in the humidity-change experiment. In contrast, these two sulfates, particularly $MgSO_4$ caused more extensive damage to rock specimens than NaCl (Tables 3.5 and 3.6).

The degrees of damages induced by each salt were in proportion to the amount of moisture absorption during the high-humidity period. Figure 4.1 shows relationship between the weight gain and reduction rates of weight or L-value for Oya tuff and Aoshima sandstone. Most of the weight reduction rates were negative, because the specimens absorbed moisture from air. The reduction rates of L-value increased with increasing weight gain.

The lower DRH of NaCl resulted in greater water absorption from the air (Table 3.3), and in turn, the greater absorption induced greater weight losses and reduction in L-value (Figures 3.17–3.19) by salt weathering. The specimens with Na_2SO_4 were less damaged than the specimens with $MgSO_4$, although the DRH of Na_2SO_4 was lower than or comparable to the DRH of $MgSO_4$. In the present experiment, as mentioned in section IV-1-1-2, the slow hydration-dehydration rates of Na_2SO_4 and the high DRH of mirabilite (decahydrate) would have restricted their activity. Na_2SO_4

is generally regarded as one of the most aggressive salts in both field and laboratory (Smith and McGreevy, 1983; Goudie and Viles, 1995, 1997; Thomachot-Schneider *et al*., 2011). However, the relative importance of $MgSO_4$ to Na_2SO_4 might increase in environments in which air humidity oscillated over a short interval.

Cracking parallel to the rock surface, which occurred in the Aoshima sandstone with $MgSO_4$ (Figure 3.22d) and in the Oya tuff with Na_2SO_4 (Figure 3.23b), reveals that salt weathering occurred only within several-millimeter depths from the surface. The interiors were not weathered much, because the P-wave velocities of the specimens did not decrease (Figures 3.17 and 3.18). López-Arce *et al*. (2011) suggested that porous dolostone is sensitive to diurnal cycles of air humidity at depths up to 3 cm. For the shorter interval of humidity change in the present experiment, the depth at which air humidity was effective would be less than a centimeter from the rock surface. Ruiz-Agudo *et al*. (2007) carried out a laboratory experiment using solutions of Na_2SO_4 and $MgSO_4$. Na_2SO_4 and $MgSO_4$ were both extremely damaging to rock specimens in their experiment. They reported that Na_2SO_4 caused localized damage and detachment, whereas $MgSO_4$ induced cracks and fractures. Balboni *et al*. (2011) explained that the different behaviors of the two sulfates are due to the different viscosities of their solutions. They assumed that the high viscosity of $MgSO_4$ retards solution transport and crystal nucleation, and result in crack propagation.

The specimens with NaCl did not show distinct crack for Oya tuff and Aoshima sandstone (Figure 3.22). Although Ubara sandstone split into two cm-scale fragments at 40 cycles, granular disintegration was dominant. NaCl tends to crystallize on the surface, and this crystallization pattern is referred to as efflorescence. In contrast, Na_2SO_4 and $MgSO_4$ tends to crystallize within rock pores, referred to as subflorescence. Salt subflorescence induces greater crystallization pressure than salt efflorescence (Rodriguez-Navarro and Doehne, 1999; Doehne, 2002; Mottershead, 2013). The difference in the crystallization patterns might cause the absence or presence of cracks on the specimen surface.

IV-1-4. Relationship between rock properties and weathering rate

Pore-size distribution, micro-pore volume, and specific surface area generally affect susceptibility to physical weathering (Zehnder and Arnold, 1989; Matsuoka, 1990; Matsukura and Matsuoka, 1996; Ordóñez *et al*., 1997; Benavente *et al*., 2004; Yu and Oguchi, 2010b). Matsukura and Matsuoka (1996) assumed that rock fracture occurs when salt crystallization pressure exceeds tensile strength of rock, and defined Weathering Susceptibility Index *WSI*, which is calculated by:

$$WSI = \frac{P}{S_t} \tag{6}$$

where P is total pressure generated in unit volume of rock, given by:

$$P = \sum_{i=1}^{4} p_i V_i \rho_{bulk} \tag{7}$$

where p_i and V_i are crystallization pressure and pore volume per unit weight of rock for each grade of pores, assuming median pore diameter to be 10 μm for large pores (d_1-size), 1 μm for medium pores (d_2-size), 0.1 μm for small pores (d_3-size), and 0.01 μm for very small pores (d_4-size), respectively. V_1, V_2, V_3, V_4 are total volumes of pores with diameters of $10^{1.5}$–$10^{0.5}$ μm (large pore), $10^{0.5}$–$10^{-0.5}$ μm (median pore), $10^{-0.5}$–$10^{-1.5}$ μm (small pore), and less than $10^{-1.5}$ μm (very small pore), respectively. Table 2.3 shows the pore volumes of rocks used for experiments. P_i is given by following equation:

$$p_i = \frac{4\sigma}{d_i} \tag{8}$$

where σ is surface tension between solid and liquid, and d_i is the median diameter of each grade of pore. Table 4.1 shows the surface tension of saturated salt solutions or distilled water at 20°C. The surface tension data were referred to Gauri *et al*. (1990) for NaCl, Ruiz-Agudo *et al*. (2007) for Na_2SO_4 and $MgSO_4$, and Hardy (1977) for

distilled water, although the surface tension is varied by method and environment for measurement. Figure 4.2 shows relationship between *WSI* and the reduction rate of L-value in the humidity-change experiment at 20°C. Two mudstones were excluded from the figure, because these mudstones showed slaking. The relationship between *WSI* and the L-value reduction was indistinct compared with the relationship between moisture absorption and the L-value reduction (Figure 4.1). The deliquescence susceptibility of salt had more influence on the L-value reduction than the salt weathering index.

Ubara sandstone showed the greater weight losses than Oya tuff in the humidity-change experiment (Figures 3.17 and 3.19). These two types of rock have comparable properties with higher porosity and lower tensile strength (Table 2.2). V_{total} of Ubara tuff was lower than that of Oya tuff, although Ubara sandstone has comparable effective porosity with Oya tuff (Table 2.3). In addition, Ubara sandstone had a large proportion of V_1. Ubara sandstone would have greater volume of mm-scale pores which are larger than 200 μm in diameter, while Oya tuff would also have mm-scale pores resulting from the alternation of pumice. The larger volume of mm-scale pores might promote moisture infiltration to interior rock and resulted in the greater weight losses than Oya tuff.

IV-2. Interpretation of freeze-thaw experiment

IV-2-1. Salt crystallization processes and strain in freeze-thaw experiment

Salt crystallization processes in the freeze-thaw experiment were composed of two sequences. First, salt would crystallize from saturated solution prior to freezing, because salt solubility decreases with temperature falls. According to phase diagrams by Jerwood *et al*. (1990a), NaCl theoretically crystallizes as dihydrate form below –0.1°C, and as anhydrate form above the temperature. Na_2SO_4 crystallizes as mirabilite (decahydrate) until freezing. $MgSO_4$ crystallizes as epsomite (heptahydrate) above 1.8°C, and as dodecahydrate form below the temperature.

Aoshima sandstone and Shirakawa tuff with Na_2SO_4 solution showed surface expansion prior to freezing (Figures 3.35b and 3.36b). The other specimens did not show the expansion prior to freezing. The reduction in solubility of Na_2SO_4 with falling temperature is larger than those of the other two salts (Table 2.4). A larger amount of crystals of Na_2SO_4 would crystallize in rock pores prior to freezing than the other two salts. The surface expansions prior to freezing would be induced by the crystallization from saturated solution prior to freezing.

In addition, Na_2SO_4 tends to crystallize in smaller pores due to lower viscosity of solution compared with $MgSO_4$ (Ruiz-Agudo *et al*., 2007). Mirabilite would have crystallized and filled the micro pores of the specimens, and caused the surface expansion prior to freezing. The lower proportion of V_3 and V_4 of both Aoshima

sandstone and Shirakawa tuff (Table 2.3), also facilitated the filling of micro-pores by mirabilite.

Secondly, ice formation and salt crystallization simultaneously occur after termination of supercooling below a freezing point of salt solutions. Ice and salt crystal form eutectic crystal referred to as cryohydrate, although the behavior of the cryohydrate is unclear. Most expansion of specimens during freeze-thaw experiment were induced by the second process. The freezing strains for salt solution of two sulfates were significantly greater than those for distilled water (Table 3.4). A large proportion of the freezing strain would be induced by salt crystallization of sulfates.

In contrast, the freezing strains induced by NaCl solution was comparable with the values induced by distilled water (Table 3.4). NaCl solution in pores would be mostly frozen, because rock temperature decreased again before the end of freezing period (Figures 3.34–3.39). In addition, the freezing of NaCl began more than 3 hours before the end of freezing period. At least, the freezing expansion by saturated NaCl solution should have occurred for Oya tuff and Aoshima sandstone, because these specimens showed comparable reductions of L-value and P-wave velocity than the specimens with two sulfates (Table 3.5).

The absence of salt crystallization prior to freezing may restrict the freezing expansion, the cause of the small expansion of specimens with NaCl is not clear. As described above, crystal of sulfates, particularly Na_2SO_4 would fill micro pores of the

specimens prior to freezing. Therefore, sulfate crystals would easily induce freezing expansion when freezing began. In contrast, NaCl may not be able to fill the micro pores of the specimen prior to freezing, because the reduction in solubility of NaCl with falling temperature is smaller than the two sulfates. The different salt behavior prior to freezing may result in the difference in the freezing strain.

IV-2-2. Effect of thermal stress during freeze-thaw cycles

The oven-dried specimens of Oya tuff did not show any disintegration and crack propagation (Figures 3.45). Only the specimen with NaCl showed minor decrease in weight. Moisture absorption from air would cause salt deliquescence and leaching from rock surface, and resulted in the decrease in weight. L-value and P-wave velocity of the specimens did not show any sign of breakdown. The strain of the specimens showed only cyclic thermal contraction and expansion (Figure 3.38), and no cumulation at 301 freeze-thaw cycles (Figure 3.43). Rock breakdown by thermal stress would be negligible for all the specimens with salt solutions as well as the oven-dried specimens.

IV-2-3. Effects of salt and rock type on weathering in freeze-thaw experiment

NaCl induced comparable damages on rock specimens with Na_2SO_4, same as the freeze-thaw experiment using saturated salt solution in an early work by Williams and

Robinson (1981). The specimens with $MgSO_4$ solution produced the largest weight loss, reductions of L-value, P-wave, and freezing strain under the condition for the present experiment (Tables 3.4 and 3.5). In contrast, $MgSO_4$ was assumed to be relatively inactive salt in freeze-thaw experiment using salt solution with mild or dilute concentration (McGreevy, 1982; Fahey, 1985; Jerwood *et al*., 1990a, b). Fahey (1985) noted that "the presence of $MgSO_4$ in solution had no noticeable effect". These works with exception of Jerwood *et al*. (1990b) employed an open system condition in which rock specimen was partly immersed in salt solution. In such a condition, salt solutions continuously migrate from the saturated part to freezing front (Akagawa and Fukuda, 1981; Matsuoka, 2001), which favors ice segregation and expansion of rock specimen. As described in the section IV-3, solution of $MgSO_4$ has high viscosity compared with the other two salts. The high viscosity would retard moisture migration to freezing front, and result in the ineffectiveness of $MgSO_4$.

The specimens were isolated from additional moisture in the present freeze-thaw experiment. In addition, freezing at rock surface and interior occurred simultaneously as described in section III-2-1. Moisture migration and ice segregation rarely occurred in such condition, salt solutions in pores would freeze on site. Further discussion on the greatest damage by $MgSO_4$ is described in section IV-4-2.

Matsuoka (1990) applied the adsorption force theory to frost shattering of rocks under open-system condition, and revealed that specific surface areas of rock

specimens showed the better correlation with reductions of P-wave velocity of the specimens than an index based on the capillary force theory. The index based on the adsorption force theory I_a is calculated by:

$$I_a = \frac{\rho_{bulk} SSA}{V} \tag{9}$$

Figure 4.3 shows relationship between I_a and freezing strain, reduction rates of L-value and P-wave velocity. Figure 4.4 also shows relationship between *WSI* and freezing strain, reduction rates of L-value and P-wave velocity, although *WSI* is essentially used as a weathering index for salt weathering. *WSI* can be employed as an alternative index based on the capillary force theory, because *WSI* are calculated using surface tension of pore water. Andesite was excluded from the figure, because Andesite did not show any sign of weathering (Figures 3.49 and 3.62).

WSI of salt weathering index showed the better correlation than I_a of index for frost shattering. The freezing strain, reduction rates of L-value and P-wave velocity increased with increasing *WSI.* The freezing strain and reduction rate of L-value are also correlated to I_a (Figures 4.3a and 4.4a), although correlation of reduction rate of P-wave velocity and I_a was indistinct. Occurrence of salt crystallization in addition to ice formation would be the cause of the weak correlation with I_a, which is an index

for frost shattering without the effect of salts. In contrast, *WSI* showed the better correlation by evaluating the surface tension of each salt solution in addition to the effect of pore-size distribution of rock. Further discussion on the correlation with *WSI* is described in section IV-4-2

IV-3. Salt crystallization processes in total immersion experiment

The less hydrated forms of each salt, i.e., halite, thenardite (anhydrate), and kieserite (monohydrate), would be crystallized by oven drying at 110°C. Crack propagation and disintegration of the specimens with sulfates mainly occurred when the specimens were immersed in distilled water. Hydration of thenardite and kieserite would have occurred during the immersion. Distilled water was used in the wetting sequence (Figure 2.11), whereas the previous experiments often used salt solutions with various concentrations. Distilled water penetrated into the rock specimens while the water dissolved thenardite and kieserite, and their solution would have reached saturation. There was no sign of rock breakdown during the subsequent oven drying and immersion in salt solution, although crystallization and hydration would have been possible if salt remained in the specimens. For NaCl, only halite should crystallize and dissolve in the present total immersion experiment. NaCl does not hydrate in the experimental condition, because dihydrate of NaCl can form for ambient temperature below –0.1°C.

Among the three salts, $MgSO_4$ induced the largest damage to the rock specimens in the total immersion experiment using saturated salt solution both at 10°C and 20°C. (Figures 3.63–3.65 and 3.76–79, and Table 3.6). NaCl induced greater damage than Na_2SO_4 in the experiment using saturated salt solution at 10°C (Table 3.6). In contrast, inverse results were obtained in the experiment using saturated salt solution at 20°C.

Figure 4.5 shows relationship between *WSI* and reduction rates of L-value. L-values in the experiment using saturated salt solution at 20°C showed the better correlation with *WSI*, because *WSI* is calculated using surface tensions of saturated salt solutions at 20°C. The relationship between *WSI* and reduction in L-value is totally conformable the results of the past total immersion experiment (Yamada *et al*., 2005). The effectiveness of each salt in the present total immersion experiment is reasonable compared with the previous studies described in section I-2-2.

IV-4. General discussion

IV-4-1. Different weathering pattern between humidity-change experiment and total immersion experiment

Oya tuff and Aoshima sandstone subjected to the humidity oscillation showed concentrated damage on their surfaces (Figure 3.22). In contrast, the specimens subjected to total immersion cycles showed entire disintegration and crack propagation (Figures 3.66–3.71 and 3.79–3.84). As described in the section IV-3, the

dominant weathering processes in the total immersion experiment would be salt crystallization of halite and hydration of thenardite (anhydrate) or kieserite (monohydrate). These processes are almost the same as those expected in the humidity-change experiment, i.e., deliquescence-recrystallization of halite, hydration of thenardite and hexahydrate of $MgSO_4$. Therefore, the weathering mechanisms are not a major cause of the difference in damages between the humidity-change experiment and total immersion experiment, though crystallization/hydration pressures vary with temperature and humidity (Flatt, 2002). The difference between humidity-change experiment and total immersion experiment is mainly due to the difference in the methods of water supply. As described in section IV-1-3, the depth at which air humidity was effective would be less than a centimeter from the rock surface in the present humidity change experiment (López-Arce *et al*., 2011). In contrast, salt solutions immersed in deep part of the rock specimens.

$MgSO_4$ showed particularly distinct difference in weathering patterns between the two experiments. The overall crack propagation and rock breakdown by $MgSO_4$ occurred in the present total immersion experiment (e.g., Figures 3.60 and 3.68). In contrast, cracking parallel to rock surface occurred on rock surface with $MgSO_4$ in the humidity-change experiment (3.22d). NaCl did not induce such a highly localized cracking, although NaCl also induced flaking on rock surface. The high viscosity of $MgSO_4$ retards solution transport and crystal nucleation, and result in crack

propagation when abundant salt water is supplied to the rock specimen (Ruiz-Agudo *et al*., 2007; Balboni *et al*., 2011). In contrast, the high viscosity hindered moisture infiltration into rock interior and induced highly concentrated cracking in the humidity-change experiment.

IV-4-2. Comparison between freeze-thaw experiment and total immersion experiment

Among the three salts, $MgSO_4$ induced the largest damage to the rock specimens in the freeze-thaw experiment (Figures 3.45–47 and Table 3.5). NaCl induced comparable damages on rock specimens with Na_2SO_4. The greater damage by $MgSO_4$ was also observed in the present total immersion experiment using saturated salt solutions at 10˚C (Figures 3.76–3.78 and Table 3.6). Na_2SO_4 induced relatively larger rock breakdown than NaCl. Reduction rates of L-value for freeze-thaw experiment (Figure 4.4b) and those for total immersion experiment (Figure 4.5) ranged at almost the same magnitude and order. L-value reductions in the present freeze-thaw experiment using saturated salt solution are similar to the reduction in the total immersion experiment using same salt solution. In addition, freezing strains, reduction rates of L-value and P-wave velocity are correlated with *WSI*, as described in section IV-2-3. These results imply significant contribution of salt crystallization to rock breakdown due to freezing of saturated salt solutions.

Salt crystallization facilitated rock breakdown in the freeze-thaw experiment using saturated salt solution. Jerwood *et al*. (1990b) carried out freeze-thaw experiment in two ways using salt solutions with dilute or mild concentrations. They suggested that salt crystallization was dominant weathering process in low-moisture environments, while frost shattering process was dominant when a large amount of moisture is supplied. The specimens were isolated from moisture source during the present freeze-thaw experiment, while the specimens were saturated with salt solutions. In addition, the present freeze-thaw experiment employed saturated salt solution instead of dilute concentration. As described in Jerwood *et al*. (1990b), salt crystallization significantly contributes to rock breakdown in the present freeze-thaw experiment.

The reduction rates of L-value in the freeze-thaw experiment were smaller than the values in the total immersion experiment at 10°C, although ice formation also occurred in addition to salt crystallization. Salt crystallization in freeze-thaw experiment only occurred during freezing period. In contrast, the two-step salt reaction occurred during one total immersion cycle, i.e., crystallization by oven drying and hydration when the specimens were immersed in distilled water. The two-step reaction, particularly the hydration process would induce the greater rock breakdown in the total immersion experiment.

IV-4-3. Application to field weathering

Figure 4.6 shows schematic diagrams of the dominant weathering processes under variable temperature and moisture conditions. Salt weathering by repeated wetting-drying with salt solution or salt crystallization with ice formation becomes dominant when liquid water is supplied to rock surface (Figure 4.6a). The crystallization due to freezing is dominant only below freezing point of salt solutions. Both temperature and salt concentration control freezing point of salt solutions, and occurrence of the crystallization due to freezing (Figure 4.6a). For the three salts employed in the present experiments, salt crystallization process due to freezing is substantially dominant in natural condition below approximately –7°C because saturated solutions of Na_2SO_4 and $MgSO_4$ freeze below –3.3°C and –6.7°C, respectively (Figure 4.6a). For NaCl, seawater which is a typical solution of NaCl in natural conditions freezes approximately at –2.5°C (Figure 4.6b) (Robinson and Jerwood, 1987), although the saturated solution of NaCl employed in the present freeze-thaw experiment froze below approximately –24°C. The freezing of seawater in coastal areas easily occurs compared with the present experimental conditions.

The intensive rock breakdown similar to the present freeze-thaw experiment may occur when liquid water is supplied to rock surface with abundant salt accumulation. For example, rock exposure with salt-rich layer in natural conditions found in Antarctic inlands (Selby and Wilson, 1971; Matsuoka *et al*., 2006), saline lakes

(Goudie and Cooke, 1984; Dickson *et al*., 2013) and RSL on the Martian surface (McEwen *et al*., 2011, 2013).

Salt deliquescence with humidity fluctuation only occurs when amount of moisture on rock surface is limited, in other words, liquid water is not directly supplied to rock surface (Figure 4.6b). In contrast, salt hydration-dehydration of sulfates can occur in various environments with wider ranges of moisture conditions (Figure 4.6a and b), although the hydration-dehydration process hardly occurred in the present humidity-change experiment in which air humidity fluctuates in a short interval (Figure 4.6b).

Air humidity oscillation induced significant salt weathering to specimens with NaCl. The weathering process of salt deliquescence and recrystallization occurs when relative humidity in air fluctuates across approximately 75%RH regardless of temperature, although water vapor pressure equivalent to 75%RH increases with increasing air temperature (Figure 4.6b). In humid coastal areas where a large amount of NaCl exists in sea water, NaCl supplied to and precipitated on the rock surface, and subsequent diurnal humidity fluctuation easily induces repetitions of the deliquescence and recrystallization of NaCl. The salt weathering due to humidity fluctuation would commonly occur on the rock surface, such as upper part of coastal cliff and tafoni in coastal spray zone.

Both Na_2SO_4 and $MgSO_4$ commonly exist on t surface of rocks and building

materials. As described in section IV-1-3, Na_2SO_4 was inactive when air humidity fluctuates in a short interval, although the hydration-dehydration of Na_2SO_4 is possible (Figure 4.6b). Salt weathering by Na_2SO_4 may occur in a field environments with long-term humidity fluctuation, because rock breakdown and seasonal crystallization and deliquescence of Na_2SO_4 were observed at the same place (e.g., Goudie, 1977; Matsukura and Kanai, 1988; Benavente *et al*., 2011; Schnepfleitner *et al*., 2016).

The relative importance of $MgSO_4$ to Na_2SO_4 would increase for salt weathering by diurnal humidity fluctuation. $MgSO_4$ commonly exists in cold deserts such as Antarctic inlands (Keys and Williams, 1981; Goudie and Cooke, 1984; Gore *et al*., 1996; Matsuoka *et al*., 2006; Strini *et al*., 2008) and the Martian surface (e.g., Gellert *et al*., 2004; Rieder *et al*., 2004; Campbell *et al*., 2008). The deliquescence of $MgSO_4$ rarely occurs in these cold environments, because the solution of $MgSO_4$ generally freezes regardless of a concentration of the solution under temperature condition in Antarctica and the Martian surface (Figure 4.6b). The hydration and dehydration of $MgSO_4$ would be major salt weathering process under these environments. Under warmer environments, the deliquescence of $MgSO_4$ barely occurs due to high DRH of epsomite (84–95% at 0–40°C) (Steiger *et al*., 2008). In contrast, the hydration-dehydration of $MgSO_4$ does not occur below the equilibrium RH of anhydrate crystal (Figure 4.6b). The deliquescence and recrystallization of $MgSO_4$

can induce damages particularly to cloister of stone heritages, cave wall and interior of tafoni where direct rainfall and runoff are avoided (Matsukura *et al*., 2004; López-Arce *et al*., 2008, 2011).

Chapter V. Conclusions

This study highlights that salt weathering obviously occurs where the source of moisture is limited to air humidity. Humidity oscillation induce cycles of repeated salt deliquescence-recrystallization and hydration-dehydration. Porous and weak sandstones with sodium chloride were completely broken down after 100 cycles of humidity change. The other two types of rock also showed concentrated damage on their surfaces.

The degrees of damage are strongly correlated with the moisture amount absorbed in the rock specimens. Sodium chloride causes the greatest damage to the specimens. The lower DRH of sodium chloride results in more water being absorbed from the air, which in turn induces greater weight losses and L-value reductions than the below two sulfates. The absence of hydrated forms would also have facilitated water absorption from the air. Sodium chloride is supplied to and precipitates on coastal tafoni in stormy weather; subsequent humidity fluctuations would easily induce salt weathering.

The salt crystallization process of sodium sulfate would be deliquescence of thenardite (anhydrate) and subsequent recrystallization of mirabilite (decahydrate). For magnesium sulfate, deliquescence of hexahydrate and recrystallization of epsomite (heptahydrate) would also occur. Magnesium sulfate induced damage in all of the rock specimens, whereas sodium sulfate was ineffective in the present

experiment. Sulfates are often found on building materials, and sodium sulfate has been thought to be one of the most aggressive salts. However, the restricted activity of sodium sulfate in the present experiment suggests that sodium sulfate can induce only minor salt decay by daily humidity fluctuation, because of slow hydration process. The volume expansion with hydration of sodium sulfate may hinder infiltration of moisture into the rock. The high DRH of mirabilite would also prevent salt deliquescence. Magnesium sulfate would be more effective than sodium sulfate where the water supply is limited, and air humidity fluctuates in hourly interval.

This study also highlights that salt crystallization facilitates rock breakdown due to freezing in environment with abundant salt, regardless of moisture abundance. Saturated salt solutions of sodium chloride, sodium sulfate or magnesium sulfate induce greater weight loss, and reductions of L-value and P-wave velocity than distilled water. Magnitude of L-value reductions in freeze-thaw experiment using saturated salt solution were same as the reduction in total immersion experiment using same salt solution. Salt crystallization significantly contributes to rock breakdown due to freezing of saturated salt solution.

Sodium and magnesium sulfate crystallized from saturated solution induce rock expansion prior to freezing. The salt crystals would fill micro-pores in rock and facilitated rock expansion and breakdown due to freezing. Although the previous studies reported that magnesium sulfate was ineffective in freeze-thaw experiment,

magnesium sulfate solution also cause intensive weathering in a freeze-thaw environment where saturated salt solutions are available.

Acknowledgements

This study was financially supported by the Grant-in-Aid (No. 25560143; principal investigator, N. Matsuoka) of Japan Society for the promotion of Science from the Ministry of Education, Culture, Sports, Science and Technology.

I am deeply grateful to my supervisor, Dr. Tsuyoshi Hattanji, University of Tsukuba, for the direction to study, logistic support and valuable discussions. I give special thanks to Prof. Norikazu Matsuoka, University of Tsukuba, for the financial support and fruitful discussion. I also express my gratitude to Dr. Chiaki T. Oguchi, University of Saitama, for to use of the mercury intrusion porosimeter. I acknowledge Dr. Atsushi Ikeda, Dr. Tomohiro Sekiguchi, Dr. Thomas Parkner, Dr. Tetsuya Shinozaki and the graduate students in the geomorphology group of the Graduate School of Life and Environmental Science, University of Tsukuba, for their helpful comments and discussions. I appreciate the following formerly graduate students, University of Tsukuba: Mr. Yasuhiro Inomata, Mr. Shinya Aoki, Mr. Naofumi Takeda, Mr. Akihiko Kawai, Mr. Akinori Nawata, for their supports in laboratory, Mr. Tsubasa Saito and Ms. Tamayo Aoki for their assistance in the field. Finally, I am thankful to my family for their hearty and patient encouragement.

References

Akagawa, S. and Fukuda, M. (1991) Frost heave mechanism in welded tuff: *Permafrost and Periglacial Processes*, **2**, 301–309.

Allen, C. E., Darmody, R. G., Thorn, C. E., Dixon, J. C. and Schlyter, P. (2002) Clay mineralogy, chemical weathering, and landscale evolution in Arctic-Alpine Sweden: *Geoderma*, **99**, 277–294.

Aly, N., Gomez-Heras, M., Hamed, A., Álvarez De Buergo, M. and Soliman, F. (2015) The influence of temperature in a capillary imbibition salt weathering simulation test on Mokattam limestone: *Materiales de Construccion*, **65**, e044.

Anderson, R. (1998) Near-surface thermal profiles in Alpine bedrock: implications for the frost weathering of rock: *Arctic and Alpine Research*, **30**, 362–372.

Andrè, M. and Hall, K. (2005) Honeycomb development on Alexander island, glacial history of George VI sound and palaeoclimatic implications (two step cliffs/Mars Oasis, W Antarctica): *Geomorphology*, **65**, 117–138.

Aoki, H. and Matsukura, Y. (2007) A new technique for non-destructive field measurement of rock-surface strength: an application of an Equotip hardness tester to weathering studies: *Earth Surface Processes and Landforms*, **32**, 1759–1769.

Apelblat, A. and Korin, E. (1998) The vapour pressures of saturated aqueous solutions of sodium chloride, sodium bromide, sodium nitrate, sodium nitrite, potassium iodate, and rubidium chloride at temperatures from 227 K to 323 K: *The*

Journal of Chemical Thermodynamics, **30**, 59–71.

Apelblat, A. and Korin, E. (2002) The vapour pressure of water over saturated solutions of sodium sulfate, calcium bromide, ferric chloride, zinc nitrate, calcium nitrate, and lithium nitrate at temperatures from 278.15 K to 323.15 K: *The Journal of Chemical Thermodynamics*, **34**, 1621–1637.

Apelblat, A. and Manzurola, E. (2003) Solubilities and vapour pressures of saturated aqueous solutions of sodium tetraborate, sodium carbonate, and magnesium sulfate and freezing-temperature lowerings of sodium tetraborate and sodium carbonate solutions: *The Journal of Chemical Thermodynamics*, **35**, 221–238.

Arnold, A. and Zehnder, K. (1989) Salt weathering on monuments: in *Proceedings of 1st international symposium on the conservation of monuments in the Mediterranean Basin*, 31–58.

Balboni, E., Espinosa-Marzal, R. M., Doehne, E. and Scherer, G. W. (2011) Can drying and re-wetting of magnesium sulfate salts lead to damage of stone?: *Environmental Earth Sciences*, **63**, 1463–1473.

Bell, J. F., Squyres, S. W., Arvidson, R. E., Arneson, H. M., Bass, D., Blaney, D., Cabrol, N., Calvin, W., Farmer, J., Farrand, W. H., Goetz, W., Golombek, M., Grant, J. A., Greeley, R., Guinness, E., Hayes, A. G., Hubbard, M. Y. H., Herkenhoff, K. E., Johnson, M. J., Johnson, J. R., Joseph, J., Kinch, K. M., Lemmon, M. T., Li, R., Madsen, M. B., Maki, J. N., Malin, M., McCartney, E.,

McLennan, S., McSween, H. Y., Ming, D. W., Moersch, J. E., Morris, R. V., Dobrea, E. Z. N., Parker, T. J., Proton, J., Rice, J .W., Seelos, F., Soderblom, J., Soderblom, L. A., Sohl-Dickstein, J. N., Sullivan, R. J., Wolff, M. J. and Wang, A. (2004) Pancam multispectral imaging results from the Spirit Rover at Gusev Crater: *Science*, **305**, 800–806.

Benavente, D., García del Cura, M. A., García-Guinea, J., Sánchez-Moral, S. and Ordóñez, S. (2004) Role of pore structure in salt crystallisation in unsaturated porous stone: *Journal of Crystal Growth*, **260**, 532–544.

Benavente, D., Sanchez-Moral, S., Fernandez-Cortes, A., Cañaveras, J. C., Elez, J. and Saiz-Jimenez, C. (2011) Salt damage and microclimate in the Postumius Tomb, Roman Necropolis of Carmona, Spain: *Environmental Earth Sciences*, **63**, 1529–1543.

Bradley, W. C., Hutton, J. T. and Twidale, C. R. (1978) Role of salts in development of granitic tafoni, South Australia: *Journal of Geology*, **86**, 647–656.

Brandmeier, M., Kuhlemann, J., Krumrei, I., Kappler, A. and Kubik, P. W. (2011) New challenges for tafoni research. A new approach to understand processes and weathering rates: *Earth Surface Processes and Landforms*, **36**, 839–852.

Buenestado, J. F., Zorzano, M. P. and Martín-Torres, J. (2015) Liquid water at Crater Gale, Mars: *Journal of Astrobiology & Outreach*, **3**, 131.

Burr, D. M., Tanaka, K. L. and Yoshikawa, K. (2009) Pingos on Earth and Mars:

Planetary and Space Science, **57**, 541–555.

Campbell, I. B. and Claridge, G. G. C. (1987) *Antarctica: Soils, weathering processes and environment*. Elsevier, Amsterdam, 367p.

Campbell, J. L., Gellert, R., Lee, M., Mallett, C. L., Maxwell, J. A. and O'Meara, J. M. (2008) Quantitative in situ determination of hydration of bright high-sulfate Martian soils: *Journal of Geophysical Research*, **113**, E06S11.

Charola, A. E., Pühringer, J. and Steiger, M. (2006) Gypsum: a review of its role in the deterioration of building materials: *Environmental Geology*, **52**, 339–352.

Chevrier, V. F. and Rivera-Valentin, E. G. (2012) Formation of recurring slope lineae by liquid brines on present-day Mars: *Geophysical Research Letters*, **39**, L21202.

Chipera, S. J. and Vaniman, D. T. (2007) Experimental stability of magnesium sulfate hydrates that may be present on Mars: *Geochimica et Cosmochimica Acta*, **71**, 241–250.

Chou, I-. M. and Seal, R. R. (2003) Determination of epsomite–hexahydrite equilibria by the humidity–buffer technique at 0.1 MPa with implications for phase equilibria in the system $MgSO_4$–H_2O: *Astrobiology*, **3**, 619–630.

Clark, B. C. and Van Hart, D. C. (1981) The salts of Mars: *Icarus*, **45**, 370–378.

Cooke, R. U. (1981) Salt weathering in deserts: in *Proceedings of the Geologists' Association*, **92**, 1–16.

Cooke, R. U. (1994) Salt weathering and the urban water table in deserts: in Robinson,

D. A. and Williams, R. B. G. eds., *Rock weathering and landform evolution*, John Wiley & Sons, Chichester, 193–205.

Cooke, R. U. and Smalley, I. J. (1968) Salt weathering in deserts: *Nature*, **220**, 1226–1227.

Dickson, J. L., Head, J. W., Levy, J. S. and Marchant, D. R. (2013) Don Juan Pond, Antarctica: Near-surface $CaCl_2$-brine feeding Earth's most saline lake and implications for Mars: *Scientific Report*, **3**, 1166.

Doehne, E. (2002) Salt weathering: a selective review: in Siegfried, S., Thomas, W. and Axel, V. eds., *Natural stone, weathering phenomena, conservation strategies and case studies: introduction*, Geological Society of London, London, 51–64.

Espinosa-Marzal, R. M. and Scherer, G. W. (2013) Impact of in-pore salt crystallization on transport properties: *Environmental Earth Sciences*, **69**, 2657–2669.

Fahey, B. D. (1985) Salt weathering as a mechanism of rock breakup in cold climates: an experimental approach: *Zeitschrift für Geomorphologie N. F.*, **29**, 99–111.

Flatt, R. J. (2002) Salt damage in porous materials: how high supersaturations are generated: *Journal of Crystal Growth*, **242**, 435–454.

French, H. and Guglielmin, M. (2002) Observations on granite weathering phenomena, Mount Keinath, Northern Victoria Land, Antarctica: *Permafrost and*

Periglacial Processes, **13**, 231–236.

Friedman, E. (1982) Endolithic microorganisms in the Antarctic cold desert: *Science*, **215**, 1045–1053.

Gauri, K. L. (1990) Decay and preservation of stone in modern environments: *Environmental Geology and Water Sciences*, **15**, 45–54.

Gauri, K. L., Chowdhury, A. N., Kulshreshtha, N. P. and Punuru, A. R. (1990) Geologic features and durability of limestones at the Sphinx: *Environmental Geology and Water Sciences*, **16**, 57–62.

Gellert, R., Rieder, R., Anderson, R. C., Brückner, J., Clark, B. C., Dreibus, G., Economou, T., Klingelhöfer, G., Lugmair, G. W., Ming, D. W., Squyres, S. W., D'Uston, C., Wänke, H., Yen, A. and Zipfel, J. (2004) Chemistry of rocks and soils in Gusev Crater from the Alpha Particle X-ray Spectrometer: *Science*, **305**, 829–832.

Gore, D. B., Creagh, D. C., Burgess, J. S., Colhoun, E. A., Spate, A. P. and Baird, A. S. (1996) Composition, distribution and origin of surficial salts in the Vestfold Hills, East Antarctica: *Antarctic Science*, **8**, 73–84.

Goudie, A. S. (1974) Further experimental investigation of rock weathering by salt and other mechanical processes: *Zeitschrift für Geomorphologie*, *Supplementband*, **21**, 1–12.

Goudie, A. S. (1977) Sodium sulphate weathering and the disintegration of

Mohenjo-Daro, Pakistan: *Earth Surface Processes and Landforms*, **2**, 75–86.

Goudie, A. S. (1986) Laboratory simulation of "the wick effect" in salt weathering of rock: *Earth Surface Processes and Landforms*, **11**, 275–285.

Goudie, A. S. (1993) Salt weathering simulation using a single-immersion technique: *Earth Surface Processes and Landforms*, **18**, 369–376.

Goudie, A. S. and Cooke, R. U. (1984) Salt efflorescences and saline lakes; a distributional analysis: *Geoforum*, **15**, 563–582.

Goudie, A. S. and Day, M. J. (1980) Disintegration of fan sediments in Death Valley, California, by salt weathering: *Physical Geography*, **2**, 126–137.

Goudie, A. S. and Viles, H. A. (1995) The nature and pattern of debris liberation by salt weathering: a laboratory study: *Earth Surface Processes and Landforms*, **20**, 437–449.

Goudie, A. S. and Viles, H. A. (1997) *Salt weathering hazard*. John Wiley & Sons, Chichester, 241p.

Goudie, A. S., Cooke, R. and Evans, I. (1970) Experimental investigation of rock weathering by salts: *Area*, **2**, 42–47.

Goudie, A. S., Viles, H. A. and Parker, A. G. (1997) Monitoring of rapid salt weathering in the central Namib Desert using limestone blocks: *Journal of Arid Environments*, **37**, 581–598.

Gough, R. V., Chevrier, V. F. and Tolbert, M. A. (2016) Formation of liquid water at

low temperatures via the deliquescence of calcium chloride: implications for Antarctica and Mars: *Planetary and Space Science*, **131**, 79–87.

Gough, R. V., Wong, J., Dickson, J. L., Levy, J. S., Head, J. W., Marchant, D. R. and Tolbert, M. A. (2017) Brine formation via deliquescence by salts found near Don Juan Pond, Antarctica: laboratory experiments and field observational results: *Earth and Planetary Science Letters*, **476**, 189–198.

Gunzburger, Y. and Merrien-Soukatchoff, V. (2011) Near-surface temperatures and heat balance of bare outcrops exposed to solar radiation: *Earth Surface Processes and Landforms*, **36**, 1577–1589.

Hall, K. (1987) The physical properties of quartz-micaschist and their application to freeze-thaw weathering studies in the maritime Antarctic: *Earth Surface Processes and Landforms*, **12**, 137–149.

Hall, K. and Andrè, M. (2001) New insights into rock weathering from high-frequency rock temperature data: an Antarctic study of weathering by thermal stress: *Geomorphology*, **41**, 23–31.

Hall, K., Thorn, C. E., Matsuoka, N. and Prick, A. (2002) Weathering in cold regions: some thoughts and perspectives: *Progress in Physical Geography*, **26**, 577–603.

Hall, K., Guglielmin, M. and Strini, A. (2008) Weathering of granite in Antarctica: I. Light penetration into rock and implications for rock weathering and endolithic communities: *Earth Surface Processes and Landforms*, **33**, 295–307.

Hardy, S. C. (1977) A grain boundary groove measurement of the surface tension between ice and water: *The Philosophical Magazine: A Journal of Theoretical Experimental and Applied Physics*, **35**, 471–484.

Heinz, J., Schulze-Makuch, D. and Kounaves, S. P. (2016) Deliquescence-induced wetting and RSL-like darkening of a Mars analogue soil containing various perchlorate and chloride salts: *Geophysical Research Letters*, **43**, 4880–4884.

Hœrlé, S. (2006) Rock temperatures as an indicator of weathering processes affecting rock art: *Earth Surface Processes and Landforms*, **31**, 383–389.

Ishimaru, S. and Yoshikawa, K. (2000) The weathering of granodiorite porphyry in the Thiel Mountains, inland Antarctica: *Geografiska Annaler Series A, Physical Geography*, **82**, 45–57.

Jagoutz, E. (2006) Salt-induced rock fragmentation on Mars: the role of salt in the weathering of Martian rocks: *Advances in Space Research*, **38**, 696–700.

Jerwood, L. C., Robinson, D. A. and Williams, R. B. G. (1990a) Experimental frost and salt weathering of chalk –I: *Earth Surface Processes and Landforms*, **15**, 611–624.

Jerwood, L. C., Robinson, D. A. and Williams, R. B. G. (1990b) Experimental frost and salt weathering of chalk –II: *Earth Surface Processes and Landforms*, **15**, 699–708.

Kamh, G. M. E. (2005) The impact of landslides and salt weathering on Roman

structures at high latitudes—Conway Castle, Great Britain: a case study: *Environmental Geology*, **48**, 238–254.

Keys, J. R. and Williams, K. (1981) Origin of crystalline, cold desert salts in the McMurdo region, Antarctica: *Geochimica et Cosmochimica Acta*, **45**, 2299–2309.

Kuchitsu, N., Ishizaki, T. and Nishiura, T. (2000) Salt weathering of the brick monuments in Ayutthaya, Thailand: *Developments in Geotechnical Engineering*, **84**, 319–327.

Kwaad, F. J. P. M. (1970) Experiments on the granular disintegration of granite by salt action: *University Amsterdam Fysisch Geografi sch en Bodemkundig Laboratorium Publicatie*, **16**, 67–80.

Levy, J. S., Head, J. W. and Marchant, D. R. (2009) Cold and dry processes in the Martian Arctic: geomorphic observations at the Phoenix landing site and comparisons with terrestrial cold desert landforms: *Geophysical Research Letters*, **36**, L21203.

López-Arce, P., Doehne, E., Martin, W. and Pinchin, S. (2008) Magnesium sulfate salts and historic building materials: experimental simulation of limestone flaking by relative humidity cycling and crystallization of salts: *Materials de Construcción*, **58(289–290)**, 125-142.

López-Arce, P., Garcia-Guinea, J., Benavente, D., Tormo, L. and Doehne, E. (2009) Deterioration of dolostone by magnesium sulphate salt: an example of

incompatible building materials at Bonaval Monastery, Spain: *Construction and Building Materials*, **23**, 846–855.

López-Arce, P., Gomez-Villalba, L. S., Pinho, L., Fernández-Valle, M. E., Álvarez de Buergo, M. and Fort, R. (2010) Influence of porosity and relative humidity on consolidation of dolostone with calcium hydroxide nanoparticles: effectiveness assessment with non-destructive techniques: *Materials Characterization*, **61**, 168–184.

López-Arce, P., Fort, R., Gómez-Heras, M., Pérez-Monserrat, E., Varas-Muriel, M. J. (2011) Preservation strategies for avoidance of salt crystallization in El Paular Monastery cloister, Madrid, Spain: *Environmental Earth Sciences*, **63**, 1487–1509.

Lubelli, B., Cnudde, V., Diaz-Goncalves, T., Franzoni, E. van Hees, R. P. J., Ioannou, I., Menendez, B., Nunes, C., Siedel, H., Stefanidou, M., Verges-Belmin, V. and Viles, H. (2018) Towards a more effective and reliable salt crystallization test for porous building materials: state of the art: *Materials and Structures*, **51**, 55.

Malin, M. C. (1974) Salt weathering on Mars. *Journal of Geophysical Research*, **79**, 3888–3894.

Marchant, D. R. and Head, J. W. (2007) Antarctic Dry Valleys: microclimate zonation, variable geomorphic processes, and implications for assessing climate change on Mars: *Icarus*, **192**, 187–222.

Martín-Torres, F. J., Zorzano, M.-P., Valentín-Serrano, P., Harri, A.-M., Genzer, M.,

Kemppinen, O., Rivera-Valentin, E. G., Jun, I., Wray, J., Bo Madsen, M., Goetz, W., McEwen, A. S., Hardgrove, C., Renno, N., Chevrier, V. F., Mischna, M., Navarro-González, R., Martínez-Frías, J., Conrad, P., McConnochie, T., Cockell, C., Berger, G., Vasavada, A. R., Sumner, D. and Vaniman, D. (2015) Transient liquid water and water activity at Gale Crater on Mars: *Nature Geoscience*, **8**, 357–361.

Matsukura, Y. and Kanai, H. (1988) Salt fretting in the valley cliff of the Asama volcano region, Japan: *Earth Surface Processes and Landforms*, **13**, 85–90.

Matsukura, Y. and Matsuoka, N. (1991) Rates of tafoni weathering on uplifted shore platforms in Nojima-Zaki, Boso Peninsula, Japan: *Earth Surface Processes and Landforms*, **16**, 51–56.

Matsukura, Y. and Matsuoka, N. (1996) The effect of rock properties on rates of tafoni growth in coastal environments: *Zeitschrift für Geomorphologie N. F., Supplementband*, **106**, 57–72.

Matsukura, Y. and Tanaka, Y. (2000) Effect of rock hardness and moisture content on tafoni weathering in the granite of Mount Doeg-sung, Korea: *Geografiska Annaler, Series A, Physical Geography*, **82**, 59–87.

Matsukura, Y., Oguchi, C. T. and Kuchitsu, N. (2004) Salt damage to brick kiln walls in Japan: spatial and seasonal distribution of efflorescence and moisture content: *Bulletin of Engineering Geology and the Environment*, **63**, 167–176.

Matsuoka, N. (1990) Mechanisms of rock breakdown by frost action: an experimental approach: *Cold Regions Science and Technology*, **17**, 253–270.

Matsuoka, N. (2001) Microgelivation versus macrogelivation: towards bridging the gap between laboratory and field frost weathering: *Permafrost and Periglacial Processes*, **12**, 299–313.

Matsuoka, N., Moriwaki, K. and Hirakawa, K. (1996) Field experiments on physical weathering and wind erosion in an Antarctic cold desert: *Earth Surface Processes and Landforms*, **21**, 687–699.

Matsuoka, N., Thomachot, C. E., Oguchi, C. T., Hatta, T., Abe, M. and Matsuzaki, H. (2006) Quaternary bedrock erosion and landscape evolution in the Sør Rondane Mountains, East Antarctica: reevaluating rates and processes: *Geomorphology*, **81**, 408–420.

McBride, E. F. and Picard, M. D. (2000) Origin and development of tafoni in tunnel spring tuff, Crystal Peak, Utah, USA: *Earth Surface Processes and Landforms*, **25**, 869–879.

McEwen, A. S., Ojha, L., Dundas, C. M., Mattson, S. S., Byrne, S., Wray, J. J., Cull, S. C., Murchie, S. L., Thomas, N. and Gulick, V. C. (2011) Seasonal flows on warm Martian slopes: *Science*, **333**, 740–743.

McEwen, A. S., Dundas, C. M., Mattson, S. S., Toigo, A. D., Ojha, L., Wray, J. J., Chojnacki, M., Byrne, S., Murchie, S. L. and Thomas, N. (2013) Recurring slope

lineae in equatorial regions of Mars: *Nature Geoscience*, **7**, 53–58.

McFadden, L. D., Eppes, M. C., Gillespie, A. R. and Hallet, B. (2005) Physical weathering in arid landscapes due to diurnal variation in the direction of solar heating: *Geological Society of America Bulletin*, **117**, 161–173.

McGreevy, J. P. (1981) Some perspectives on frost shattering: *Progress in Physical Geography*, **5**, 56–75.

McGreevy, J. P. (1982) 'Frost and salt' weathering: further experimental results: *Earth Surface Processes and Landforms*, **7**, 475–488.

McGreevy, J. P. and Smith, B. J. (1982) Salt weathering in hot desert: observation on the design of simulation experiments: *Geografiska Annaler Series A, Physical Geography*, **64**, 161–170.

Mellon, M. T., Malin, M. C., Arvidson, R. E., Searls, M. L., Sizemore, H. G., Heet, T. L., Lemmon, M. T., Keller, H. U. and Marshall, J. (2009) The periglacial landscape at the Phoenix landing site: *Journal of Geophysical Research*, **114(E1)**, E00E06.

Miotke, F. (1982) Physical weathering in Taylor Valley, Victoria Land, Antartica: *Polar Geography and Geology*, **6**, 71–98.

Mol, L. (2014) Investigations into the relationship between changes in internal moisture regimes and rock surface deterioration in cavernous sandstone features: *Earth Surface Processes and Landforms*, **39**, 914–927.

Mol, L. and Viles, H. A. (2012) The role of rock surface hardness and internal

moisture in tafoni development in sandstone: *Earth Surface Processes and Landforms*, **37**, 301–314.

Mottershead, D. N. (1982) Coastal spray weathering of bedrock in the supratidal zone at East Prawle, South Devon: *Field Studies*, **5**, 663–684.

Moreno, F., Vilela, S. A. G., Antunes, Â. S. G. and Alves, C. A. S. (2006) Capillary-rising salt pollution and granitic stone erosive decay in the parish church of Torre de Moncorvo (NE Portugal)-implications for conservation strategy: *Journal of Cultural Heritage*, **7**, 56–66.

Mottershead, D. N. (1994) Spatial variations in intensity of alveolar weathering of a dated sandstone structure in a coastal environment, Weston-super-Mare, UK: in Robinson, D. A. and Williams, R. B. G. eds., *Rock weathering and landform evolution*, John Wiley & Sons, Chichester, 151–174.

Mottershead, D. N. (2013) Coastal weathering: *Treatise on Geomorphology*, **4**, 228–244.

Mottershead, D. N. and Pye, K. (1994) Tafoni on coastal slopes, South Devon, U.K.: *Earth Surface Processes and Landforms*, **19**, 543–563.

Murton, J. B., Peterson, R. and Ozouf, J. C. (2006) Bedrock fracture by ice segregation in cold regions: *Science*, **314**, 1127–1129.

Mustoe, G. (1982) The origin of honeycomb weathering: *Geological Society of America Bulletin*, **93**, 108–115.

Mutch, T. A., Binder, A. B., Huck, F. O., Levinthal, E. C., Liebes Jr., S., Morris, E. C., Patterson, W. R., Pollack, J. B., Sagan, C. and Taylor, G. R. (1976a) The surface of Mars: the view from the Viking 1 lander: *Science*, **193**, 791–801.

Mutch, T. A., Grenander, S. U., Jones, K. L., Patterson, W., Arvidson, R. E., Guinness, E. A., Avrin, P., Carlston, C. E., Binder, A. B., Sagan, C., Dunham, E. W., Fox, P. L., Pieri, D. C., Huck, F. O., Rowland, C. W., Taylor, G. R., Wall, S. D., Kahn, R., Levinthal, E. C., Liebes, S., Tucker, R. B., Morris, E. C., Pollack, J. B., Saunders, R. S. and Wolf, M. R. (1976b) The surface of Mars: the view from the Viking 2 lander: *Science*, **194**, 1277–1283.

Oguchi, C. T. and Yuasa, H. (2010) Simultaneous wetting/drying, freeze/thaw and salt crystallization experiments of three types of Oya tuff: in Přikryl, R. and Török, Á. eds., *Natural stone resources for historical monuments*, Geological Society of London, London, 59–62.

Oguchi, C. T., Matsukura, Y. and Kuchitsu, N. (2002) Environmental and seasonal influences on the spatial distribution of salt efflorescence and weathering on brick kiln walls: *Transactions, Japanese Geomorphological Union*, **23**, 335–348.

Ojha, L., McEwen, A., Dundas, C., Byrne, S., Mattson, S., Wray, J., Masse, M. and Schaefer, E. (2014) HiRISE observations of Recurring Slope Lineae (RSL) during southern summer on Mars: *Icarus*, **231**, 365–376.

Ordóñez, S., Fort, R. and García del Cura, M. A. (1997) Pore size distribution and the

durability of a porous limestone: *Quarterly Journal of Engineering Geology and Hydrogeology*, **30**, 221–230.

Parsons, R. L., Head, J. W. and Marchant, D. R. (2005) Weathering pits in the Antarctic Dry Valleys: insolation-induced heating and melting, and applications to Mars: in *Proceedings of 36th Annual Lunar and Planetary Science Conference,* 1138.

Rieder, R., Gellert, R., Anderson, R. C., Brückner, J., Clark, B. C., Dreibus, G., Economou, T., Klingelhöfer, G., Lugmair, G. W., Ming, D. W., Squyres, S. W., D'Uston, C., Wänke, H., Yen, A. and Zipfel, J. (2004) Chemistry of rocks and soils at Meridiani Planum from the Alpha Particle X-ray Spectrometer: *Science*, **306**, 1746–1749.

Robinson, D. A. and Jerwood, L. C. (1987) Sub-aerial weathering of chalk shore platforms during harsh winters in southeast England: *Marine Geology*, **77**, 1–14.

Robinson, D. A. and Williams, R. B. G. (1982) Salt weathering of rock specimens of varying shape: *Area*, **14**, 293–299.

Robinson, D. A. and Williams, R. B. G. (2000) Experimental weathering of sandstone by combinations of salts: *Earth Surface Processes and Landforms*, **25**, 1309–1315.

Rodriguez-Navarro, C. (1998) Evidence of honeycomb weathering on Mars: *Geophysical Research Letters*, **25**, 3249–3252.

Rodriguez-Navarro, C. and Doehne, E. (1999) Salt weathering: influence of

evaporation rate, supersaturation and crystallization pattern: *Earth Surface Processes and Landforms*, **24**, 191–209.

Ruiz-Agudo, E., Mees, F., Jacobs, P. and Rodriguez-Navarro, C. (2007) The role of saline solution properties on porous limestone salt weathering by magnesium and sodium sulfates: *Environmental Geology*, **52**, 269–281.

Schnepfleitner, H., Sass, O., Fruhmann, S., Viles, H. and Goudie, A. (2016) A multi-method investigation of temperature, moisture and salt dynamics in tafoni (Tafraoute, Morocco): *Earth Surface Processes and Landforms*, **41**, 473–485.

Selby, M. and Wilson, A. (1971) The origin of the labyrinth, Wright Valley, Antarctica: *Geological Society of America Bulletin*, **82**, 471–476.

Smith, B. J. and McGreevy, J. P. (1983) A simulation study of salt weathering in hot deserts: *Geografiska Annaler Series A, Physical Geography*, **65**, 127–133.

Smith, B. J., Warke, P. A., McGreevy, J. P. and Kane, H. L. (2005) Salt-weathering simulations under hot desert conditions: agents of enlightenment or perpetuators of preconceptions?: *Geomorphology*, **67**, 211–227.

Smith, P. H., Bell, J. F., Bridges, N. T., Britt, D. T., Gaddis, L., Greeley, R., Keller, H. U., Herkenhoff, K. E., Jaumann, R., Johnson, J. R., Kirk, R. L., Lemmon, M., Maki, J. N., Malin, M. C., Murchie, S. L., Oberst, J., Parker, T. J., Reid, R. J., Sablotny, R., Soderblom, L. A., Stoker, C., Sullivan, R., Thomas, N., Tomasko, M. G., Ward, W. and Wegryn, E. (1997) Results from the Mars Pathfinder camera:

Science, **278**, 1758–1765.

Smith, P. H., Tamppari, L. K., Arvidson, R. E., Bass, D., Blaney, D., Boynton, W. V., Carswell, A., Catling, D. C., Clark, B. C., Duck, T., Dejong, E., Fisher, D., Goetz, W., Gunnlaugsson, H. P., Hecht, M. H., Hipkin, V., Hoffman, J., Hviid, S. F., Keller, H. U., Kounaves, S. P., Lange, C. F., Lemmon, M. T., Madsen, M. B., Markiewicz, W. J., Marshall, J., McKay, C. P., Mellon, M. T., Ming, D. W., Morris, R. V., Pike, W. T., Renno, N., Staufer, U., Stoker, C., Taylor, P., Whiteway, J. A. and Zent, A. P. (2009) H_2O at the Phoenix landing site: *Science*, **325**, 58–61.

Squyres, S. W., Arvidson, R. E., Bell, J. F., Brückner, J., Cabrol, N. A., Calvin, W., Carr, M. H., Christensen, P. R., Clark, B. C., Crumpler, L., Des Marais, D. J., D'Uston, C., Economou, T., Farmer, J., Farrand, W., Folkner, W., Golombek, M., Gorevan, S., Grant, J. A., Greeley, R., Grotzinger, J., Haskin, L., Herkenhoff, K. E., Hviid, S., Johnson, J., Klingelhöfer, G., Knoll, A., Landis, G., Lemmon, M., Li, R., Madsen, M. B., Malin, M. C., McLennan, S. M., McSween, H. Y., Ming, D. W., Moersch, J., Morris, R. V., Parker, T., Rice, J.W., Richter, L., Rieder, R., Sims, M., Smith, M., Smith, P., Soderblom, L. A., Sullivan, R., Wänke, H., Wdowiak, T., Wolff, M. and Yen, A. (2004a) The Spirit Rover's Athena science investigation at Gusev Crater, Mars: *Science*, **305**, 794–799.

Squyres, S. W., Arvidson, R. E., Bell, J. F., Brückner, J., Cabrol, N. A., Calvin, W., Carr, M. H., Christensen, P. R., Clark, B. C., Crumpler, L., Des Marais, D. J.,

D'Uston, C., Economou, T., Farmer, J., Farrand, W., Folkner, W., Golombek, M., Gorevan, S., Grant, J. A., Greeley, R., Grotzinger, J., Haskin, L., Herkenhoff, K. E., Hviid, S., Johnson, J., Klingelhöfer, G., Knoll, A. H., Landis, G., Lemmon, M., Li, R., Madsen, M. B., Malin, M. C., McLennan, S. M., McSween, H. Y., Ming, D. W., Moersch, J., Morris, R. V, Parker, T., Rice Jr., J. W., Richter, L., Rieder, R., Sims, M., Smith, M., Smith, P., Soderblom, L. A., Sullivan, R., Wänke, H., Wdowiak, T., Wolff, M. and Yen, A. (2004b) The Opportunity Rover's Athena science investigation at Meridiani Planum, Mars: *Science*, **306**, 1698–1703.

Steiger, M. and Asmussen, S. (2008) Crystallization of sodium sulfate phases in porous materials: the phase diagram Na_2SO_4–H_2O and the generation of stress: *Geochimica et Cosmochimica Acta*, **72**, 4291–4306.

Steiger, M., Linnow, K., Juling, H., Gülker, G., Jarad, A. E., Brüggerhoff, S. and Kirchner, D. (2008) Hydration of $MgSO_4 \cdot H_2O$ and generation of stress in porous materials: *Crystal Growth & Design*, **8**, 336–343.

Strini, A., Guglielmin, M. and Hall, K. (2008) Tafoni development in a cryotic environment: an example from Northern Victoria Land, Antarctica: *Earth Surface Processes and Landforms*, **33**, 1502–1519.

Takahashi, K., Suzuki, T. and Matsukura, Y. (1994) Erosion rates of sandstone used for a masonry bridge pier in the coastal spray zone: in Robinson, D. A. and Williams, R. B. G. eds., *Rock weathering and landform evolution*, John Wiley &

Sons, Chichester, 175–192.

Takaya, Y. and Oguchi, C. T. (2011) Quantitative evaluation of debris production due to salt weathering of tuff in Yoshimi Hyaku-Ana, an historic site in central Japan: *Geographical Review of Japan Science*, **84**, 369–376. (in Japanese with English abstract).

Takaya, Y., Oguchi, C. T., Yamazaki, M. and Ohnishi, R. (2011) Salt weathering of tuffaceous rock and its influence factor on tunnel walls in the Yoshimi Hyaku-Ana historic site, central Japan: *Transactions, Japanese Geomorphological Union*, **32**, 279–291. (in Japanese with English abstract).

Thomachot-Schneider, C., Gommeaux, M., Fronteau, G., Oguchi, C. T., Eyssautier, S. and Kartheuser, B. (2011) A comparison of the properties and salt weathering susceptibility of natural and reconstituted stones of the Oval Abbey (Belgium): *Environmental Earth Sciences*, **63**, 1447–1461.

Trenhaile, A. S. and Rudakas, P. A. (1981) Freeze-thaw and shore platform development in Gaspé, Québec: *Géographie physique et Quaternaire*, **35**, 171–181.

Tsujimoto, H. (1985) Types of rocky coasts and the resisting force of coastal rocks in the eastern part of Chiba Prefecture, Japan: *Geographical Review of Japan Ser. A*, **58**, 180–192. (in Japanese with English abstract).

Vaniman, D. T., Bish, D. L., Chipera, S. J., Fialips, C. I., Carey, J. W. and Feldman, W.

G. (2004) Magnesium sulphate salts and the history of water on Mars: *Nature*, **431**, 663–665.

Viles, H. A. (2005) Microclimate and weathering in the central Namib Desert, Namibia: *Geomorphology*, **67**, 189–209.

Viles, H. A. and Goudie, A. S. (2013) Weathering in the central Namib Desert, Namibia: controls, processes and implications: *Journal of Arid Environments*, **93**, 20–29.

Wellman, H. W. and Wilson, A. T. (1965) Salt weathering, a neglected geological erosive agent in coastal and arid environments: *Nature*, **205**, 1097–1098.

Williams, R. B. G. and Robinson, D. A. (1981) Weathering of sandstone by combined action of frost and salt: *Earth Surface Processes and Landforms*, **6**, 1–9.

Williams, R. B. G. and Robinson, D. A. (1991) Frost weathering of rocks in the presence of salts-a review: *Permafrost and Periglacial Processes and Landforms*, **2**, 347–353.

Williams, R. B. G. and Robinson, D. A. (1998) Weathering of sandstone by alunogen and alum salts: *Quarterly Journal of Engineering Geology and Hydrogeology*, **31**, 369–373.

Winkler, E. M. (1987) Weathering and weathering rates of natural stone: *Environmental Geology and Water Sciences*, **9**, 85–92.

Winkler, E. M. and Singer, P. C. (1972) Crystallization pressure of salts in stone and

concrete: *Geological Society of America Bulletin*, **83**, 3509–3514.

Winkler, E. M. and Wilhelm, E. J. (1970) Salt burst by hydration pressures in architectural stone in urban atmosphere: *Geological Society of America Bulletin*, **81**, 567–572.

Yamada, T., Aoki, H., Takahashi, M. and Matsukura, Y. (2005) Effect of rock properties on rates of salts weathering: a laboratory experiment: *Journal of the Japan Society of Engineering Geology*, **46**, 72–78. (in Japanese with English abstract).

Yen, A. S., Gellert, R., Schröder, C., Morris, R. V., Bell, J. F., Knudson, A. T., Clark, B. C., Ming, D. W., Crisp, J. A., Arvidson, R. E., Blaney, D., Brückner, J., Christensen, P. R., Des Marais, D. J., De Souza Jr., P. A., Economou, T. E., Ghosh, A., Hahn, B. C., Herkenhoff, K. E., Haskin, L. A., Hurowitz, J. A., Joliff, B. L., Johnson, J. R., Klingelhöfer, G., Madsen, M. B., McLennan, S. M., McSween, H. Y., Richter, L., Rieder, R., Rodionov, D., Soderblom, L., Squyres, S. W., Tosca, N. J., Wang, A., Wyatt, M. and Zipfel, J. (2005) An integrated view of the chemistry and mineralogy of Martian soils: *Nature*, **436**, 49–54.

Young, A. R. M. (1987) Salt as an agent in the development of cavernous weathering: *Geology*, **15**, 962–966.

Yu, S. and Oguchi, C. T. (2010a) Is sodium sulphate invariably effective in destroying any type of rock?: in Přikryl, R. and Török, Á. eds., *Natural Stone Resources for*

Historical Monuments, Geological Society of London, London, 43–58.

Yu, S. and Oguchi, C. T. (2010b) Role of pore size distribution in salt uptake, damage, and predicting salt susceptibility of eight types of Japanese building stones: *Engineering Geology*, **115**, 226–236.

Zehnder, K. and Arnold, A. (1989) Crystal growth in salt efflorescence: *Journal of Crystal Growth*, **97**, 513–521.

Table 2.1 Combinations of rocks used for each experiment

Rock type	Geologic age	Comments	Humidity change (10°C)	Humidity change (20°C)	Freeze-thaw	Total immersion (10°C)	Total immersion (20°C)
Oya tuff	Miocene	Green, dacitic or rhyolitic marine pumice tuff	○	○	○	○	○
Shirakawa tuff	Pleistocene	White, dacitic welded tuff	-	-	○	○	○
Aoshima sandstone	Pliocene	Gray, very fine-grained, well-cemented tuff	○	○	○	○	○
Ubara sandstone	Miocene	Brownish yellow, fine-grained, weakly cemented, porous sandstone	-	○	-	-	-
Taitozaki mudstone	Pleistocene	Brown, weakly cemented, porous mudstone	-	○	-	-	-
Miiri mudstone	Miocene	Gray, cemented, porous mudstone	-	○	-	-	-
Andesite[a]	Unknown	Black, porous, porphyritic andesite composed of quartz, hornblende, and pyroxene	-	-	○	-	-

[a]Sampling site of Andesite was unknown.

Table 2.2 Physical properties of rocks used for experiments

Rock type	Bulk density ρ_{bulk} (g/cm^3)	True density ρ_{true} (g/cm^3)	Effective porosity n_e (%)	Tensile strength S_t (MPa)	Equotip rebound value L	Longitudinal wave velocity V_p (km/s)
Oya tuff	1.39	2.39	41.8	0.99	469	2.27
Shirakawa tuff	1.98	2.65	25.0	4.38[a]	542	2.86
Aoshima sandstone	2.20	2.49	7.3	7.55	566	2.97
Ubara sandstone	1.56	2.67	41.8	0.51	393	0.84
Taitozaki mudstone	1.27	2.66	52.4	0.49[a]	274	1.12
Miiri mudstone	1.47	2.56	42.5	3.63[a]	293	2.05
Andesite	2.15	2.71	20.7	2.45	629	2.49

[a]Data of tensile strength is based on *et al*. (2005) for Shirakawa tuff, and Tsujimoto (1985) for Taitozaki and Miiri mudstone.

Table 2.3 Pore volumes of rocks used for experiments

Rock type	Pore volume (mm^3/g)					Specific surface area (m^2/g) *SSA*
	Total volume of pores[a] V_{total}	Volume of large pores[a] V_1	Volume of median pores[a] V_2	Volume of small pores[a] V_3	Volume of very small pores[a] V_4	
Oya tuff	241.76	48.73	41.71	81.01	56.04	5.480
Shirakawa tuff	141.05	12.95	91.22	26.51	5.72	0.825
Aoshima sandstone	48.92	1.27	29.07	11.54	3.98	0.475
Ubara sandstone	155.45	68.03	34.69	29.96	13.26	1.555
Taitozaki mudstone	343.63	3.19	94.96	214.33	28.24	4.533
Miiri mudstone	231.56	1.71	4.03	182.40	38.83	5.326
Andesite	60.02	9.14	6.01	1.47	N.A.[b]	0.021

[a] V_{total} is total volume of pores with a range of diameter from $10^{-2.5}$ to 200 μm. V_1, V_2, V_3, V_4 are total volumes of pores with diameters of $10^{1.5}$–$10^{0.5}$ μm (large pore), $10^{0.5}$–$10^{-0.5}$ μm (median pore), $10^{-0.5}$–$10^{-1.5}$ μm (small pore), and less than $10^{-1.5}$ μm (very small pore), respectively.

[b] V_4 of Andesite was represented as “N.A.”, because measured value was negative.

Table 2.4 Solubilities (wt%) of salts used for experiments

Salt type	10°C	20°C
Sodium chloride	26.3	26.4
Sodium sulfate	8.3	19.0
Magnesium sulfate	22.0	25.2

Table 3.1 Salt content of rock specimens used in humidity-change experiment

Rock type	Sodium chloride	Sodium sulfate	Magnesium sulfate
10°C			
Oya tuff	5.1	1.7	4.6
Aoshima sandstone	0.3	0.1	0.5
20°C			
Oya tuff	7.7	4.2	8.6
Aoshima sandstone	0.5	0.2	1.0
Ubara sandstone	7.8	2.9	6.1
Taitozaki mudstone	17.4	8.8	16.9
Miiri mudstone	20.9	3.9	7.9

The values represent gram weights of salt in a 100 g salt-free rock specimen.

Table 3.2 L-value and P-wave velocity changes due to pre-treatment prior to humidity-change experiment

Rock type	Equotip rebound value		Longitudinal wave velocity (km/s)	
	value with salt L_0 / initial value $L_{initial}$ (%)		value with salt L_0 / initial value $L_{initial}$ (%)	
NaCl				
10°C				
Oya tuff	90.5	(436.6 / 482.4)	96.6	(2.35 / 2.44)
Aoshima sandstone	90.8	(581.2 / 640.2)	103.7	(3.79 / 3.65)
20°C				
Oya tuff	71.7	(342.3 / 477.4)	101.0	(2.34 / 2.31)
Aoshima sandstone	89.7	(525.9 / 586.4)	95.5	(3.29 / 3.44)
Ubara sandstone	65.5	(266.4 / 406.9)	-	
Taitozaki mudstone	64.6	(194.2 / 300.7)	-	
Miiri mudstone	107.8	(316.9 / 294.0)	-	
Na_2SO_4				
10°C				
Oya tuff	95.3	(483.6 / 507.7)	93.7	(2.17 / 2.32)
Aoshima sandstone	99.2	(639.7 / 645.0)	101.6	(3.78 / 3.72)
20°C				
Oya tuff	93.0	(419.5 / 451.2)	104.2	(2.38 / 2.28)
Aoshima sandstone	93.1	(570.5 / 612.6)	95.3	(3.30 / 3.46)
Ubara sandstone	68.1	(263.9 / 387.8)	-	
Taitozaki mudstone	89.6	(261.1 / 291.2)	-	
Miiri mudstone	105.4	(316.3 / 300.2)	-	
$MgSO_4$				
10°C				
Oya tuff	102.3	(491.5 / 480.4)	106.7	(2.50 / 2.34)
Aoshima sandstone	100.6	(612.7 / 608.9)	107.9	(3.90 / 3.62)
20°C				
Oya tuff	141.3	(631.3 / 446.8)	113.9	(2.64 / 2.32)
Aoshima sandstone	84.8	(532.3 / 627.6)	105.8	(3.73 / 3.52)
Ubara sandstone	74.9	(291.7 / 389.6)	-	
Taitozaki mudstone	84.3	(210.8 / 250.0)	-	
Miiri mudstone	44.2	(120.4 / 272.2)	-	

The values in parentheses represent initial salt-free and the cycle-0 values.

Table 3.3 Weight gains (g) in first high-humidity period

Rock type	Sodium chloride	Sodium sulfate	Magnesium sulfate	No salt
10°C				
Oya tuff	2.56	1.48	1.37	1.21
Aoshima sandstone	2.28	0.52	0.60	0.35
20°C				
Oya tuff	6.35	2.22	3.66	2.27
Aoshima sandstone	3.18	0.88	1.12	0.48

The values represent the amount of water absorbed in the specimens during the first high-humidity period.

Table 3.4 Average freezing point and strain in freeze-thaw cycles from the start to the first 20 cycles

Salt / rock type	1.0 cm		2.5 cm		Freezing strain[c] ε_f ($\times 10^{-3}$)
	Turning point[a] (°C)	Freezing point[b] (°C)	Turning point[a] (°C)	Freezing point[b] (°C)	
NaCl					
Oya tuff	−24.6 (−24.8 – −24.5)	−24.3 (−24.4 – −24.3)	−24.7 (−25.4 – −23.8)	−24.5 (−25.2 – −23.7)	0.357 (0.252 – 0.488)
Aoshima sandstone	−24.8 (−25.1 – −24.5)	−24.7 (−25.1 – −24.5)	−24.6 (−24.9 – −24.3)	−24.5 (−24.9 – −24.3)	0.022 (0.011 – 0.052)
Shirakawa tuff	−25.9 (−27.1 – −25.4)	−24.7 (−25.0 – −24.4)	−25.6 (−26.4 – −25.1)	−24.4 (−24.7 – −24.0)	0.042 (0.011 – 0.094)
Andesite	−28.8 (−30.3 – −27.5)	−25.2 (−26.4 – −24.4)	−28.6 (−30.2 – −27.3)	−25.1 (−26.2 – −24.1)	0[d]
Na_2SO_4					
Oya tuff	−4.0 (−4.4 – −3.5)	−1.9 (−2.0 – −1.6)	−3.6 (−4.4 – −3.0)	−1.3 (−1.4 – −1.3)	1.653 (1.434 – 1.866)
Aoshima sandstone	−3.6 (−4.3 – −3.1)	−2.8 (−3.3 – −2.3)	−3.5 (−4.1 – −3.0)	−2.9 (−3.3 – −2.5)	0.251 (0.078 – 0.405)
Shirakawa tuff	−4.5 (−5.2 – −3.5)	−1.6 (−1.8 – −1.6)	−4.2 (−5.0 – −3.2)	−1.6 (−1.7 – −1.5)	0.029 (0.023 – 0.035)
Andesite	−6.3 (−7.0 – −4.0)	−1.9 (−2.0 – −1.8)	−6.2 (−6.8 – −3.8)	−1.8 (−1.9 – −1.7)	0[d]
$MgSO_4$					
Oya tuff	−8.3 (−8.3 – −8.3)	−7.1 (−7.1 – −7.1)	−6.8 (−8.4 – −6.0)	−6.3 (−7.4 – −5.6)	0.864 (0.630 – 1.170)
Aoshima sandstone	−8.5 (−9.2 – −7.9)	−8.1 (−9.2 – −7.2)	−8.5 (−9.4 – −7.9)	−8.1 (−9.4 – −7.4)	0.421 (0.210 – 0.607)
Shirakawa tuff	−9.1 (−10.4 – −8.3)	−5.7 (−10.4 – −4.9)	−7.6 (−10.2 – −7.2)	−5.9 (−9.7 – −5.5)	0.117 (0.061 – 0.155)
Andesite	−9.1 (−10.5 – −8.3)	−5.6 (−10.5 – −5.0)	−9.1 (−10.5 – −8.3)	−5.6 (−10.5 – −5.0)	0[d]
Distilled water					
Oya tuff	−5.0 (−5.2 – −4.7)	−0.7 (−1.1 – −0.4)	−4.2 (−4.6 – −3.3)	−0.3 (−0.4 – −0.2)	0.486 (0.096 – 0.634)
Aoshima sandstone	−2.6 (−3.0 – −2.0)	−1.4 (−1.8 – −0.9)	−2.7 (−3.1 – −2.0)	−1.5 (−1.8 – −1.1)	0.009 (0.001 – 0.037)
Shirakawa tuff	−4.1 (−4.4 – −3.1)	−0.3 (−0.4 – −0.2)	−4.0 (−4.3 – −3.1)	−0.3 (−0.5 – −0.2)	0.013 (0.007 – 0.018)
Andesite	−3.9 (−4.5 – −1.9)	−0.5 (−0.5 – −0.4)	−3.9 (−4.4 – −1.9)	−0.5 (−0.6 – −0.5)	0[d]

[a]The turning point was also defined as last temperature prior to the sudden temperature rise. The values in parentheses represent ranges of measured values.

[b]The freezing point was defined as the constant temperature after the sudden temperature rise.

[c]The freezing strain was defined as a difference in strain between the start of expansion and the peak.

[d]The freezing strains of Andesite were represented as “0”, because Andesite did not show distinguishable increases in surface strain.

Table 3.5 Reduction rates of Equotip rebound value and longitudinal wave velocity in freeze-thaw experiments

Salt / rock type	Reduction rate of Equotip rebound value R_L (%/cycle)	Reduction rate of longitudinal wave velocity R_{Vp} (%/cycle)
NaCl		
Oya tuff	8.5 (5)	21.7 (4)
Aoshima sandstone	1.0 (50)	1.9 (40)
Shirakawa tuff	−0.1 (120)	0.1 (120)
Andesite	0 (120)	0 (120)
Na_2SO_4		
Oya tuff	6.5 (8)	12.7 (7)
Aoshima sandstone	2.1 (30)	2.6 (20)
Shirakawa tuff	0.4 (120)	0.8 (110)
Andesite	0 (120)	0 (120)
$MgSO_4$		
Oya tuff	21.9 (2)	37.4 (1)
Aoshima sandstone	3.1 (17)	10.0 (9)
Shirakawa tuff	0.8 (40)	1.8 (40)
Andesite	0 (120)	0 (120)
Distilled water		
Oya tuff	0.4 (102)	0.8 (102)
Aoshima sandstone	0.3 (80)	−0.1 (80)
Shirakawa tuff	−0.3 (120)	0.1 (120)
Andesite	0 (120)	0 (120)

The reduction rates were calculated by dividing the final value by both the cycle-0 value and the number of freeze-thaw cycles. The value in parentheses represents the cycle number when the final value was measured.

Table 3.6 Reduction rates of weight and Equotip rebound value in total immersion experiments

Salt / rock type	Reduction rate of Equotip rebound value R_W (%/cycle)	Reduction rate of Equotip rebound value R_L (%/cycle)
NaCl		
10°C		
Oya tuff	9.5 (10)	19.6 (2)
Aoshima sandstone	2.9 (20)	2.6 (20)
Shirakawa tuff	0.3 (20)	2.0 (16)
20°C		
Oya tuff	3.6 (13)	7.6 (9)
Aoshima sandstone	0.6 (20)	0.8 (20)
Shirakawa tuff	0.2 (20)	0.3 (20)
Na_2SO_4		
10°C		
Oya tuff	2.0 (20)	5.5 (10)
Aoshima sandstone	0.1 (20)	3.3 (9)
Shirakawa tuff	0.2 (20)	1.4 (20)
20°C		
Oya tuff	4.3 (13)	6.1 (9)
Aoshima sandstone	6.5 (13)	8.4 (9)
Shirakawa tuff	1.5 (20)	3.6 (12)
$MgSO_4$		
10°C		
Oya tuff	15.6 (6)	16.1 (1)
Aoshima sandstone	3.0 (20)	6.9 (9)
Shirakawa tuff	3.2 (20)	4.9 (10)
20°C		
Oya tuff	19.5 (5)	16.0 (1)
Aoshima sandstone	3.9 (20)	4.6 (9)
Shirakawa tuff	3.7 (20)	8.2 (5)

The reduction rates were calculated by dividing the final value by both initial value and the number of total immersion cycles. The value in parentheses represents the cycle number when the final value was measured.

Table 4.1 Surface tension between solid and liquid of saturated salt solutions or distilled water at 20°C

Salt type	Surface tension σ (mN/m)
Sodium chloride	90
Sodium sulfate	75.4
Magnesium sulfate	77.3
Distilled water	29.1

The surface tension data, are based on Gauri *et al*. (1990) for sodium chloride, Ruiz-Agudo *et al*. (2007) for sodium sulfate and magnesium sulfate, and Hardy (1977) for distilled water.

Figure 2.1 Rock specimens used for experiments

(a) Cubic specimens with a side of 5 cm, (b) Cylindrical specimens with a diameter and a height of 3.5 cm.

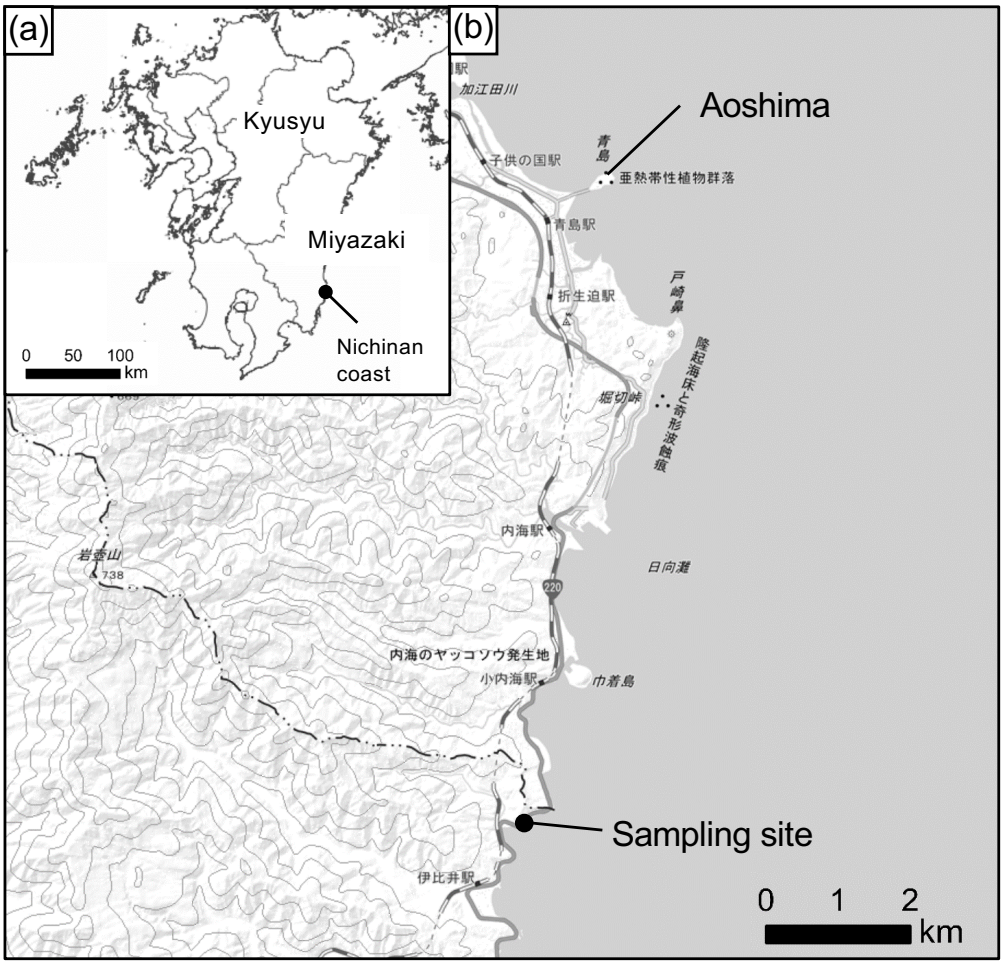

Figure 2.2 Location where Aoshima sandstone was collected

(a) General map of Miyazaki Prefecture, Kyusyu, West Japan. (b) Topography map of the Nichinan coast. Contour interval is 100 m. These maps are based on the blank map and the digital topographic map 200000 published by Geospatial Information Authority of Japan.

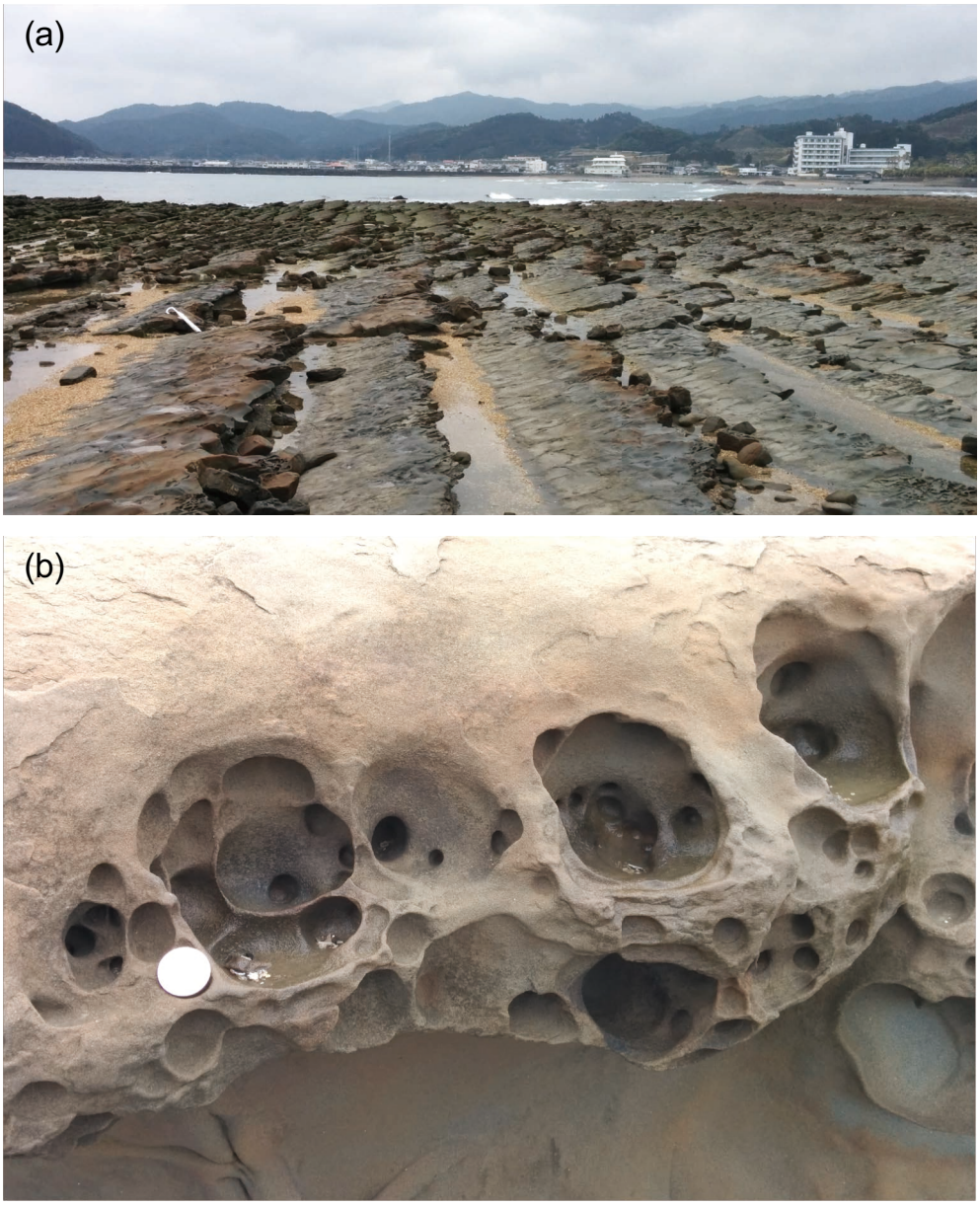

Figure 2.3 Type-B shore platform and honeycomb feature developed in Aoshima, Miyazaki Prefecture

(a) Type-B shore platform, and (b) Honeycomb feature developed on Aoshima sanstone.

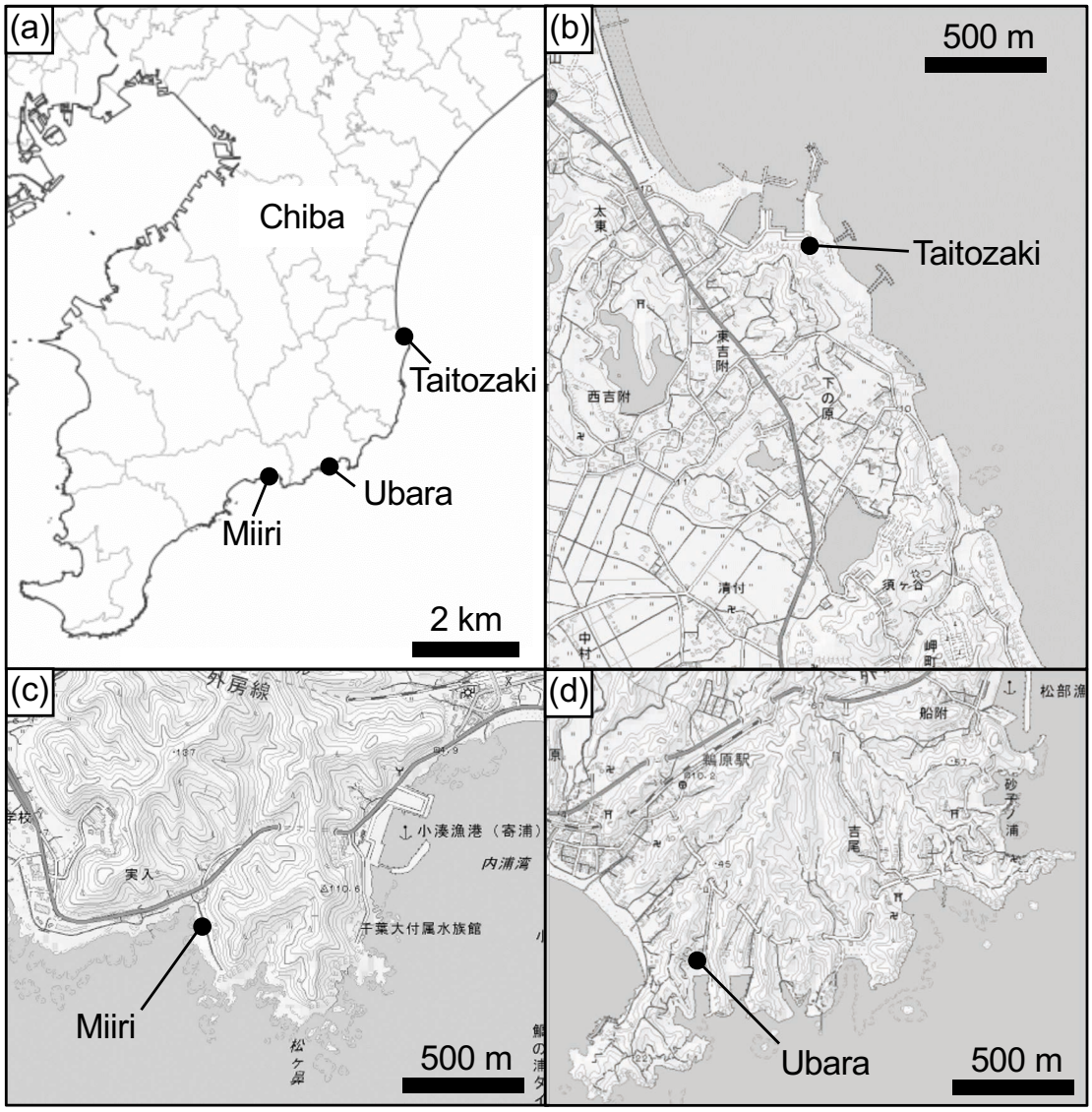

Figure 2.4 Location where Ubara sandstone, Taitozaki mudstone, and Miiri mudstone were collected

(a) General map of Chiba Prefecture, East Japan. (b) Taitozaki mudstone. (c) Miiri mudstone. (d) Ubara sandstone. Contour interval is 10 m. These maps are based on the blank map and the digital topographic map 25000 published by Geospatial Information Authority of Japan.

Figure 2.5 Weathering feature developed on coastal cliff composed of Ubara sandstone

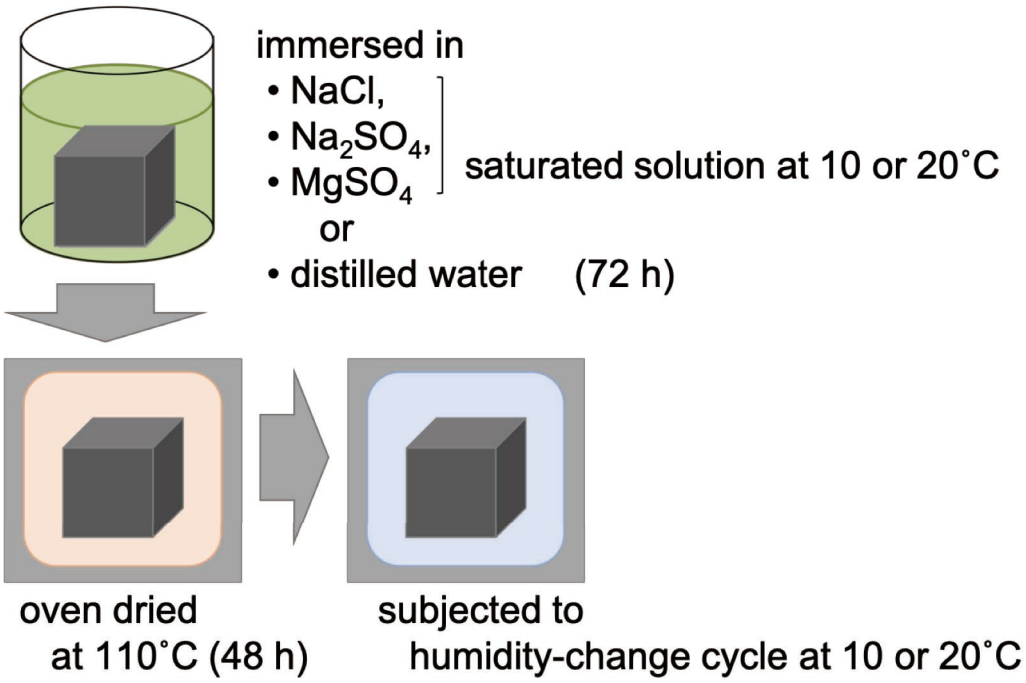

Figure 2.6 Overview of humidity-change experiment

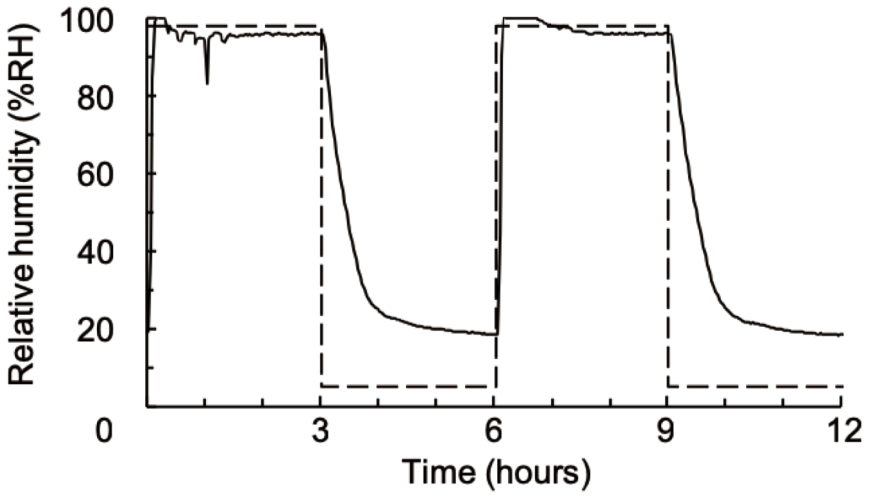

Figure 2.7 Details of humidity cycle

A cycle consists of high- and low-humidity periods lasting 3 hours in total. The solid line represents relative humidity in an ambient camber measured at 5-min intervals. The dashed line represents the setting of the chamber.

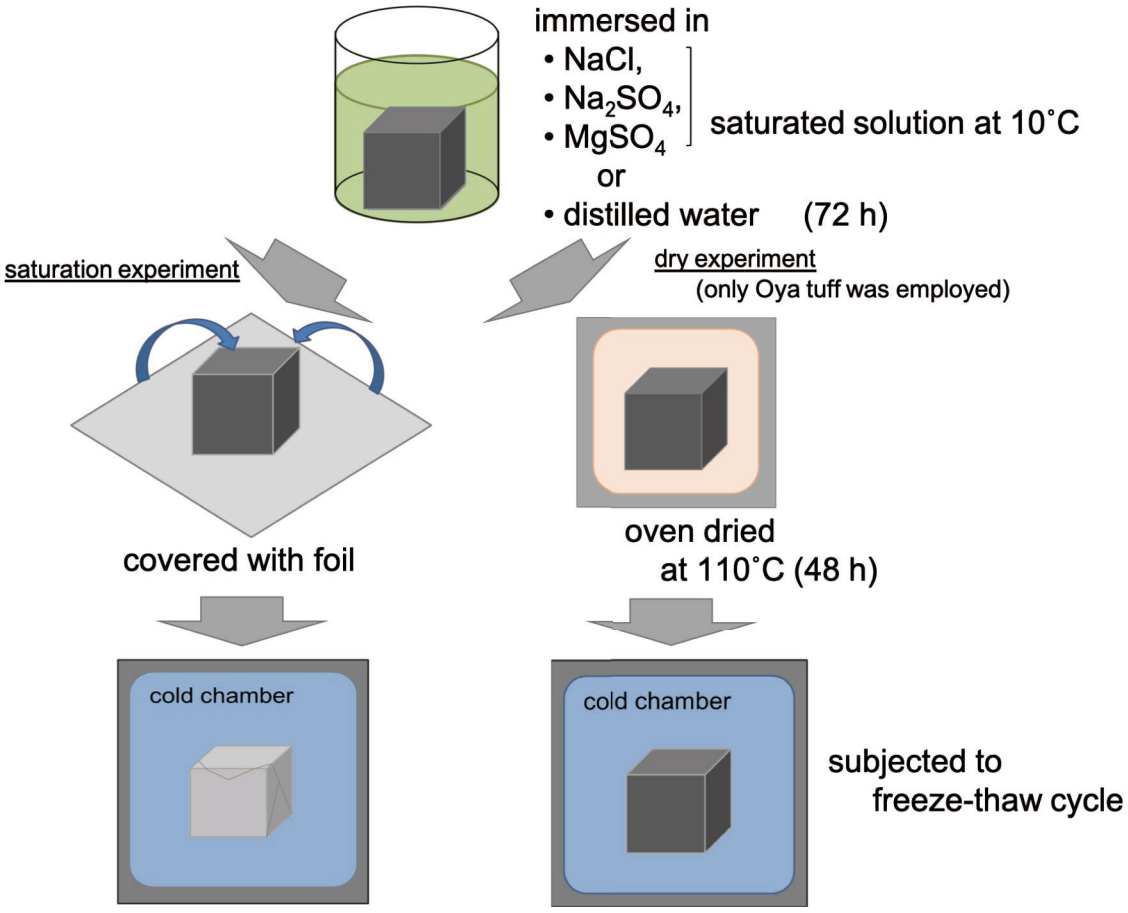

Figure 2.8 Overview of freeze-thaw experiment

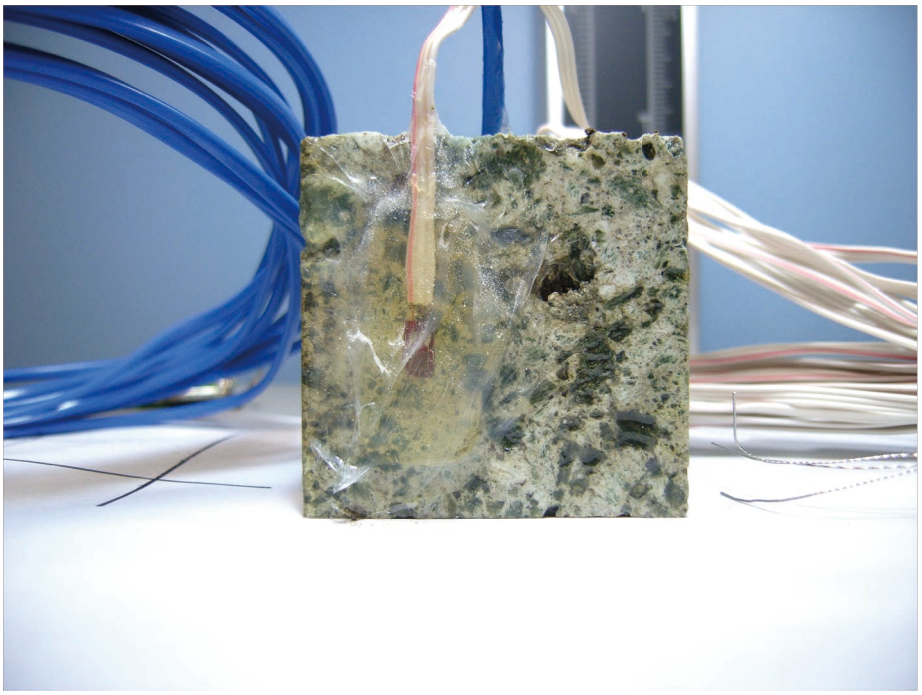

Figure 2.9 Strain gauge attached on a Oya tuff specimen

A face was coated with dedicated epoxy adhesive prior to adhering the strain gauge. The gauge-attached face was coated with silicone sealant.

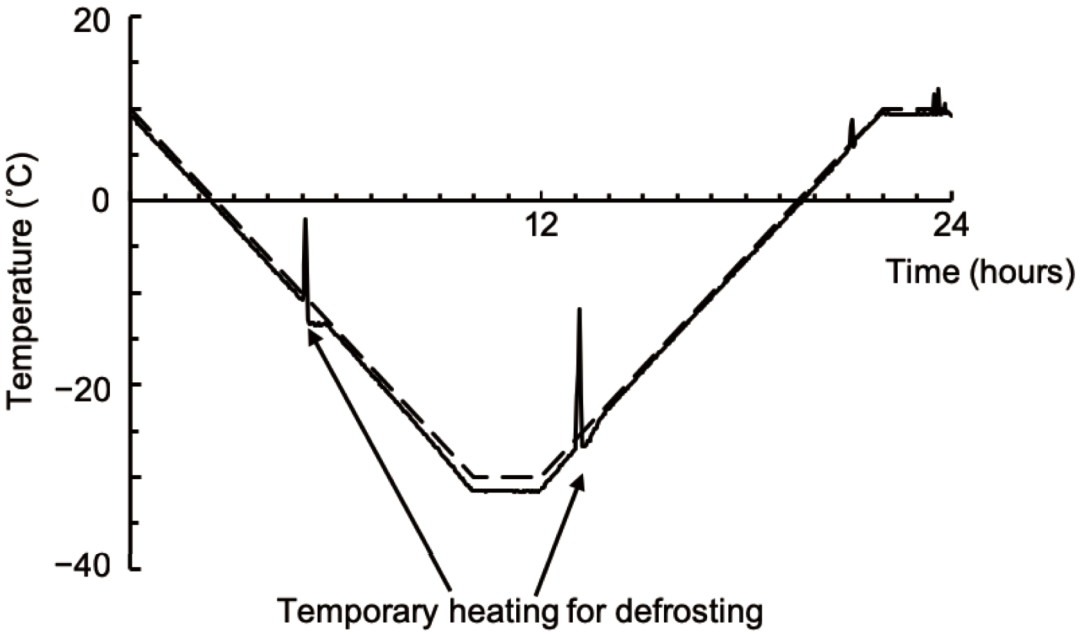

Figure 2.10 Details of freeze-thaw cycle

Air temperature oscillated from –30˚C to 10˚C every 24 hours with cooling and thawing rates of ±4˚C/h. The solid line represents temperature in an ambient chamber measured at 5-min intervals. The dashed line represents the setting of the chamber. The air temperature in the ambient chamber occasionally rose in a short period due to auto-defrosting function of the chamber.

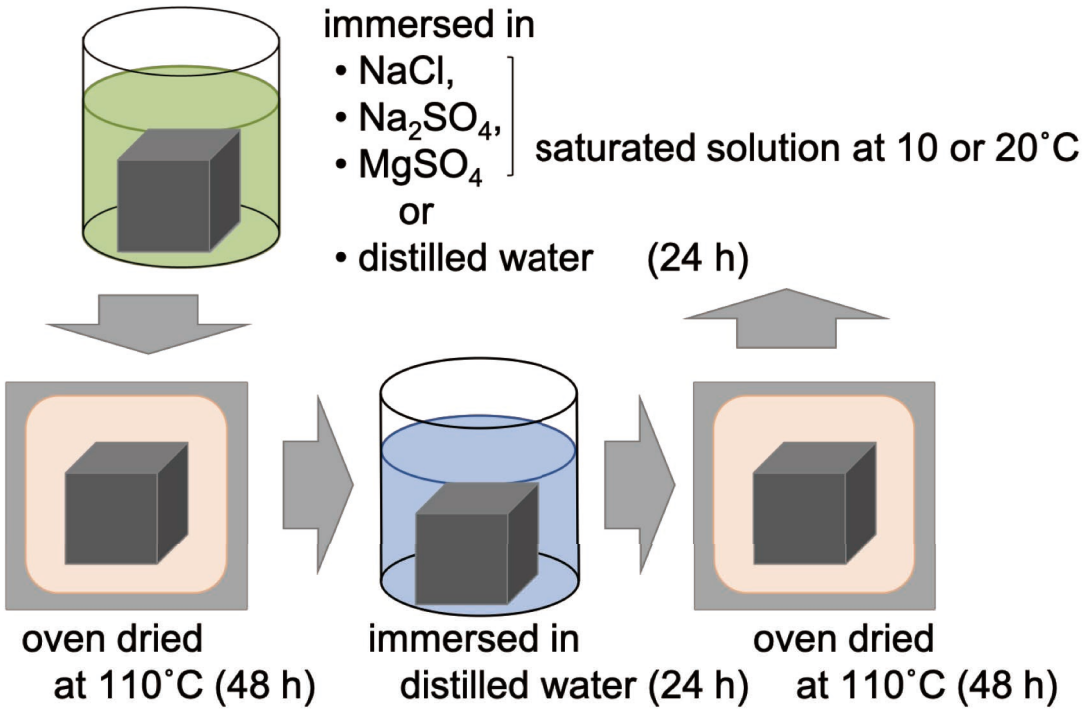

Figure 2.11 Overview of total immersion experiment

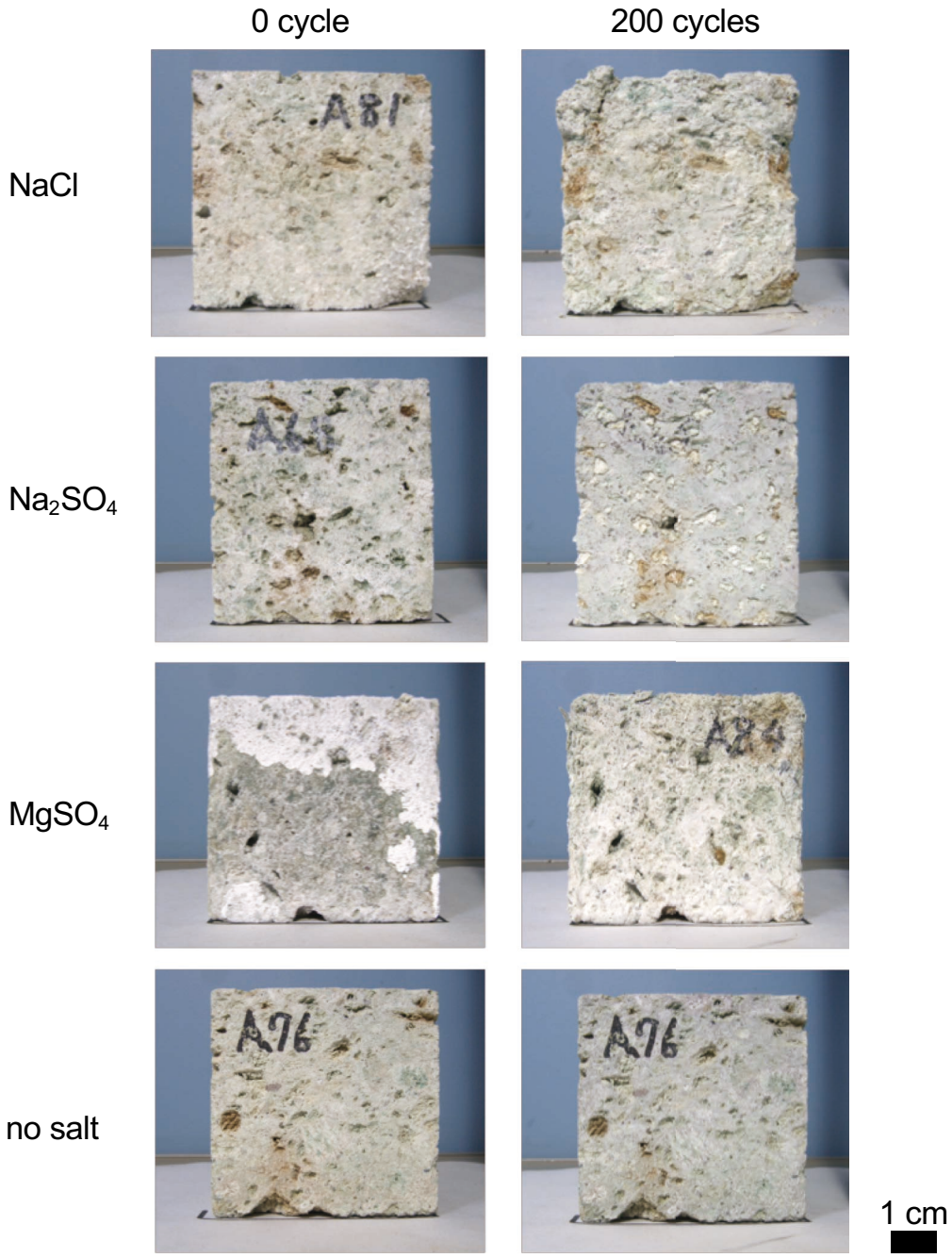

Figure 3.1 Oya tuff subjected to humidity cycles at 20˚C

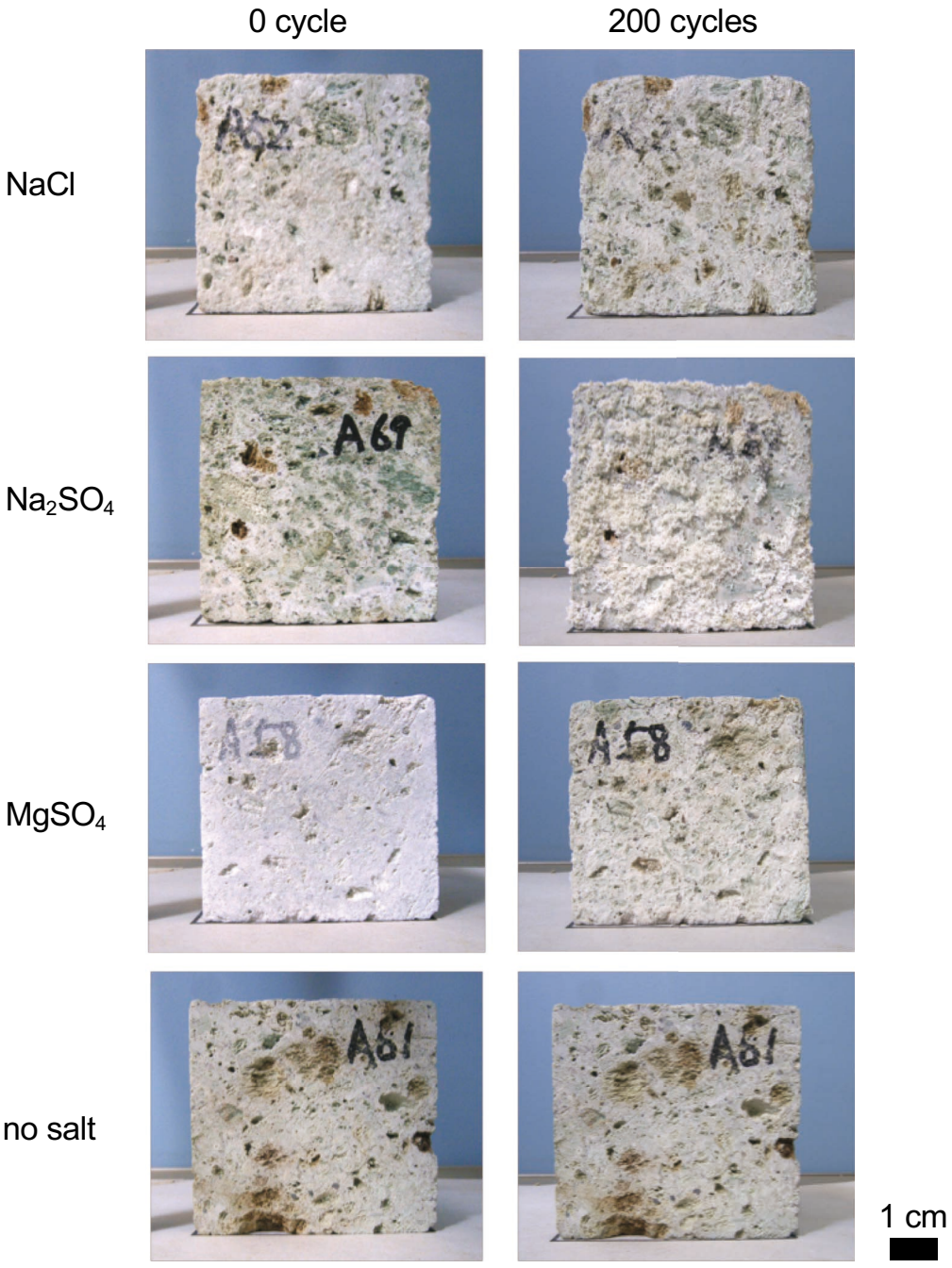

Figure 3.2 Oya tuff subjected to humidity cycles at 10˚C

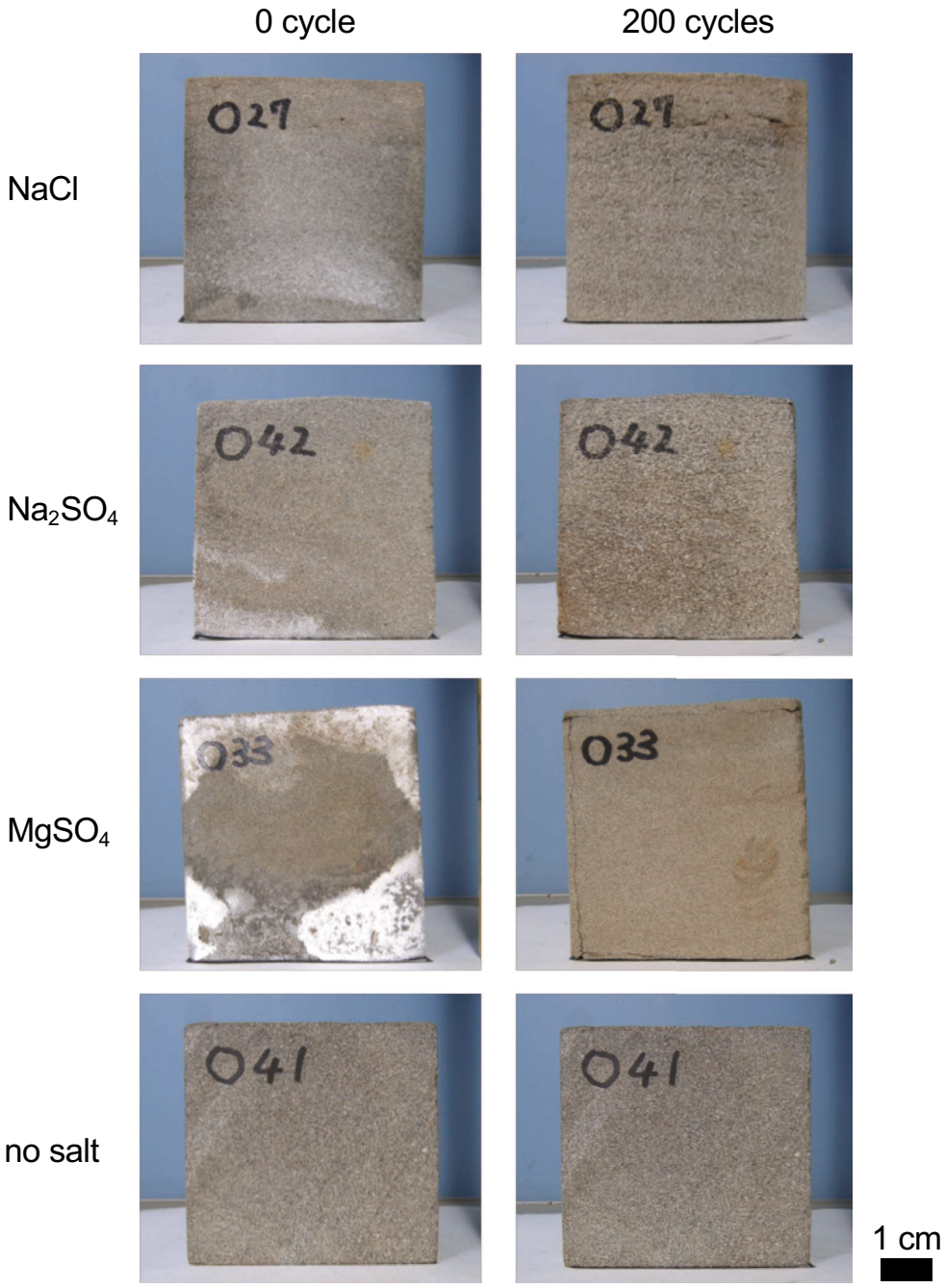

Figure 3.3 Aoshima sandstone subjected to humidity cycles at 20˚C

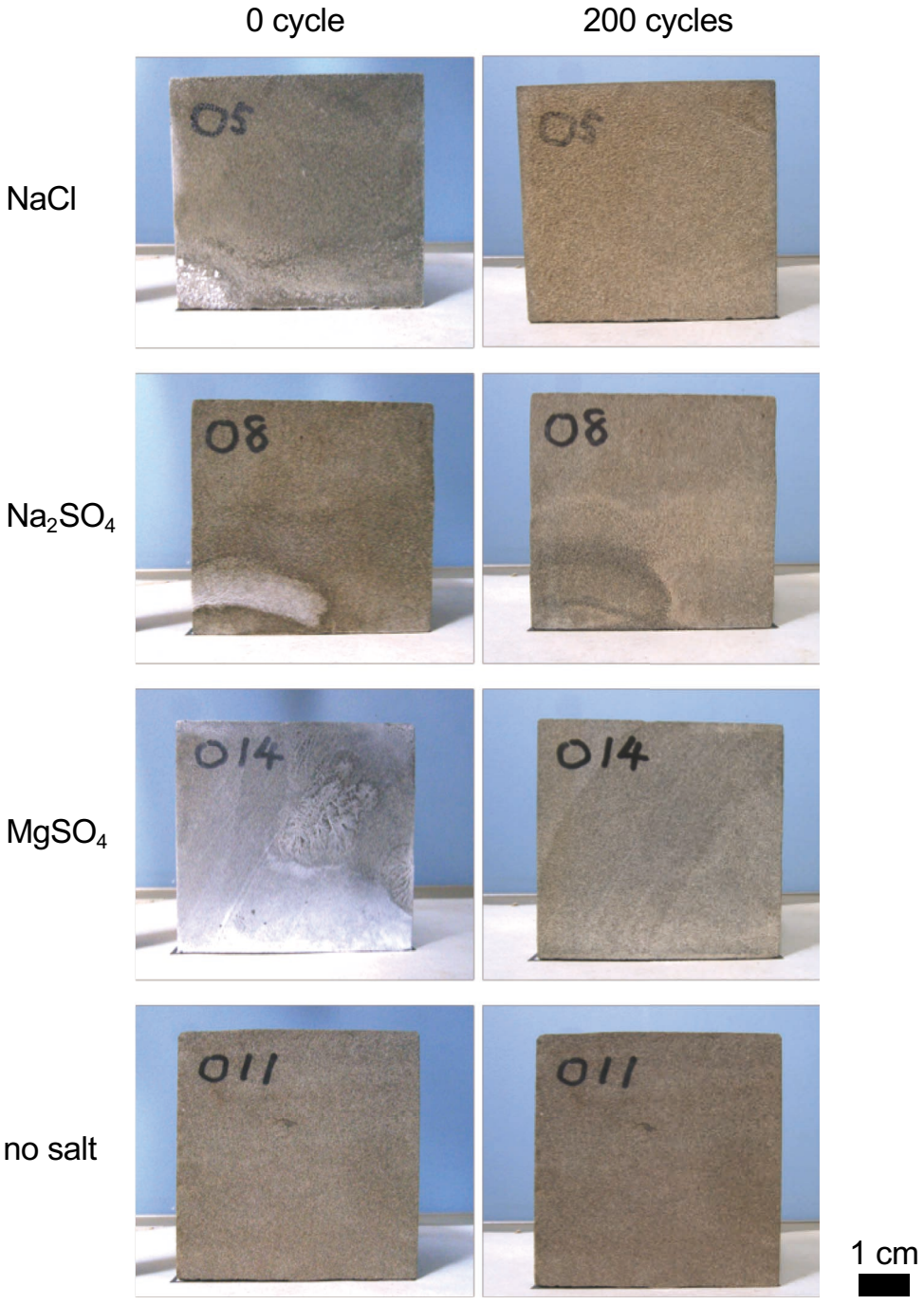

Figure 3.4 Aoshima sandstone subjected to humidity cycles at 10˚C

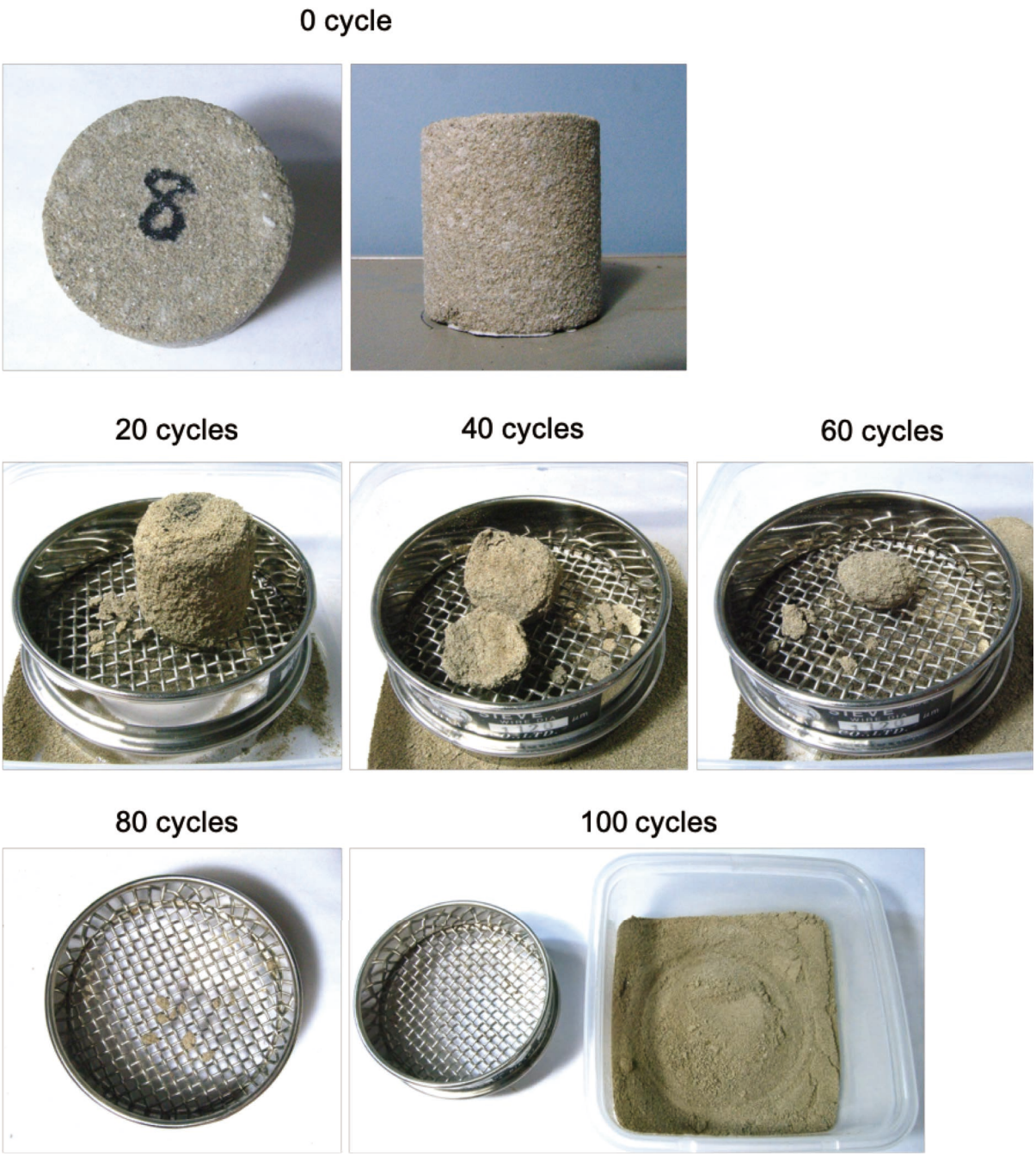

Figure 3.5 Ubara sandstone with sodium chloride, subjected to humidity cycles at 20˚C

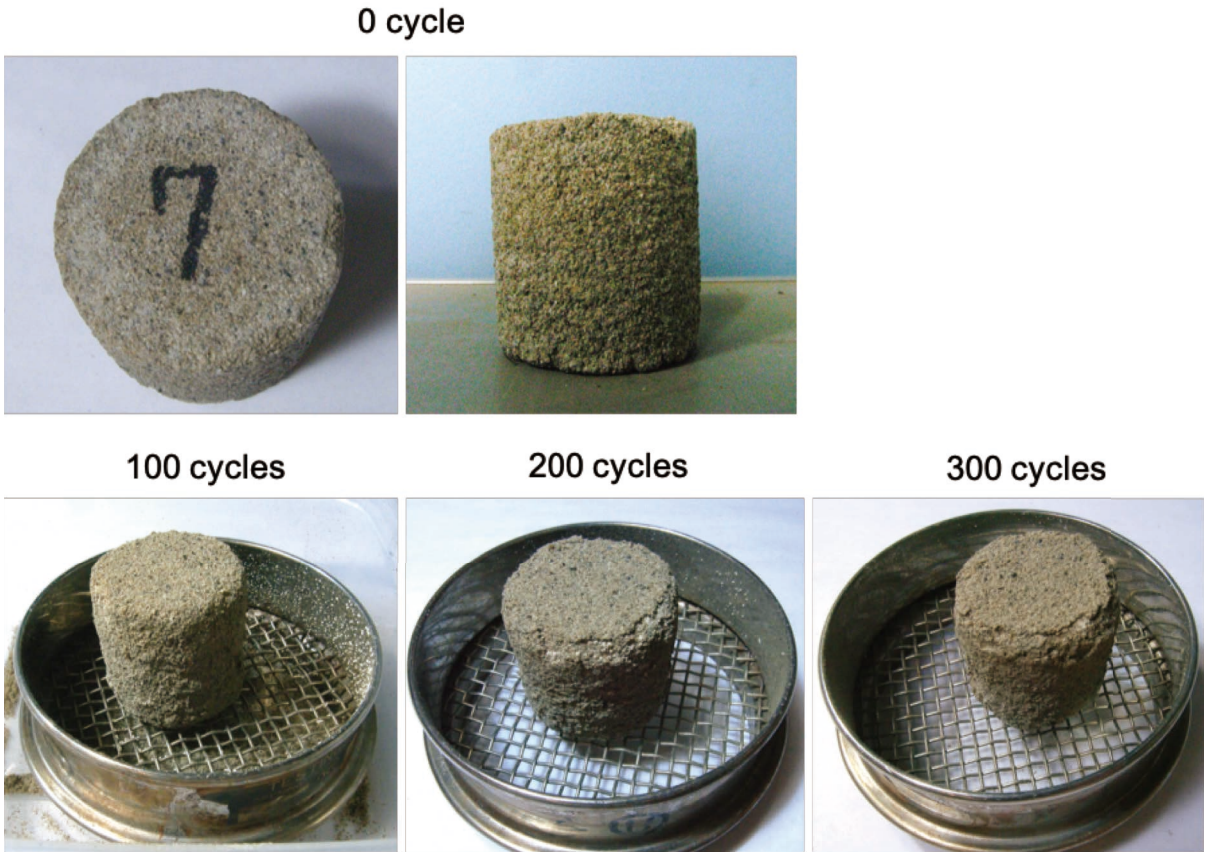

Figure 3.6 Ubara sandstone with sodium sulfate, subjected to humidity cycles at 20˚C

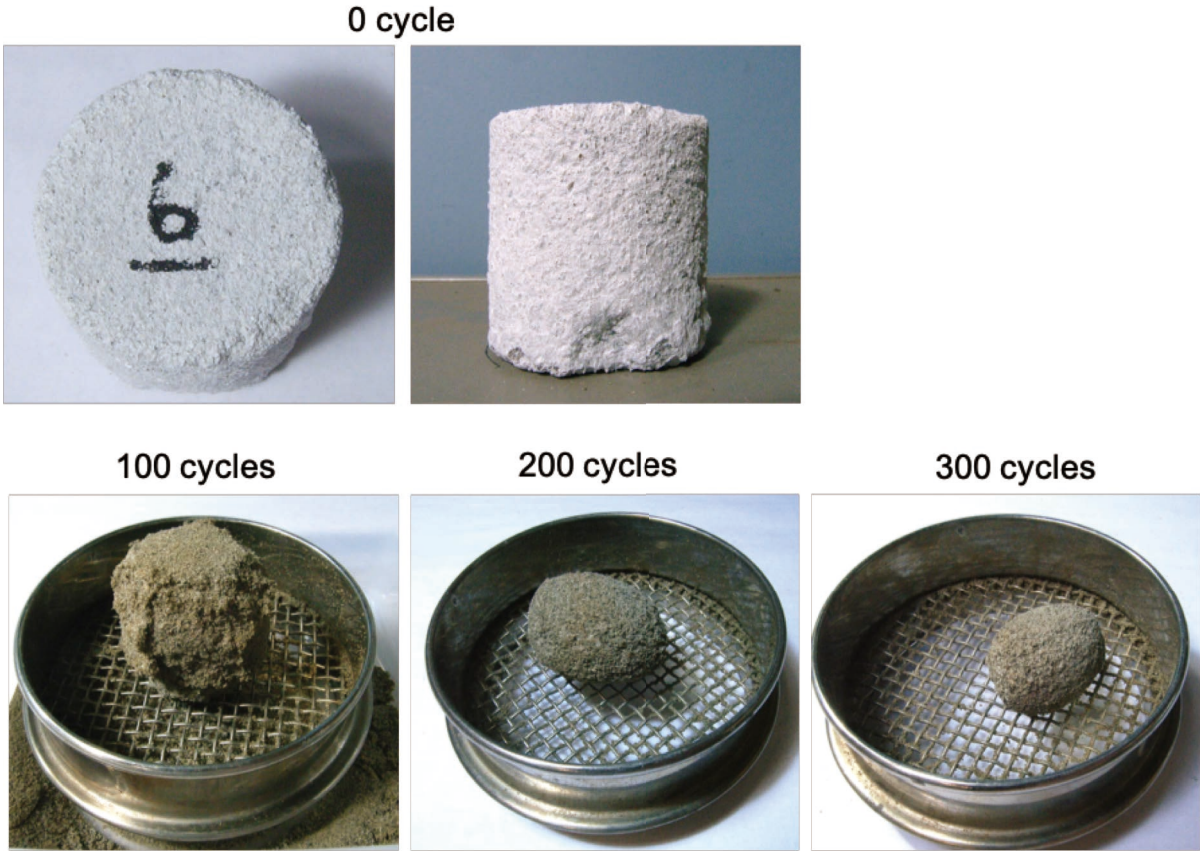

Figure 3.7 Ubara sandstone with magnesium sulfate, subjected to humidity cycles at 20˚C

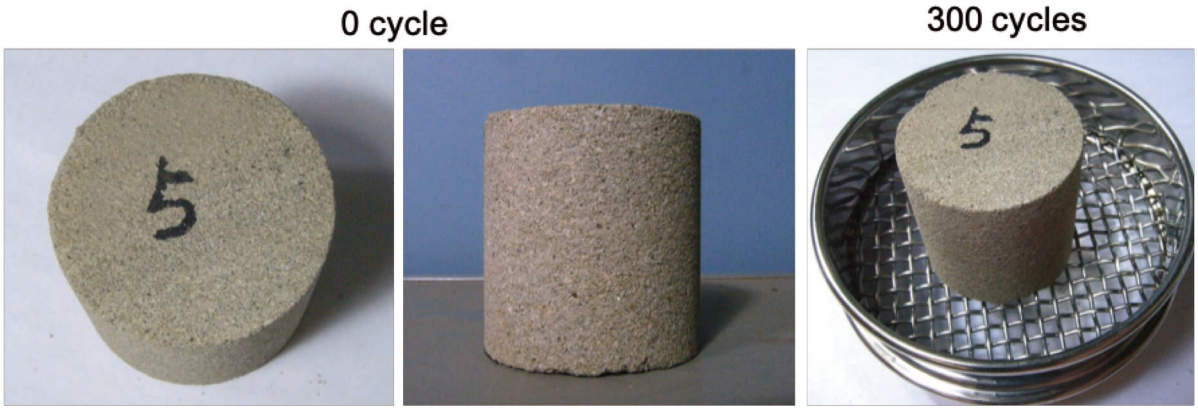

Figure 3.8 Ubara sandstone immersed in distilled water, subjected to humidity cycles at 20˚C.

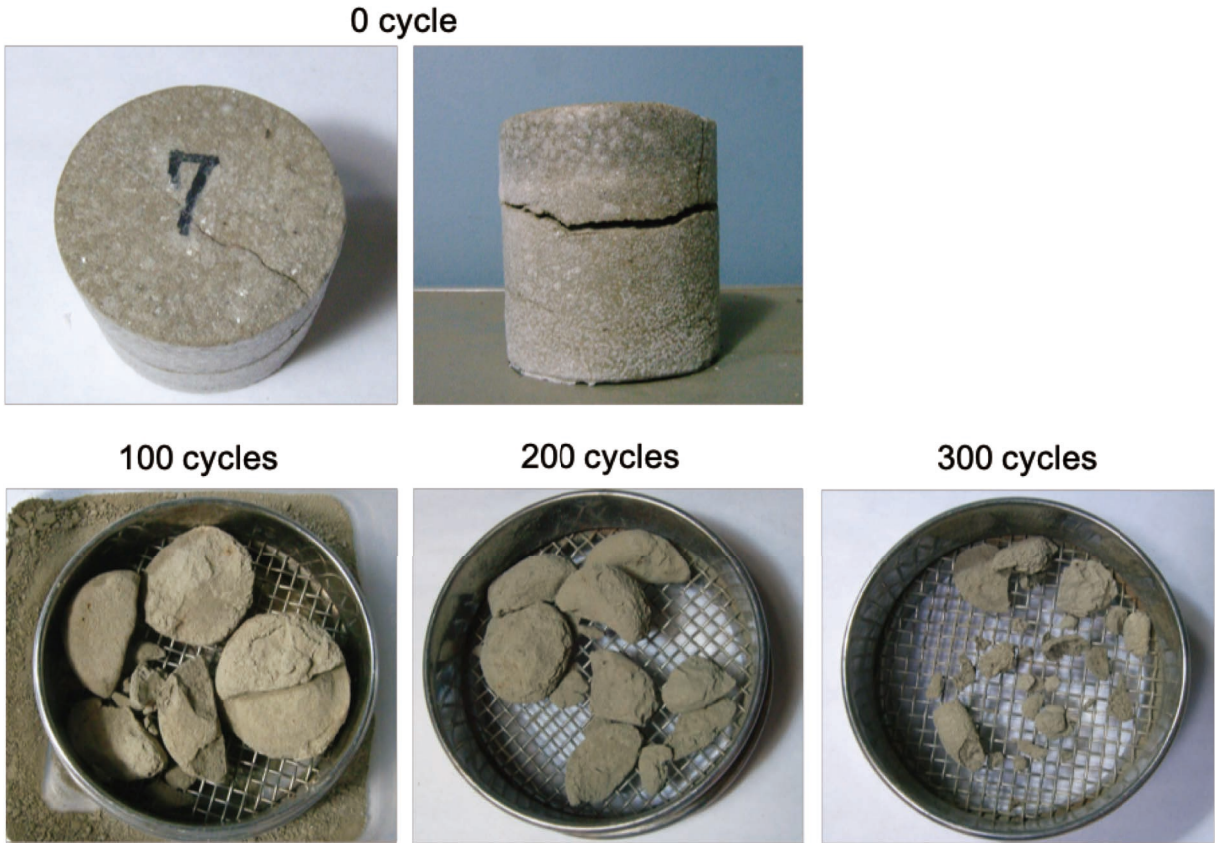

Figure 3.9 Taitozaki mudstone with sodium chloride, subjected to humidity cycles at 20˚C

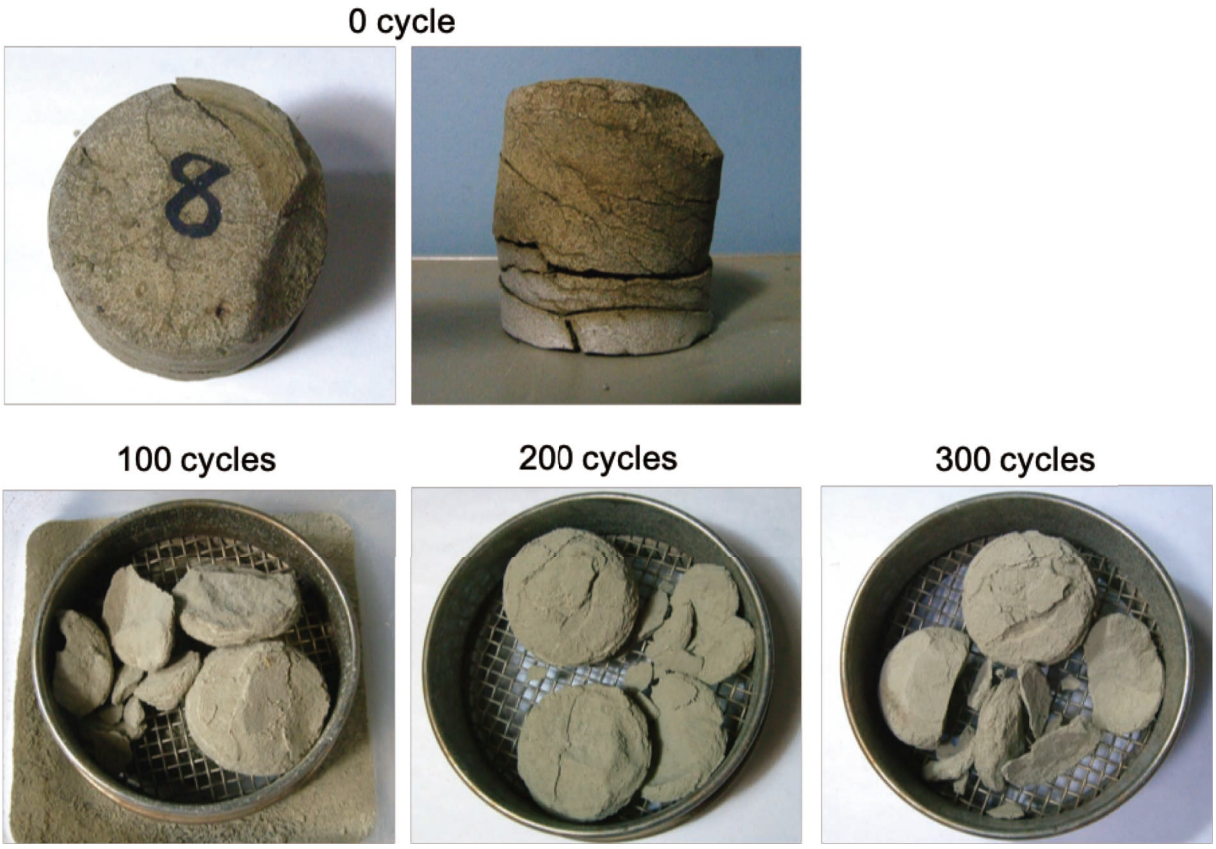

Figure 3.10 Taitozaki mudstone with sodium sulfate, subjected to humidity cycles at 20˚C

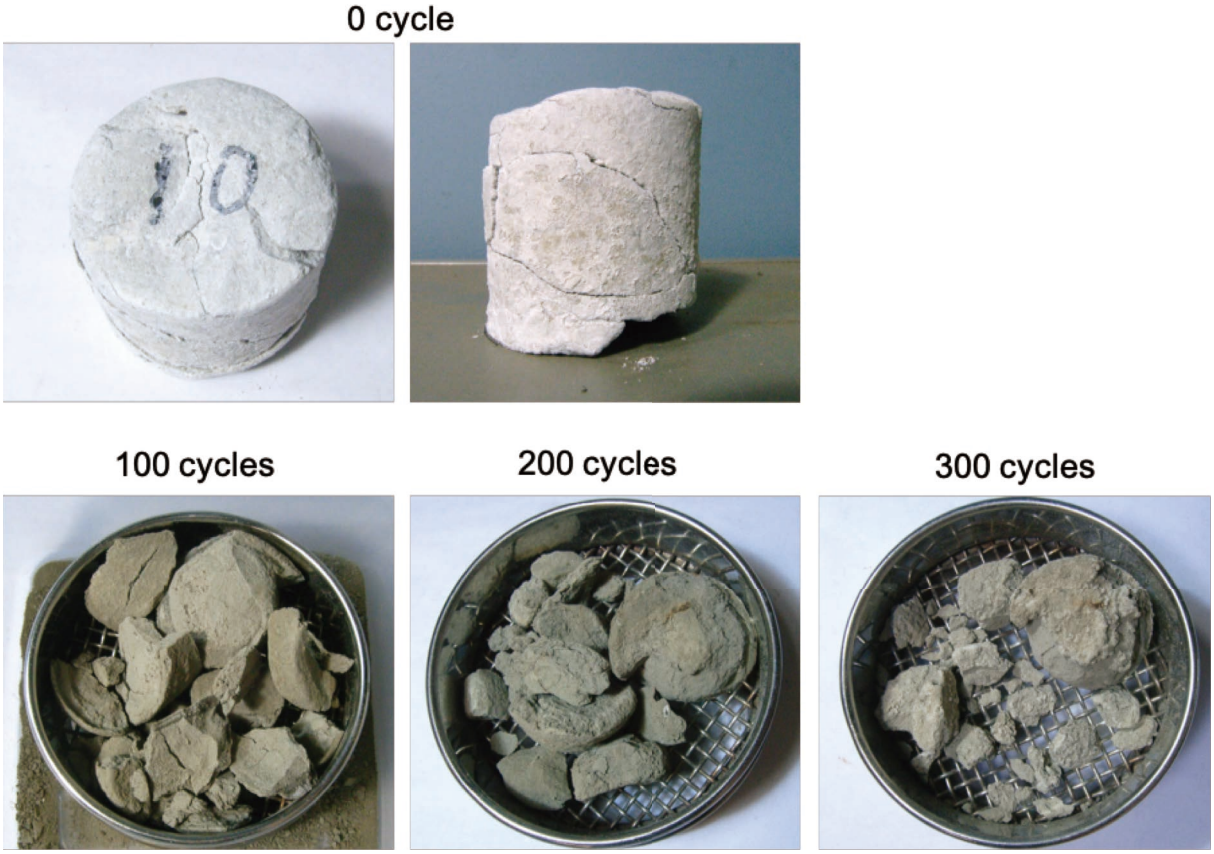

Figure 3.11 Taitozaki mudstone with magnesium sulfate, subjected to humidity cycles at 20˚C

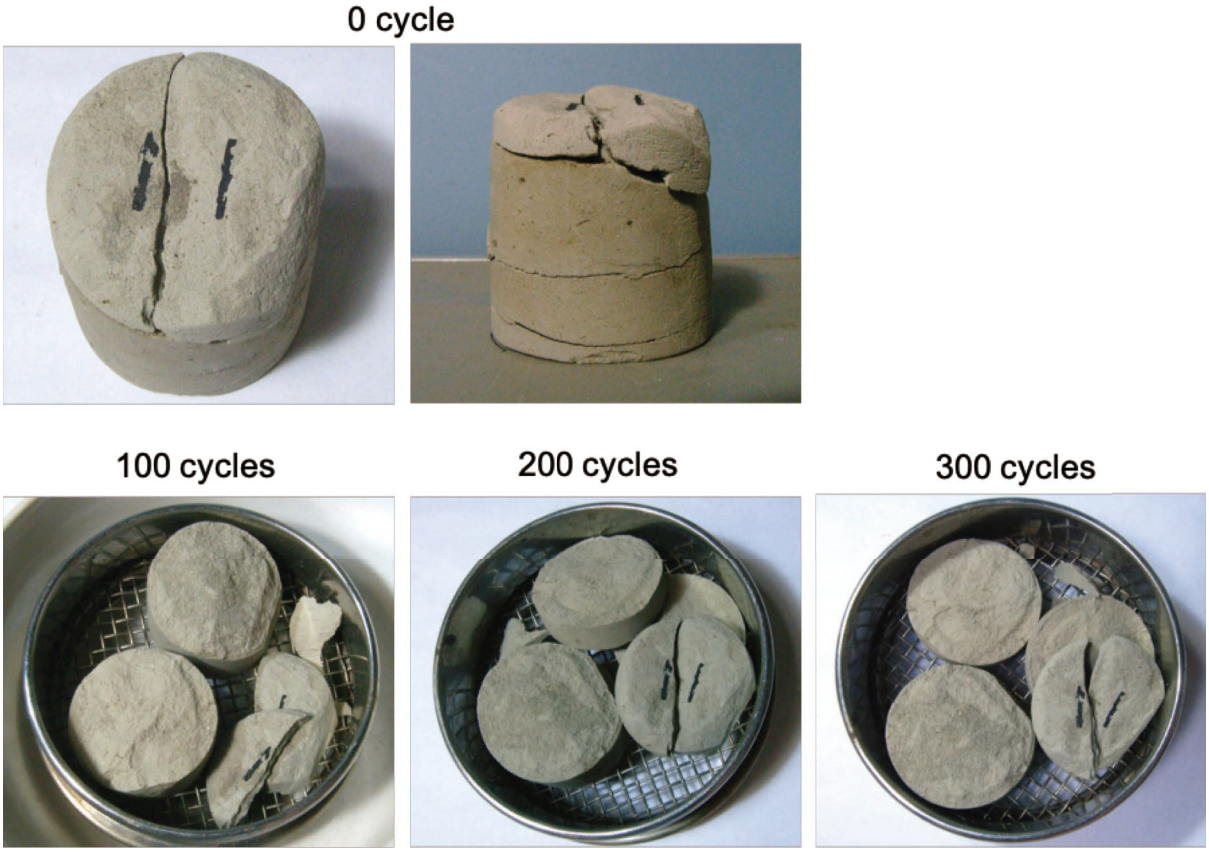

Figure 3.12 Taitozaki mudstone immersed in distilled water, subjected to humidity cycles at 20˚C

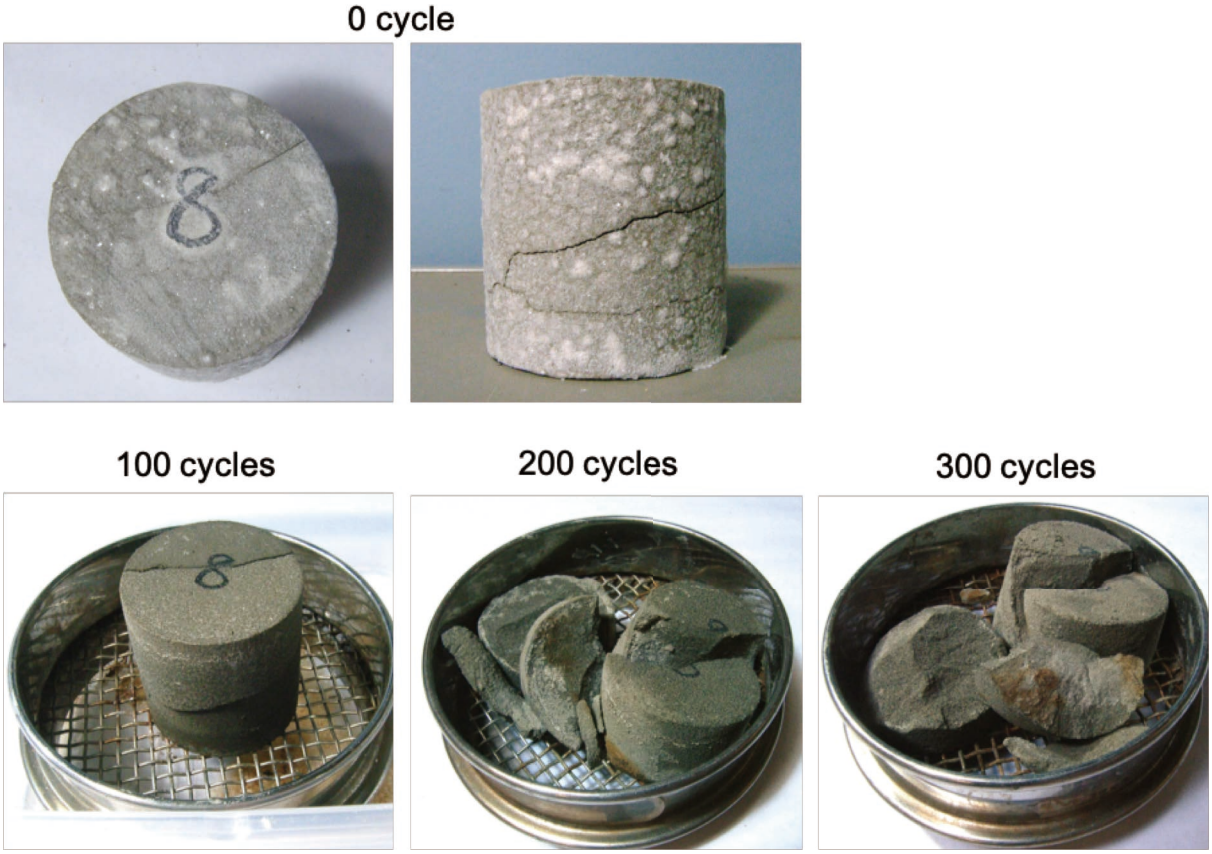

Figure 3.13 Miiri mudstone with sodium chloride, subjected to humidity cycles at 20˚C

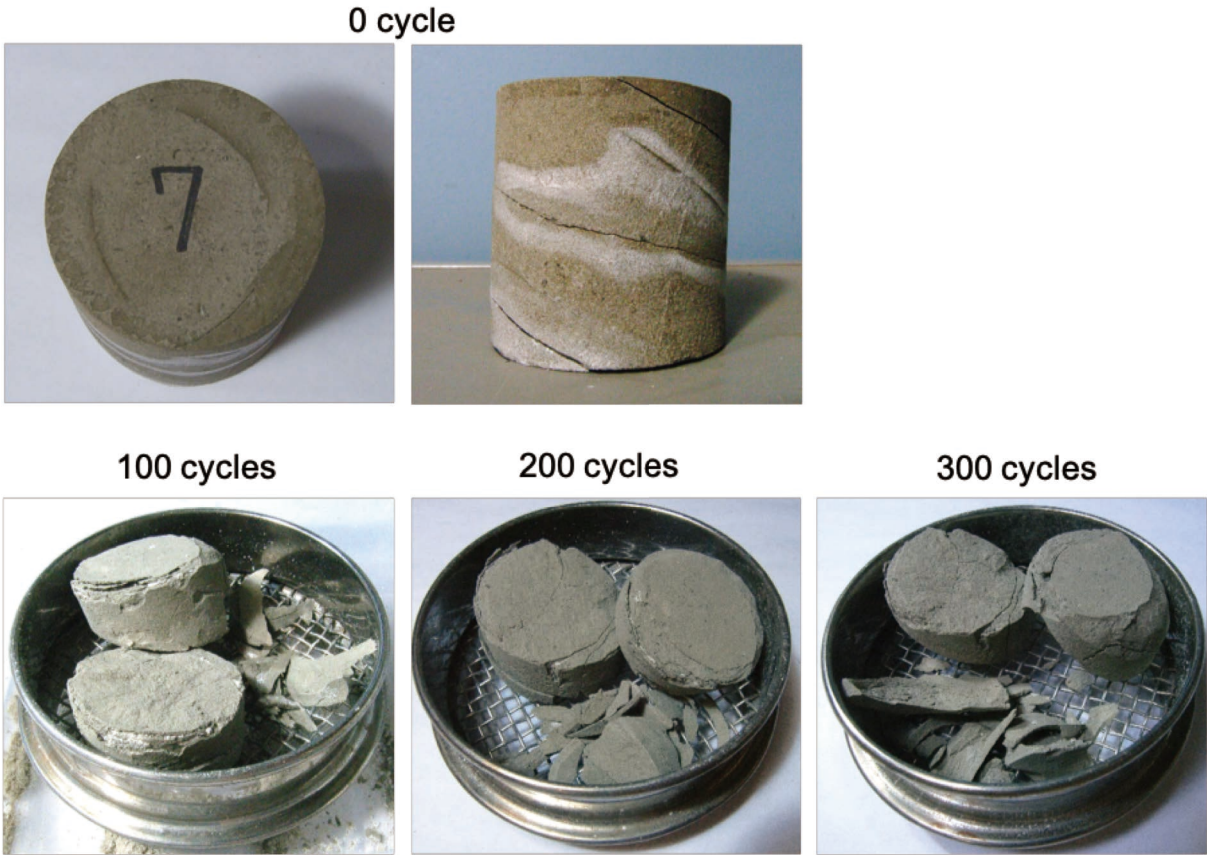

Figure 3.14 Miiri mudstone with sodium sulfate, subjected to humidity cycles at 20˚C

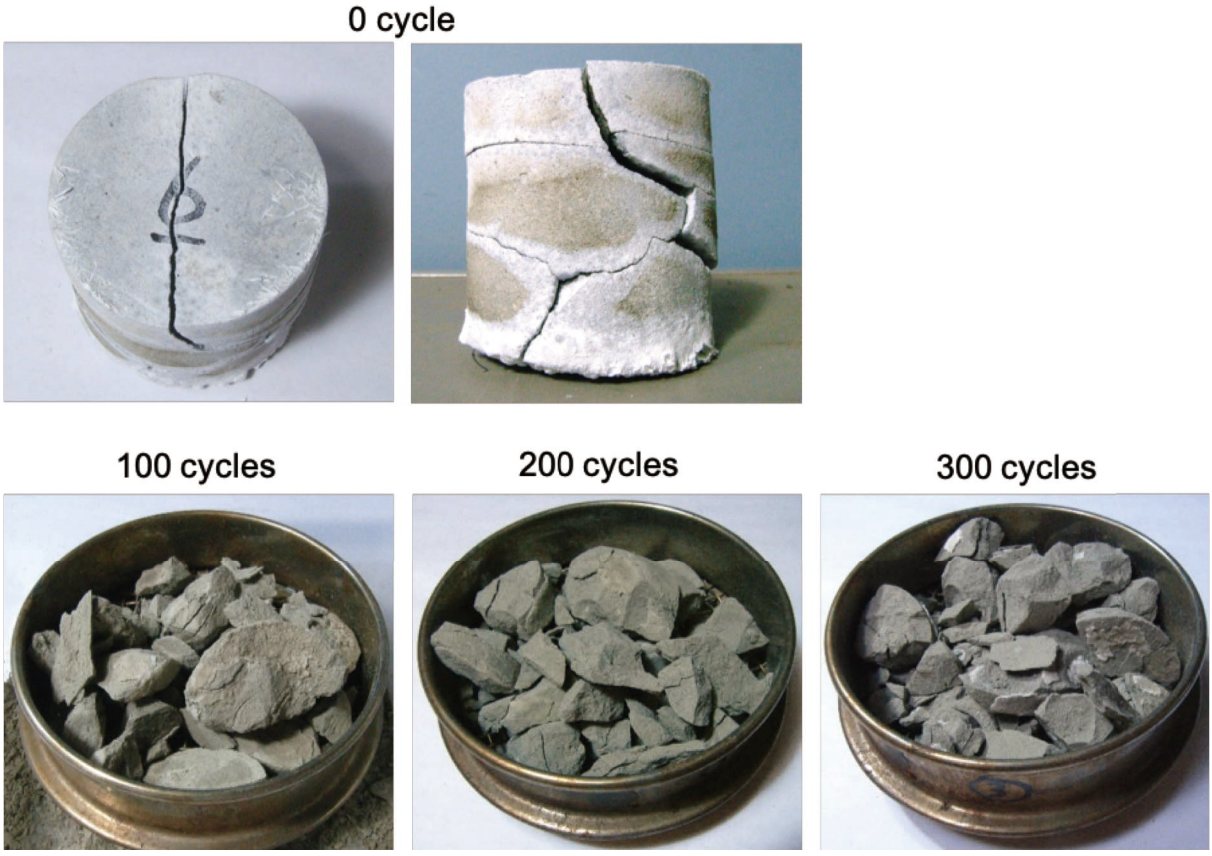

Figure 3.15 Miiri mudstone with magnesium sulfate, subjected to humidity cycles at 20˚C

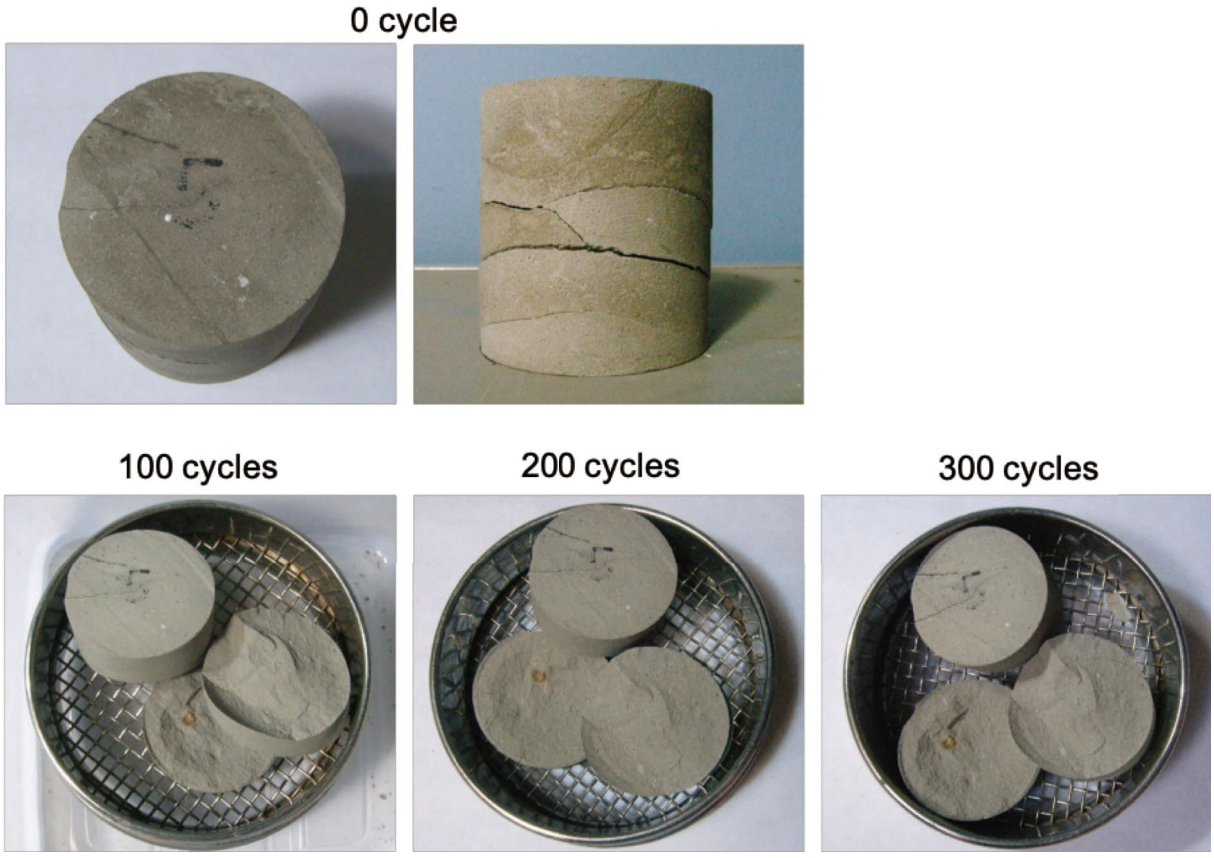

Figure 3.16 Miiri mudstone immersed in distilled water, subjected to humidity cycles at 20˚C

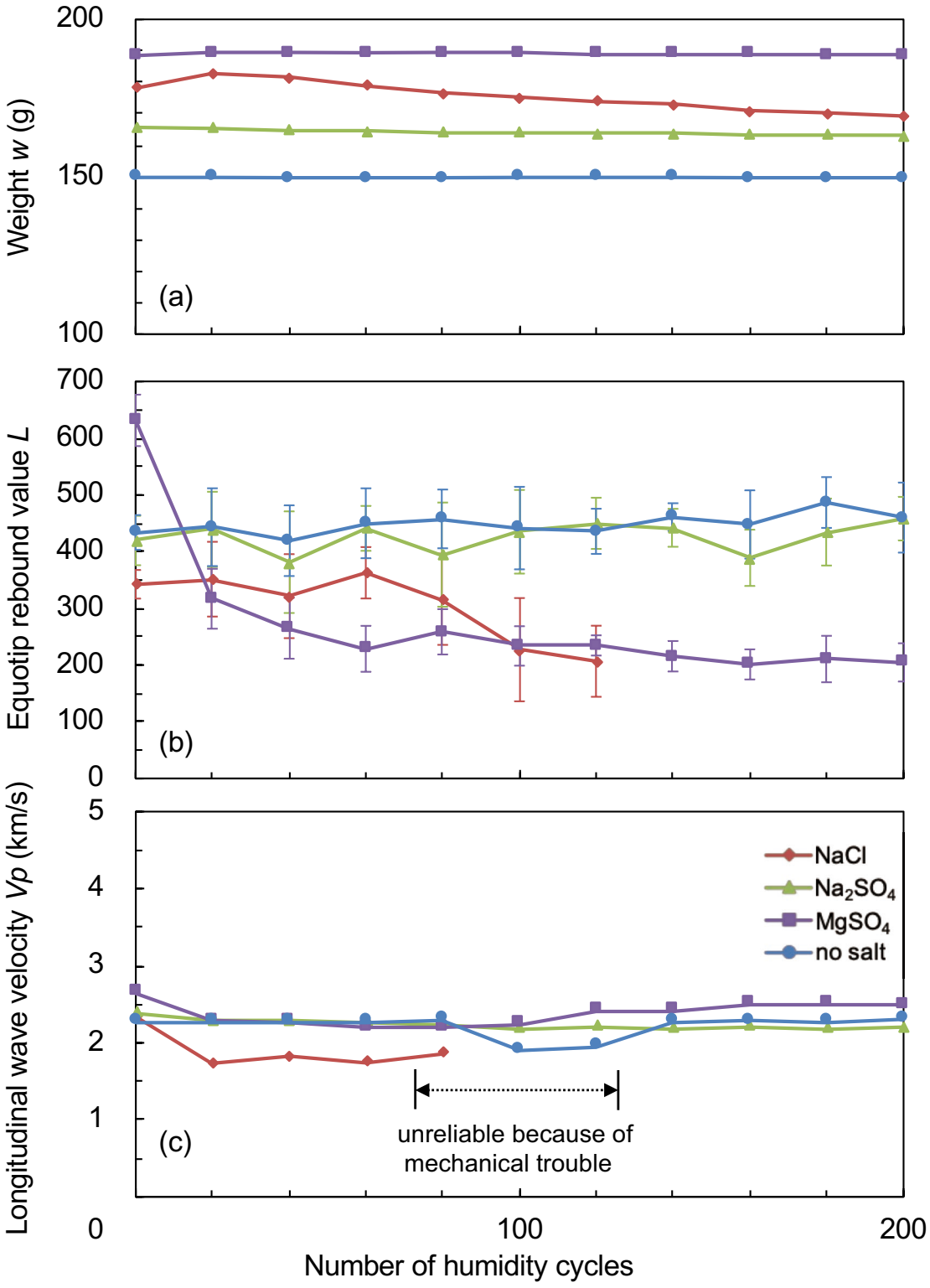

Figure 3.17 Weight (a), Equotip rebound value (b), and longitudinal wave velocity (c) measured during humidity-change experiment (Oya tuff, 20˚C)

Vertical bar in the L-value represents dispersion of 10 single impacts. Records of longitudinal wave velocity from 80 to 120 cycles are unreliable because of mechanical trouble.

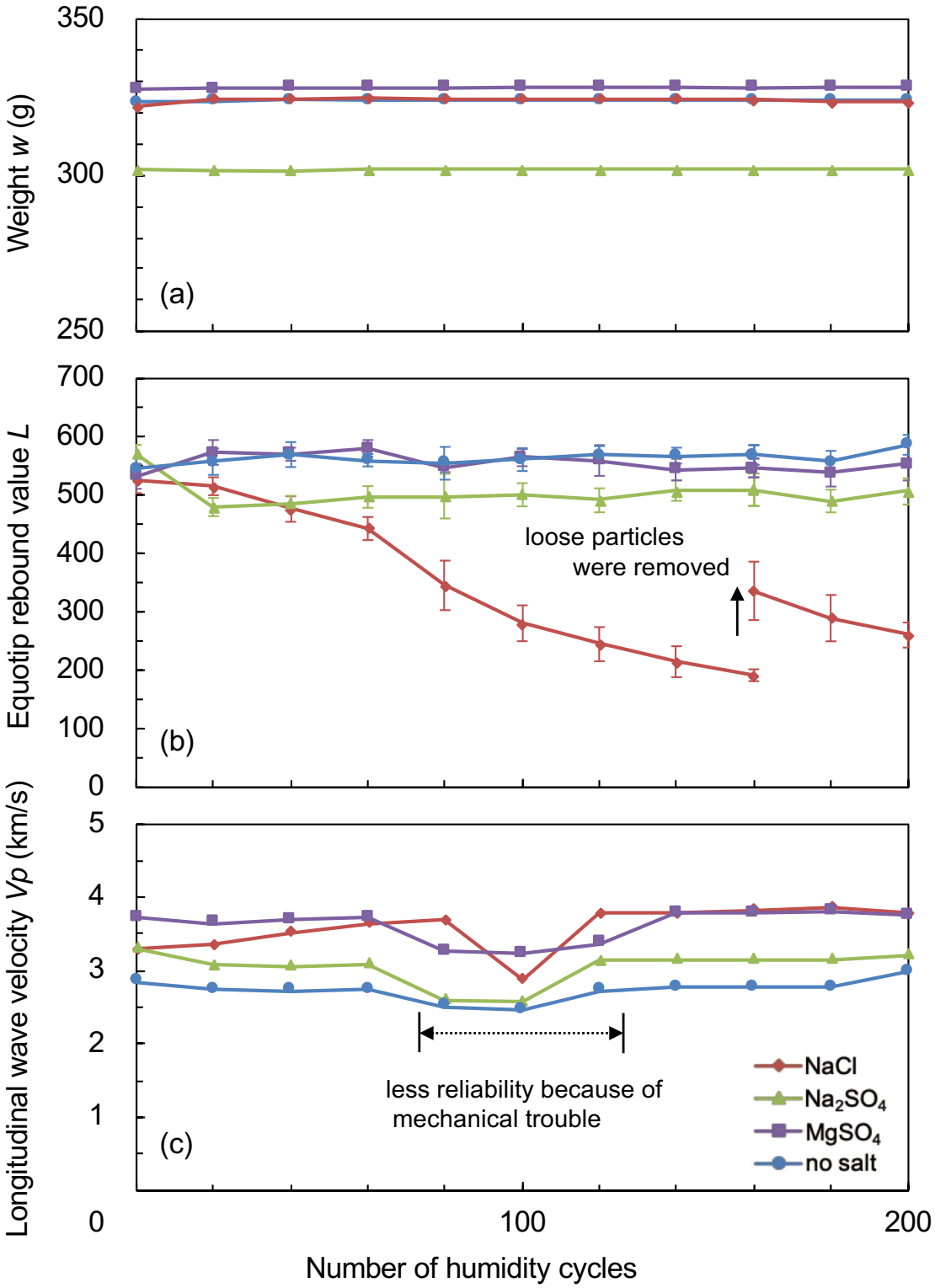

Figure 3.18 Weight (a), Equotip rebound value (b), and longitudinal wave velocity (c) measured during humidity-change experiment (Aoshima sandstone, 20˚C)

Vertical bar in the L-value represents dispersion of 10 single impacts. The L-values of Aoshima sandstone with sodium chloride from 160 to 200 cycles were measured after a treatment that loose particles on the surface were removed with paper cloth.

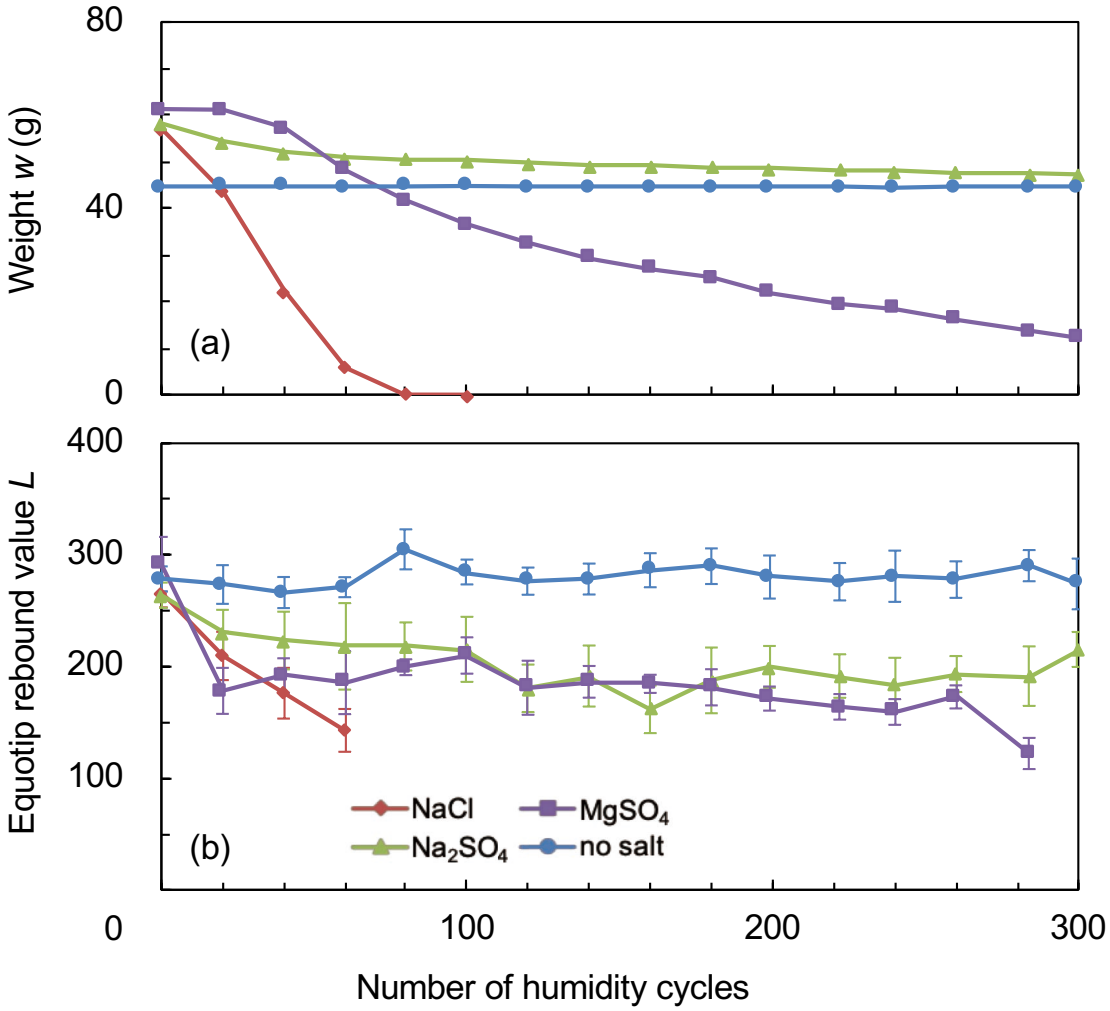

Figure 3.19 Weight (a) and Equotip rebound value (b) measured during humidity-change experiment (Ubara sandstone, 20˚C)

Vertical bar in the L-value represents dispersion of 10 single impacts.

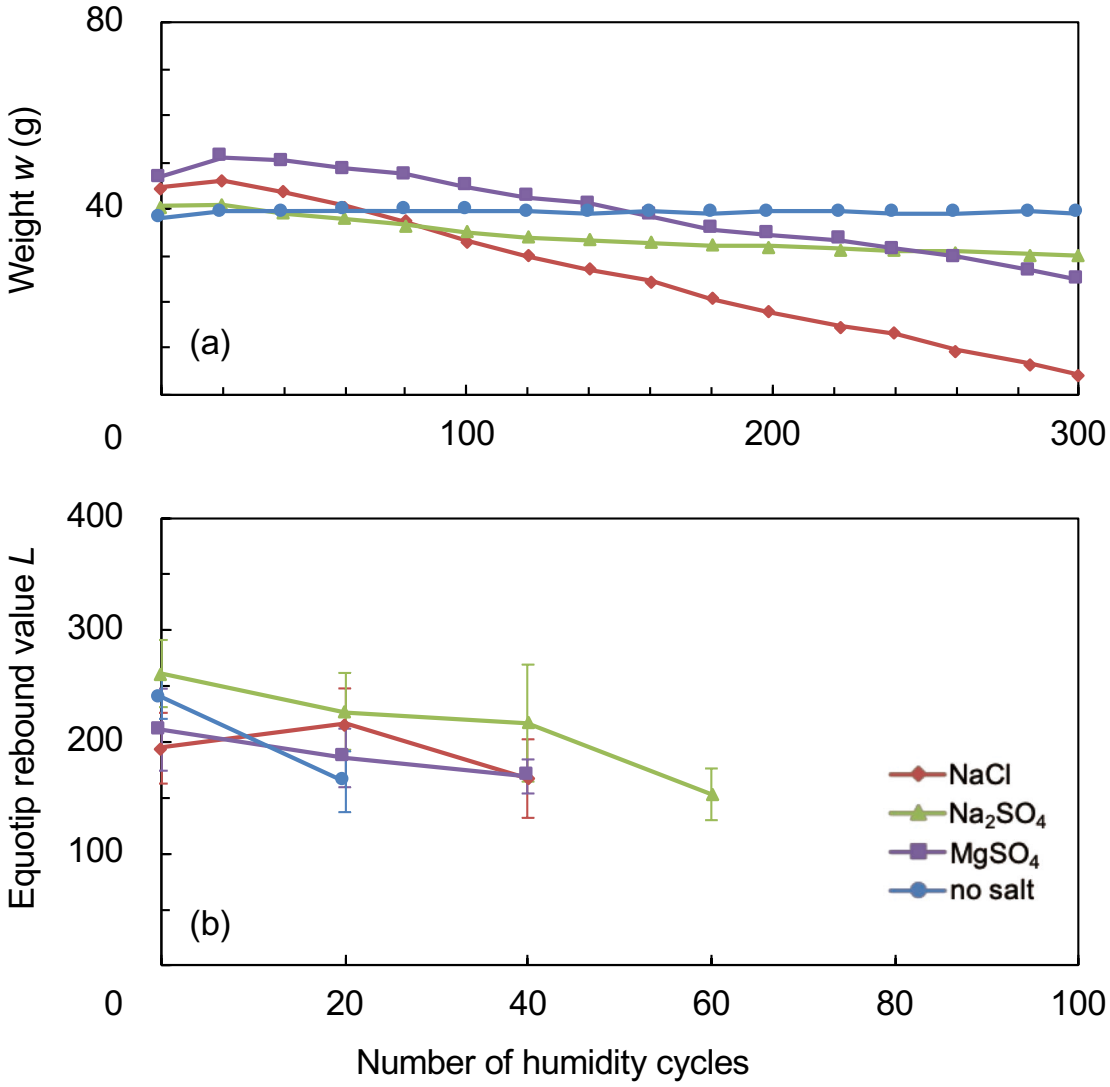

Figure 3.20 Weight (a) and Equotip rebound value (b) measured during humidity-change experiment (Taitozaki mudstone, 20˚C)

Vertical bar in the L-value represents dispersion of 10 single impacts.

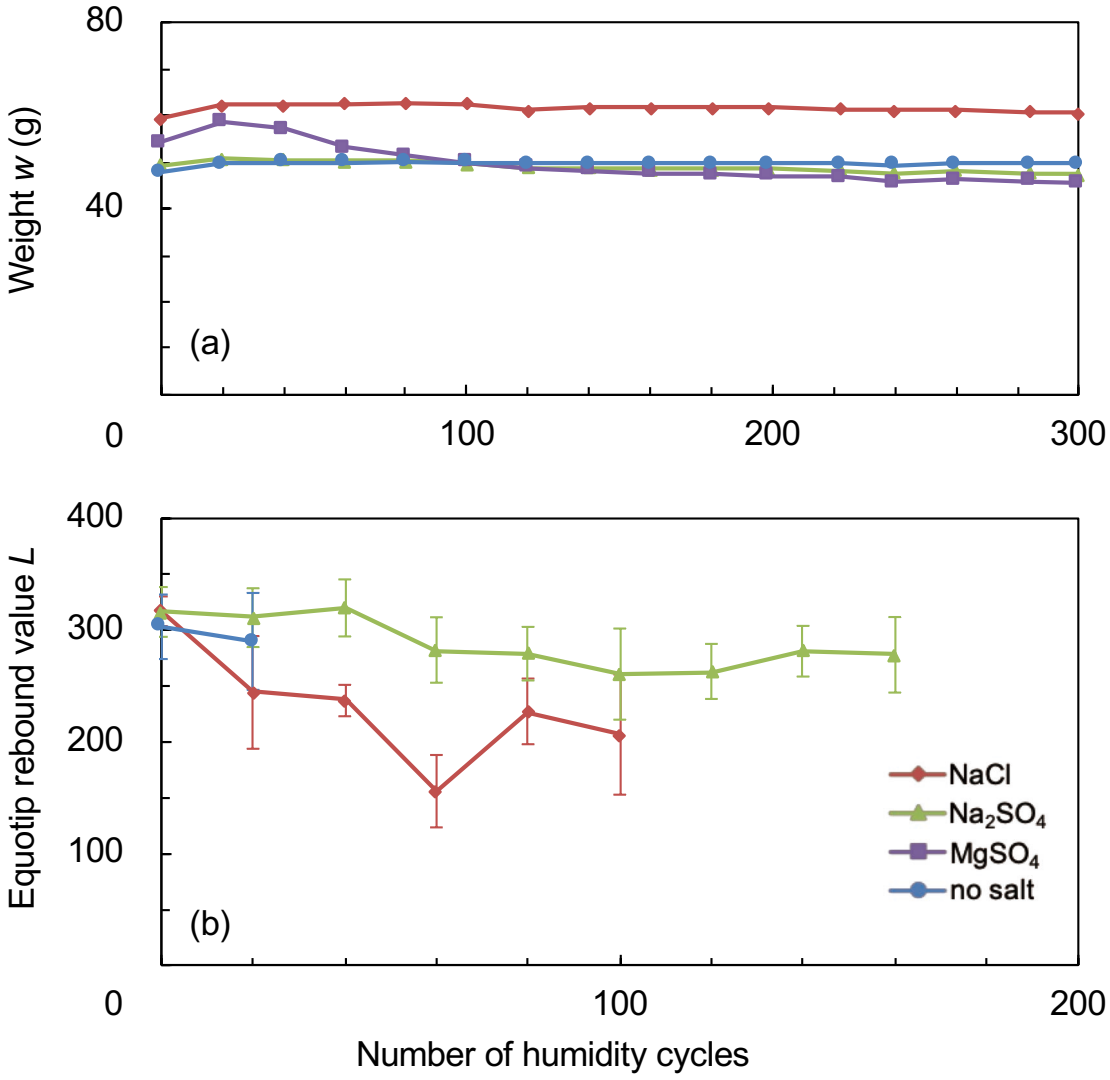

Figure 3.21 Weight (a) and Equotip rebound value (b) measured during humidity-change experiment (Miiri mudstone, 20˚C)

Vertical bar in the L-value represents dispersion of 10 single impacts.

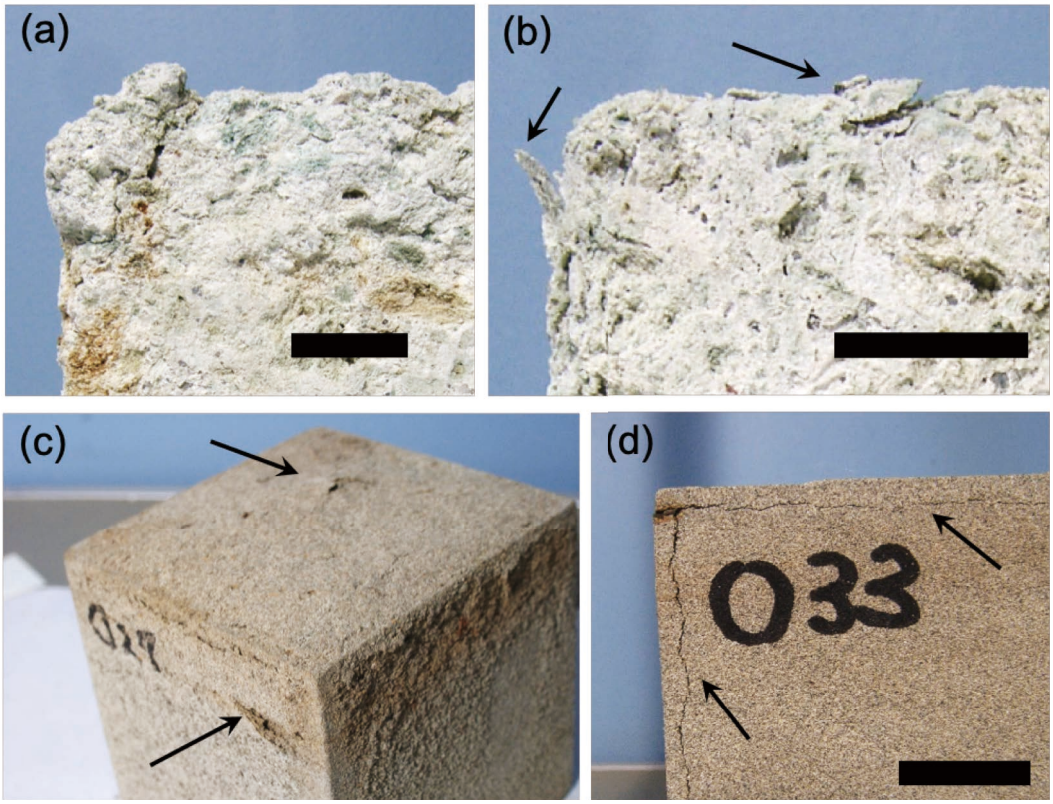

Figure3.22 Oya tuff and Aoshima sandstone with sodium chloride or magnesium sulfate subjected to 200 humidity cycles at 20˚C

The scale bars are 1-cm long. Oya tuff with sodium chloride (a) and magnesium sulfate (b) showed irregular morphology on their surface. Millimeter-scale fragments flaked from the surface of the Oya tuff with magnesium sulfate. Aoshima sandstone with sodium chloride (c) showed swelling on the surface. Cracks parallel to the rock surface were observed on the edge of the Aoshima sandstone with magnesium sulfate (d).

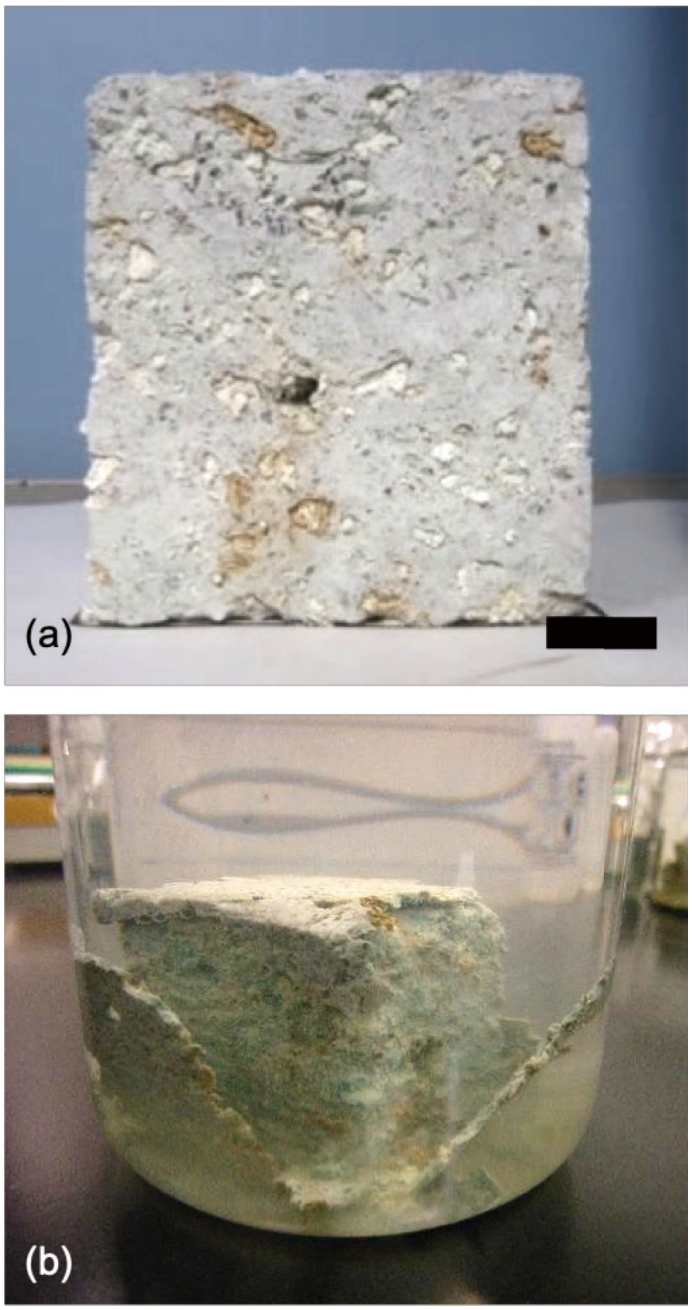

Figure 3.23 Oya tuff with sodium sulfate subjected to 200 humidity cycles at 20˚C

(a) Oya tuff with sodium sulfate subjected to 200 humidity cycles at 20˚C. The scale bar is 1-cm long. Any obvious crack, flaking, or swelling was not observed. (b) The specimen was immersed in distilled water after the humidity-change experiment. Tabular fragments flaked from surface of the specimen.

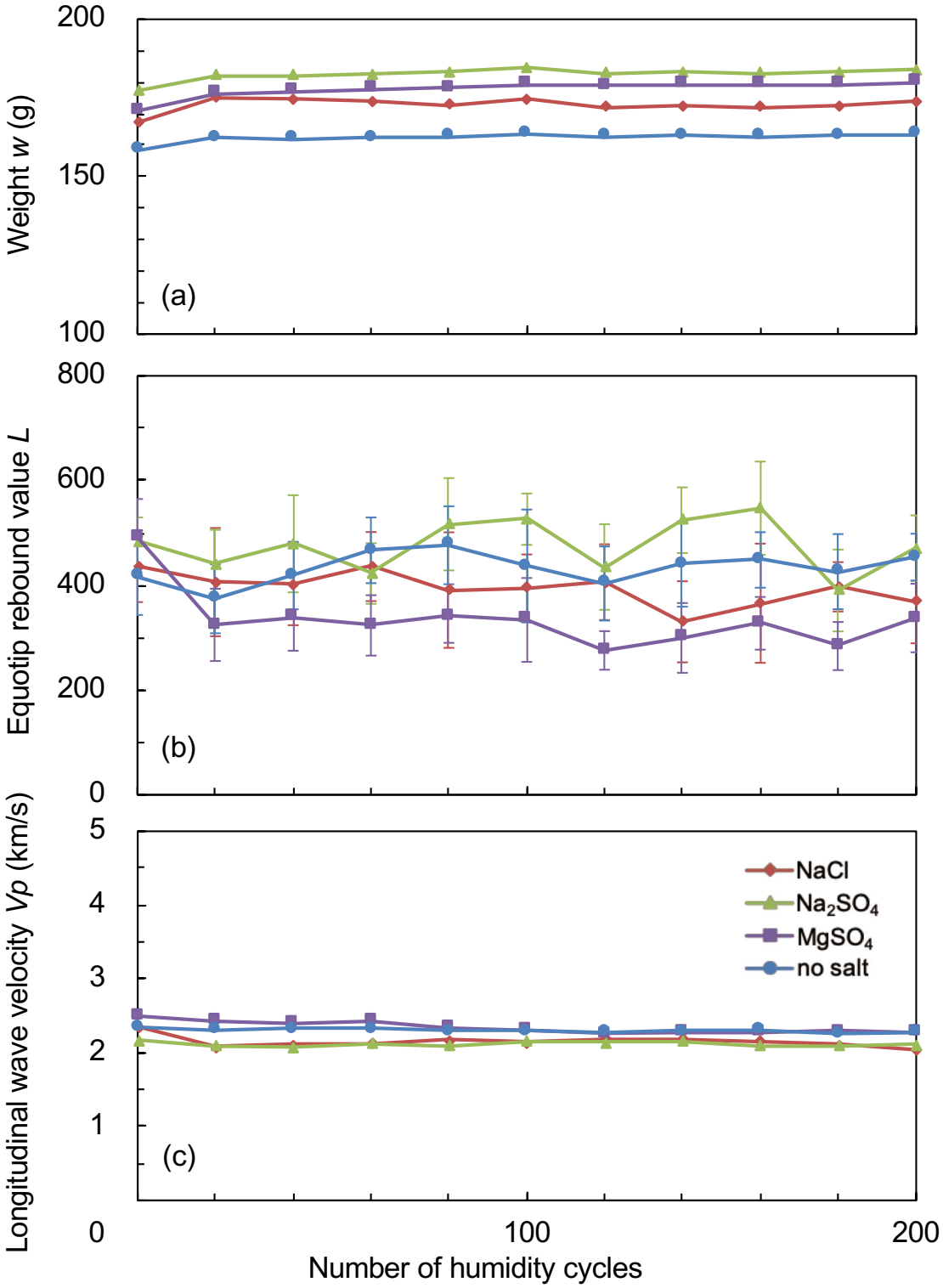

Figure 3.24 Weight (a), Equotip rebound value (b), and longitudinal wave velocity (c) measured during humidity-change experiment (Oya tuff, 10˚C)

Vertical bar in the L-value represents dispersion of 10 single impacts.

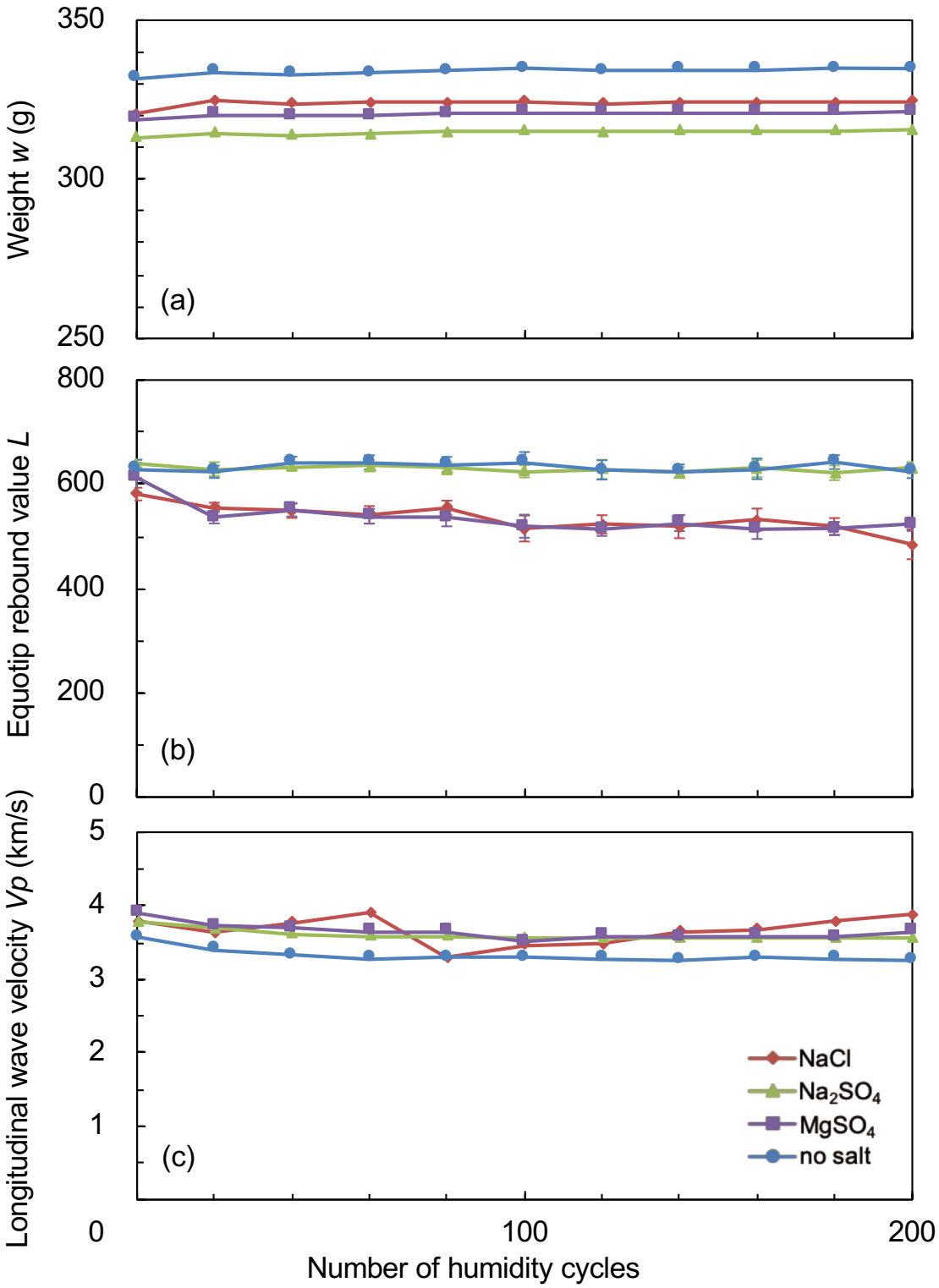

Figure 3.25 Weight (a), Equotip rebound value (b), and longitudinal wave velocity (c) measured during humidity-change experiment (Aoshima sandstone, 10˚C)

Vertical bar in the L-value represents dispersion of 10 single impacts.

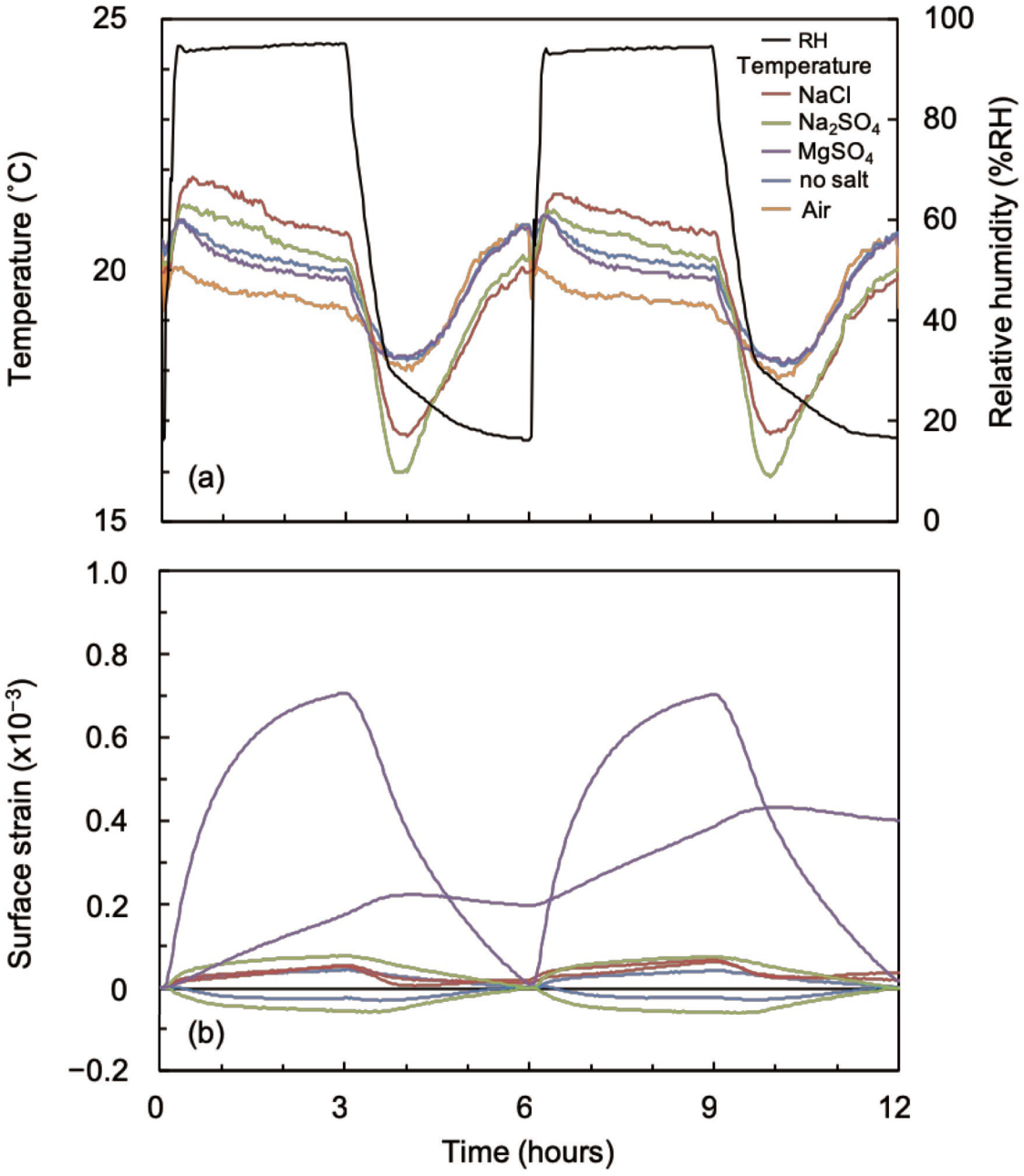

Figure 3.26 Typical temperature and humidity (a), and surface strain (b) changes in humidity cycles (Oya tuff, 20˚C, from 6 to 7 cycles)

T-type thermocouple was installed in a pit at a depth of 5 mm. Two strain gauges were adhered to different faces of a specimen. The increase in strain represents expansion.

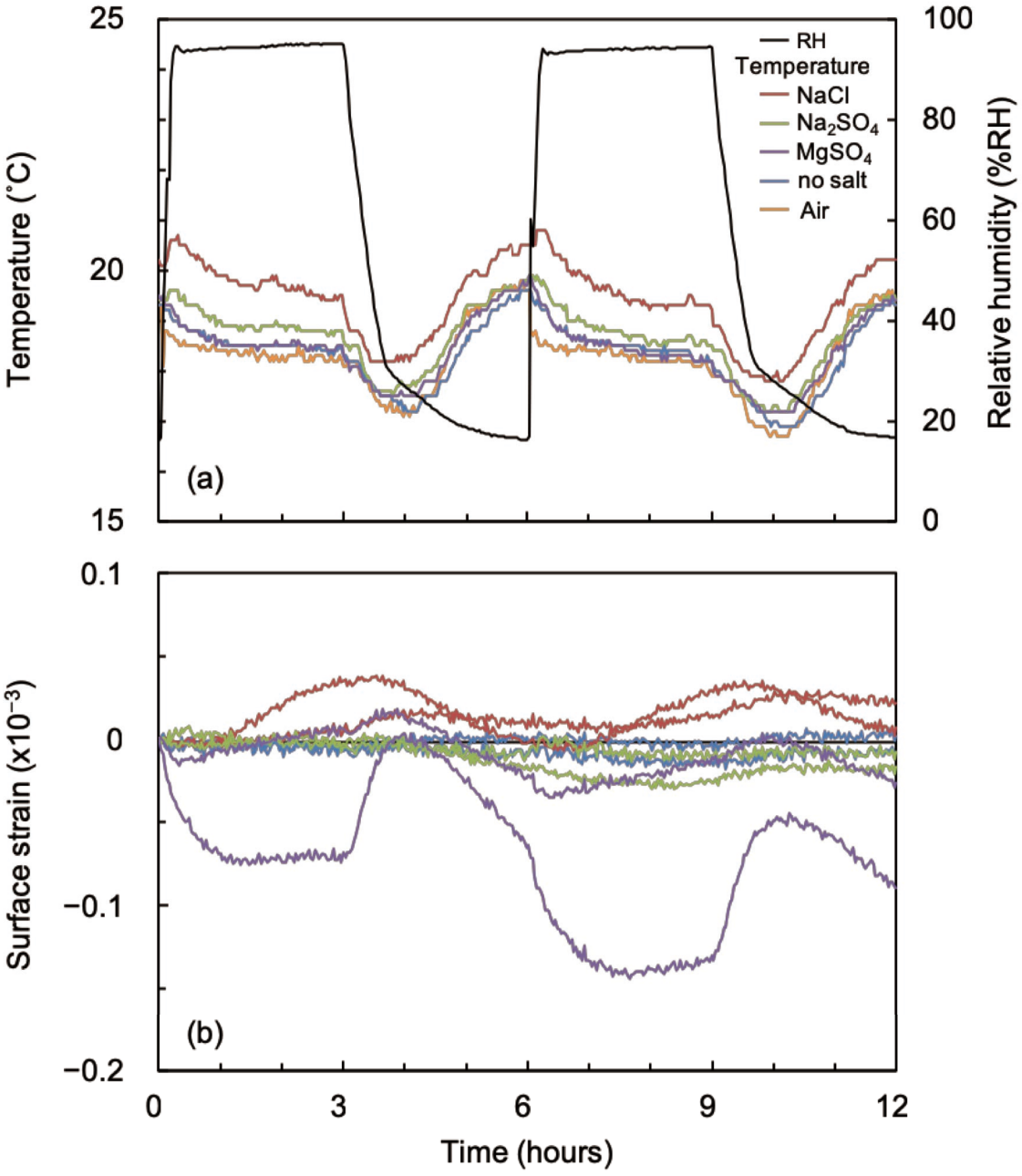

Figure 3.27 Typical temperature and humidity (a), and surface strain (b) changes in humidity cycles (Aoshima sandstone, 20˚C, from 6 to 7 cycles)

T-type thermocouple was installed in a pit at a depth of 5 mm. Two strain gauges were adhered to different faces of a specimen. The increase in strain represents expansion.

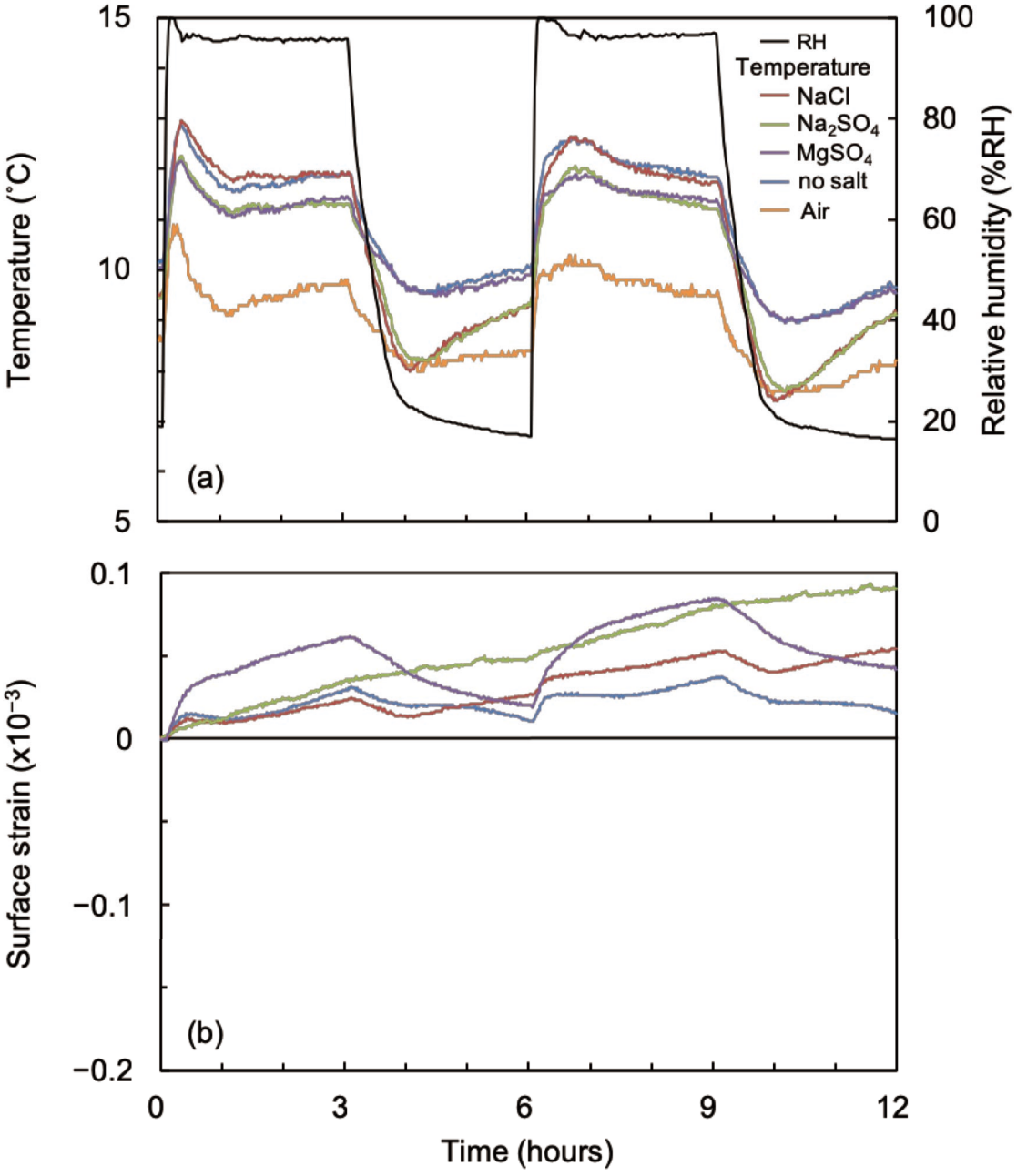

Figure 3.28 Typical temperature and humidity (a), and surface strain (b) changes in humidity cycles (Oya tuff, 10˚C, from 12 to 13 cycles)

T-type thermocouple was installed in a pit at a depth of 5 mm. The increase in strain represents expansion.

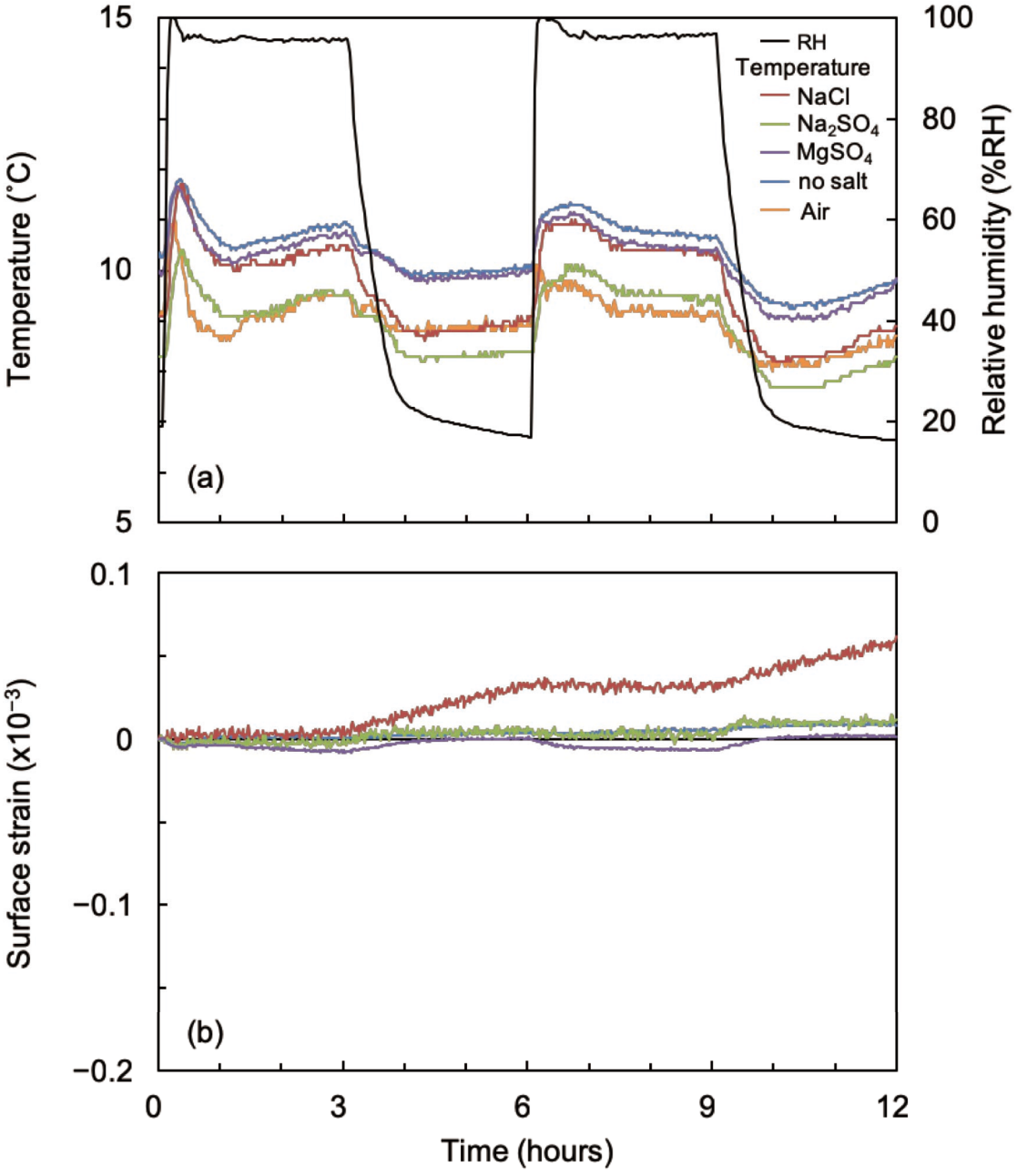

Figure 3.29 Typical temperature and humidity (a), and surface strain (b) changes in humidity cycles (Aoshima sandstone, 10˚C, from 12 to 13 cycles)

T-type thermocouple was installed in a pit at a depth of 5 mm. The increase in strain represents expansion.

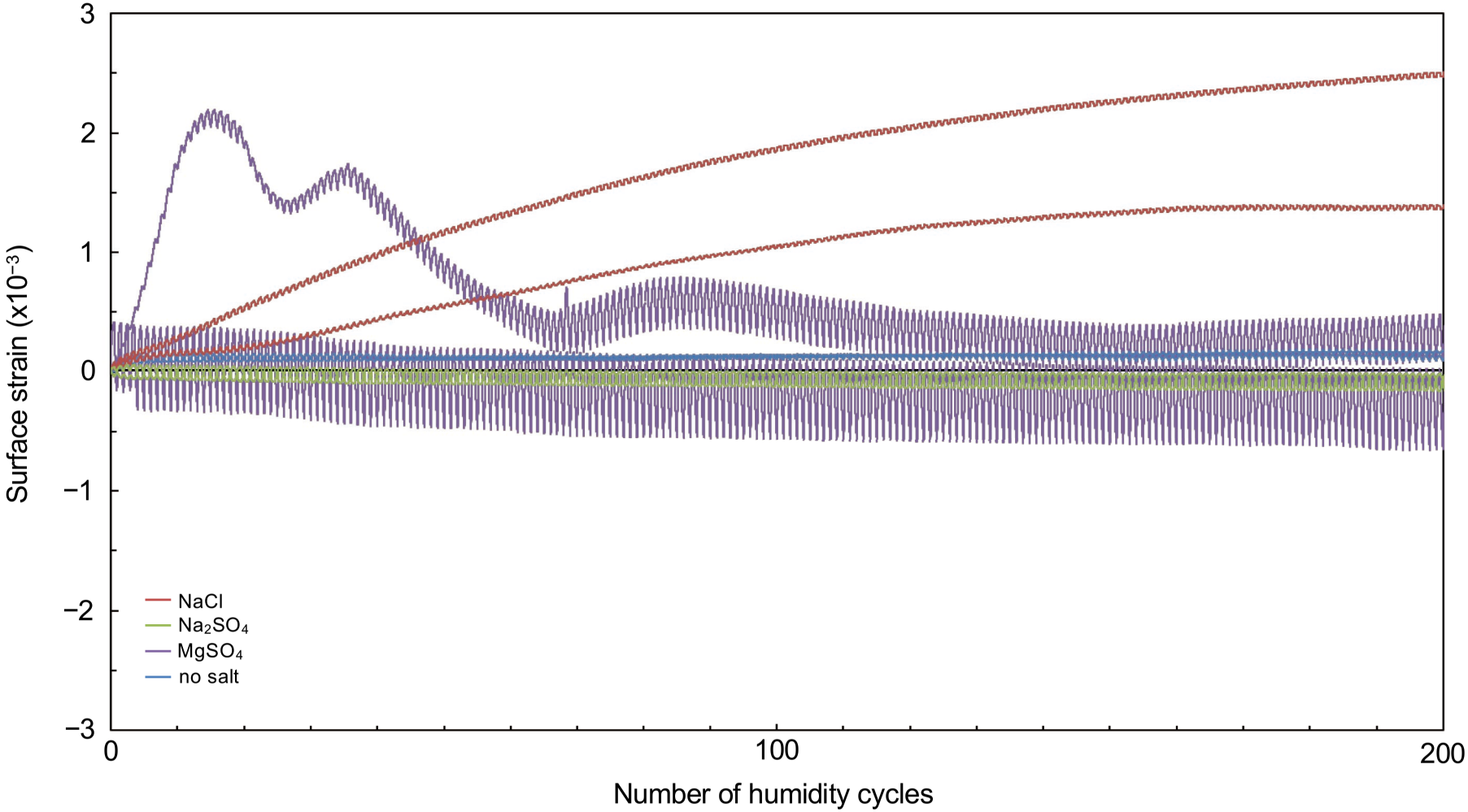

Figure 3.30 Cumulative surface strain in 200 humidity cycles (Oya tuff, 20˚C)

Two strain gauges were adhered to different faces of a specimen. The increase in strain represents expansion.

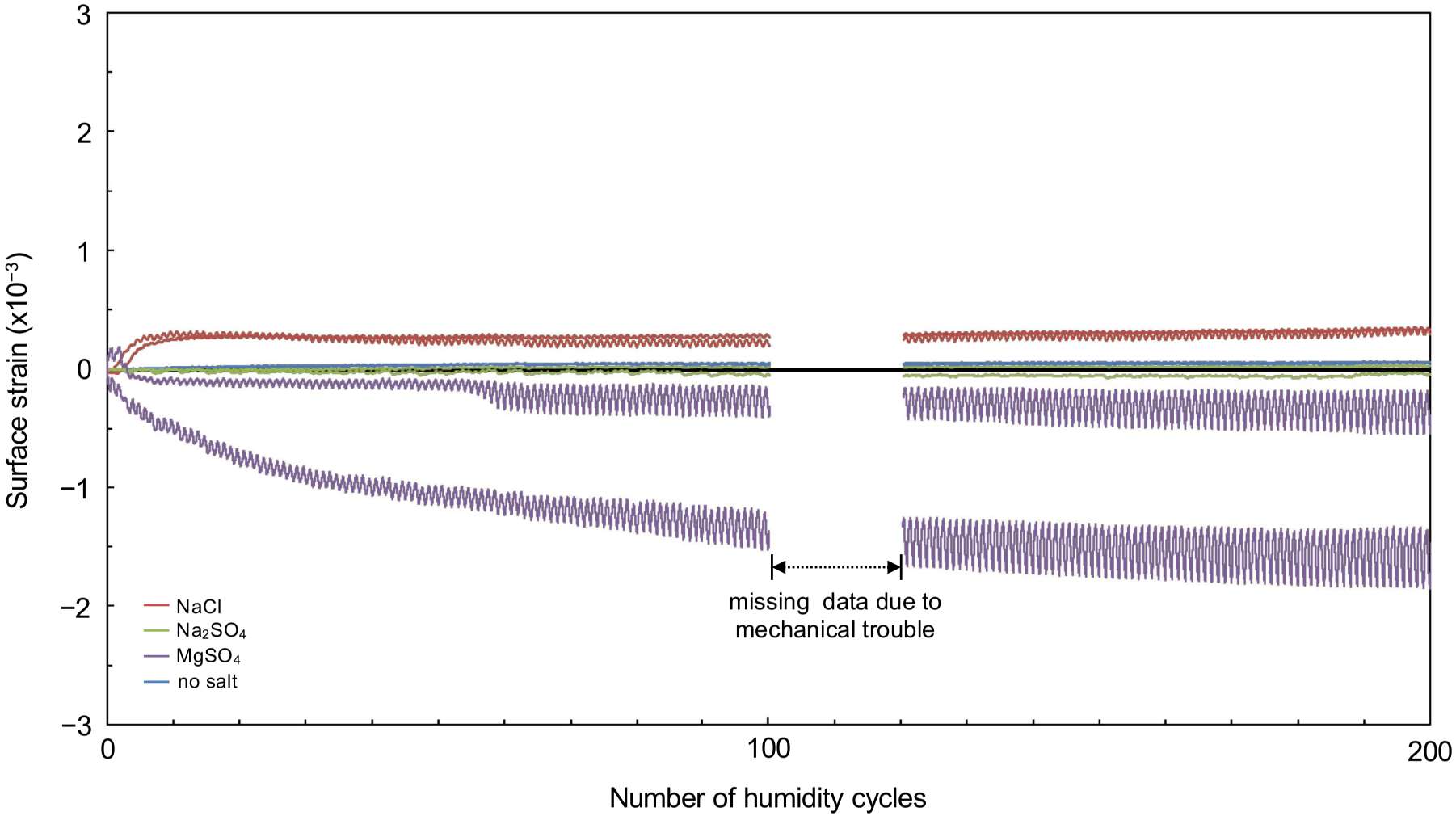

Figure 3.31 Cumulative surface strain in 200 humidity cycles (Aoshima sandstone, 20˚C)

Two strain gauges were adhered to different faces of a specimen. The increase in strain represents expansion.

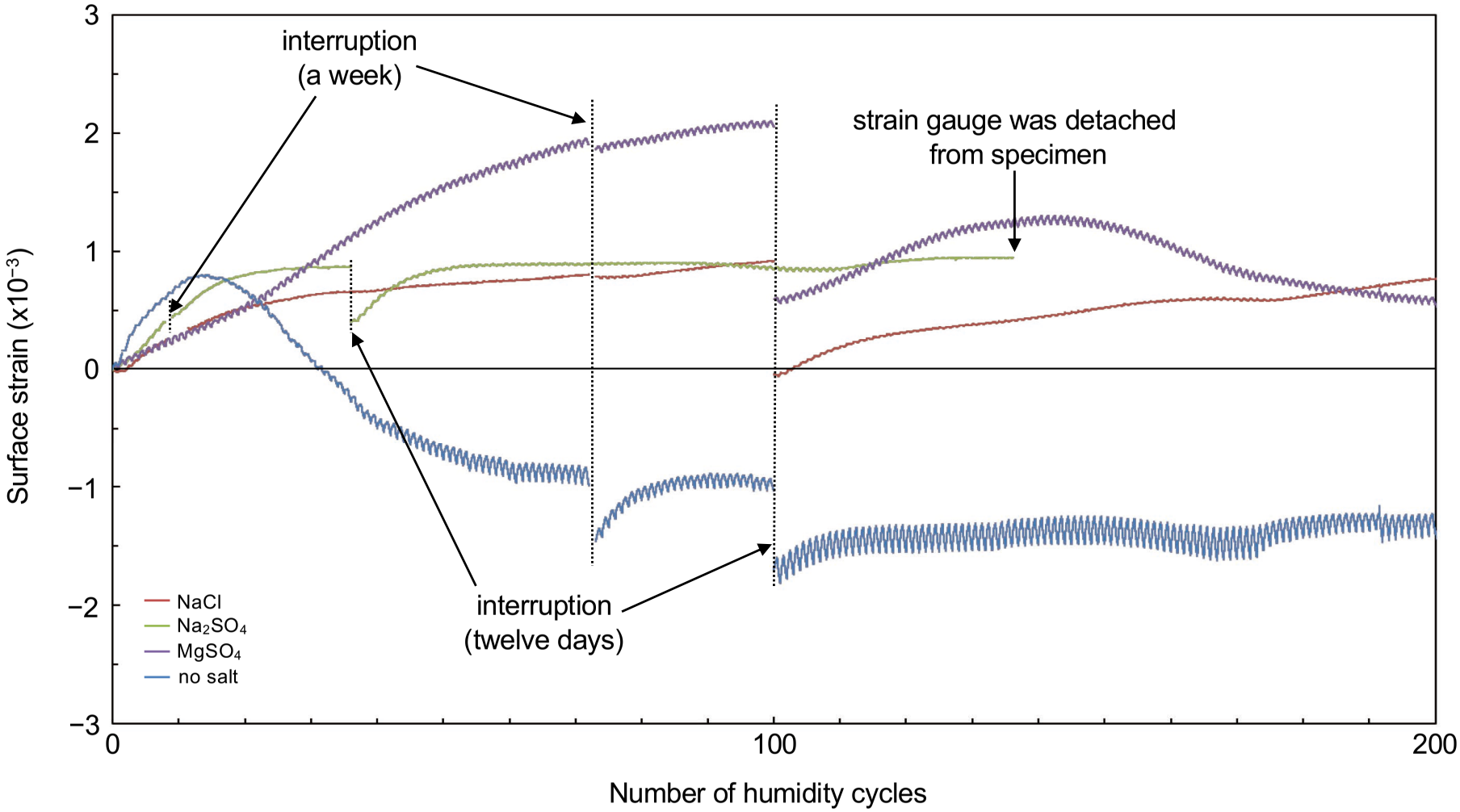

Figure 3.32 Cumulative surface strain in 200 humidity cycles (Oya tuff, 10˚C)

The increase in strain represents expansion.

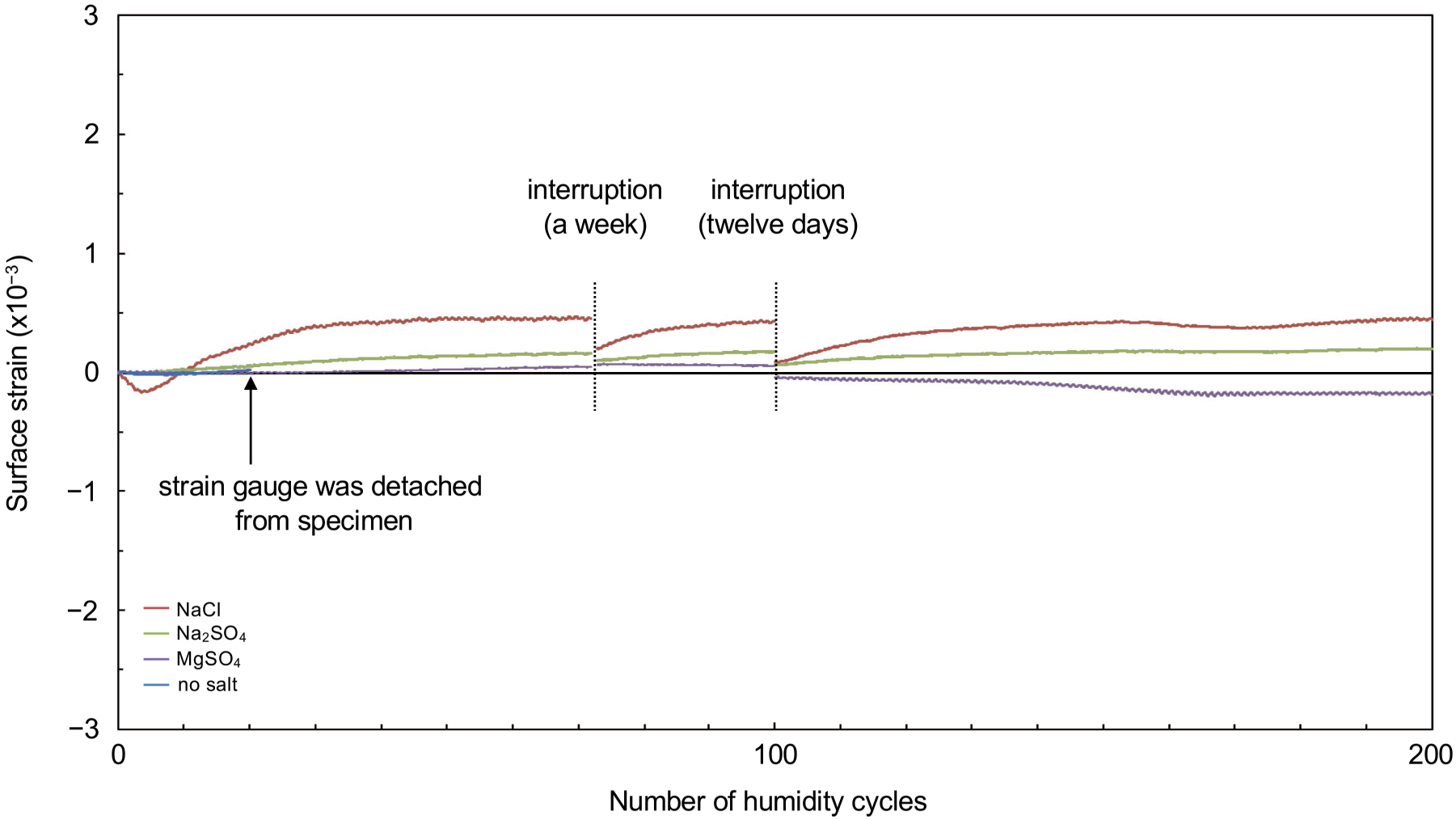

Figure 3.33 Cumulative surface strain in 200 humidity cycles (Aoshima sandstone, 10˚C)

The increase in strain represents expansion.

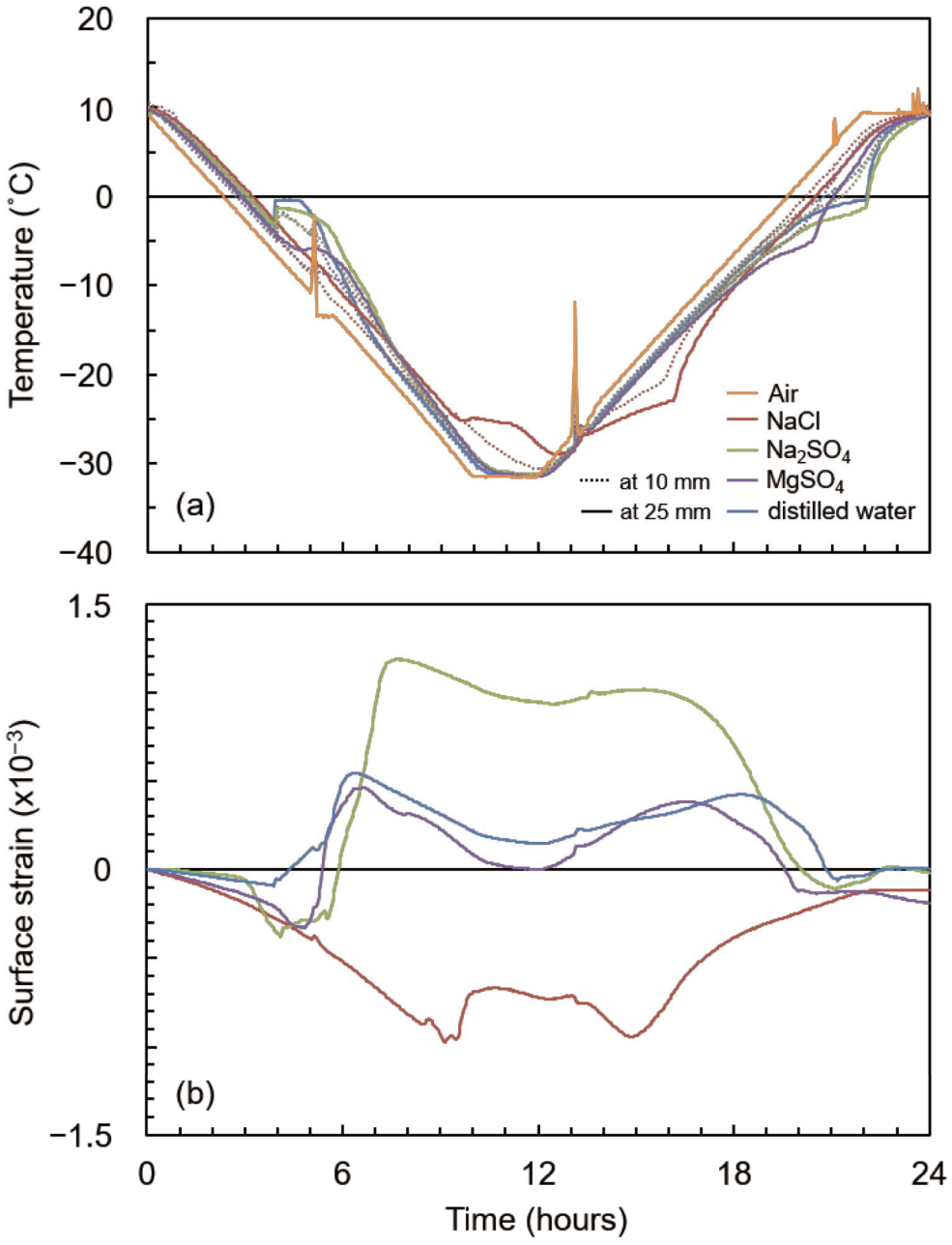

Figure 3.34 Typical temperature (a) and surface strain (b) changes in a freeze-thaw cycle (Oya tuff saturated in salt solution, in 3 cycle)

T-type thermocouples were installed in pits at depths of 10 mm and 25 mm. The increase in strain represents expansion.

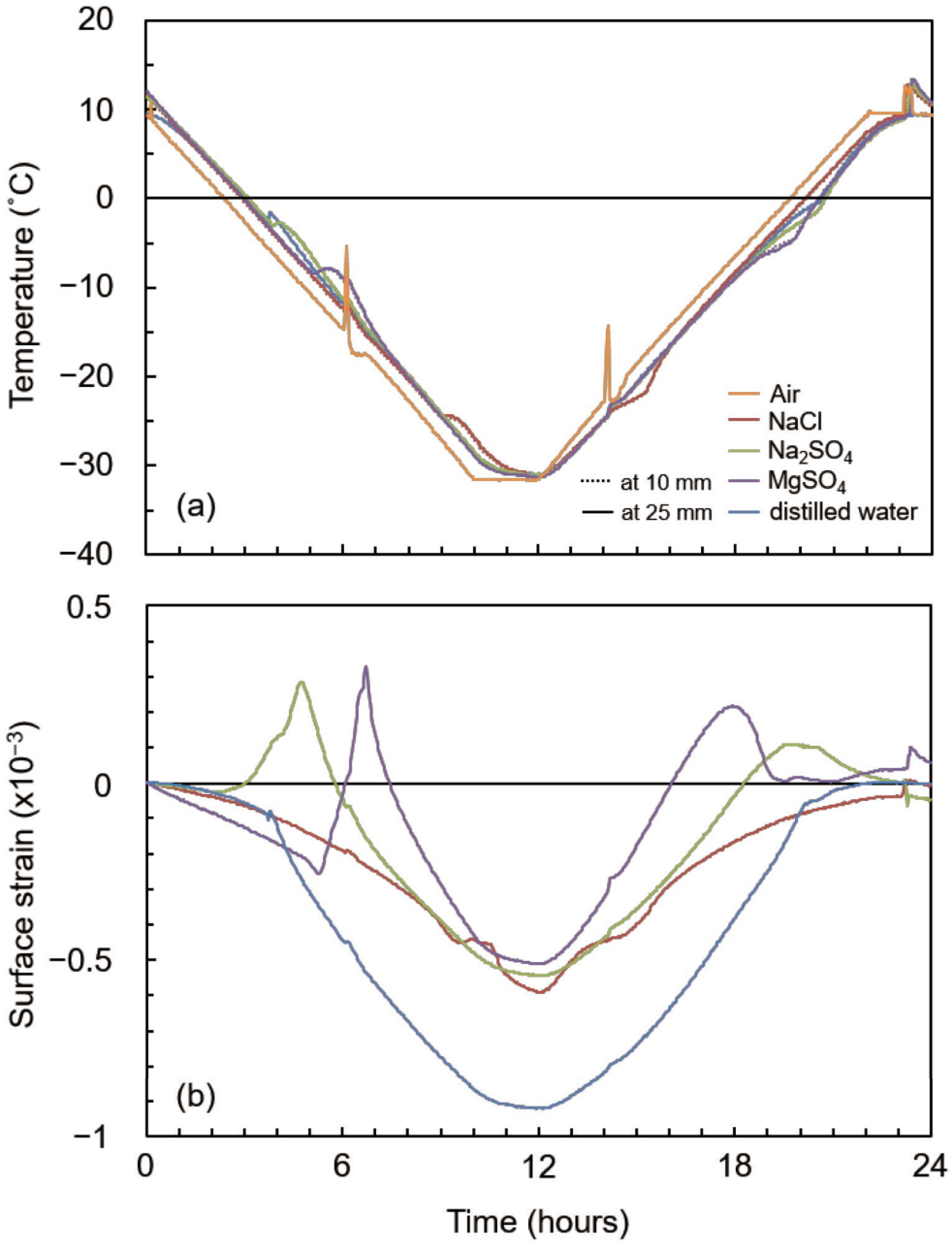

Figure 3.35 Typical temperature (a) and surface strain (b) changes in a freeze-thaw cycle (Aoshima sandstone saturated in salt solution, in 3 cycle)

T-type thermocouples were installed in pits at depths of 10 mm and 25 mm. The increase in strain represents expansion.

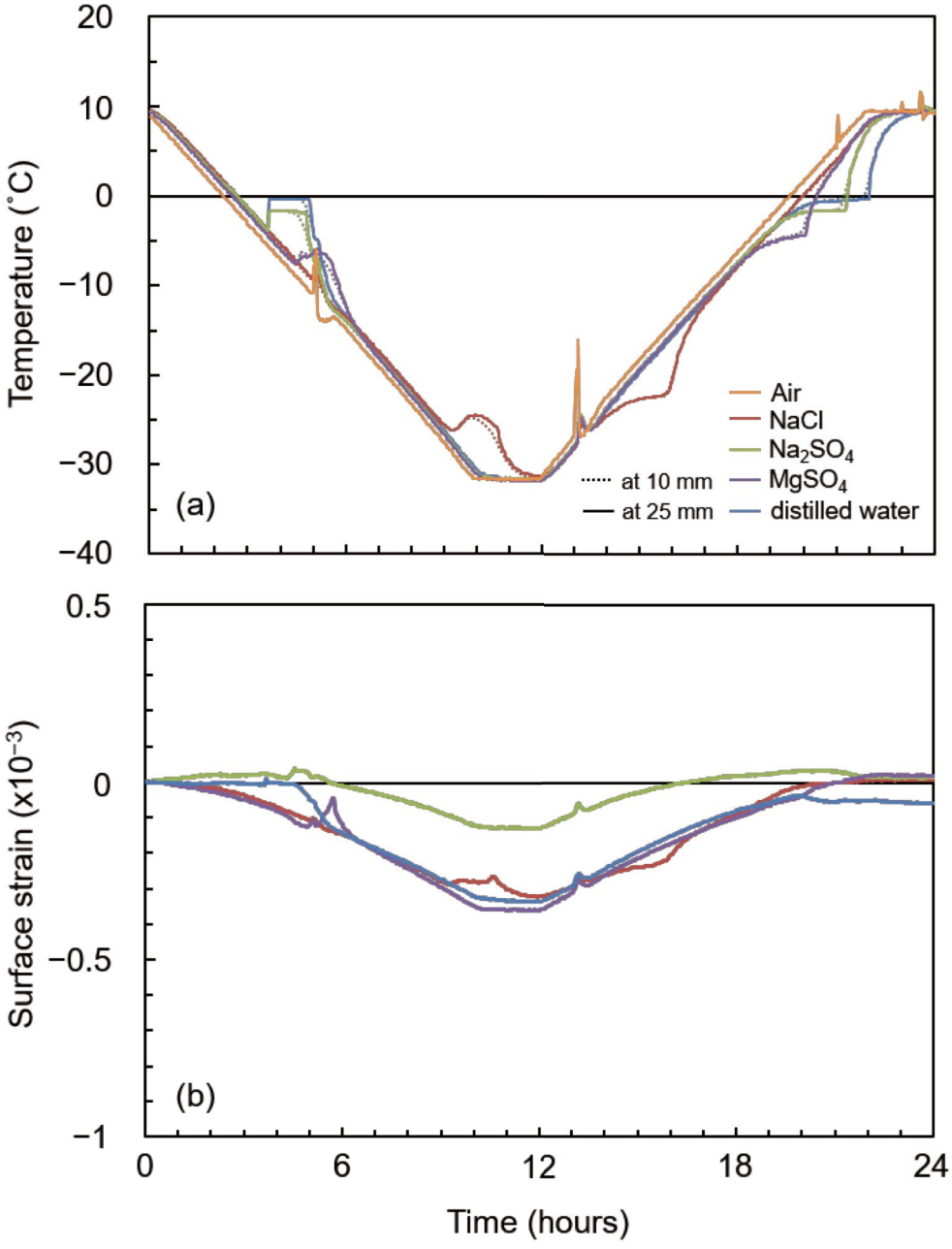

Figure 3.36 Typical temperature (a) and surface strain (b) changes in a freeze-thaw cycle (Shirakawa tuff saturated in salt solution, in 3 cycle)

T-type thermocouples were installed in pits at depths of 10 mm and 25 mm. The increase in strain represents expansion.

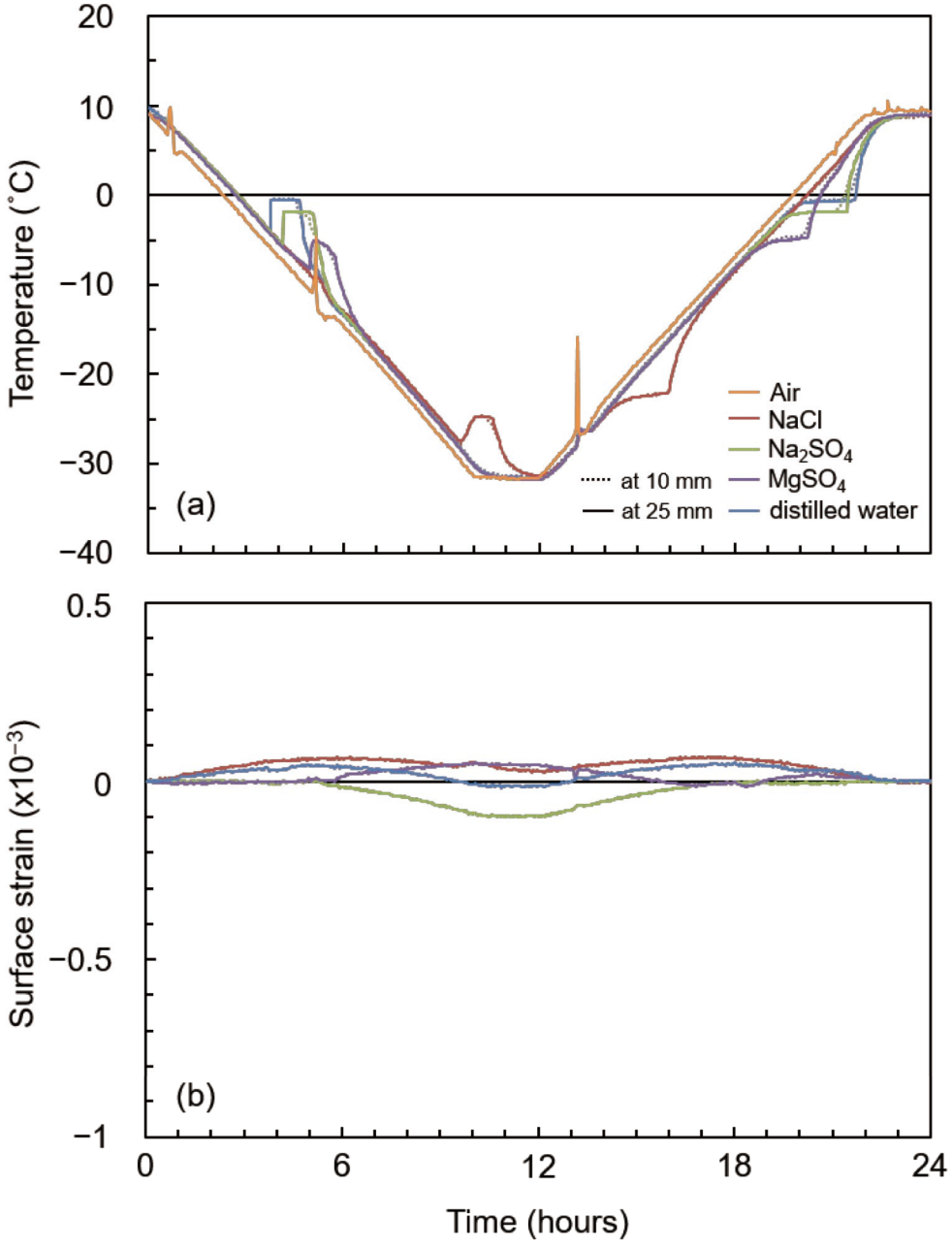

Figure 3.37 Typical temperature (a) and surface strain (b) changes in a freeze-thaw cycle (Andesite saturated in salt solution, in 3 cycle)

T-type thermocouples were installed in pits at depths of 10 mm and 25 mm. The increase in strain represents expansion.

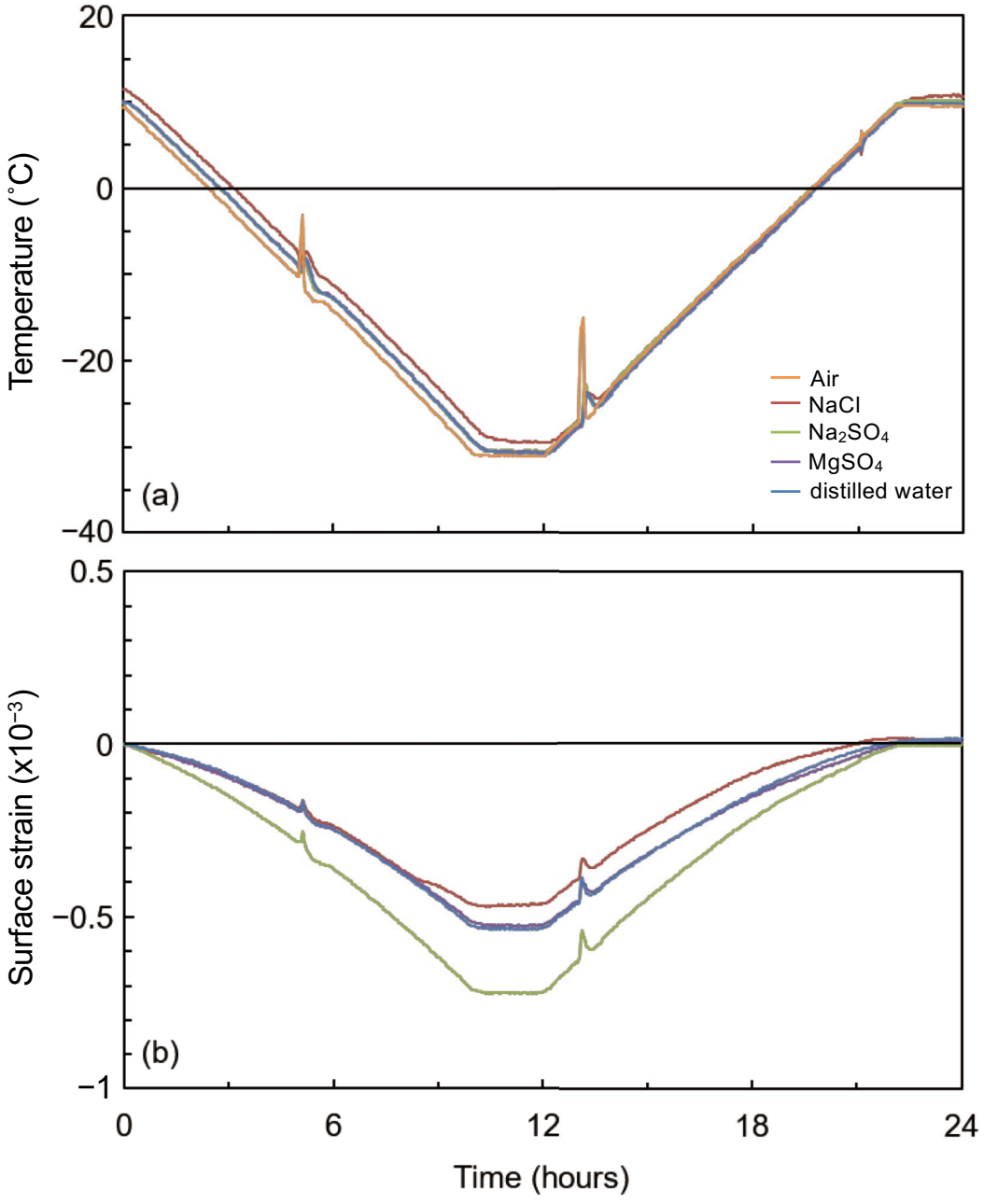

Figure 3.38 Typical temperature (a) and surface strain (b) changes in a freeze-thaw cycle (Oya tuff oven dried after saturation in salt solution, in 10 cycle)

T-type thermocouple was installed in a pit at a depth of 10mm. The increase in strain represents expansion.

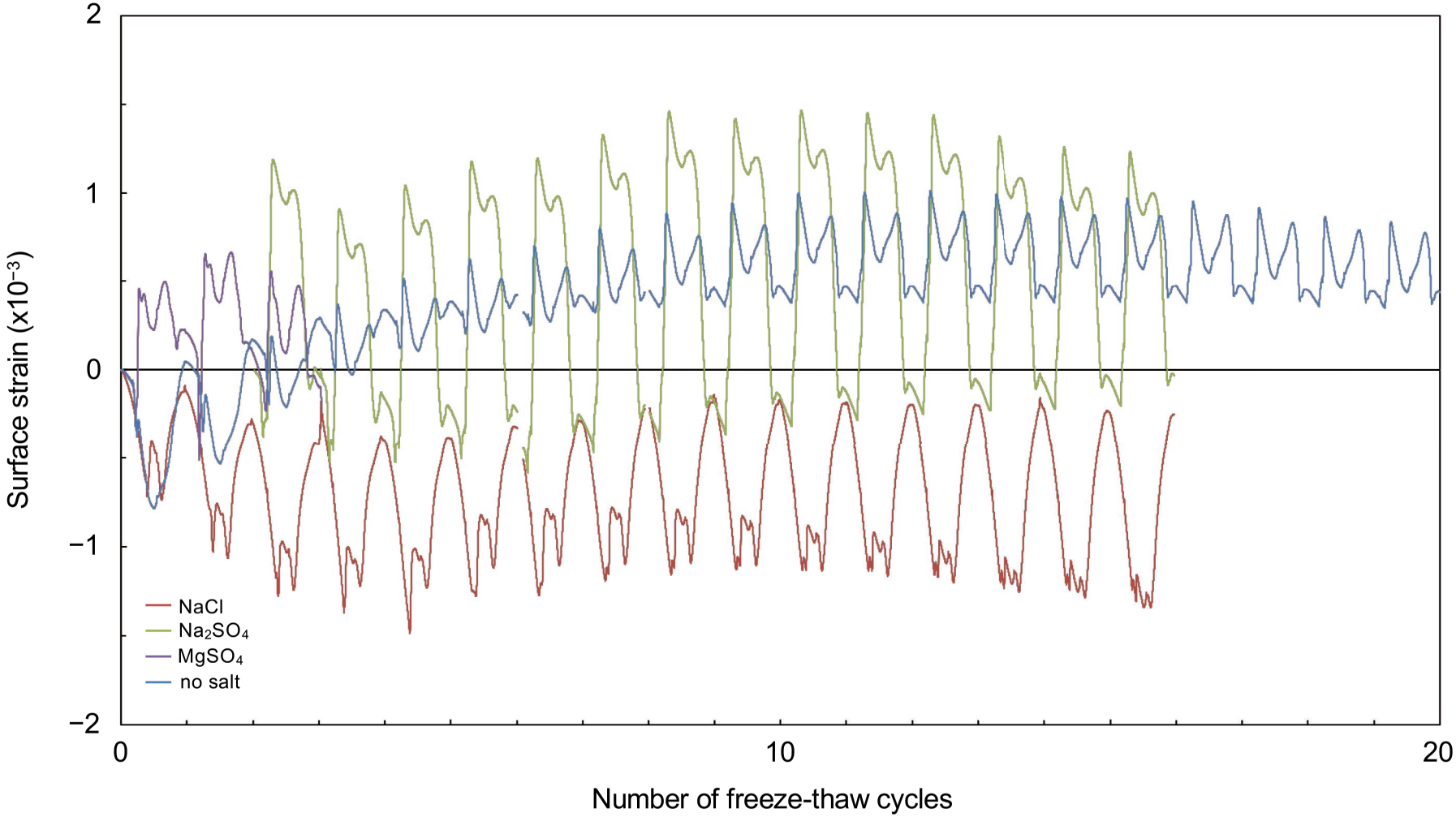

Figure 3.39 Cumulative surface strain in 20 freeze-thaw cycles (Oya tuff saturated in salt solution)

The increase in strain represents expansion.

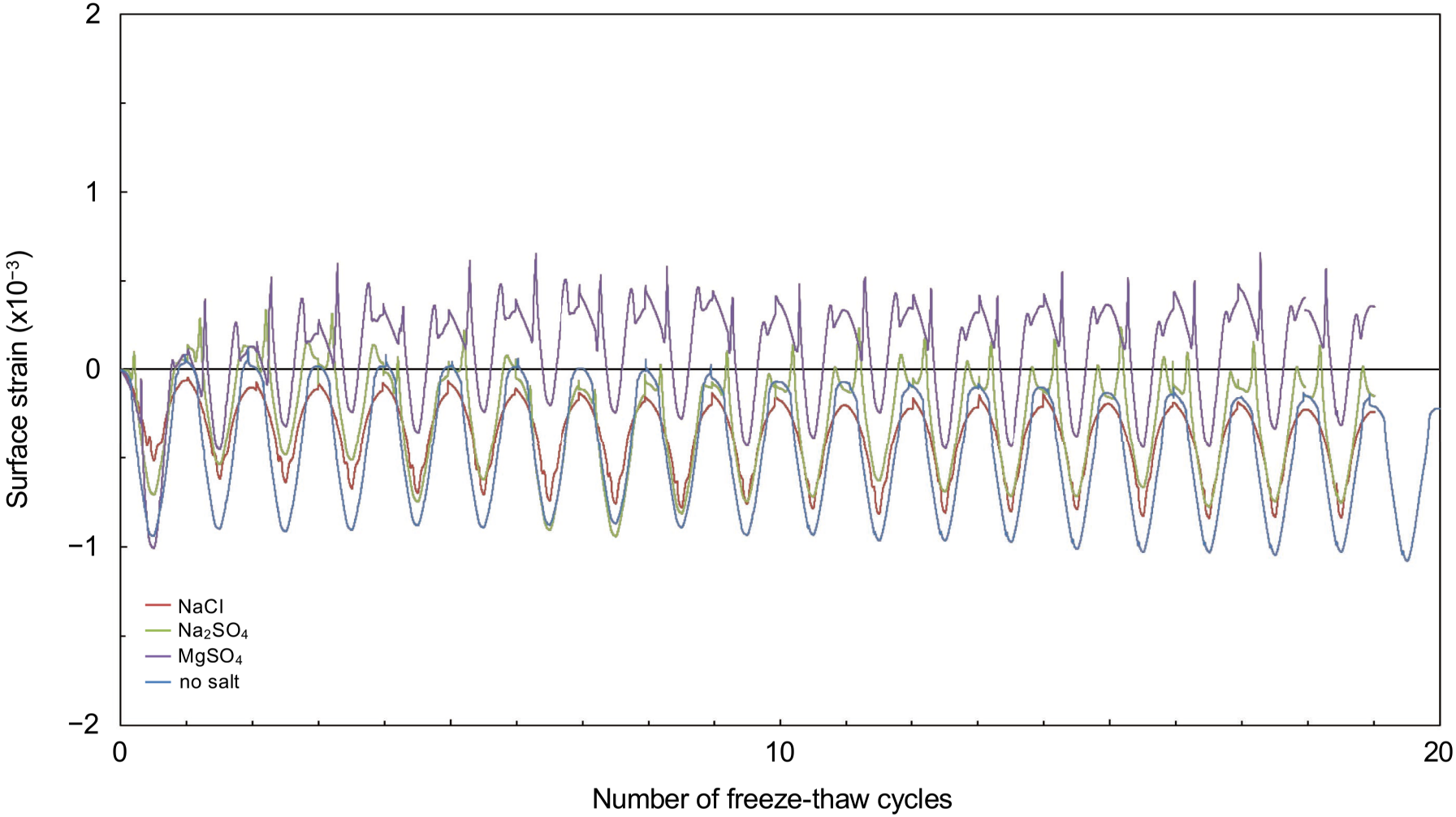

Figure 3.40 Cumulative surface strain in 20 freeze-thaw cycles (Aoshima sandstone saturated in salt solution)

The increase in strain represents expansion.

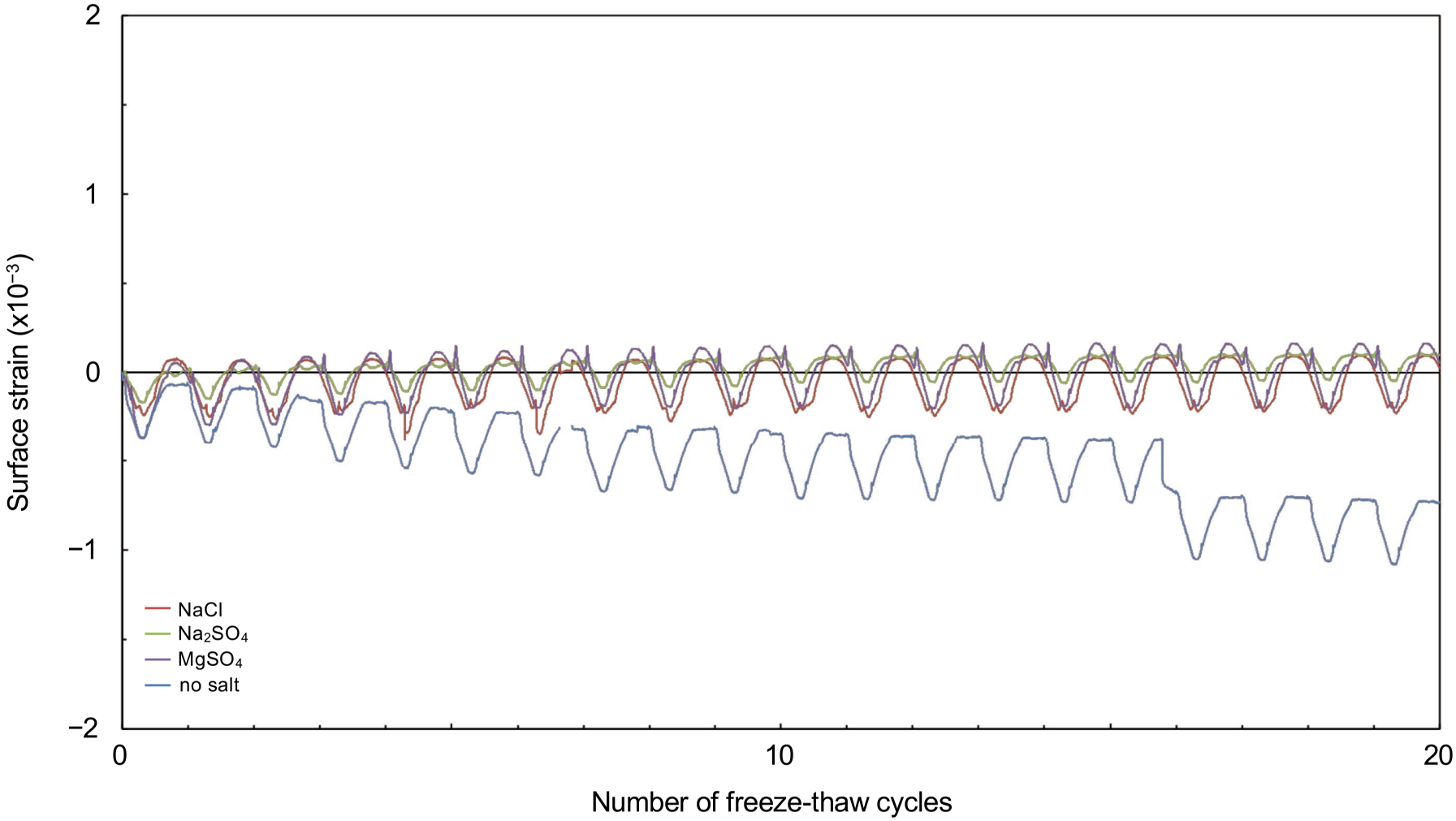

Figure 3.41 Cumulative surface strain in 20 freeze-thaw cycles (Shirakawa tuff saturated in salt solution)

The increase in strain represents expansion.

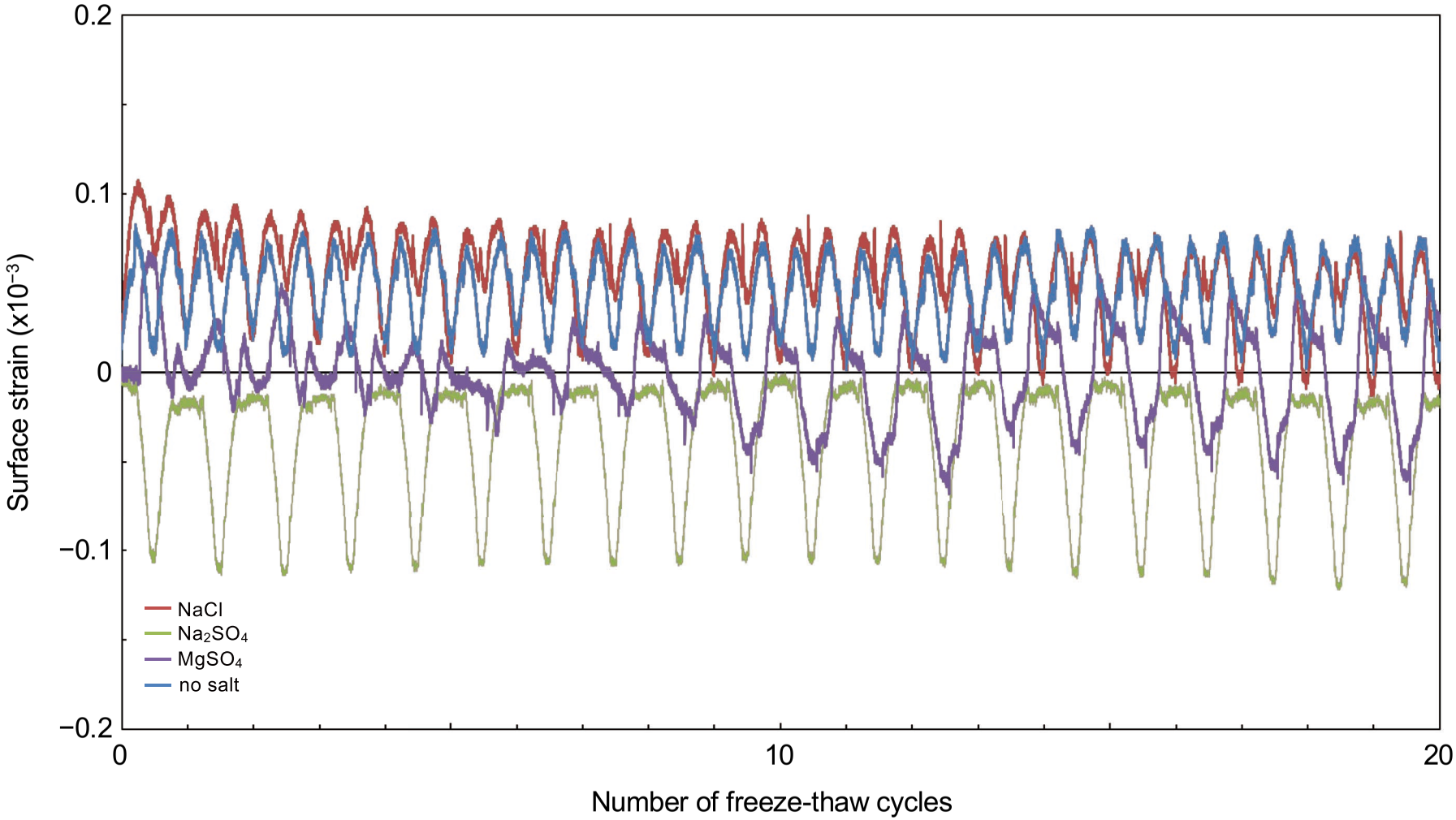

Figure 3.42 Cumulative surface strain in 20 freeze-thaw cycles (Andesite saturated in salt solution)

The increase in strain represents expansion.

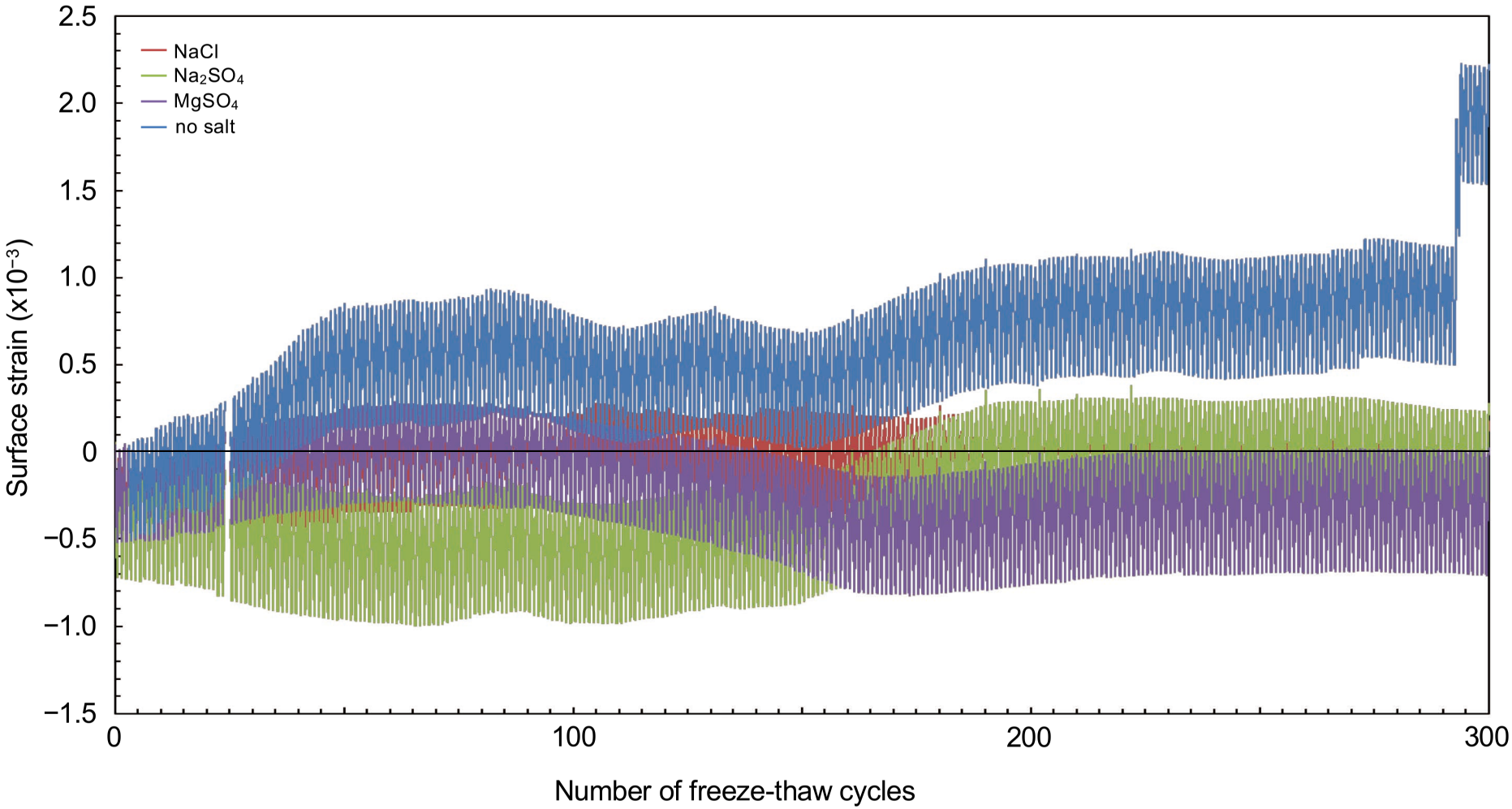

Figure 3.43 Cumulative surface strain in 300 freeze-thaw cycles (Oya tuff oven dried after saturation in salt solution)

The increase in strain represents expansion.

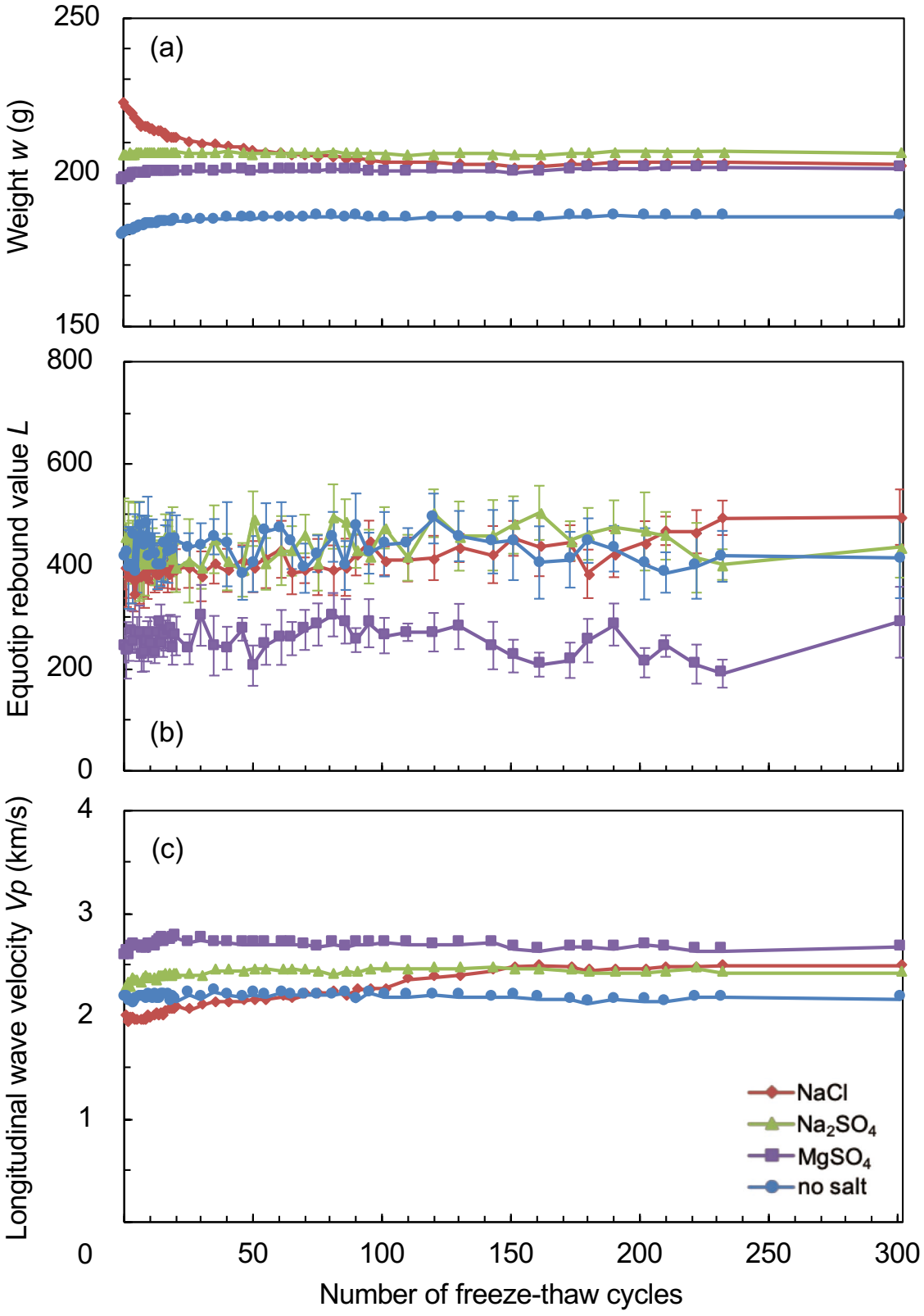

Figure 3.44 Weight (a), Equotip rebound value (b), and longitudinal wave velocity (c) measured during freeze-thaw experiment (Oya tuff oven dried after saturation in salt solution)

Vertical bar in the L-value represents dispersion of 10 single impacts.

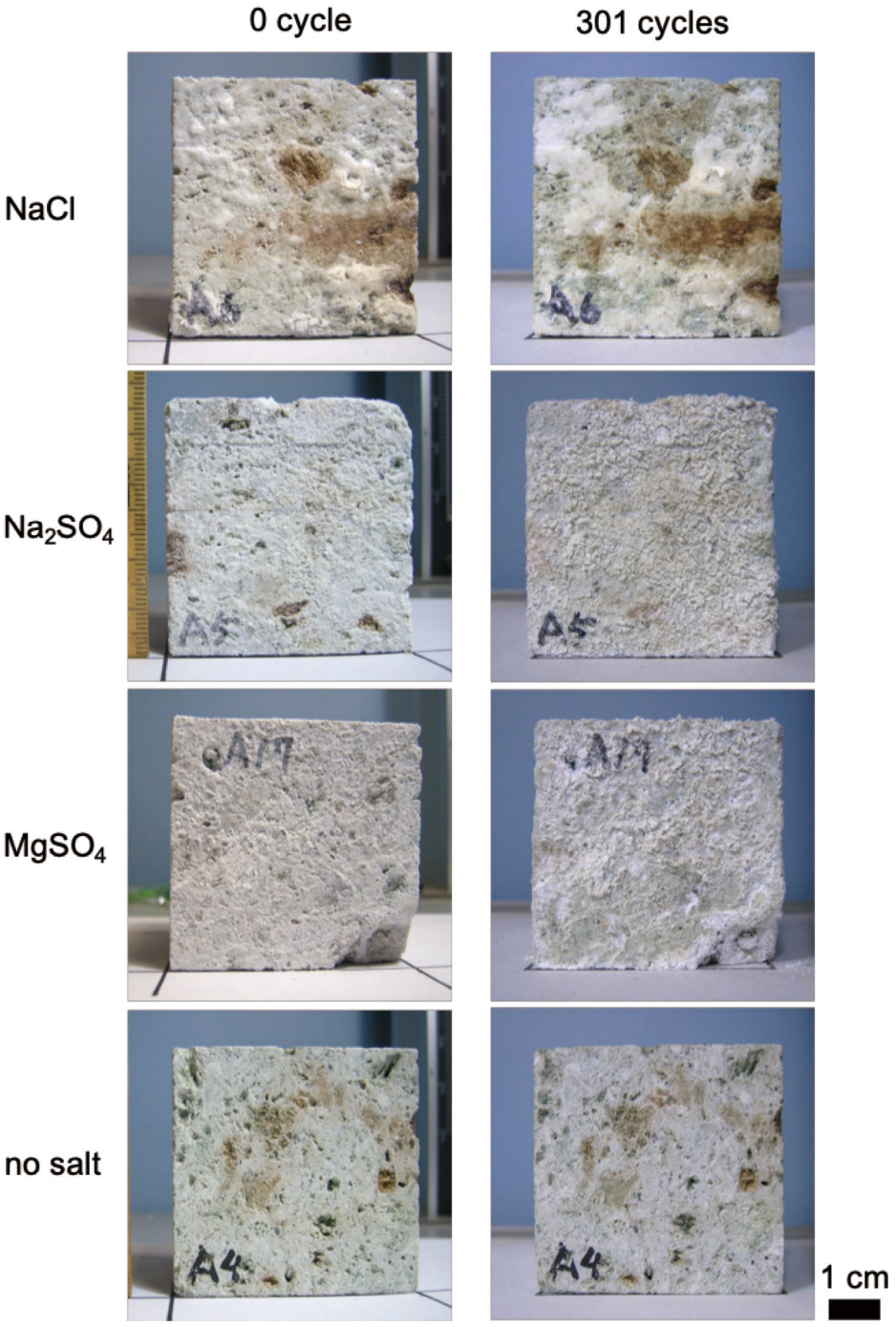

Figure 3.45 Oya tuff oven dried after saturation in salt solution, subjected to freeze-thaw cycles

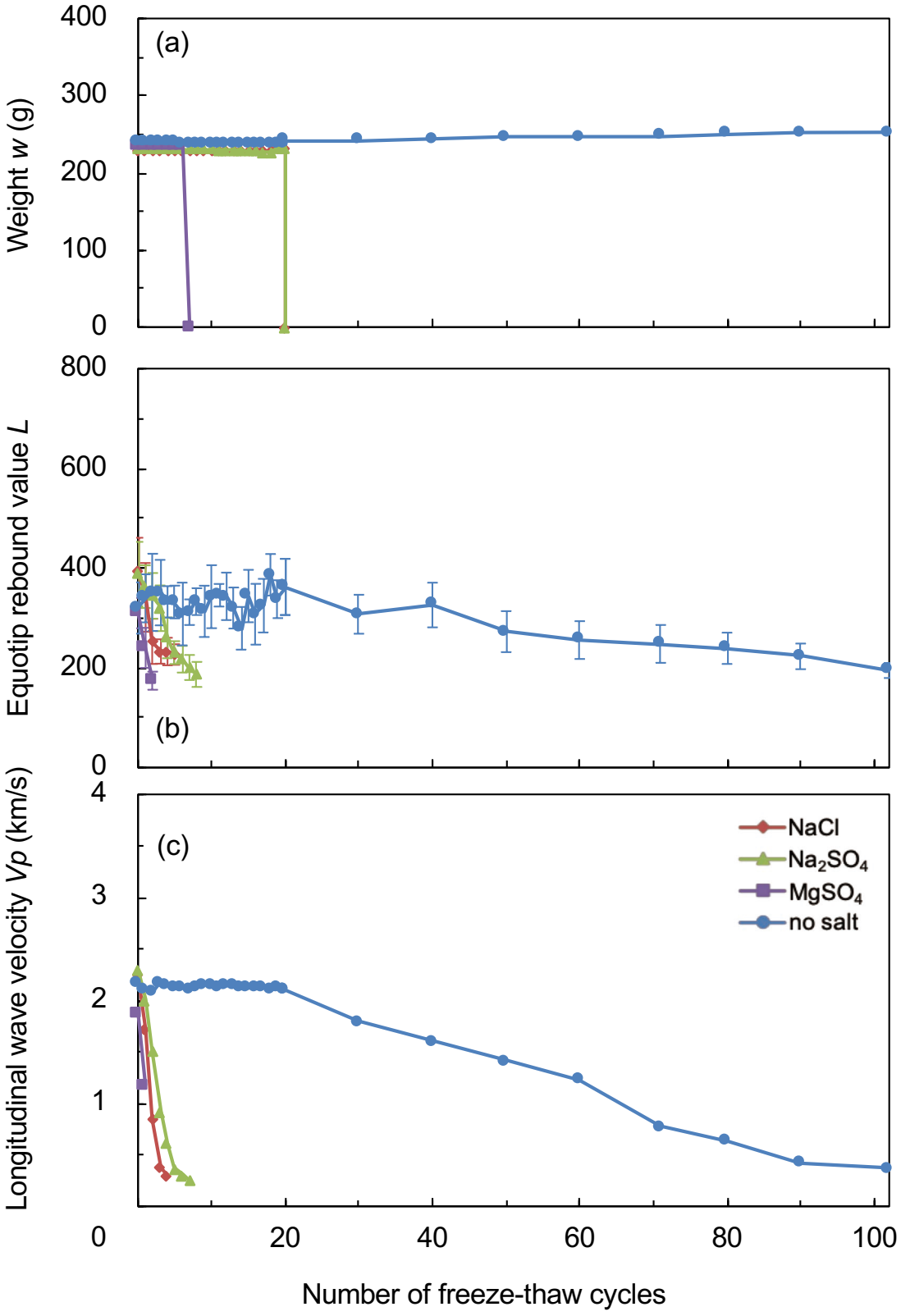

Figure 3.46 Weight (a), Equotip rebound value (b), and longitudinal wave velocity (c) measured during freeze-thaw experiment (Oya tuff saturated in salt solution)

Vertical bar in the L-value represents dispersion of 10 single impacts.

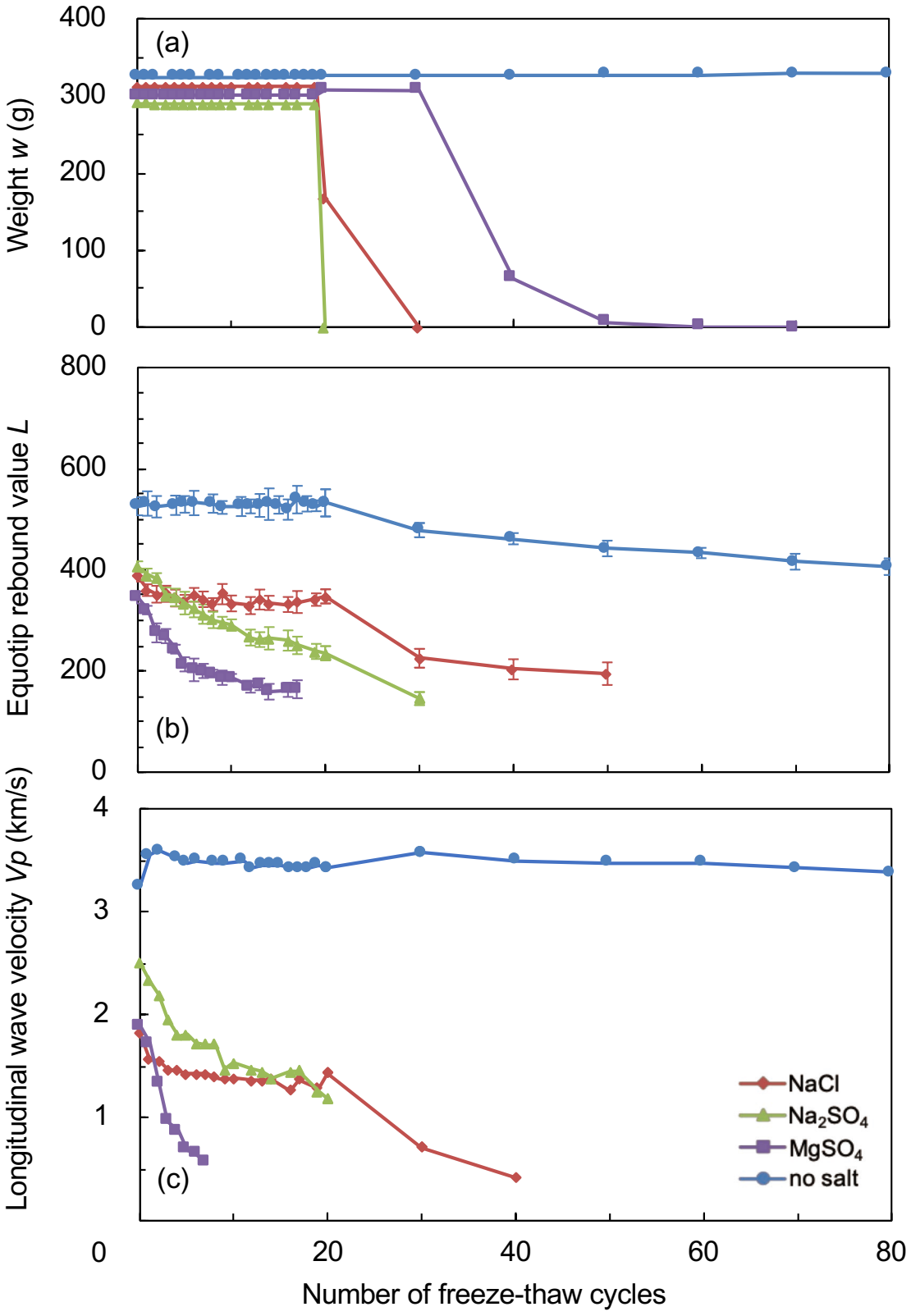

Figure 3.47 Weight (a), Equotip rebound value (b), and longitudinal wave velocity (c) measured during freeze-thaw experiment (Aoshima sandstone)

Vertical bar in the L-value represents dispersion of 10 single impacts.

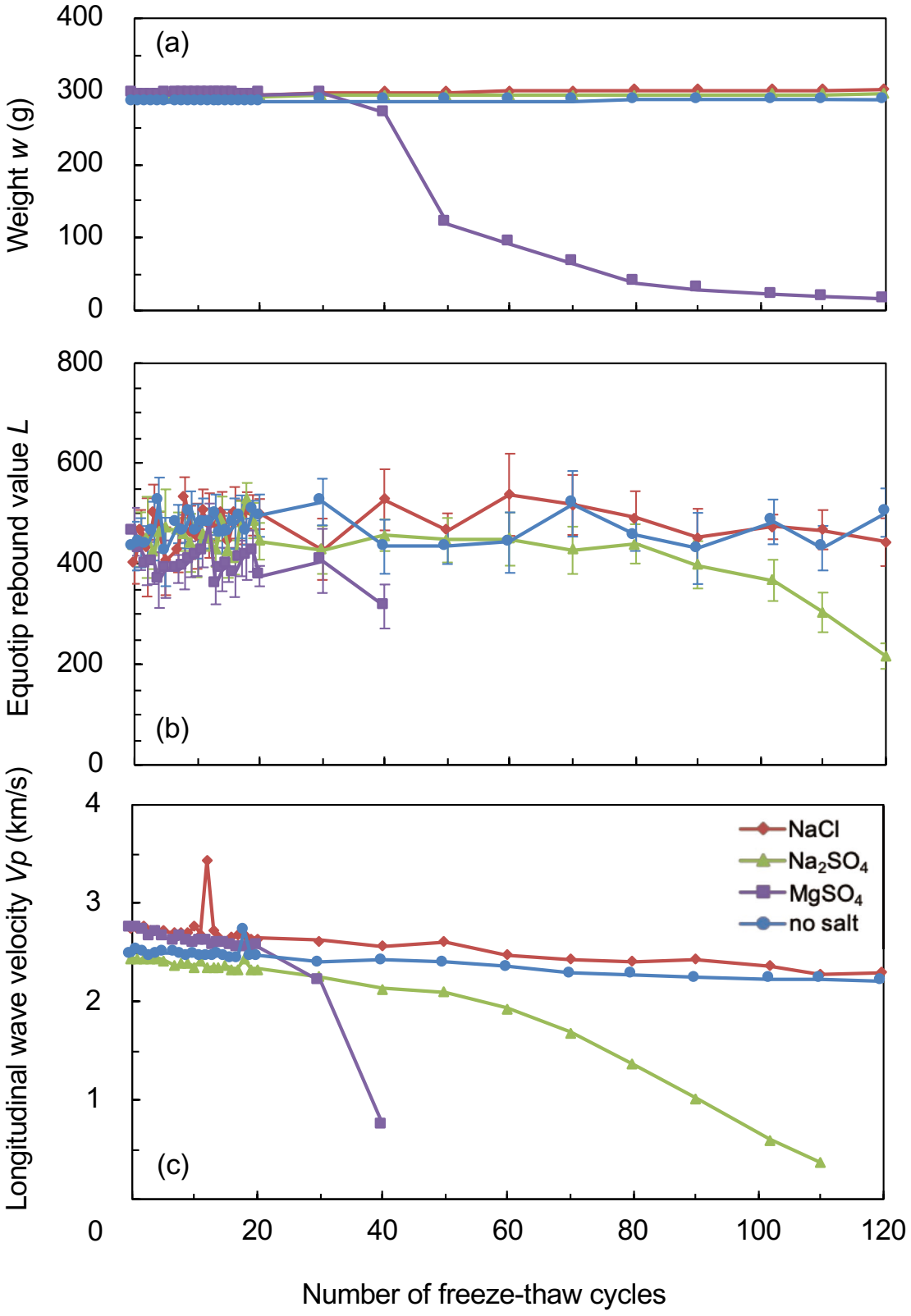

Figure 3.48 Weight (a), Equotip rebound value (b), and longitudinal wave velocity (c) measured during freeze-thaw experiment (Shirakawa tuff)

Vertical bar in the L-value represents dispersion of 10 single impacts.

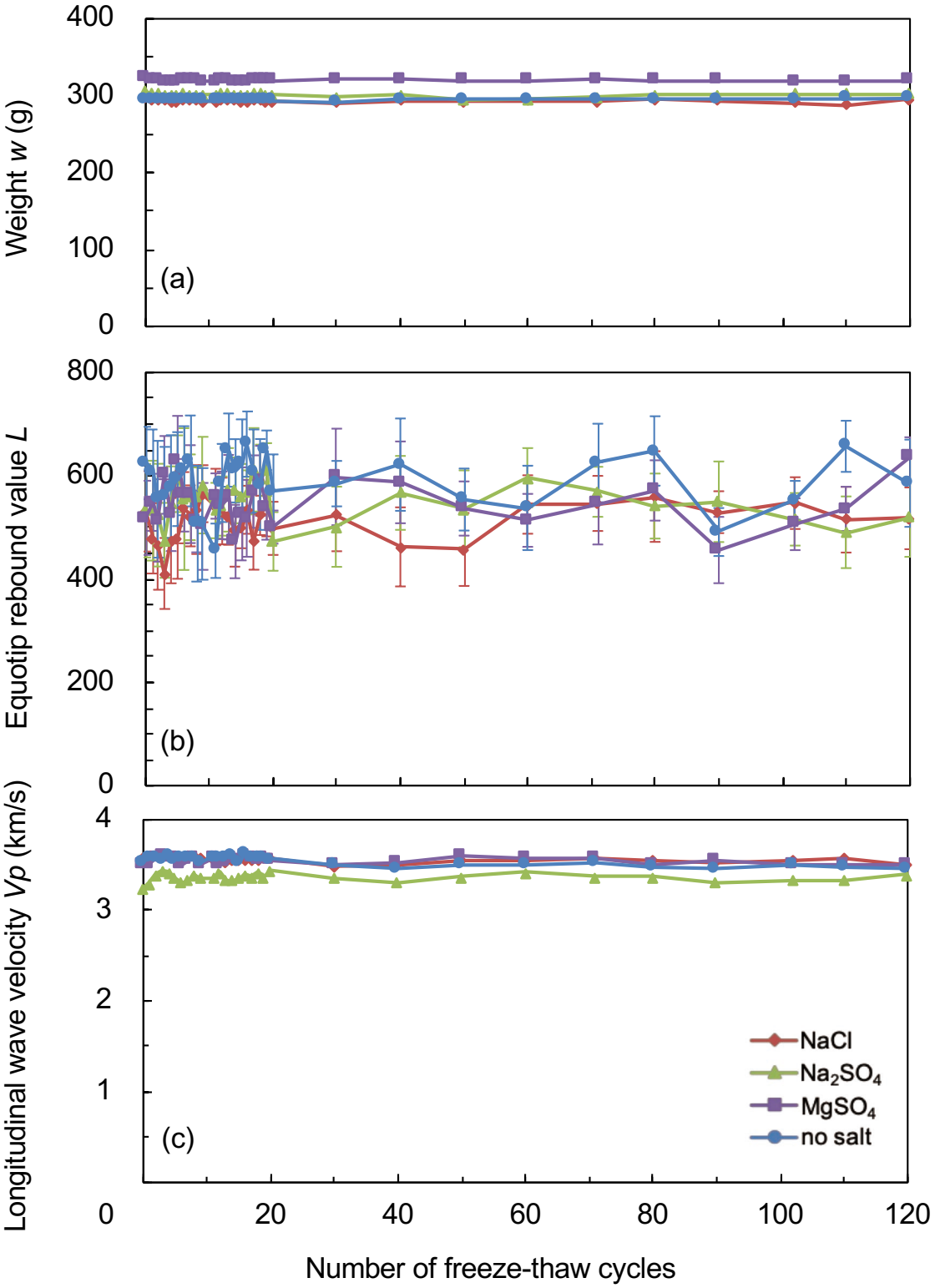

Figure 3.49 Weight (a), Equotip rebound value (b), and longitudinal wave velocity (c) measured during freeze-thaw experiment (Andesite)

Vertical bar in the L-value represents dispersion of 10 single impacts.

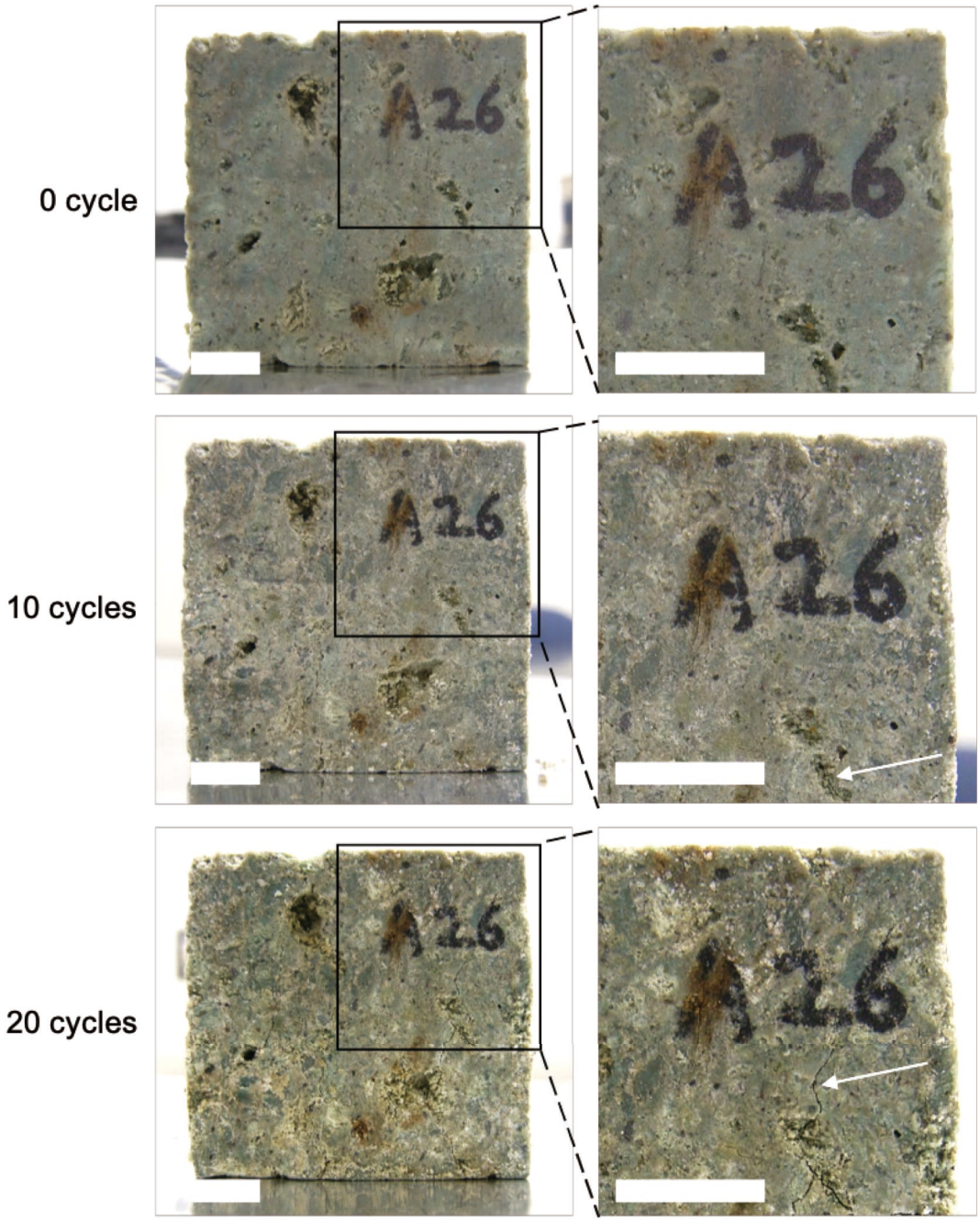

Figure 3.50 Specimen subjected to freeze-thaw cycles (Oya tuff saturated with sodium chloride solution)

Right pictures are enlarged view of upper right edge of specimen. The scale bars are 1-cm long. Cracks occurred and extended with increasing number of freeze-thaw cycles. The specimen completely disintegrated into particles smaller than 2 mm in length at 30 freeze-thaw cycles.

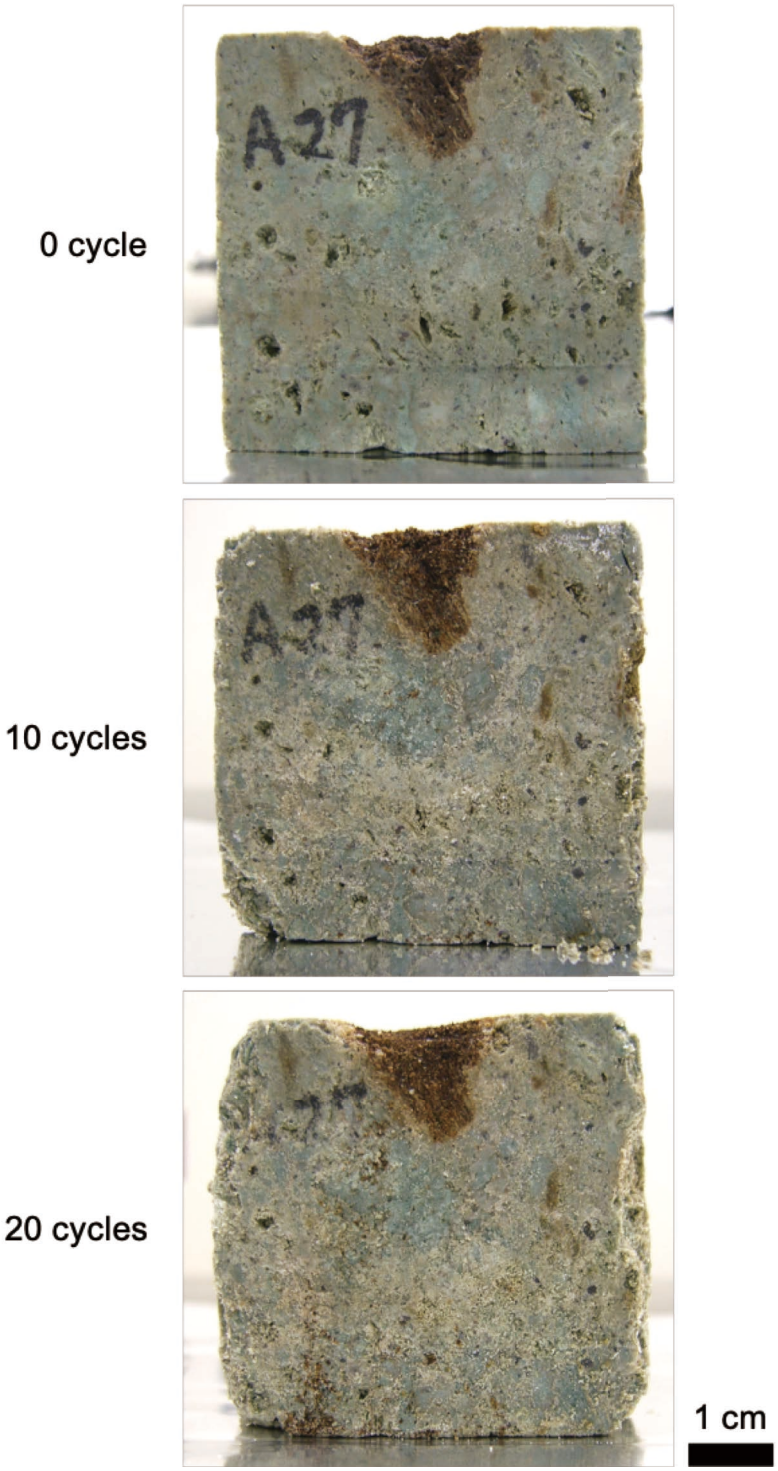

Figure 3.51 Specimen subjected to freeze-thaw cycles (Oya tuff saturated with sodium sulfate solution)

The specimen completely disintegrated into particles smaller than 2 mm in length at 30 freeze-thaw cycles.

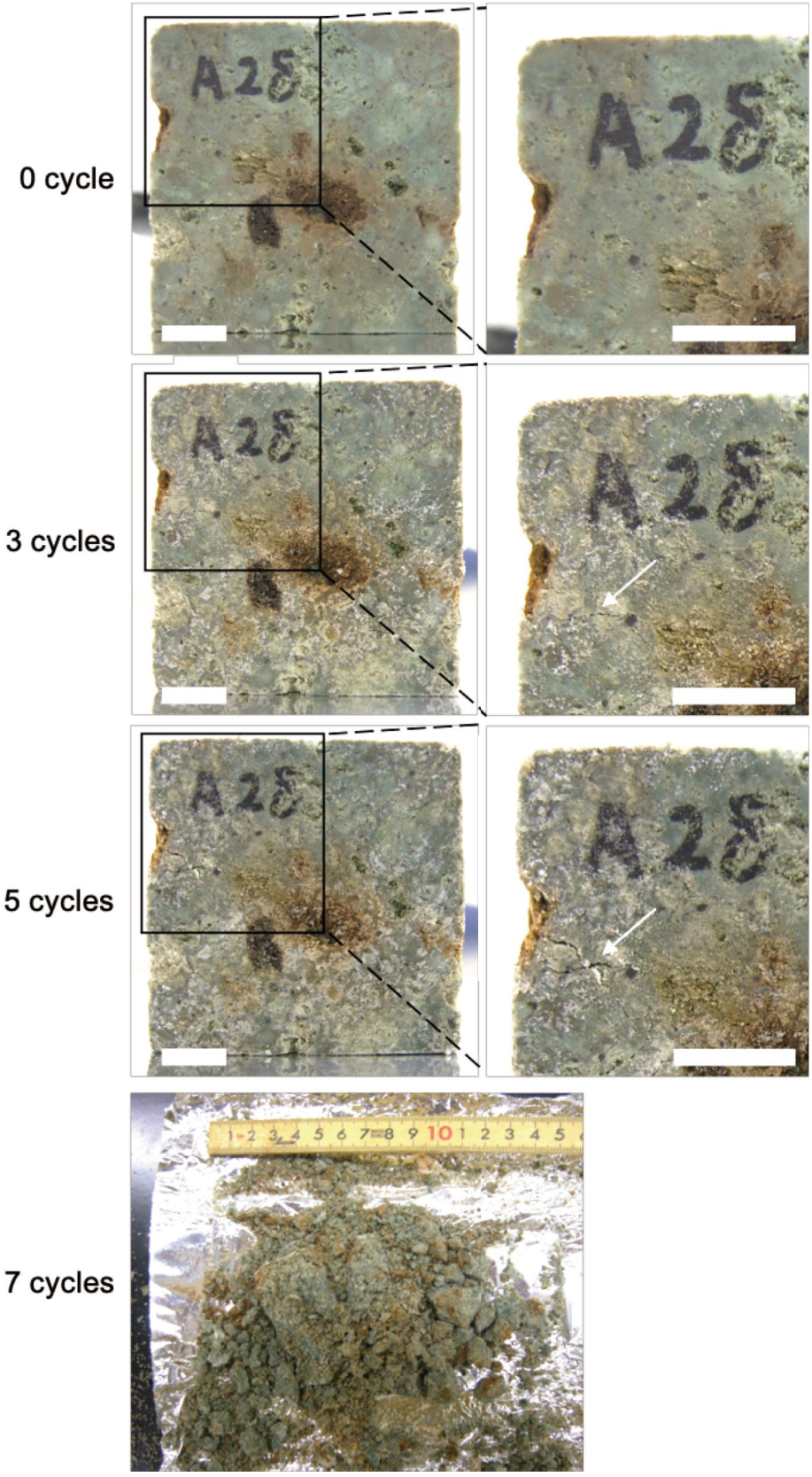

Figure 3.52 Specimen subjected to freeze-thaw cycles (Oya tuff saturated with magnesium sulfate solution)

Right pictures are enlarged view of upper left edge of specimen. The scale bars are 1-cm long. Cracks occurred and extended with increasing number of freeze-thaw cycles. The specimen completely disintegrated into particles smaller than 2 mm in length at 7 freeze-thaw cycles.

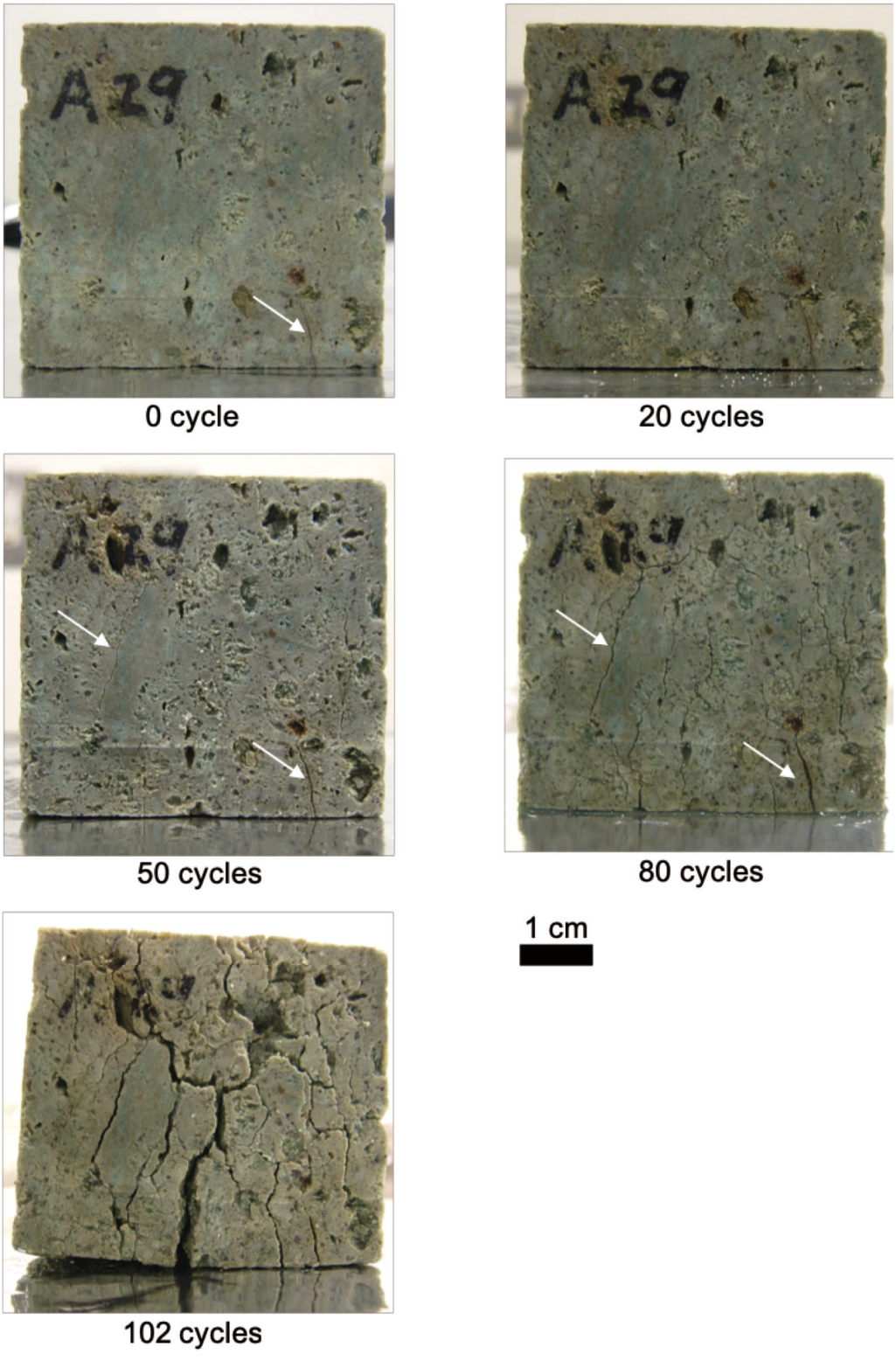

Figure 3.53 Specimen subjected to freeze-thaw cycles (Oya tuff saturated with distilled water)

Cracks occurred and extended with increasing number of freeze-thaw cycles.

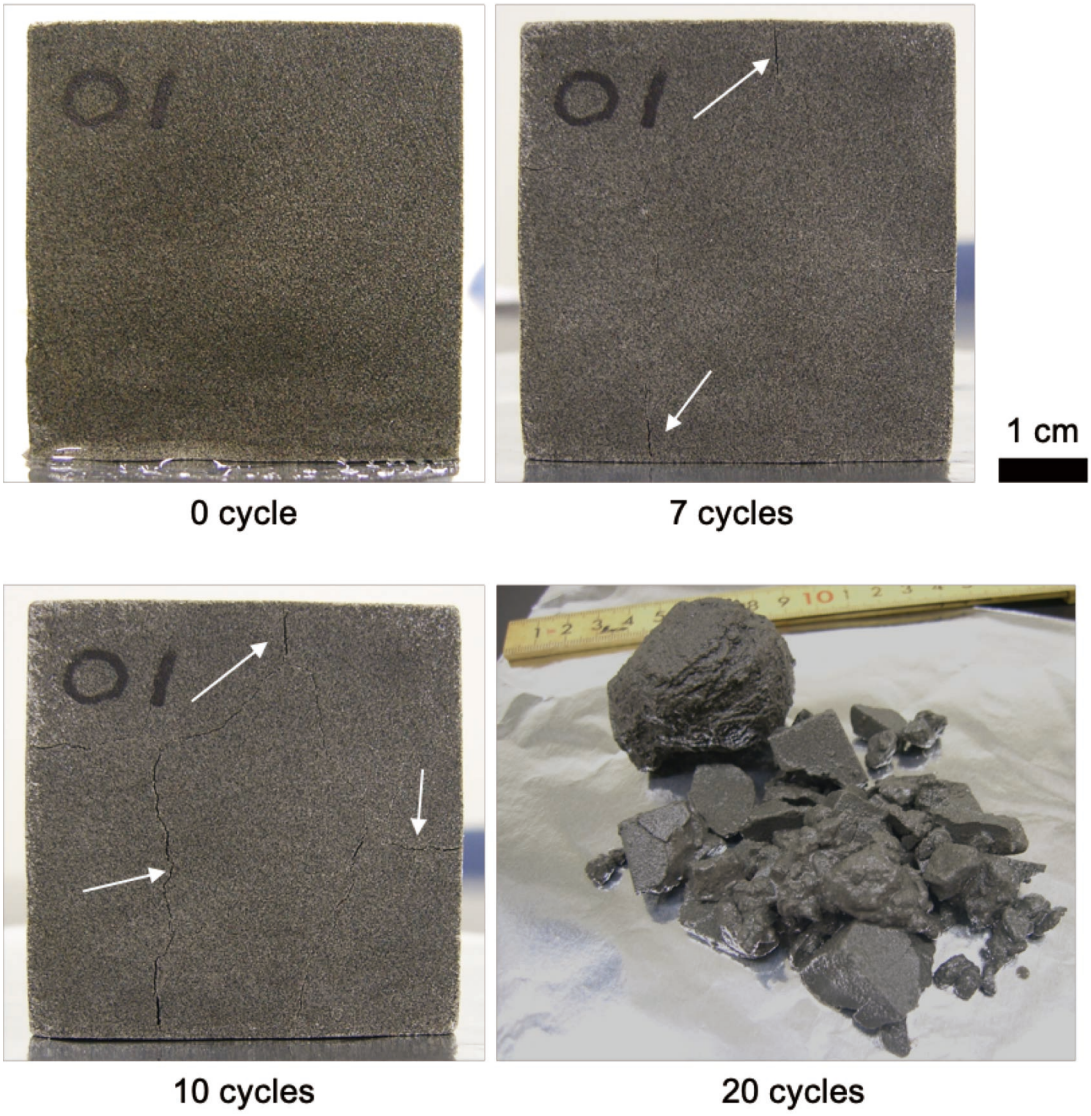

Figure 3.54 Specimen subjected to freeze-thaw cycles (Aoshima sandstone saturated with sodium chloride solution)

Cracks occurred and extended with increasing number of freeze-thaw cycles. The specimen completely disintegrated into particles smaller than 2 mm in length at 30 freeze-thaw cycles.

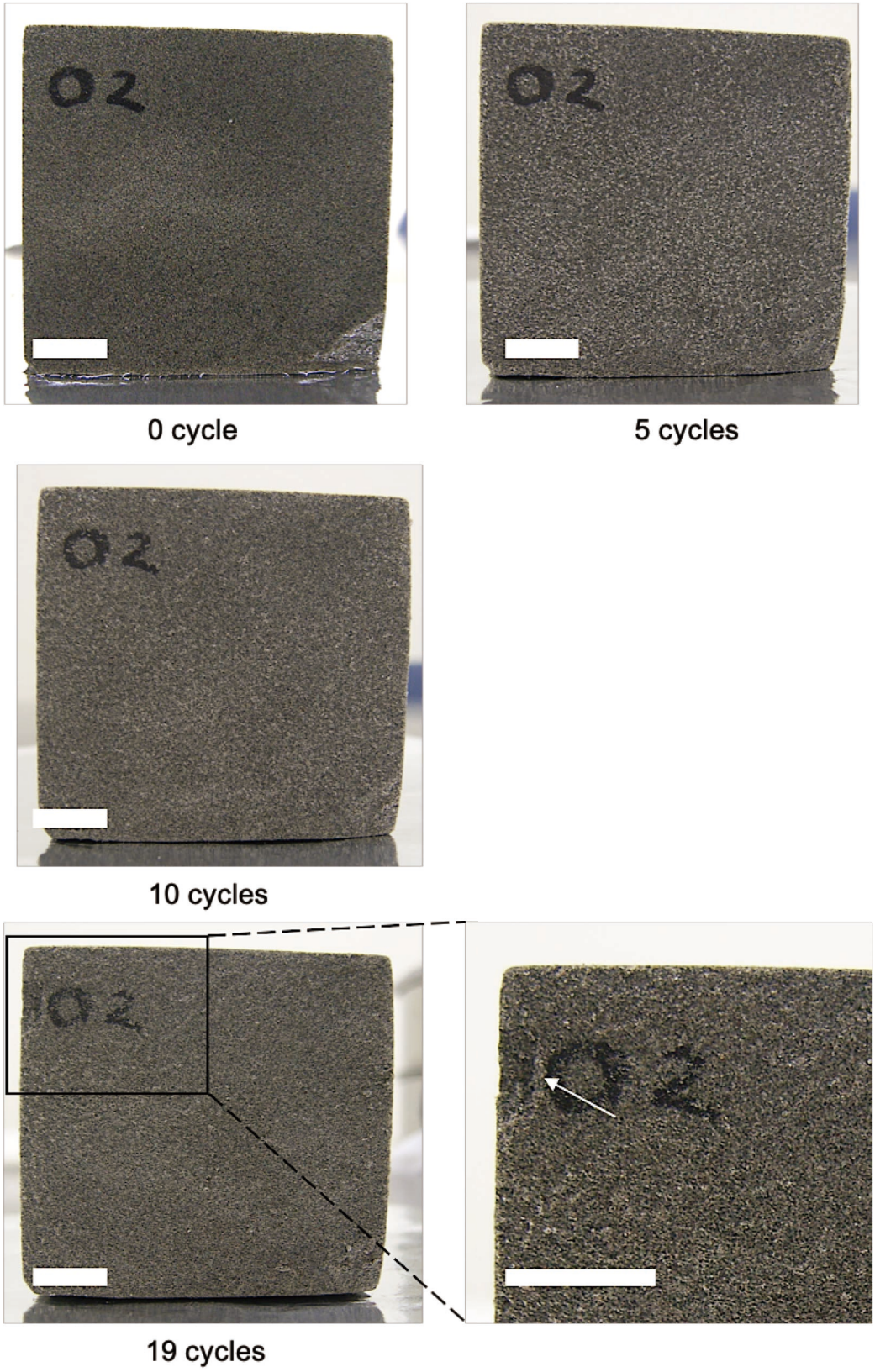

Figure 3.55 Specimen subjected to freeze-thaw cycles (Aoshima sandstone saturated with sodium sulfate solution)

The scale bars are 1-cm long. A fragment flaked from upper left part of the specimen after 19 freeze-thaw cycles. The specimen completely disintegrated into sand particles without any visible crack propagation at 20 freeze-thaw cycles.

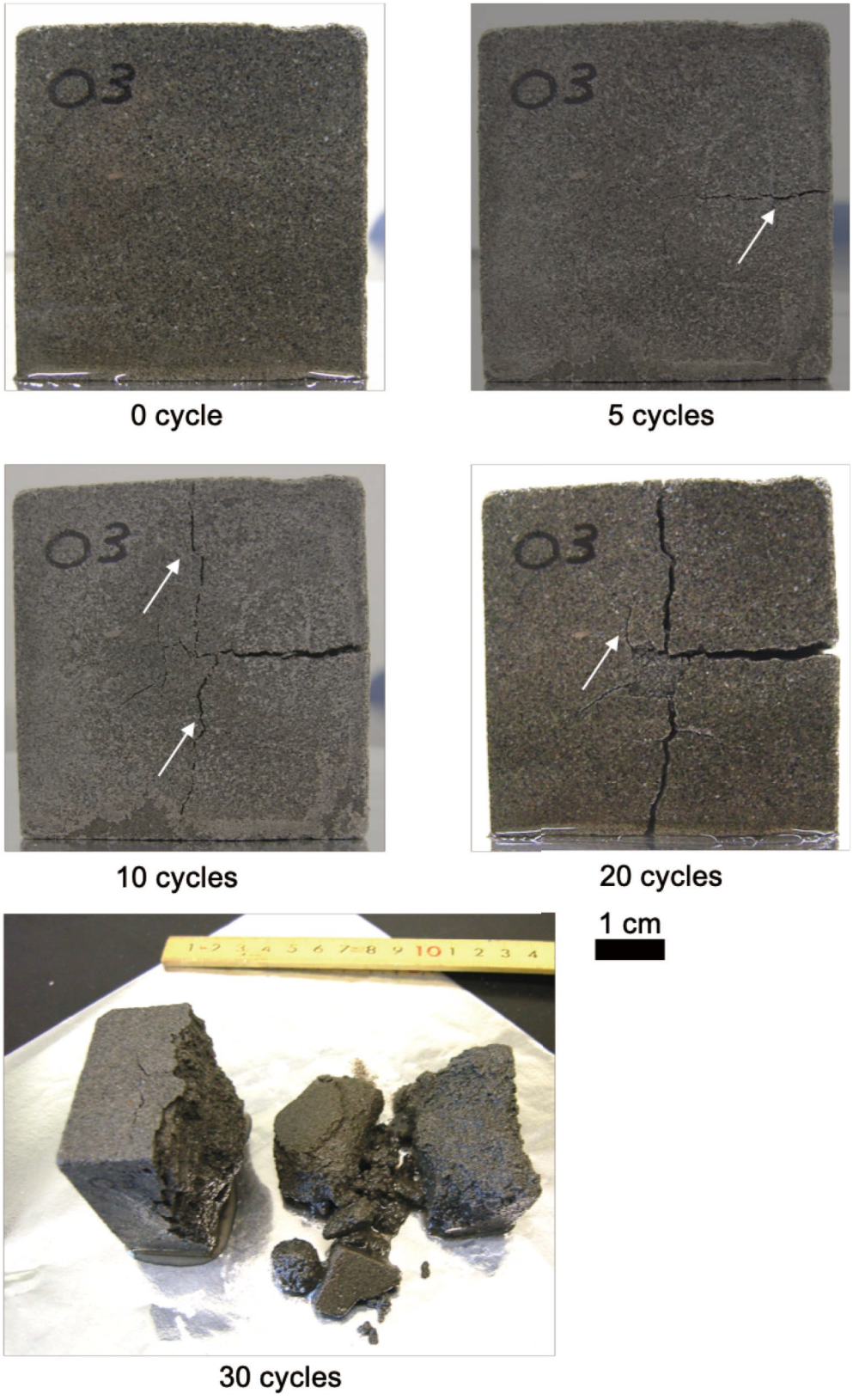

Figure 3.56 Specimen subjected to freeze-thaw cycles (Aoshima sandstone saturated with magnesium sulfate solution)

Cracks occurred and extended with increasing the number of freeze-thaw cycles. The specimen disintegrated into a lot of fragments and sand particles after 30 freeze-thaw cycles.

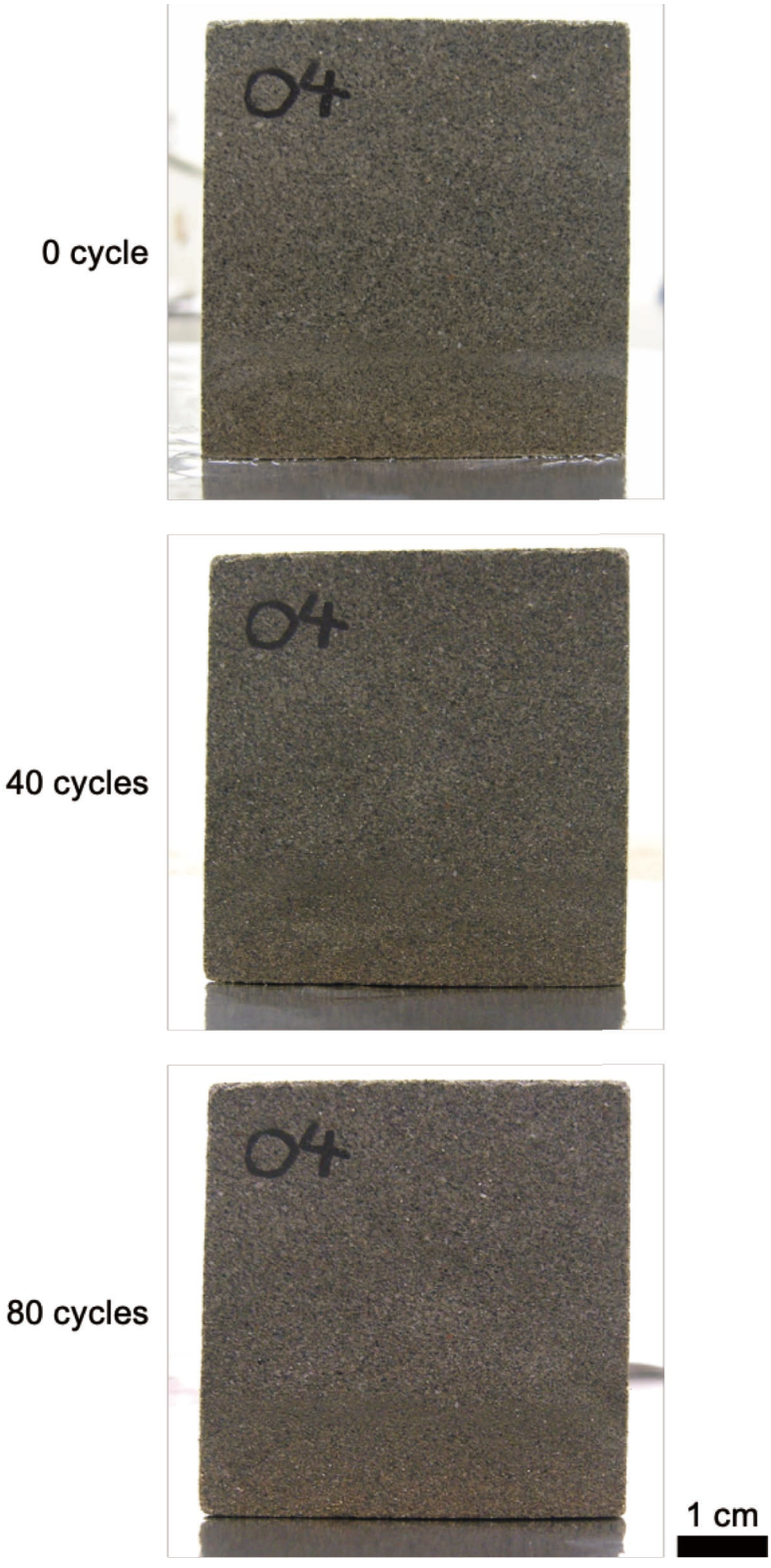

Figure 3.57 Specimen subjected to freeze-thaw cycles (Aoshima sandstone saturated with distilled water)

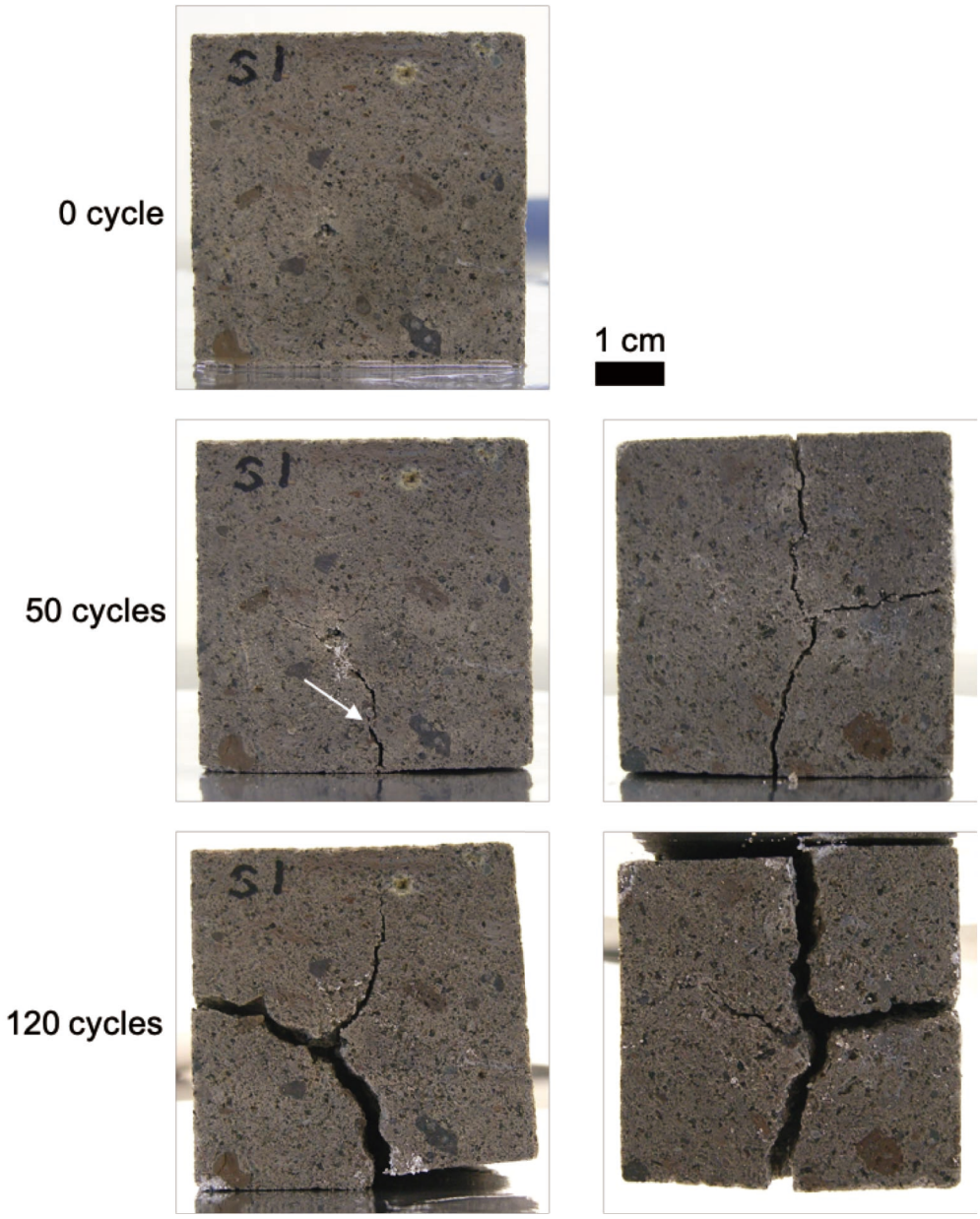

Figure 3.58 Specimen subjected to freeze-thaw cycles (Shirakawa tuff saturated with sodium chloride solution)

Right pictures are bottom face of the specimen. A crack propagated from lower part of the specimen, and extended with increasing number of freeze-thaw cycles.

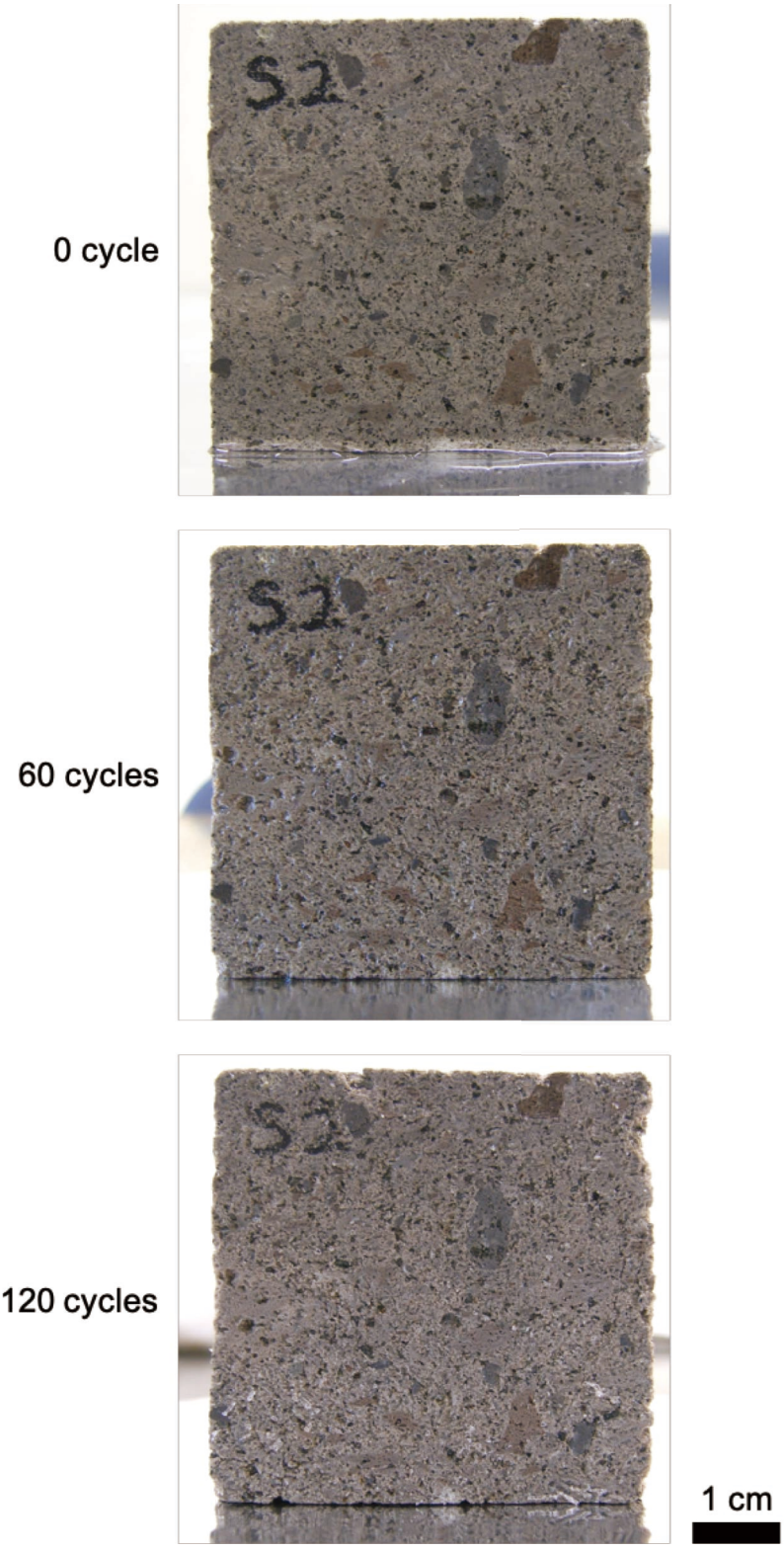

Figure 3.59 Specimen subjected to freeze-thaw cycles (Shirakawa tuff saturated with sodium sulfate solution)

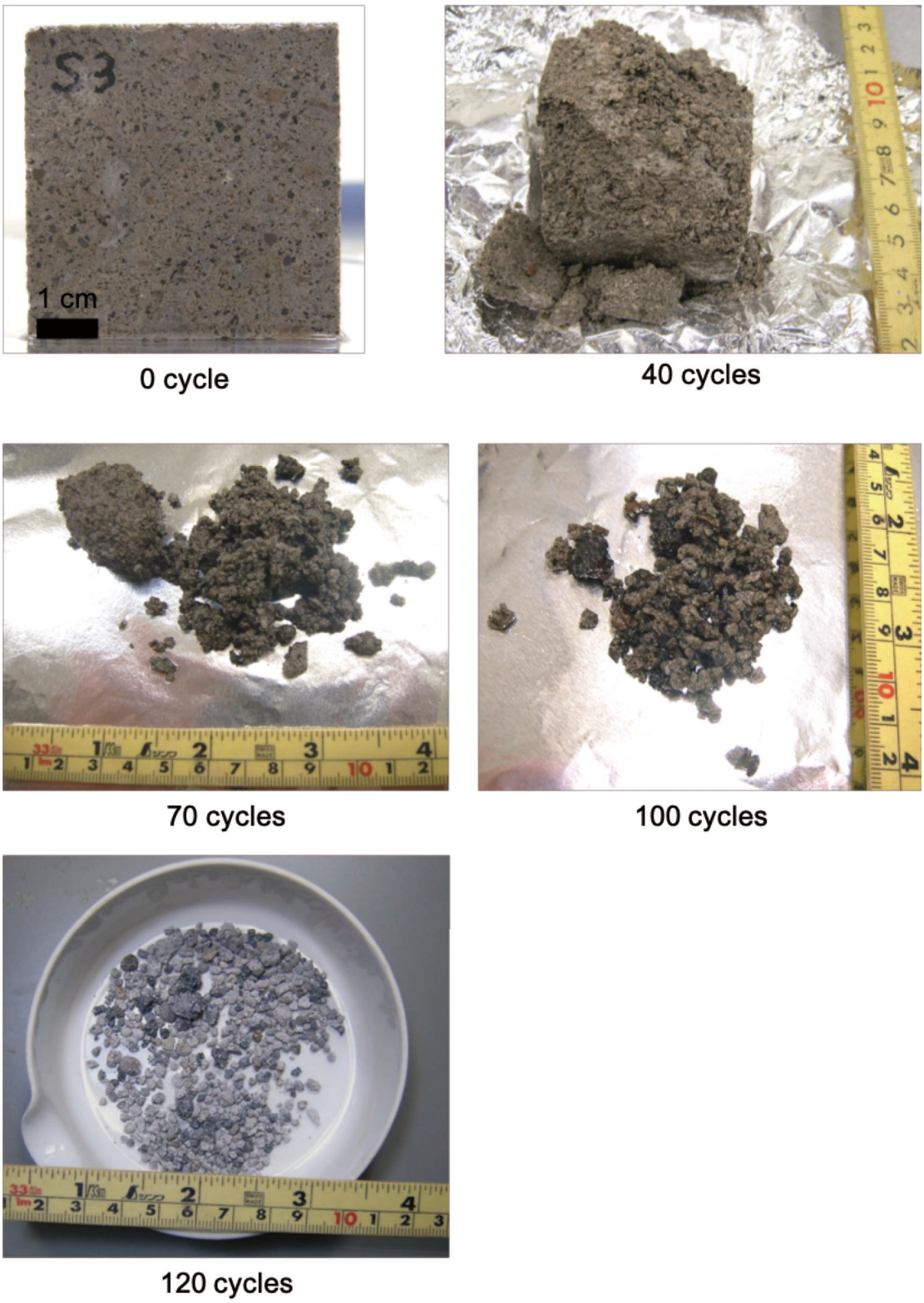

Figure 3.60 Specimen subjected to freeze-thaw cycles (Shirakawa tuff saturated with magnesium sulfate solution)

The specimen disintegrated into fragments without any visible crack propagation at 40 freeze-thaw cycles.

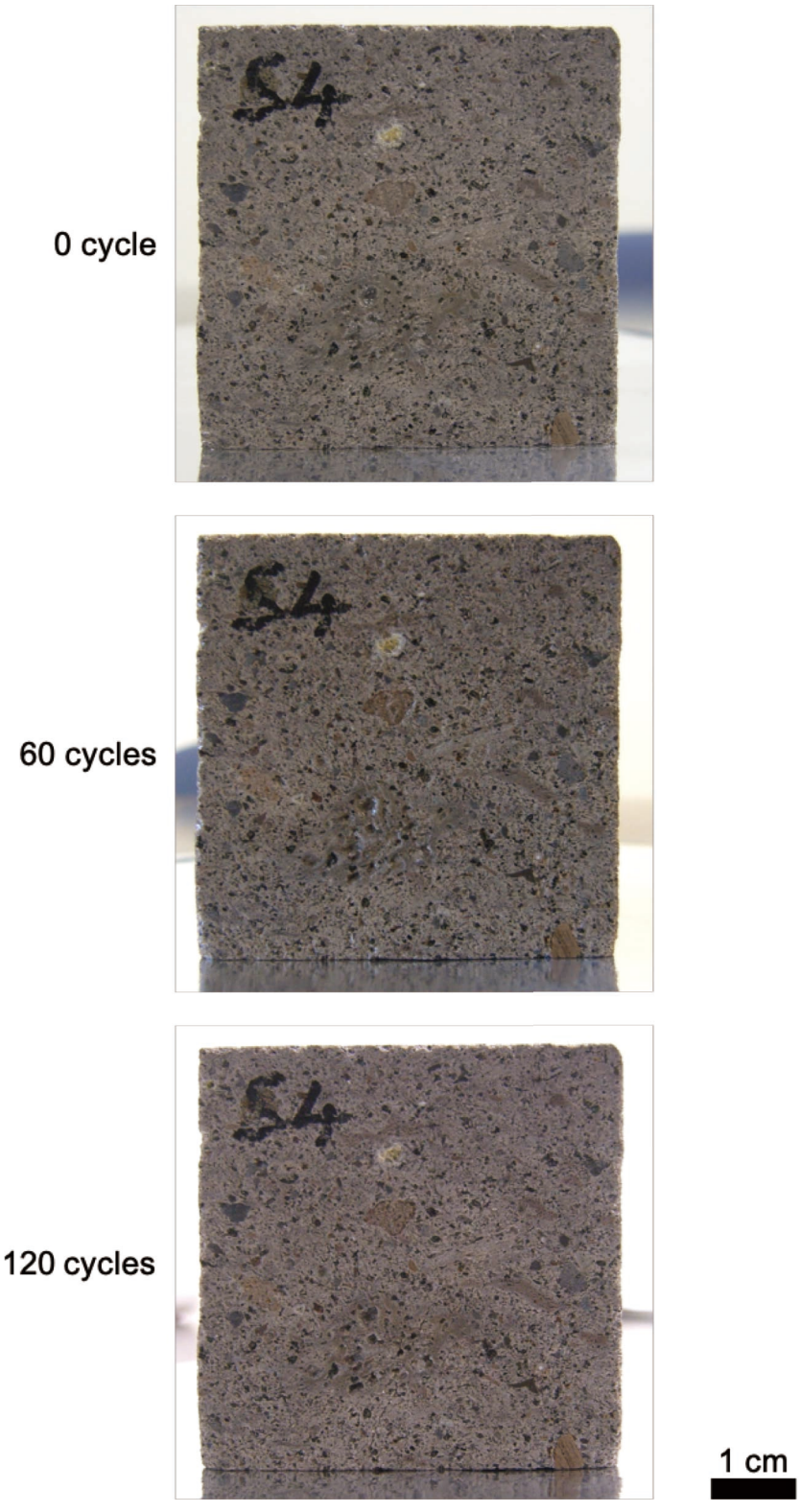

Figure 3.61 Specimen subjected to freeze-thaw cycles (Shirakawa tuff saturated with distilled water)

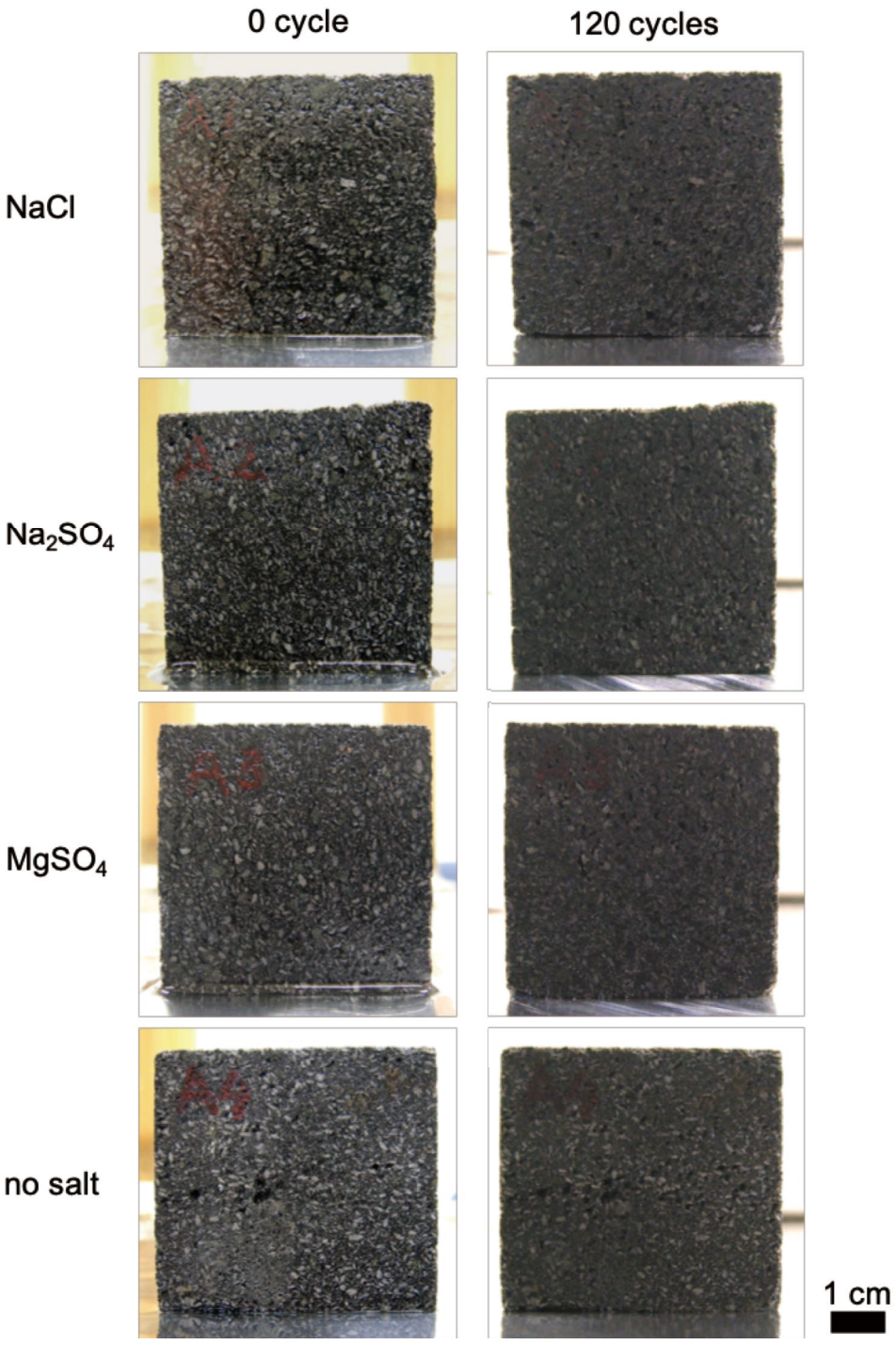

Figure 3.62 Andesite specimens subjected to freeze-thaw cycles

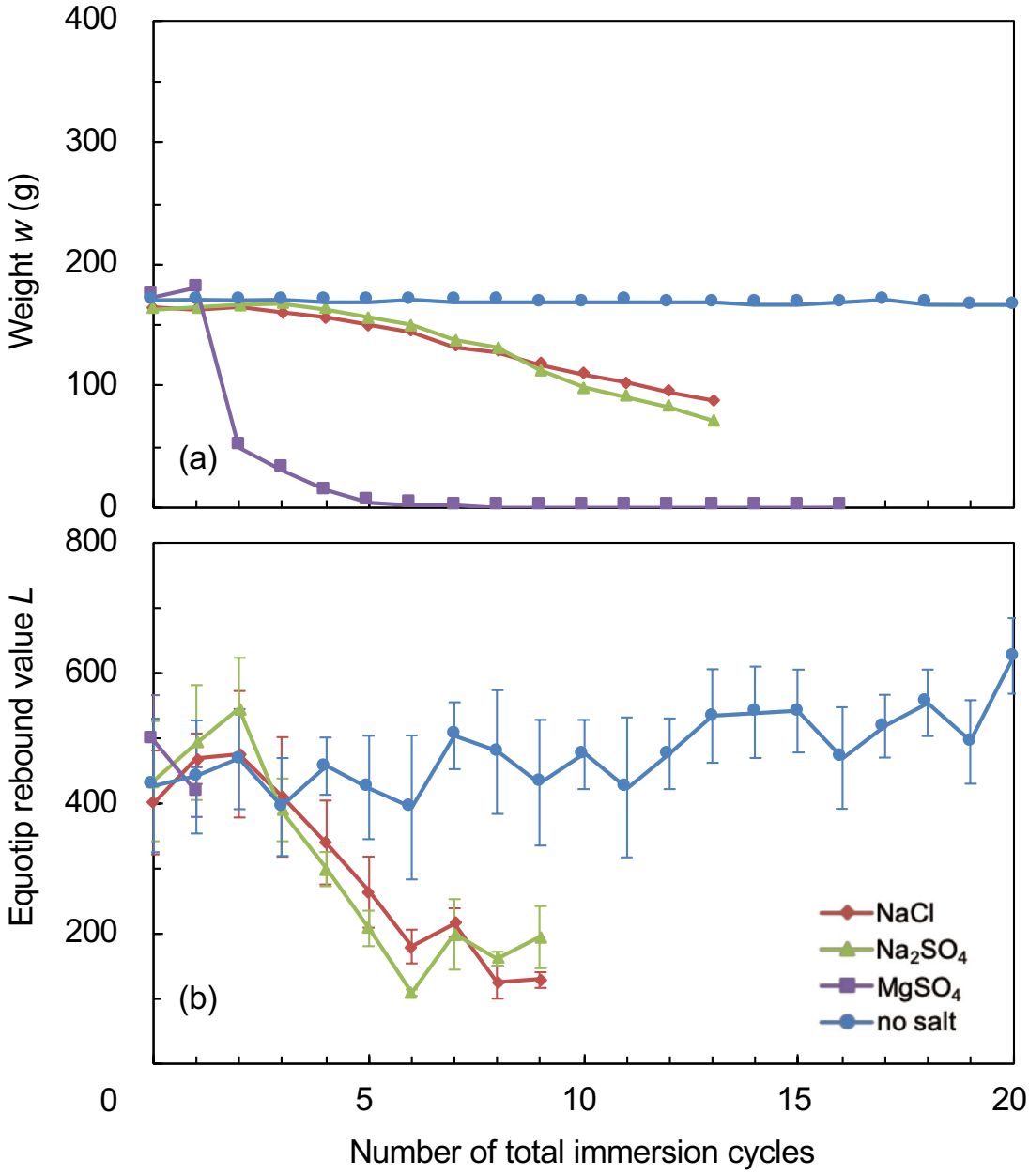

Figure 3.63 Weight (a) and Equotip rebound value (b) measured during total immersion experiment (Oya tuff, 20˚C)

Vertical bar in the L-value represents dispersion of 10 single impacts.

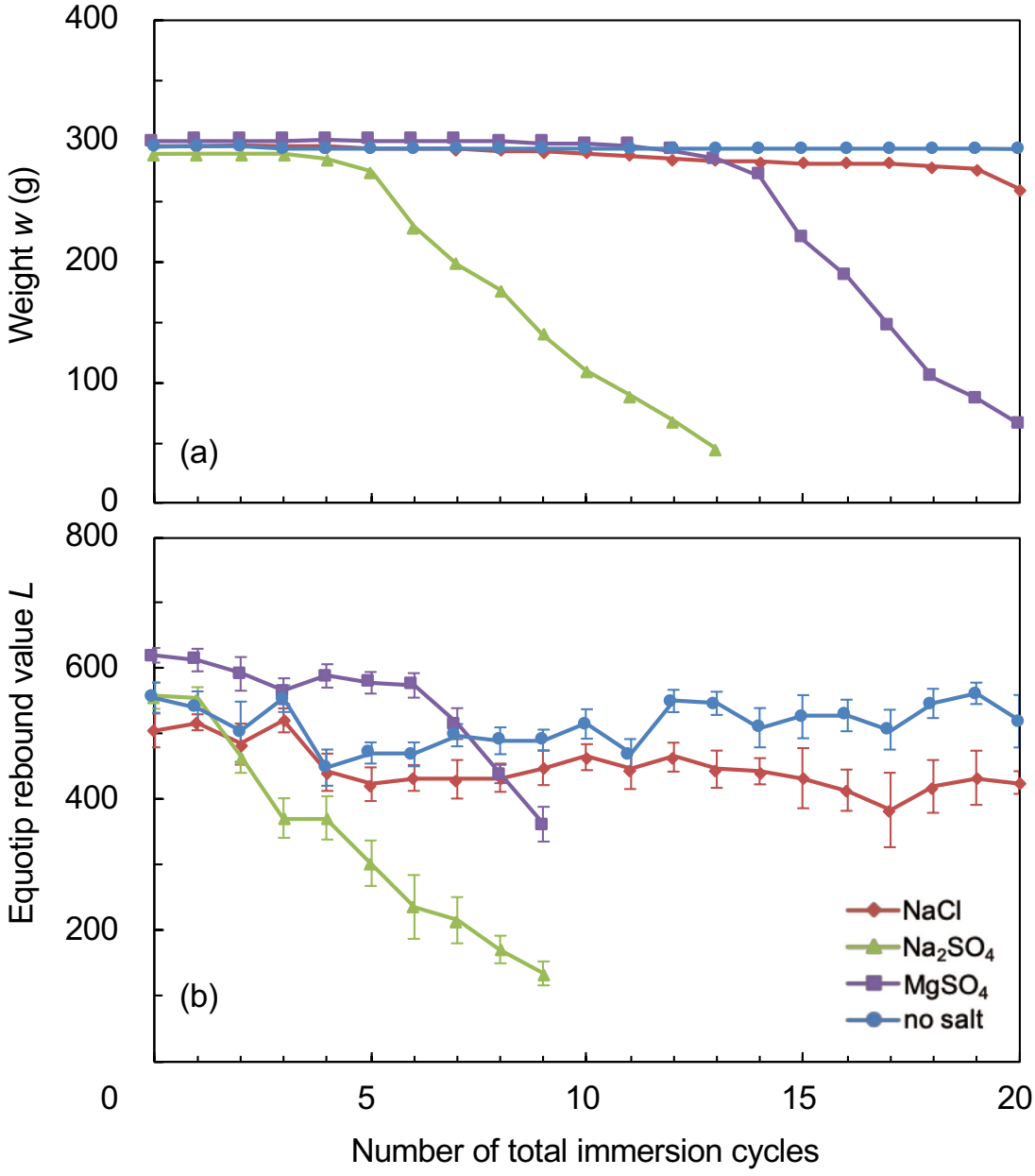

Figure 3.64 Weight (a) and Equotip rebound value (b) measured during total immersion experiment (Aoshima sandstone, 20˚C)

Vertical bar in the L-value represents dispersion of 10 single impacts.

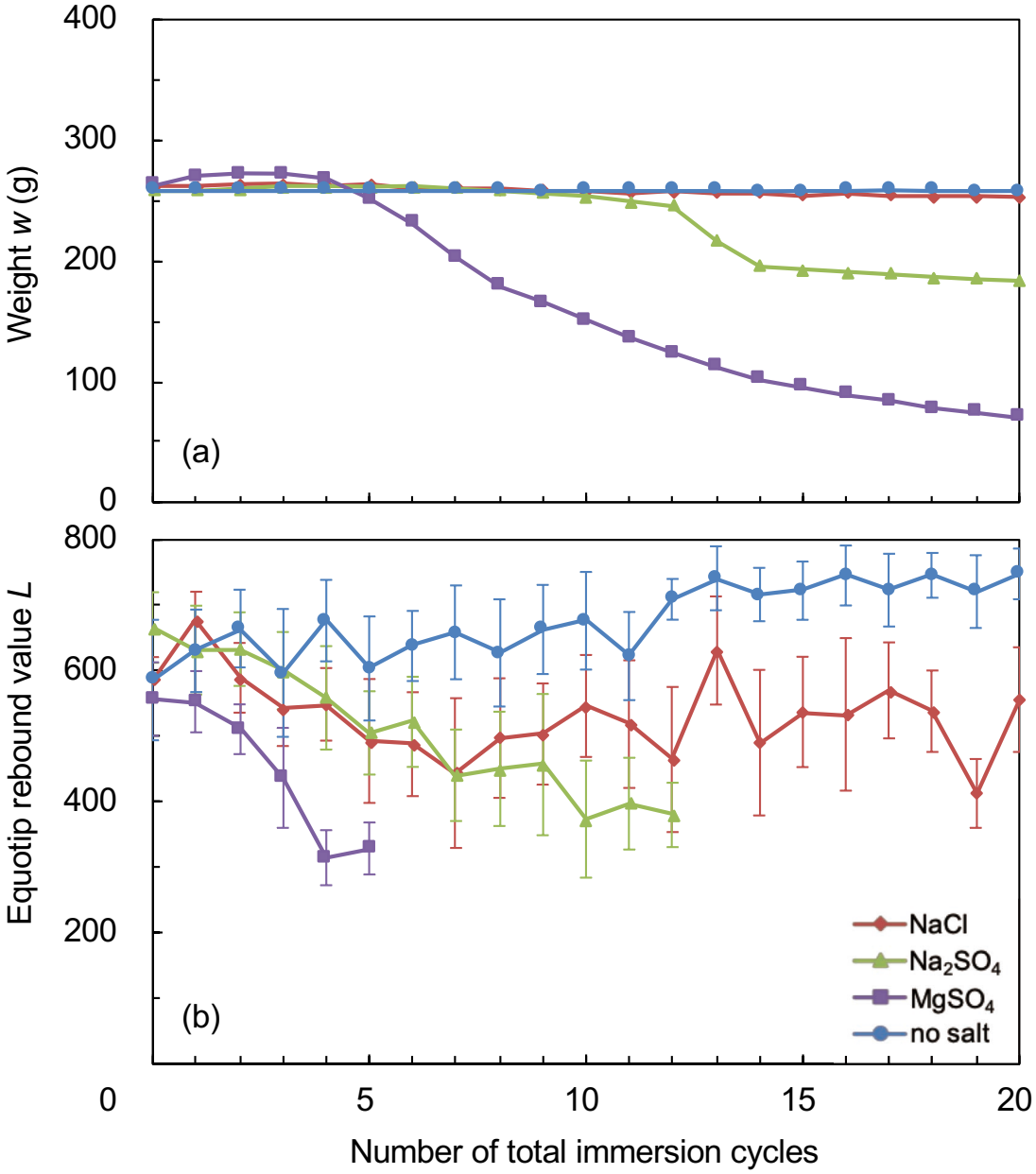

Figure 3.65 Weight (a) and Equotip rebound value (b) measured during total immersion experiment (Shirakawa tuff, 20˚C)

Vertical bar in the L-value represents dispersion of 10 single impacts.

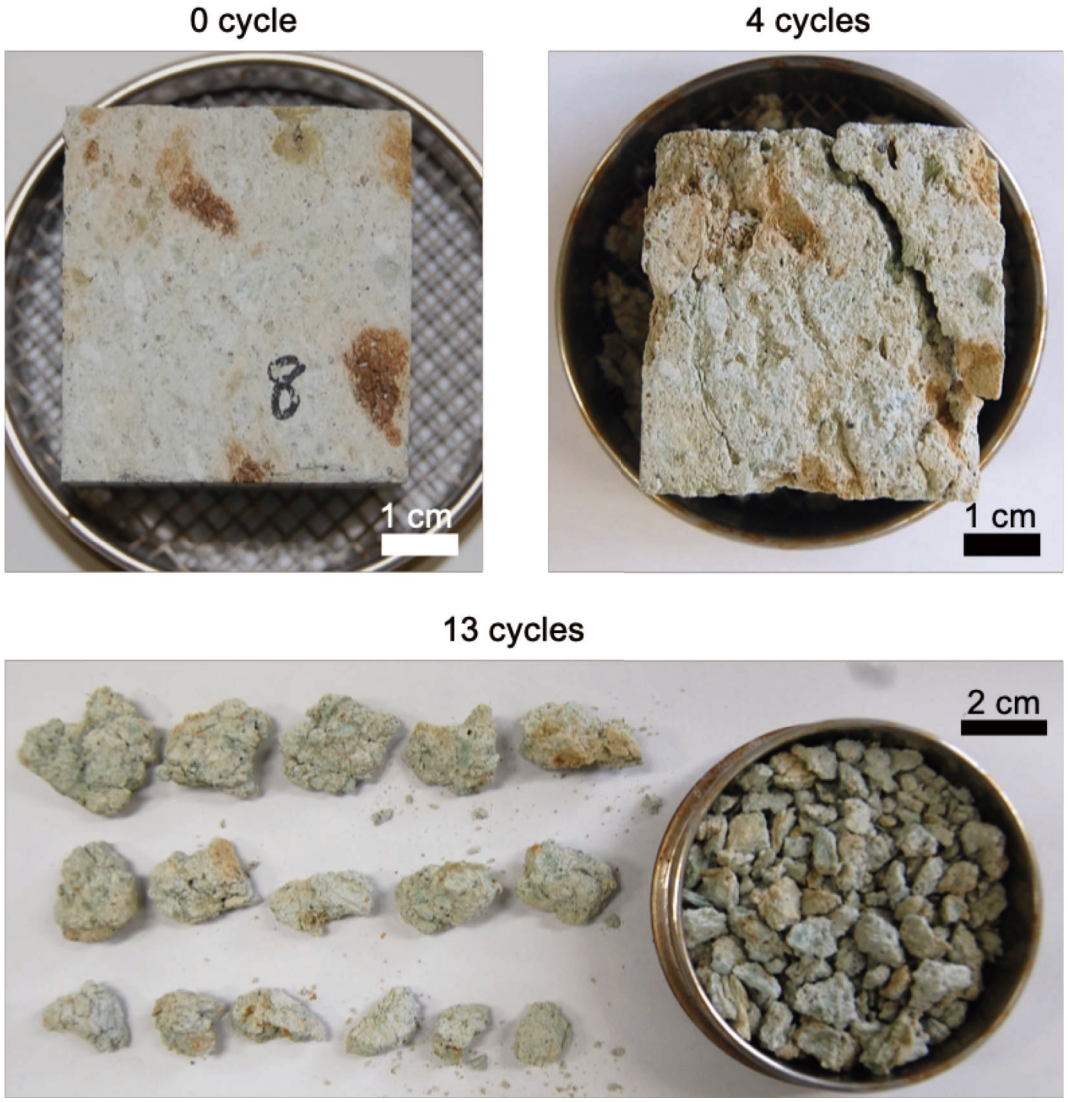

Figure 3.66 Specimen subjected to total immersion cycles (Oya tuff immersed in sodium chloride solution, 20˚C)

A lot of cracks occurred at 4 cycles, and the specimen split into a lot fragments after 5 cycles.

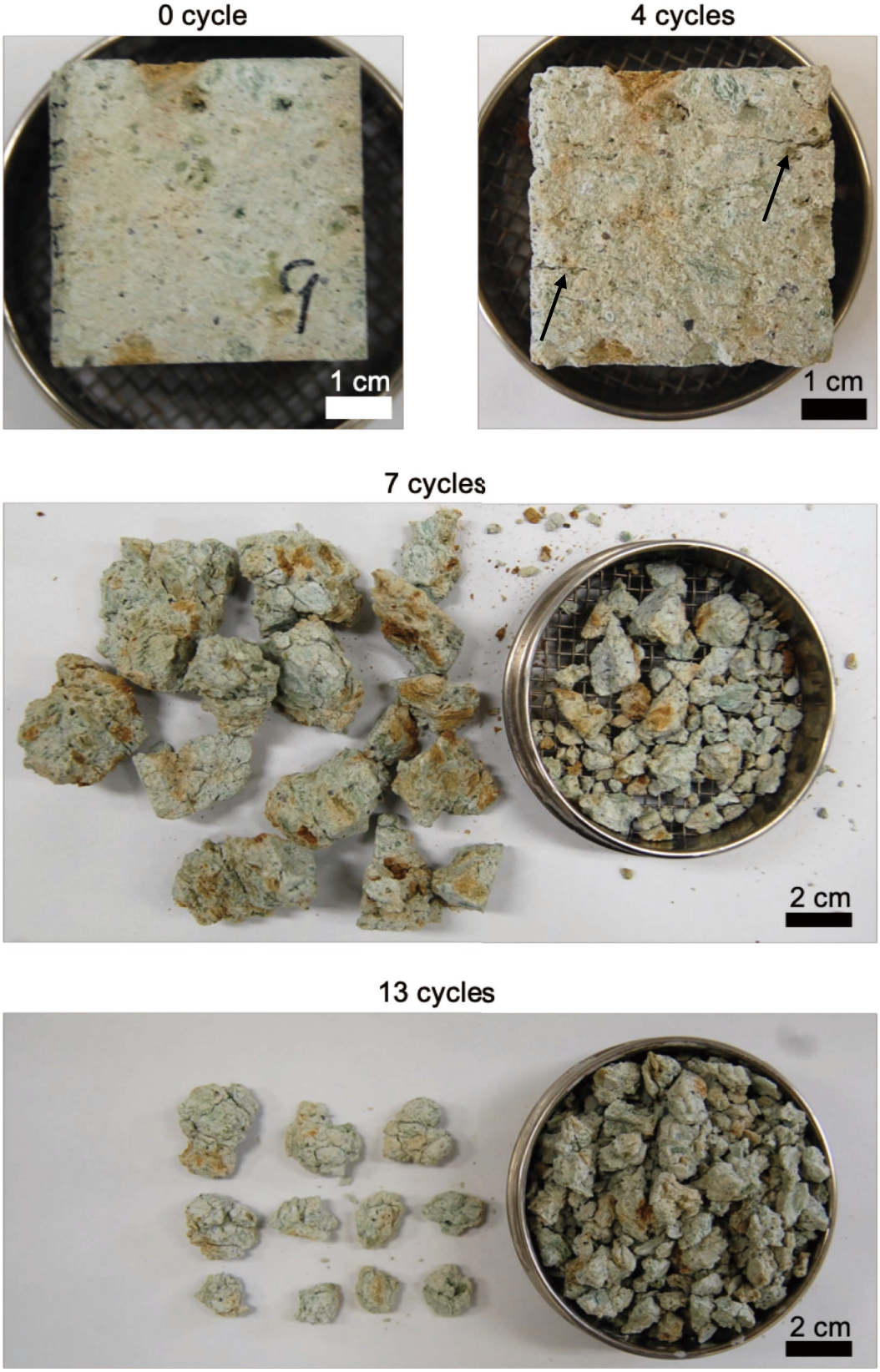

Figure 3.67 Specimen subjected to total immersion cycles (Oya tuff immersed in sodium sulfate solution, 20˚C)

Some cm-scale cracks occurred at 4 cycles, and the specimen split into a lot fragments after 7 cycles.

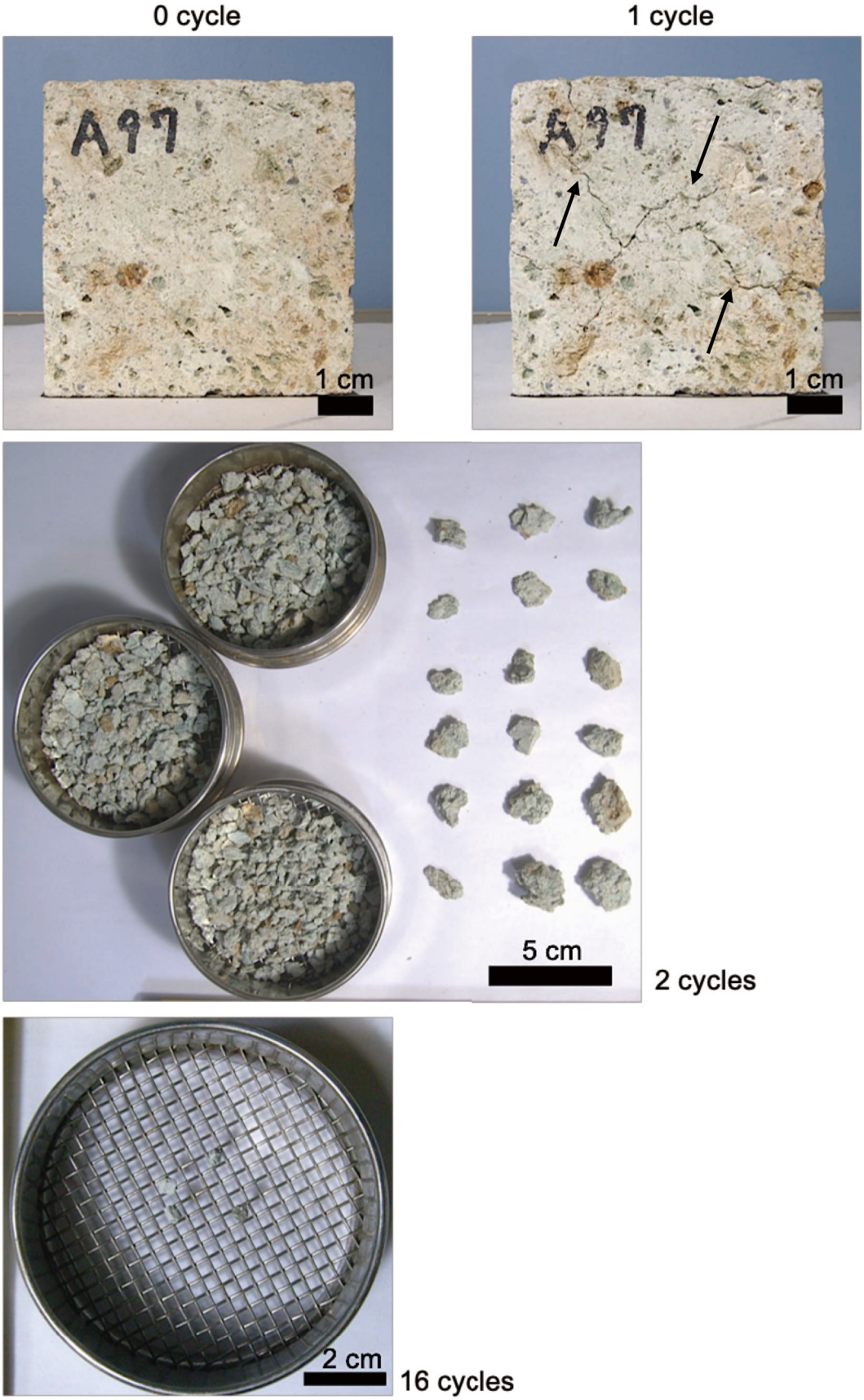

Figure 3.68 Specimen subjected to total immersion cycles (Oya tuff immersed in magnesium sulfate solution, 20˚C)

A lot of cracks occurred at a cycle, and the specimen split into a lot fragments after 2 cycles. Most of fragments were smaller than 2 mm in length at 16 cycles.

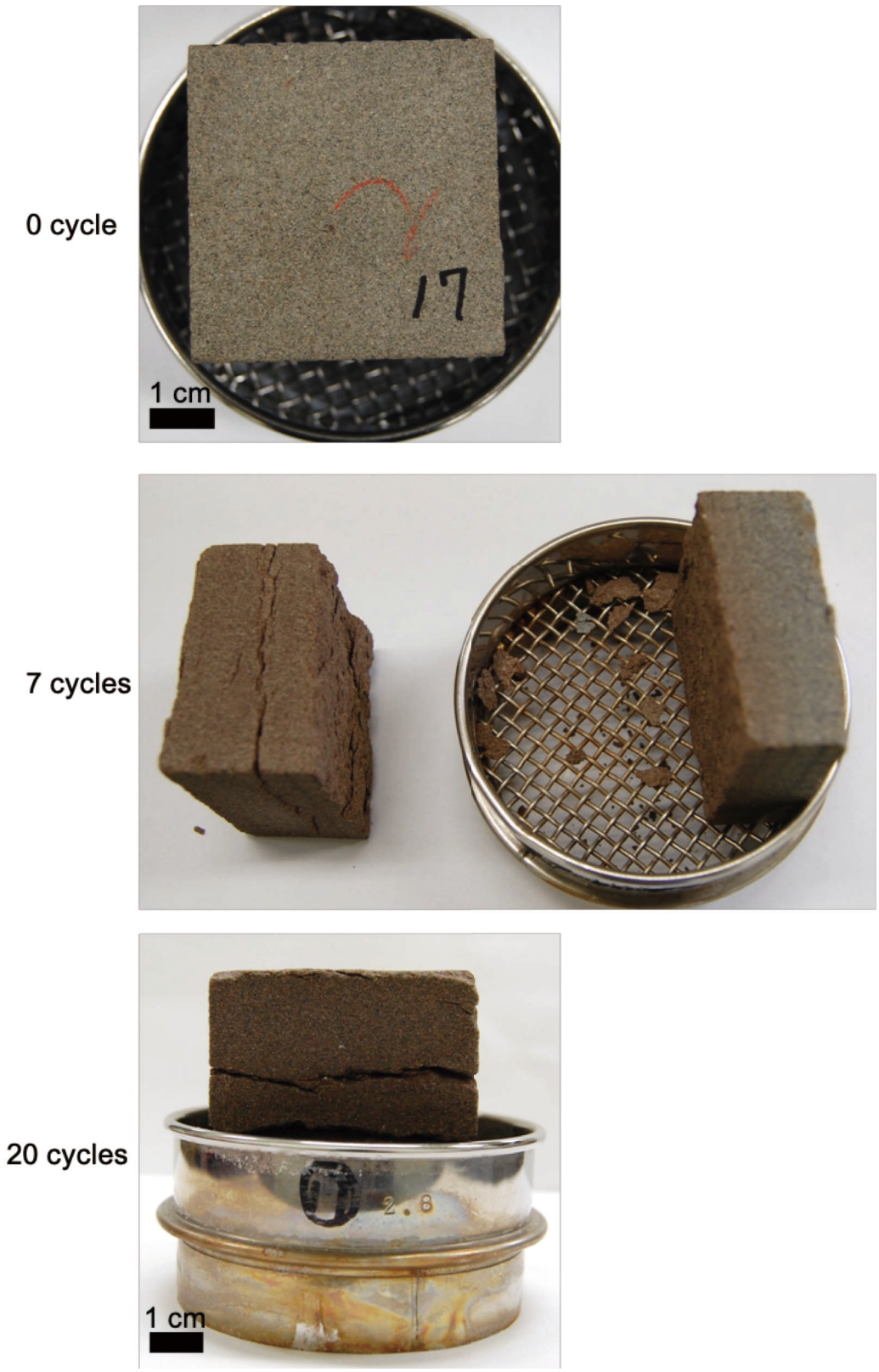

Figure 3.69 Specimen subjected to total immersion cycles (Aoshima sandstone immersed in sodium chloride solution, 20˚C)

Cracks occurred after 4 cycles. The specimen split into cm-scale fragments at 7 cycles.

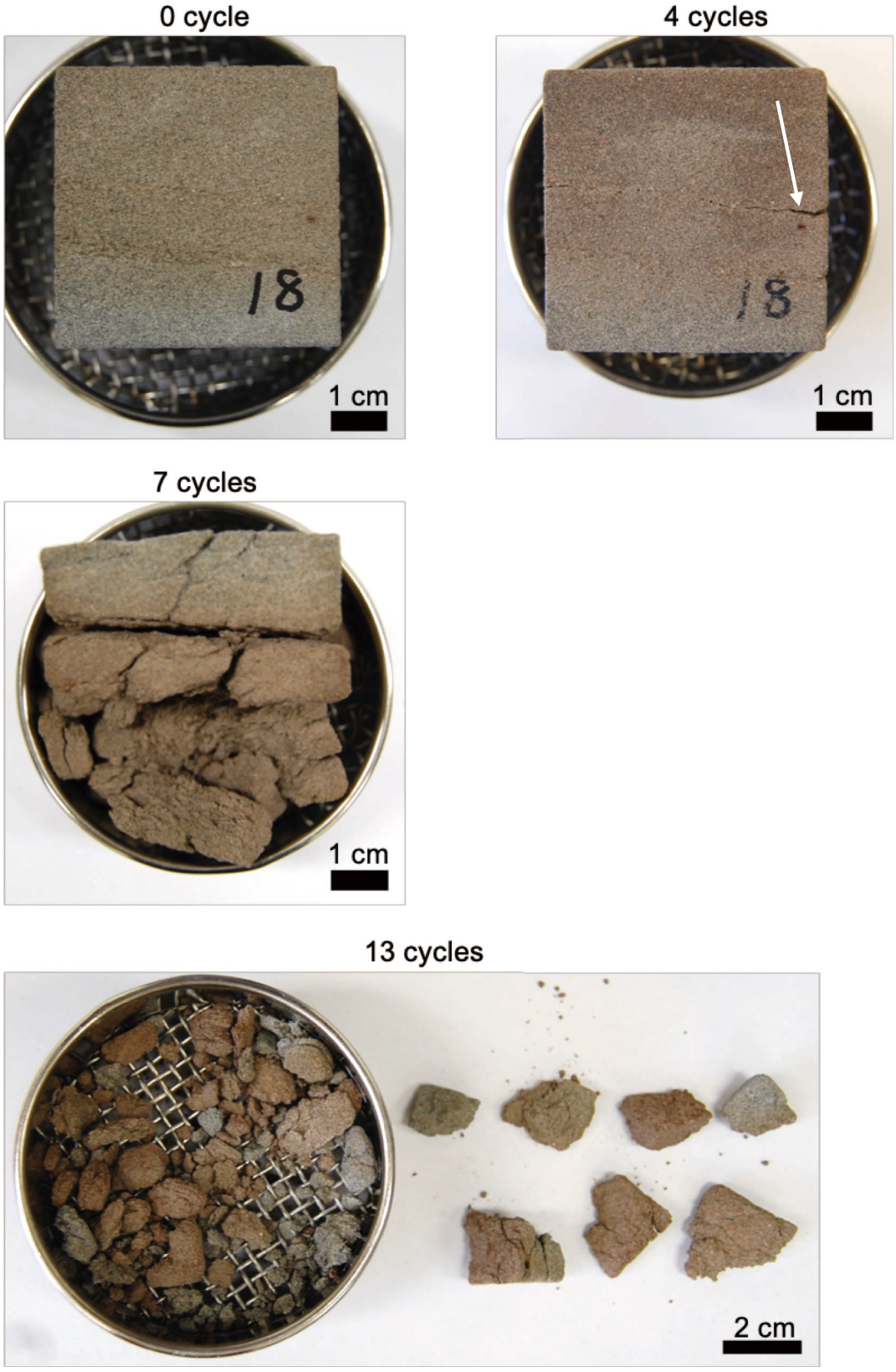

Figure 3.70 Specimen subjected to total immersion cycles (Aoshima sandstone immersed in sodium sulfate solution, 20˚C)

A cm-scale crack occurred at 4 cycles, and the specimen disintegrated into various sizes of fragments at 7 cycles.

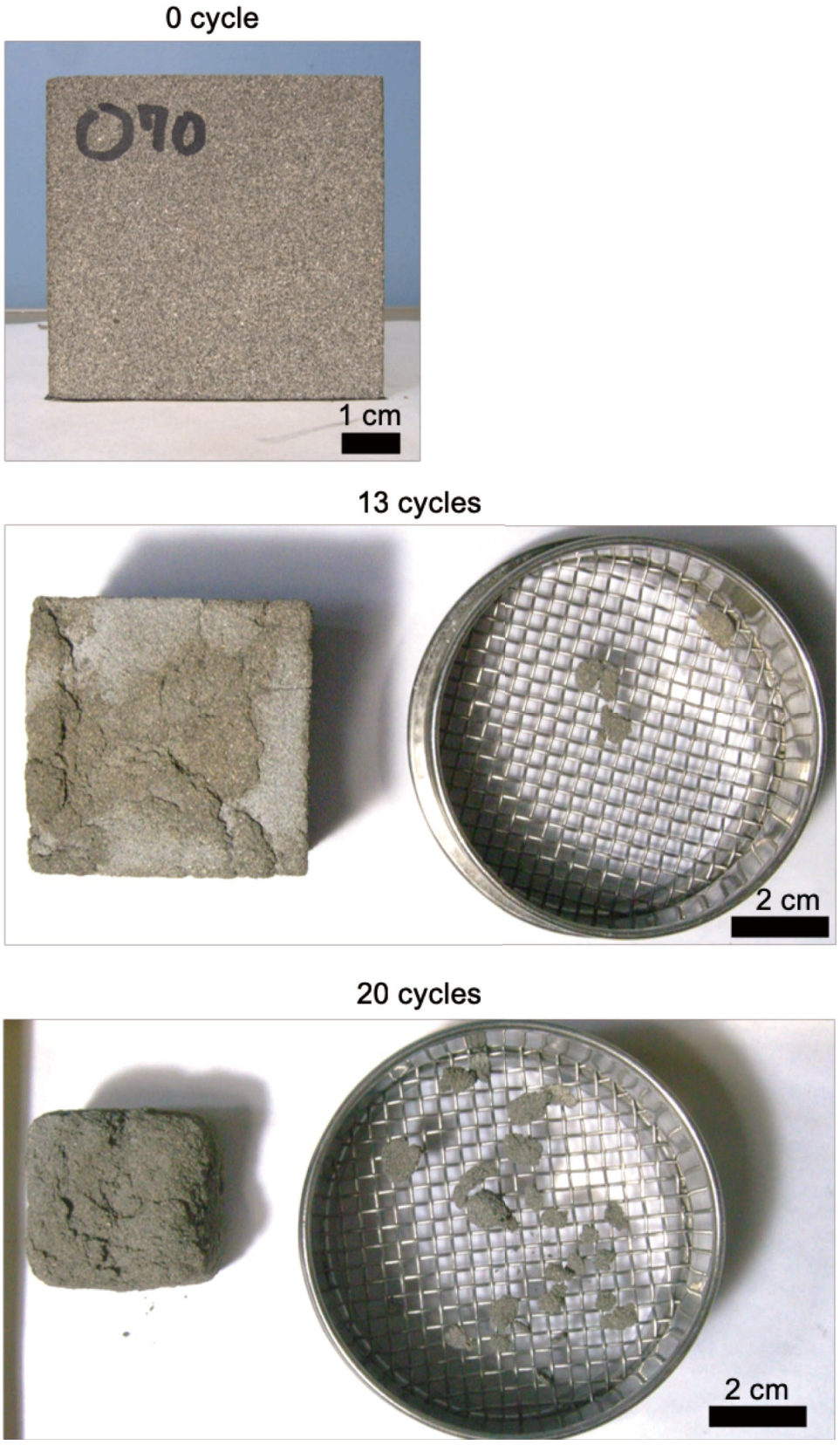

Figure 3.71 Specimen subjected to total immersion cycles (Aoshima sandstone immersed in magnesium sulfate solution, 20˚C)

Cracks extended, and mm-scale tabular fragments split from surface of the specimen at 13 cycles. Shape of the specimen gradually became rounder as an increase with number of total immersion cycles.

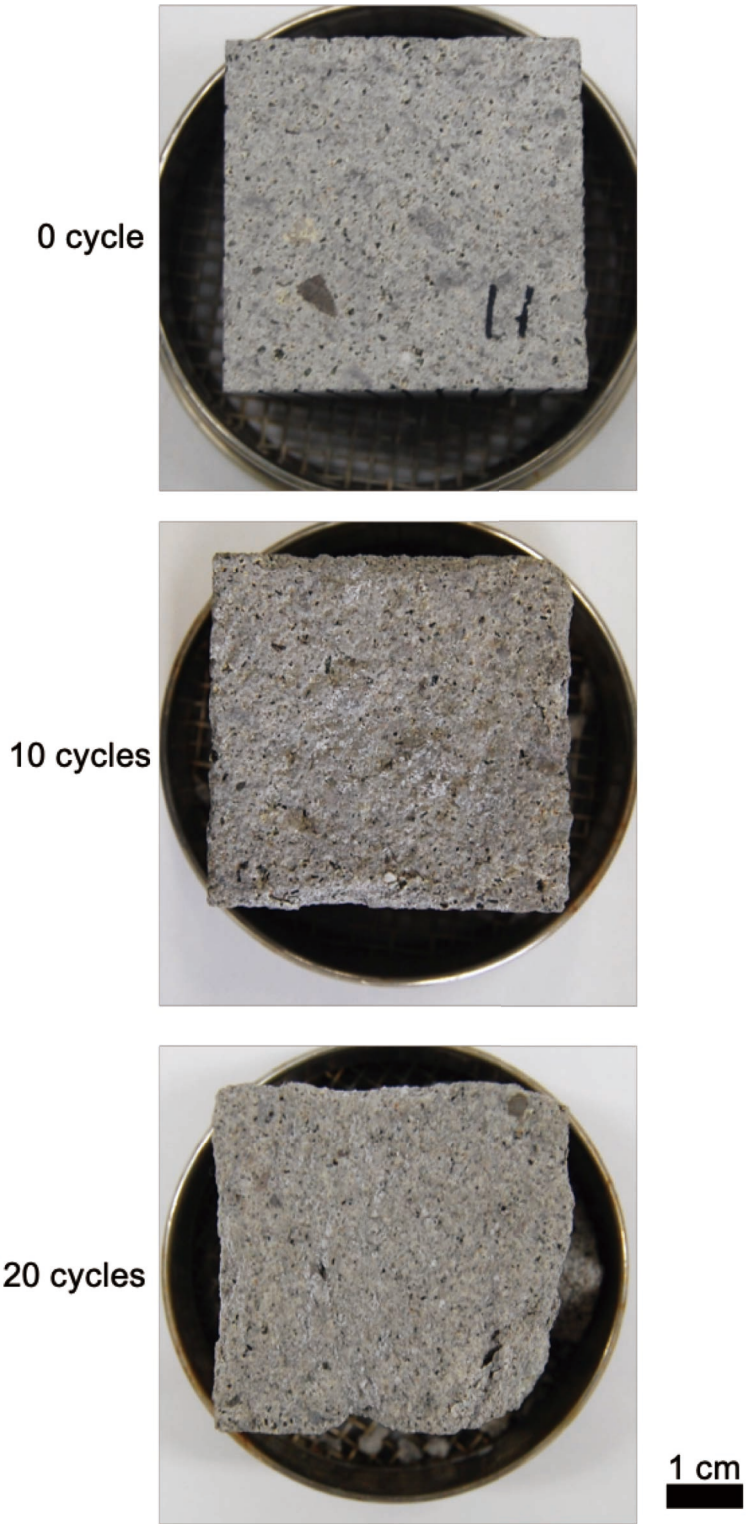

Figure 3.72 Specimen subjected to total immersion cycles (Shirakawa tuff immersed in sodium chloride solution, 20˚C)

The mm-scale fragments split from surface of the specimen, and the surface became rough as an increase with number of total immersion cycles. A cm-scale fragment split from upper edge of the specimen at 20 cycles.

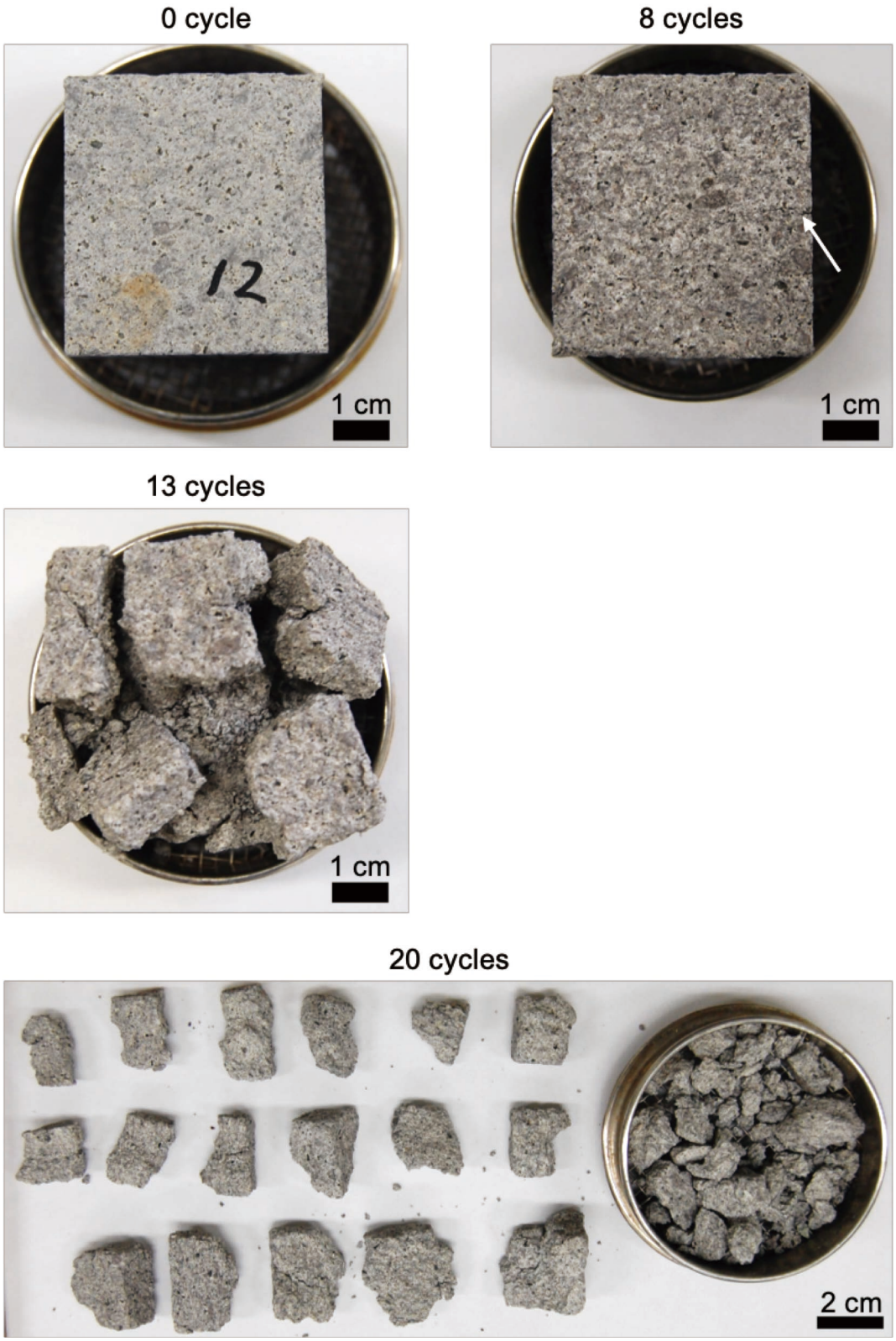

Figure 3.73 Specimen subjected to total immersion cycles (Shirakawa tuff immersed in sodium sulfate solution, 20˚C)

A cm-scale crack occurred at 8 cycles, and the specimen split into various sizes of fragments at 13 cycles.

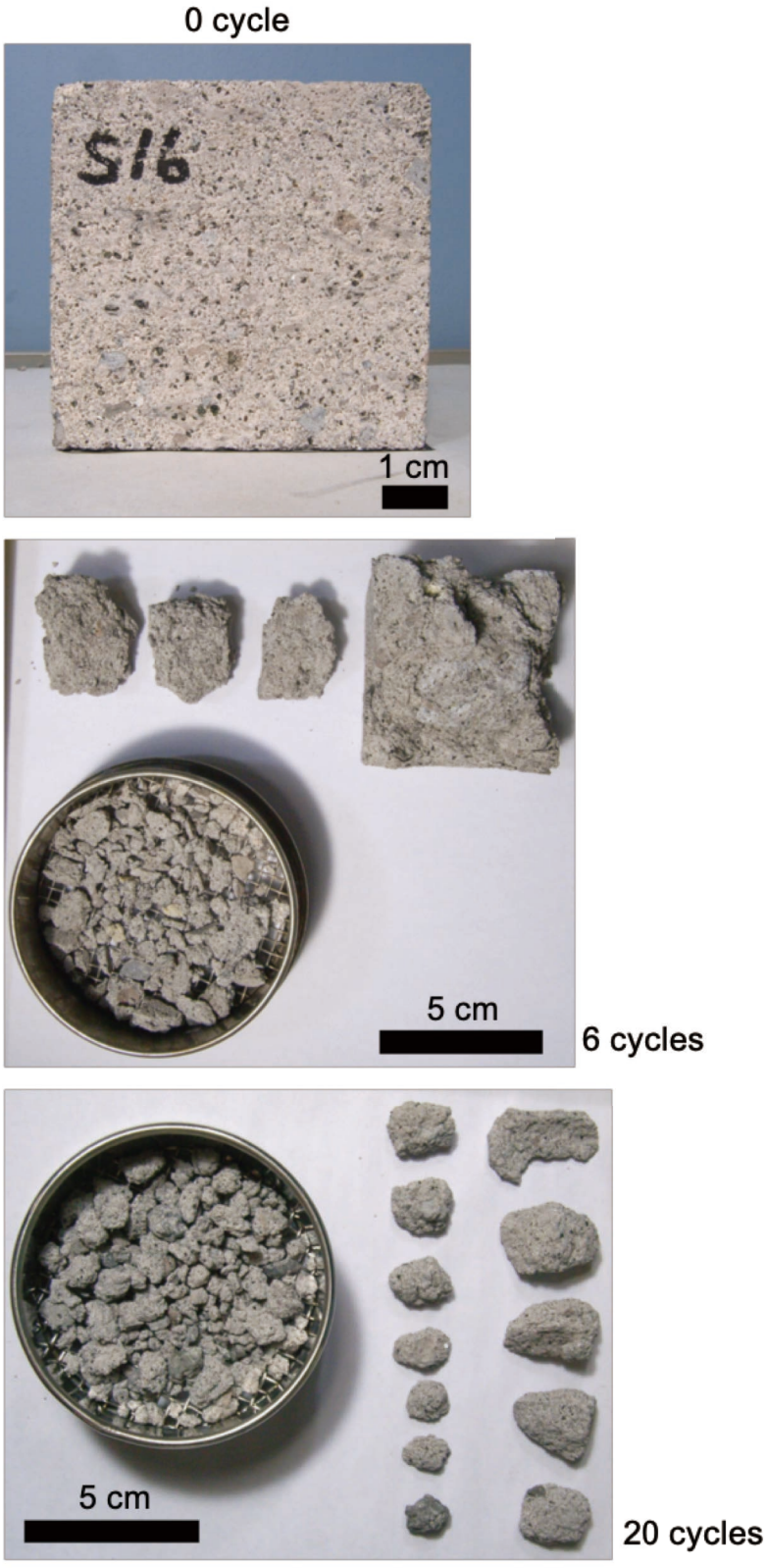

Figure 3.74 Specimen subjected to total immersion cycles (Shirakawa tuff immersed in magnesium sulfate solution, 20˚C)

The specimen split into various sizes of fragments after 6 cycles.

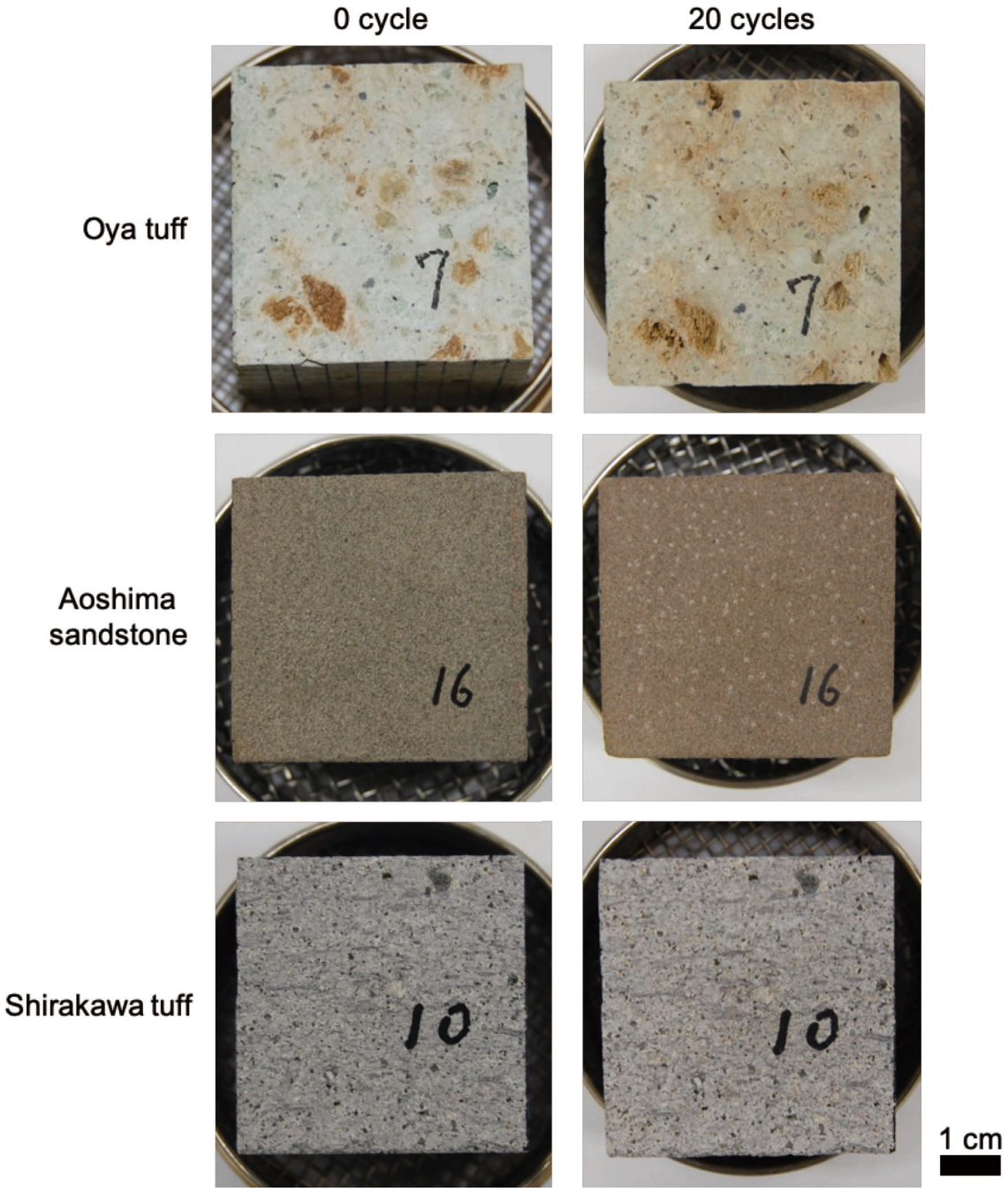

Figure 3.75 Controlled specimens subjected to total immersion cycles (specimens immersed in distilled water, 20˚C)

The specimens did not show any visible sign of breakdown.

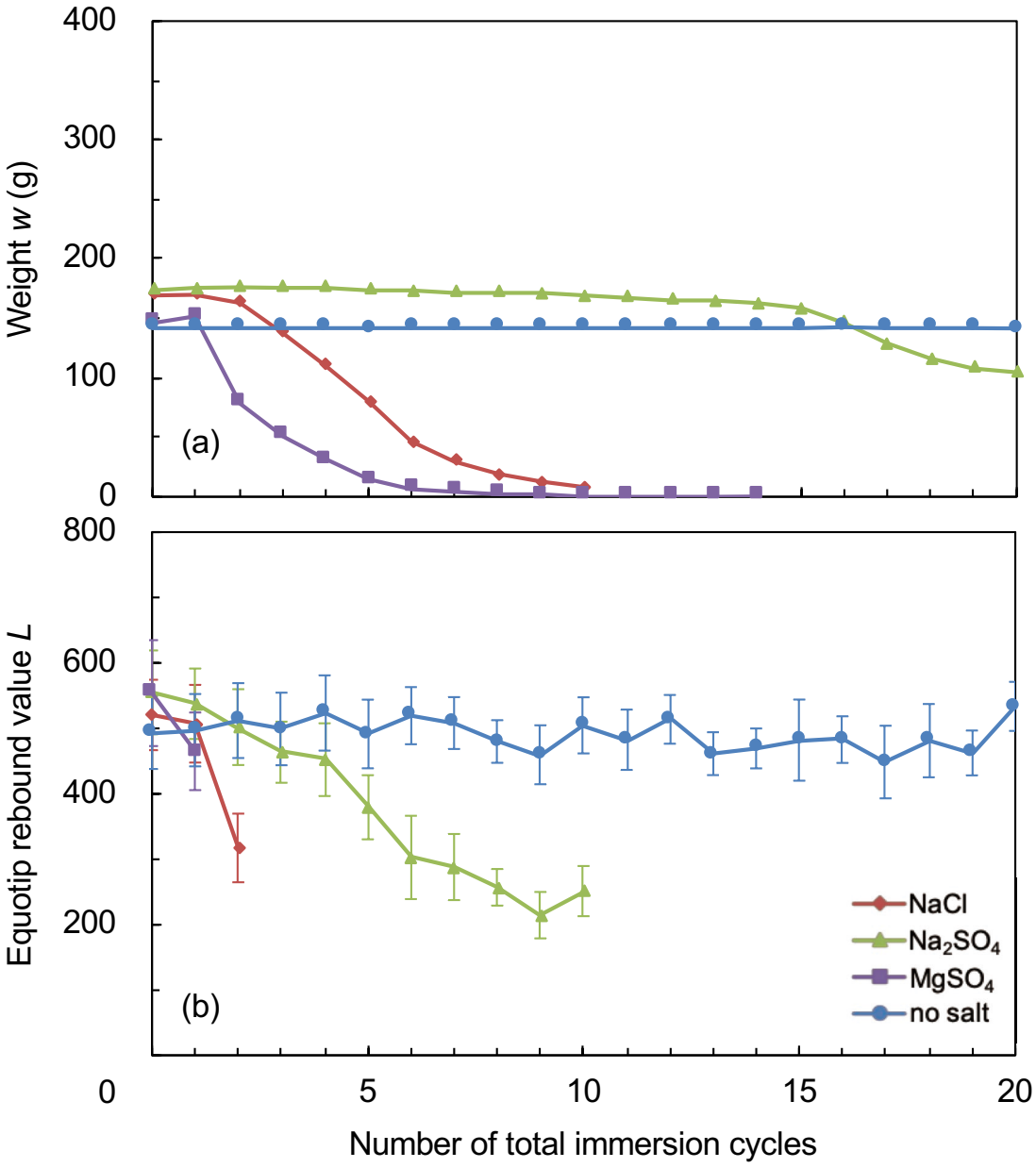

Figure 3.76 Weight (a) and Equotip rebound value (b) measured during total immersion experiment (Oya tuff, 10˚C)

Vertical bar in the L-value represents dispersion of 10 single impacts.

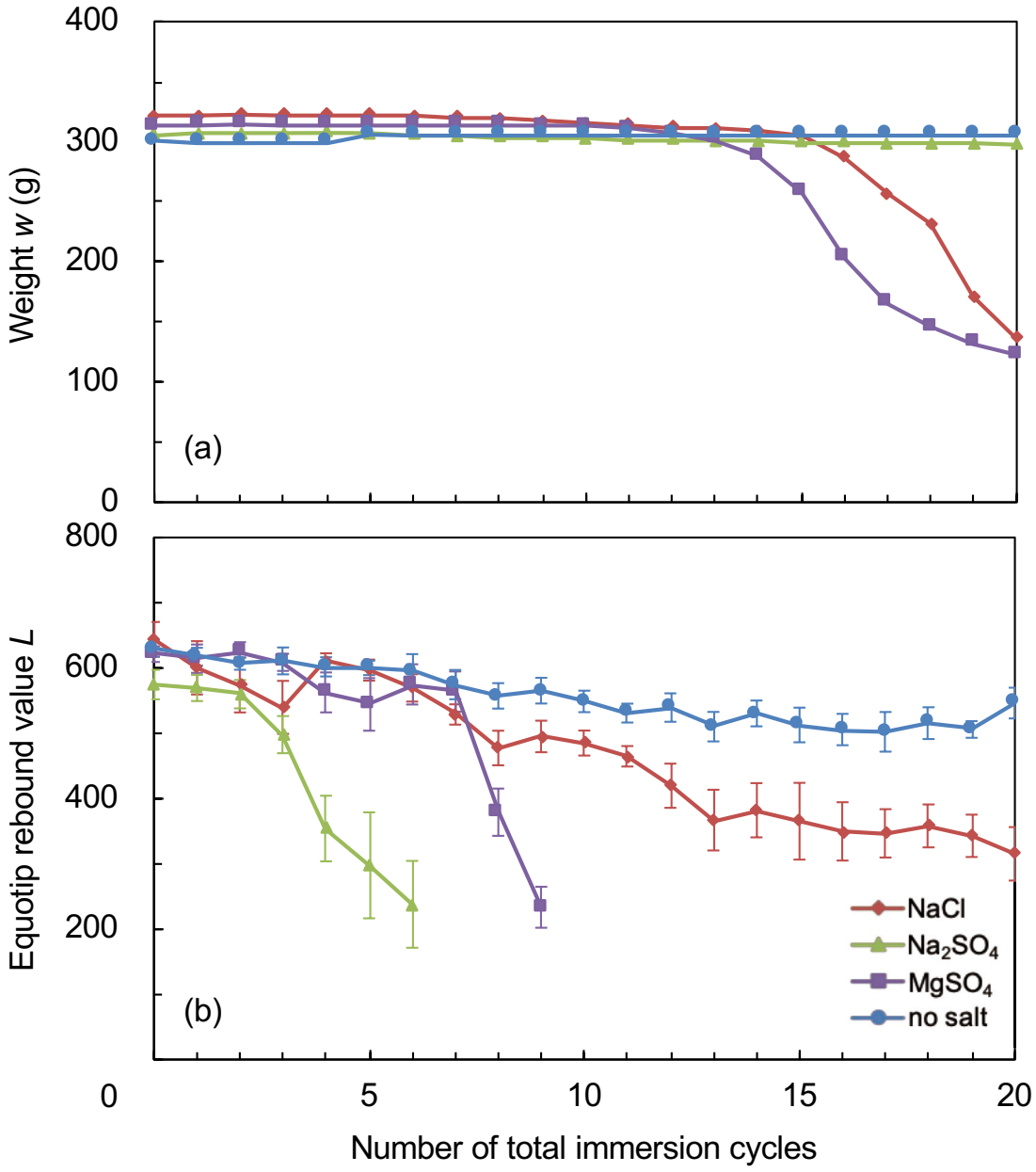

Figure 3.77 Weight (a) and Equotip rebound value (b) measured during total immersion experiment (Aoshima sandstone, 10˚C)

Vertical bar in the L-value represents dispersion of 10 single impacts.

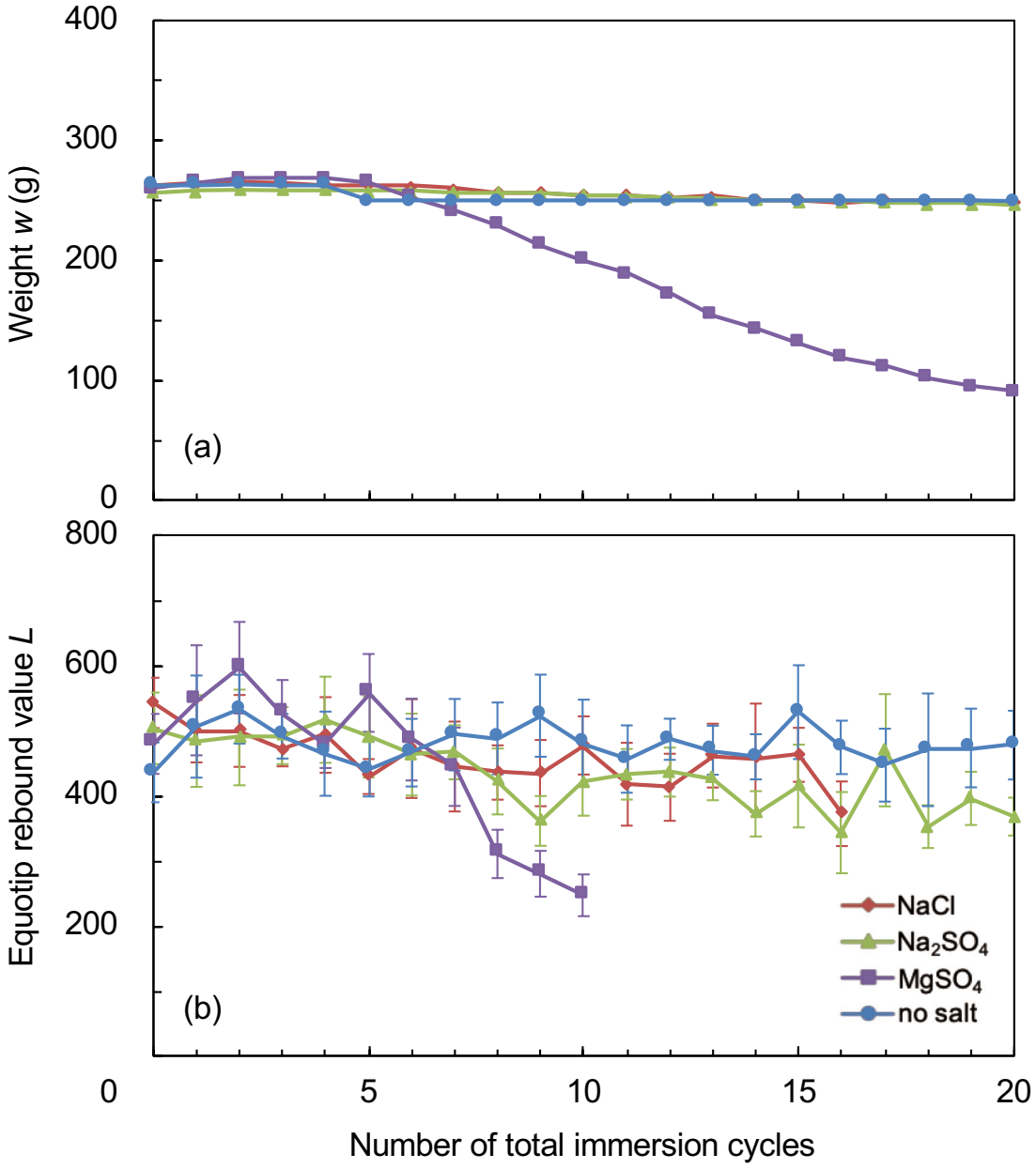

Figure 3.78 Weight (a) and Equotip rebound value (b) measured during total immersion experiment (Shirakawa tuff, 10˚C)

Vertical bar in the L-value represents dispersion of 10 single impacts.

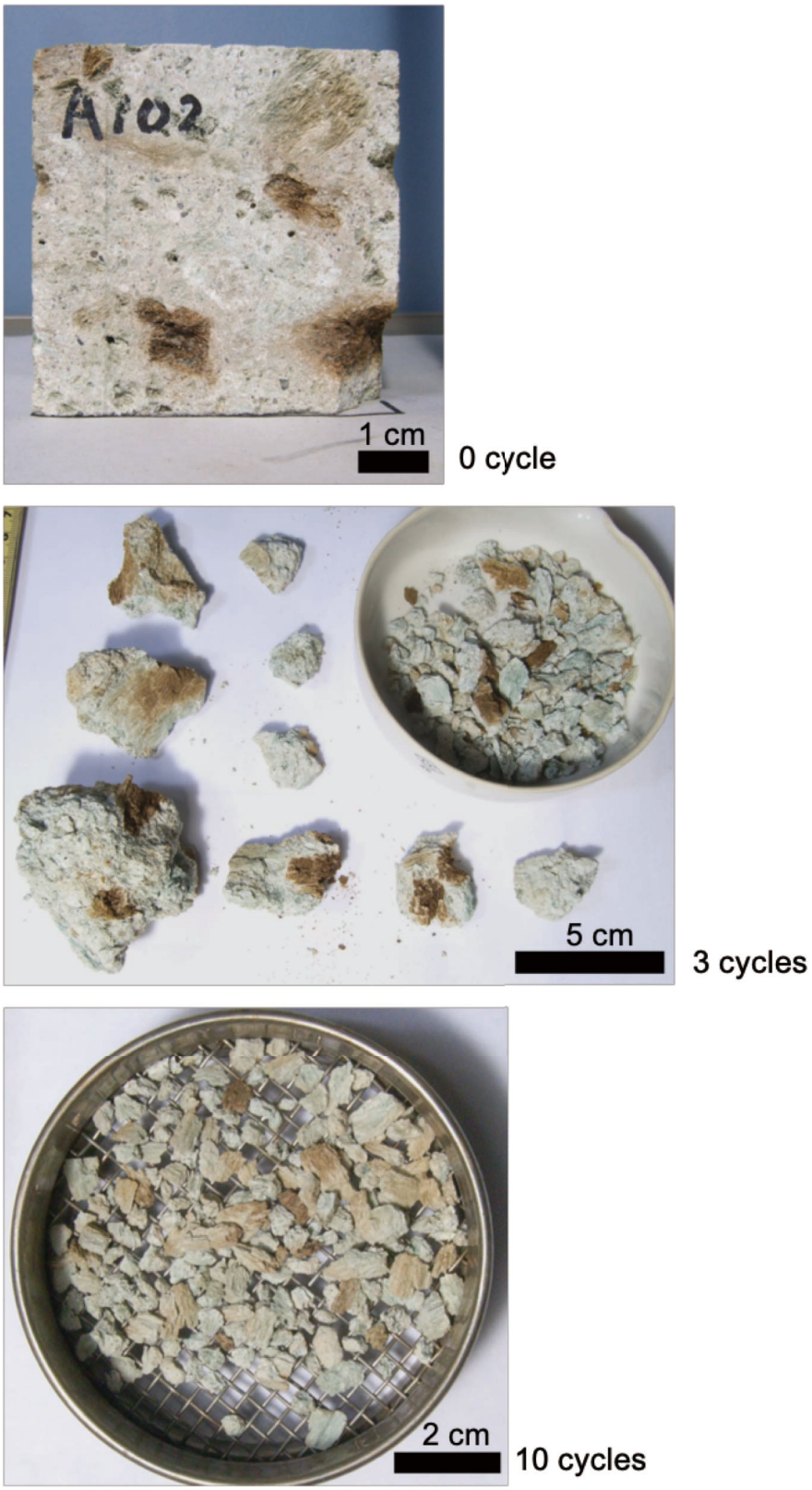

Figure 3.79 Specimen subjected to total immersion cycles (Oya tuff immersed in sodium chloride solution, 10˚C)

The specimen split into various sizes of fragments after 3 cycles.

Figure 3.80 Specimen subjected to total immersion cycles (Oya tuff immersed in sodium sulfate solution, 10˚C)

Cracks occurred at 3 cycles, and the specimen split into a lot fragments after 10 cycles.

Figure 3.81 Specimen subjected to total immersion cycles (Oya tuff immersed in magnesium sulfate solution, 10˚C)

A cm-scale crack occurred at a cycle, and the specimen split into a lot fragments after 2 cycles. Most of fragments were smaller than 2 mm in length at 14 cycles.

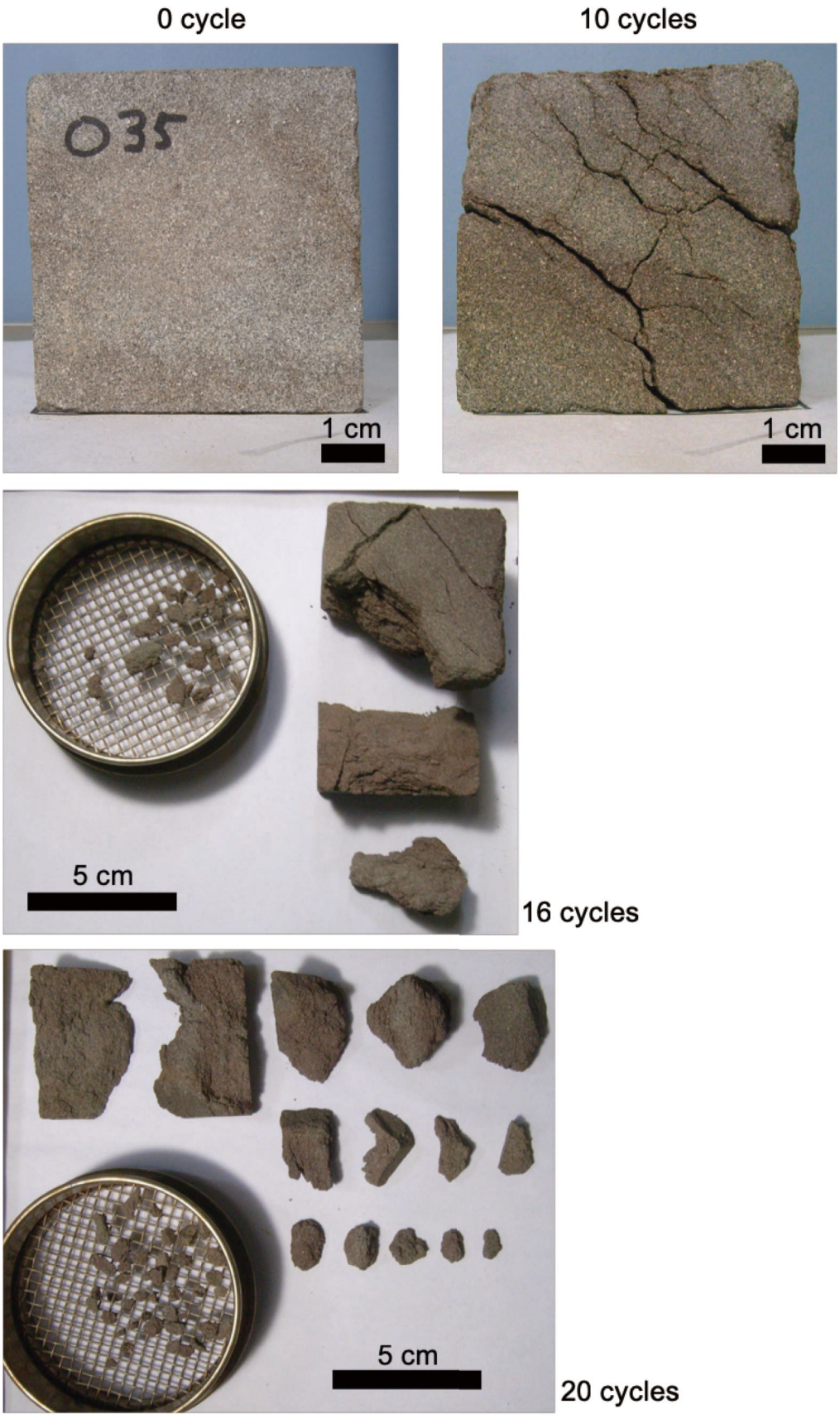

Figure 3.82 Specimen subjected to total immersion cycles (Aoshima sandstone immersed in sodium chloride solution, 10˚C)

A lot of cracks occurred at 10 cycles, and the specimen split into various sizes of fragments at 16 cycles.

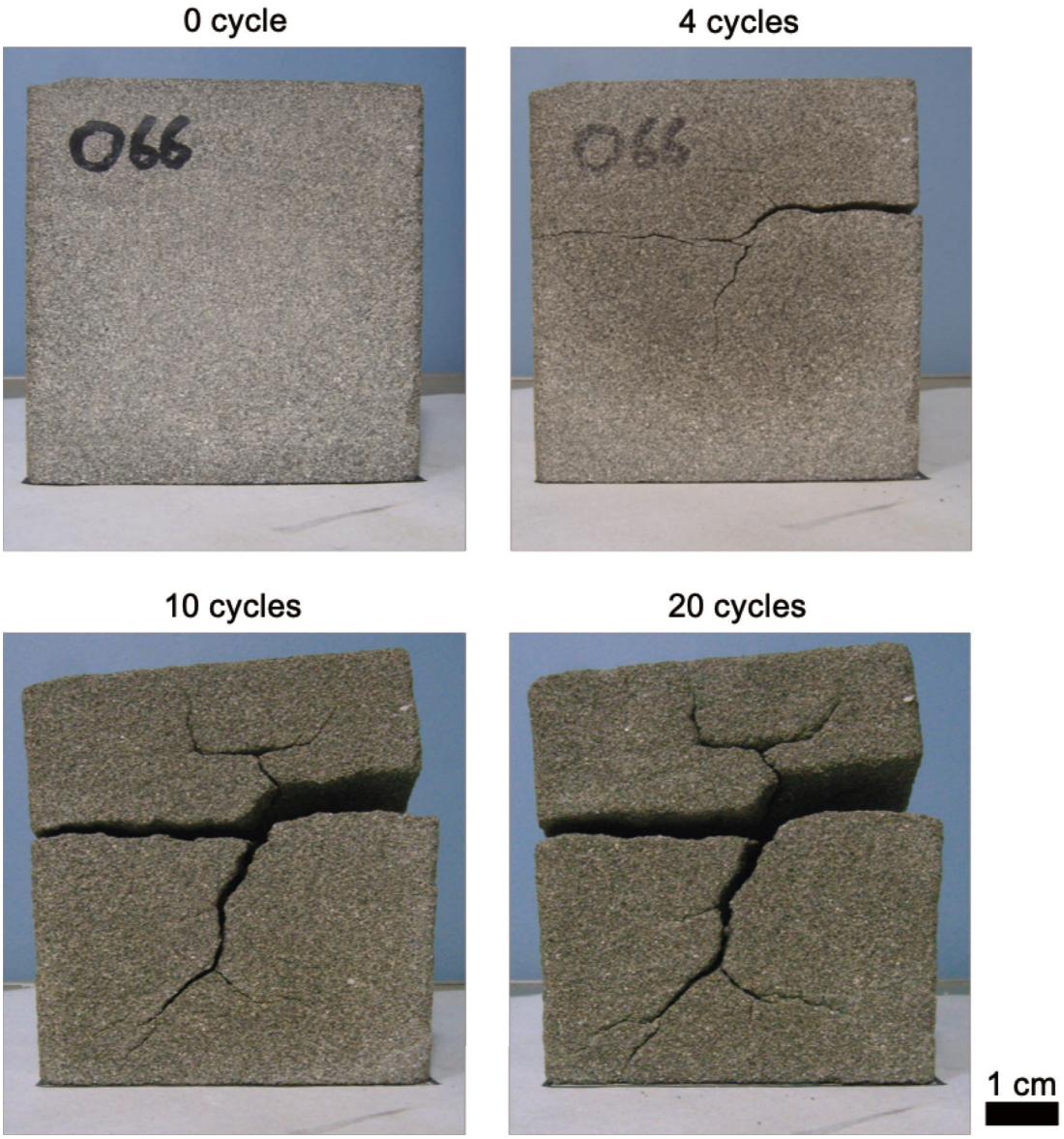

Figure 3.83 Specimen subjected to total immersion cycles (Aoshima sandstone immersed in sodium sulfate solution, 10˚C)

A lot of cracks occurred after 4 cycles.

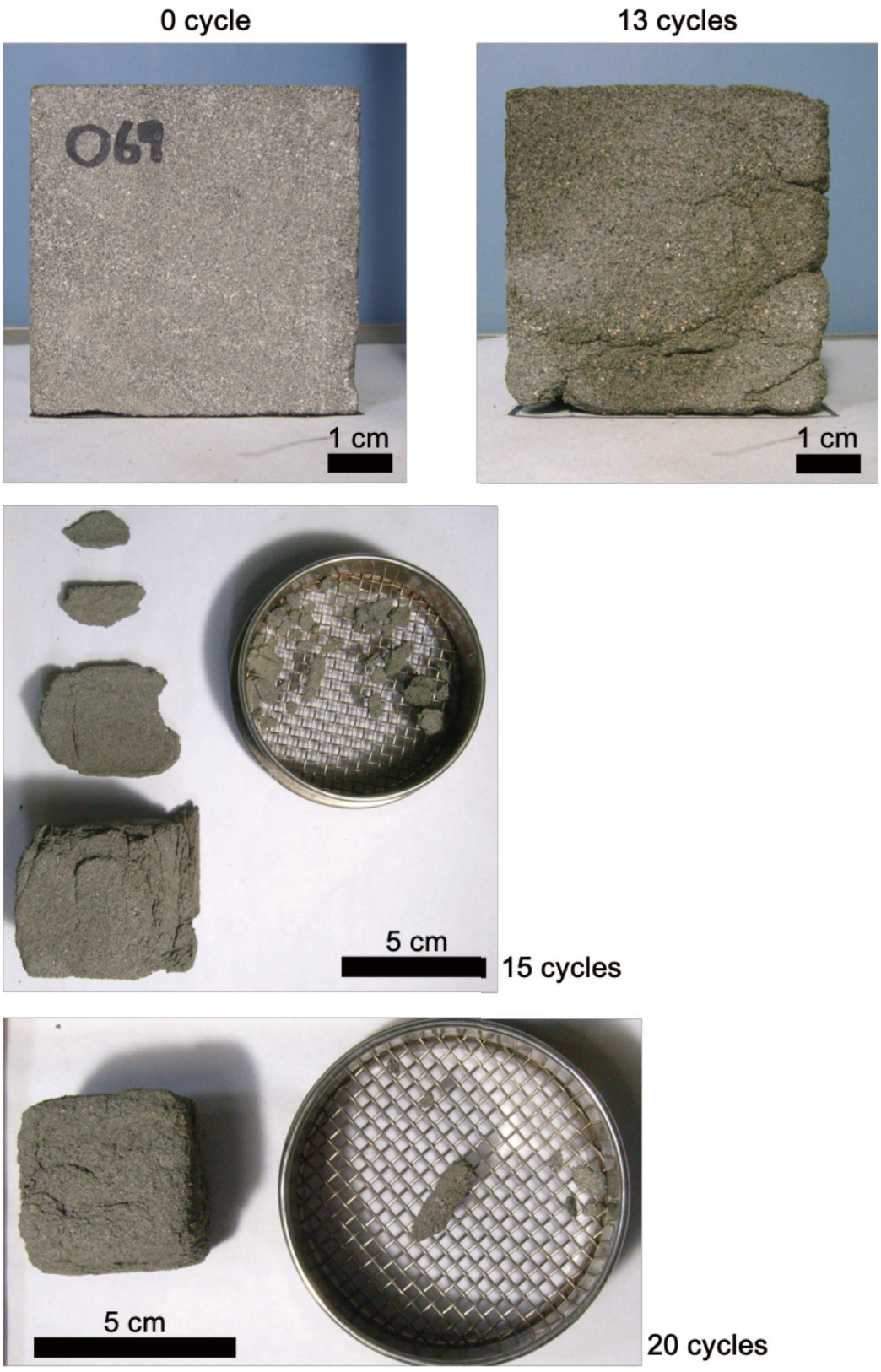

Figure 3.84 Specimen subjected to total immersion cycles (Aoshima sandstone immersed in magnesium sulfate solution, 10˚C)

Cracks extended, and sand particles split from surface of the specimen at 13 cycles. Tabular fragments split from the surface after 15 cycles, and shape of the specimen gradually became rounder as an increase with number of total immersion cycles.

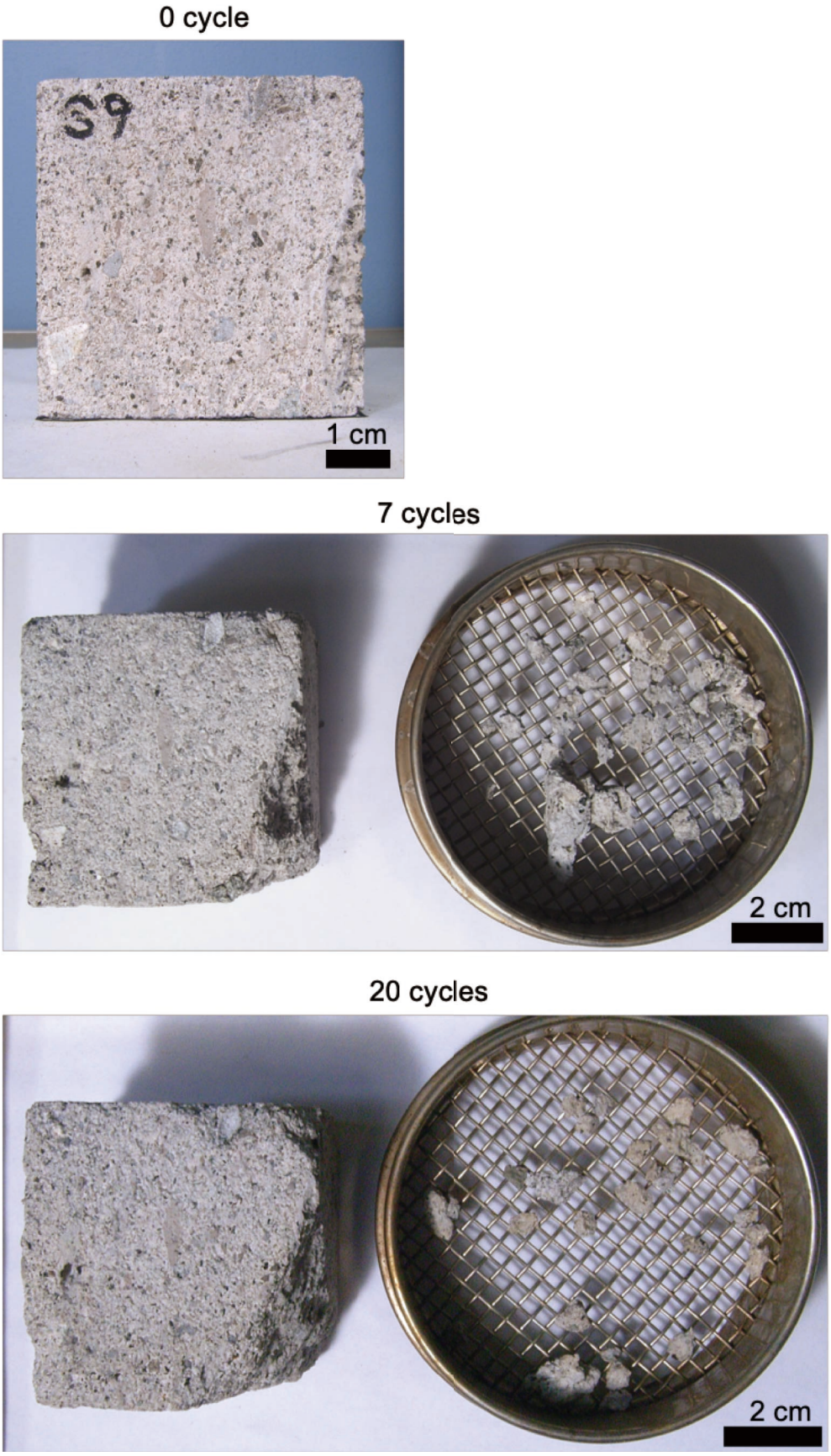

Figure 3.85 Specimen subjected to total immersion cycles (Shirakawa tuff immersed in sodium chloride solution, 10˚C)

Some mm-scale fragments split from surface of the specimen as an increase with number of total immersion cycles. A cm-scale fragment split from edge of the specimen at 7 cycles.

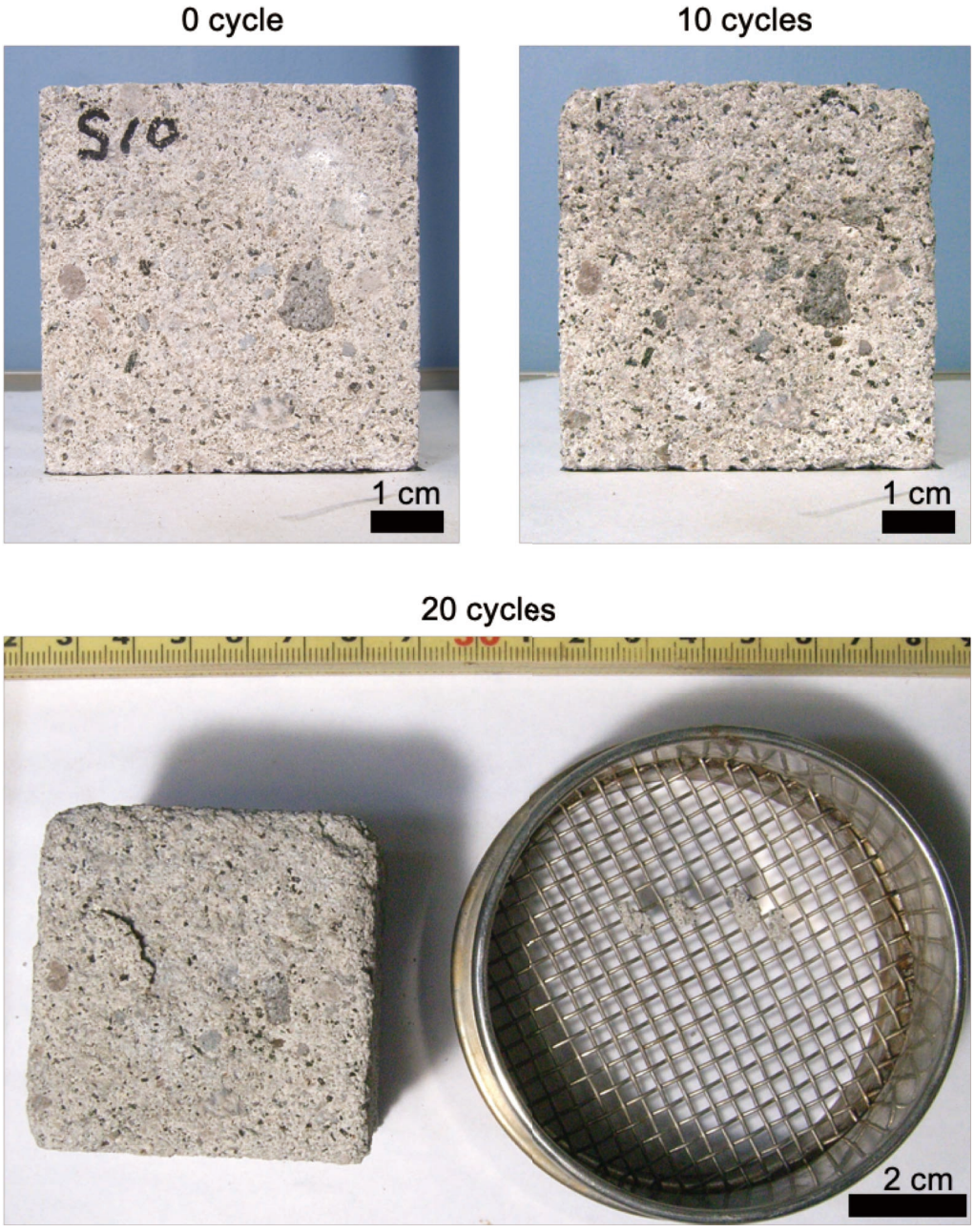

Figure 3.86 Specimen subjected to total immersion cycles (Shirakawa tuff immersed in sodium sulfate solution, 10˚C)

Shape of the specimen gradually became rounder as an increase with number of total immersion cycles. Some mm-scale tabular fragments split from surface of the specimen.

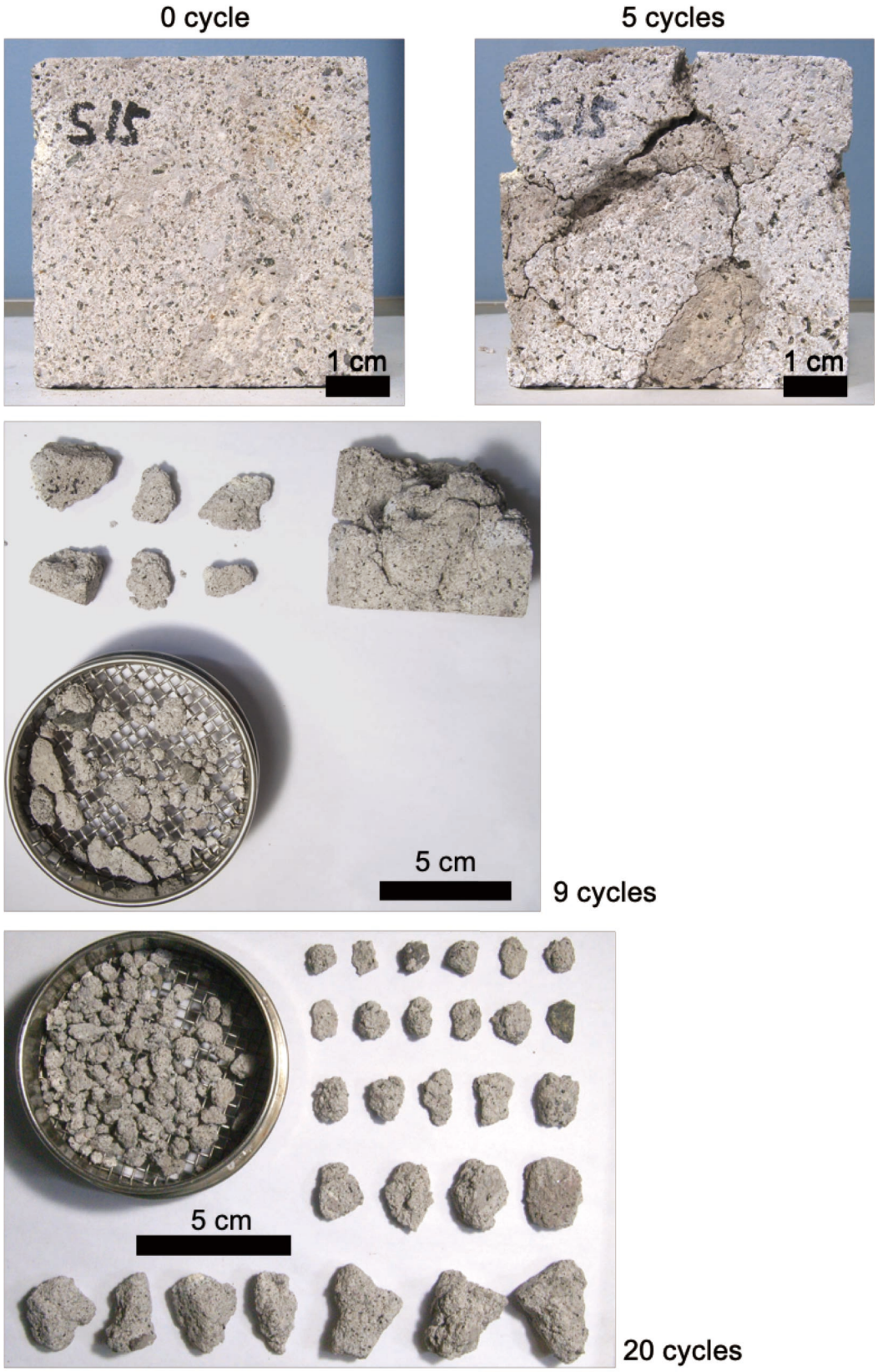

Figure 3.87 Specimen subjected to total immersion cycles (Shirakawa tuff immersed in magnesium sulfate solution, 10˚C)

A lot of cracks extended at 5 cycles, and the specimen split into various sizes of fragments at 9 cycles.

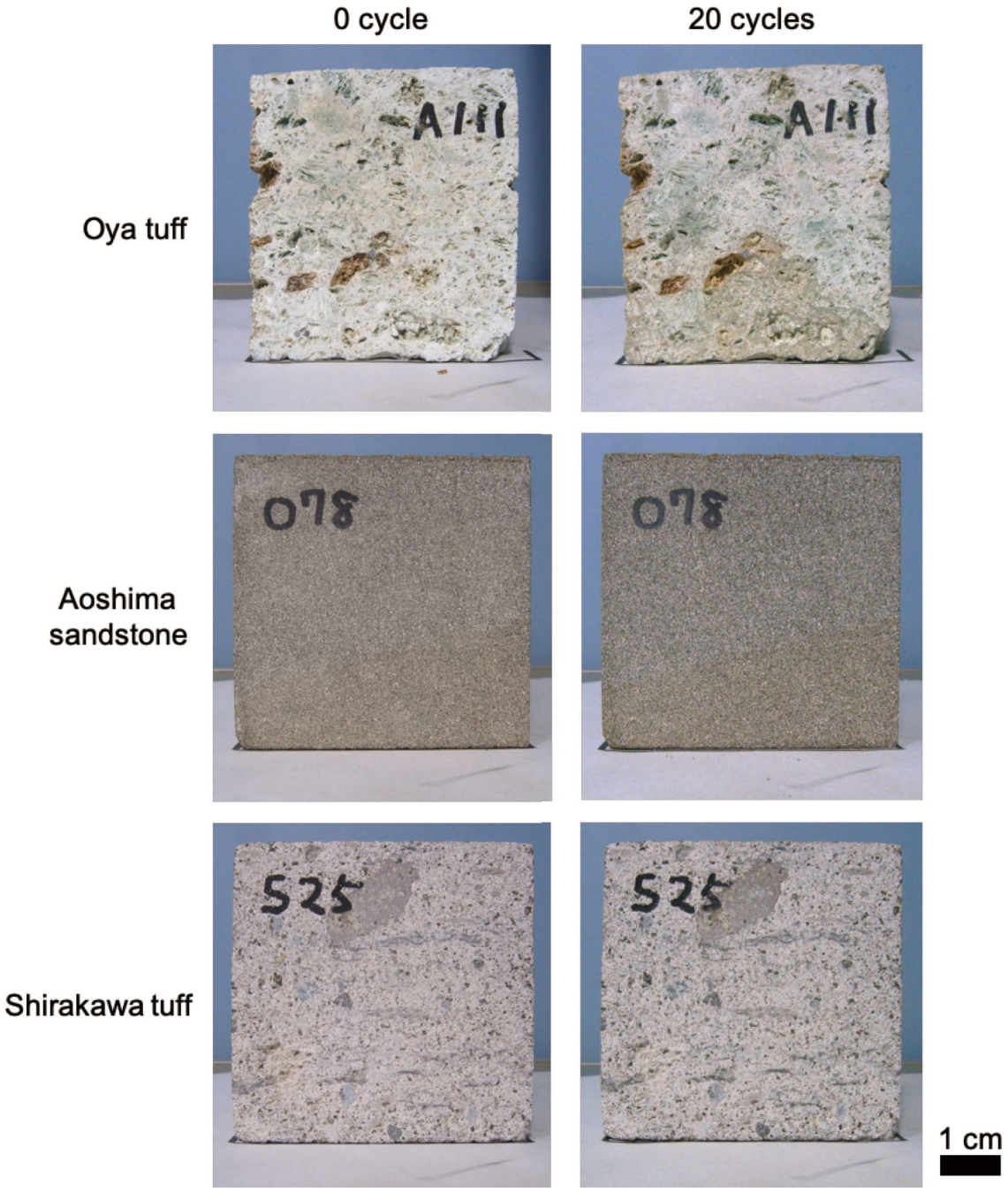

Figure 3.88 Controlled specimens subjected to total immersion cycles (specimens immersed in distilled water, 10˚C)

The specimens did not show any visible sign of breakdown.

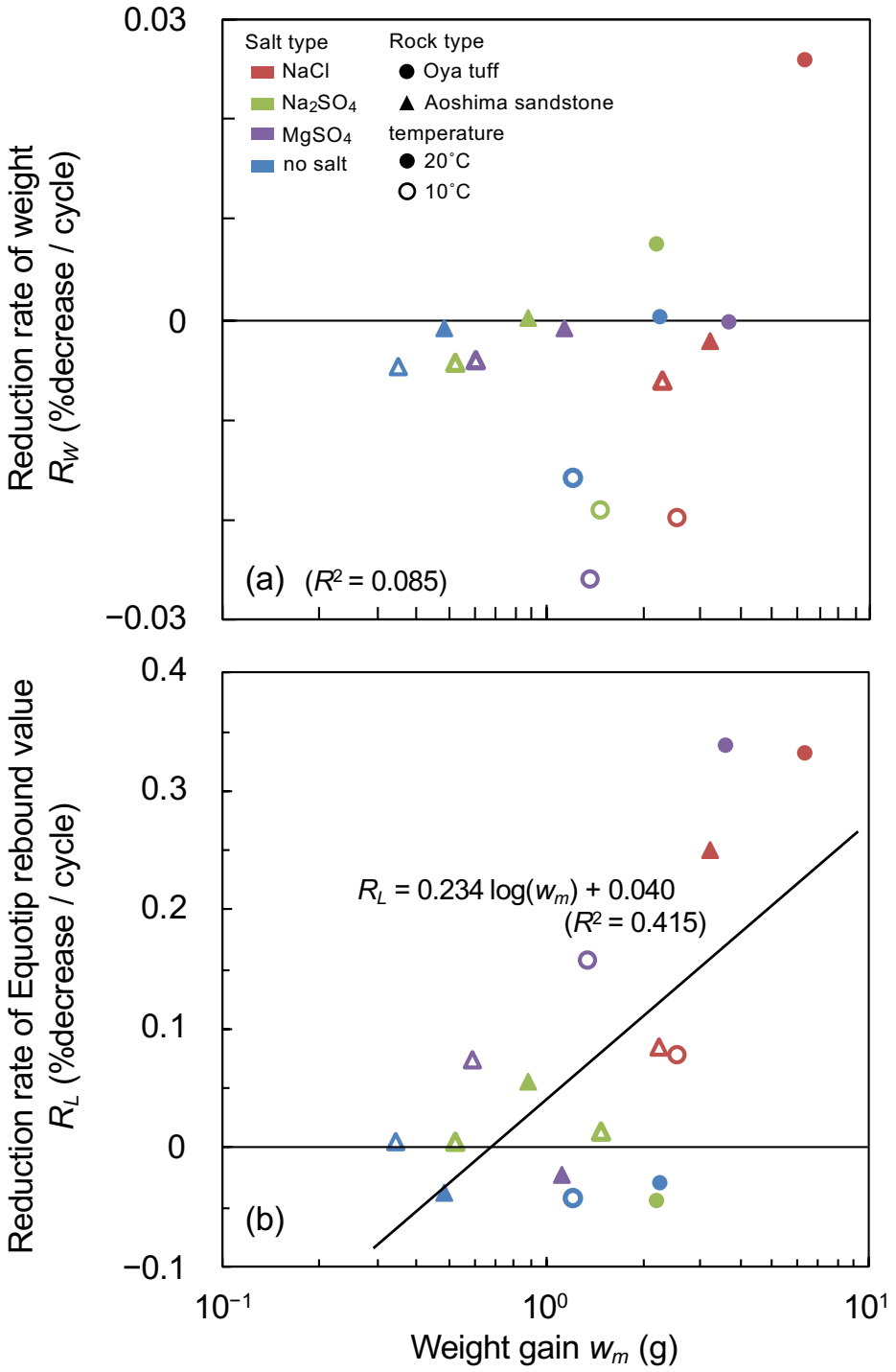

Figure 4.1 Relationship between reduction rates and weight gain in high-humidity period

(a) Weight, (b) Equotip rebound valueReduction rates were calculated by dividing the final value by both the cycle-0 value and the number of humidity cycles.

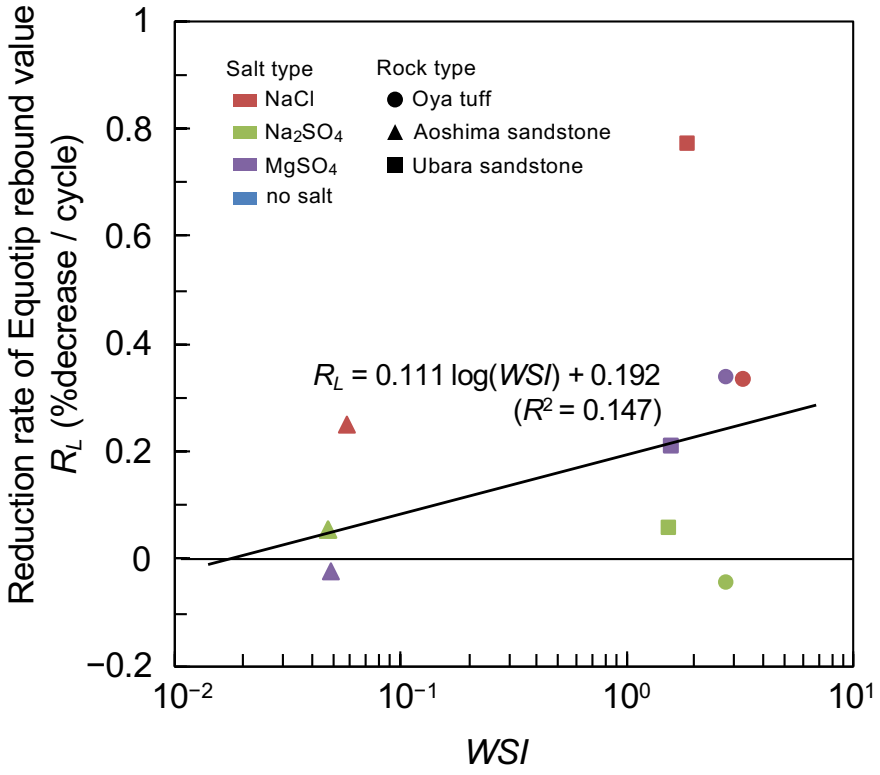

Figure 4.2 Relationship between *WSI* and reduction rate of L-value in humidity-change experiment at 20˚C

Reduction rate of Equotip rebound value was calculated by dividing the final value by both the cycle-0 value and the number of humidity cycles. *WSI* is a Weathering Susceptibility Index defined by Matsukura and Matsuoka (1996) and calculated based upon surface tension at 20˚C.

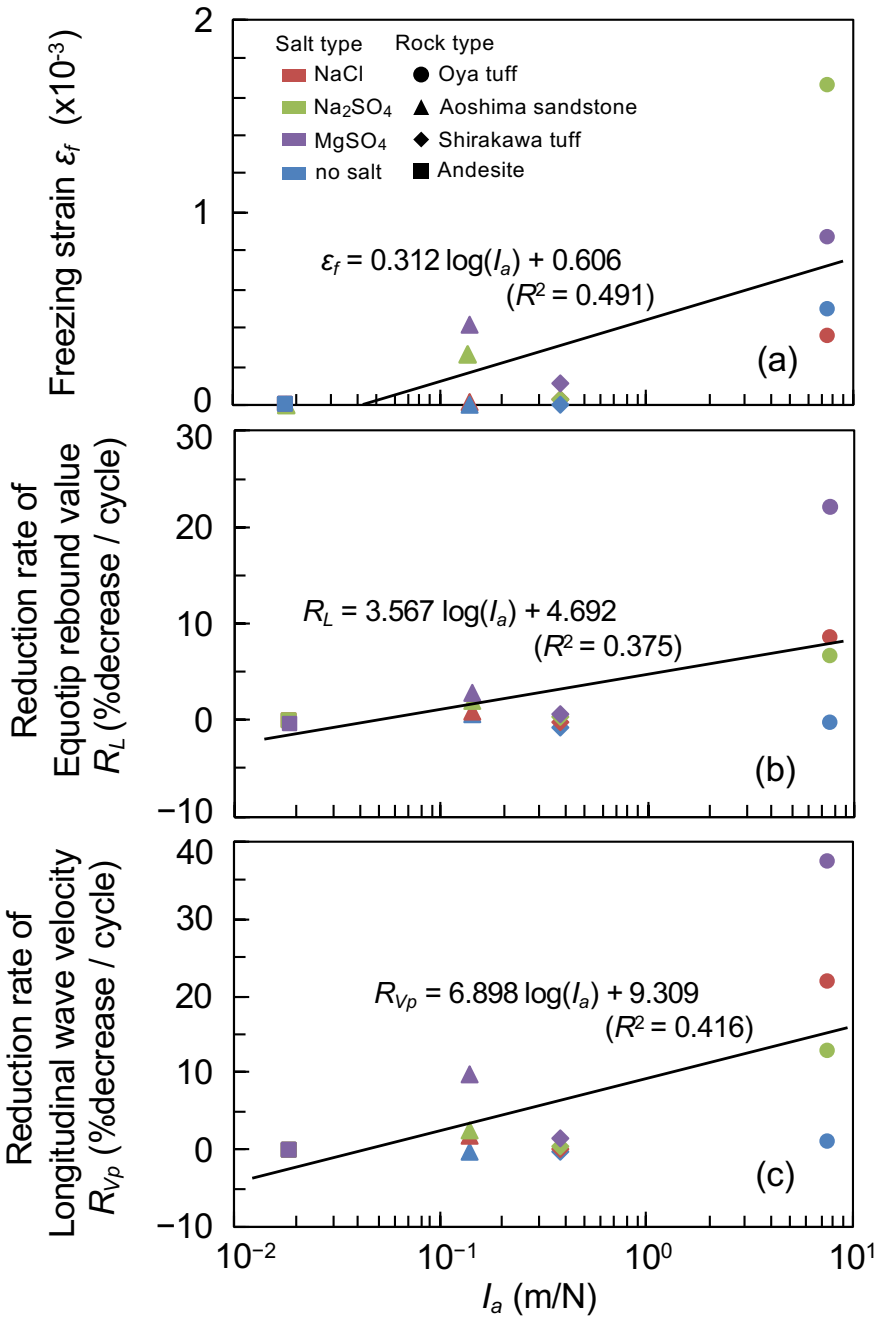

Figure 4.3 Relationship between I_a and freezing strain (a), reduction rate of Equotip rebound value (b), and reduction rate of longitudinal wave velocity (c) in freeze-thaw experiment

I_a is a weathering index based on the capillary force theory (Matsuoka, 1990). The reduction rates were calculated by dividing the final value by both the cycle-0 value and the number of freeze-thaw cycles.

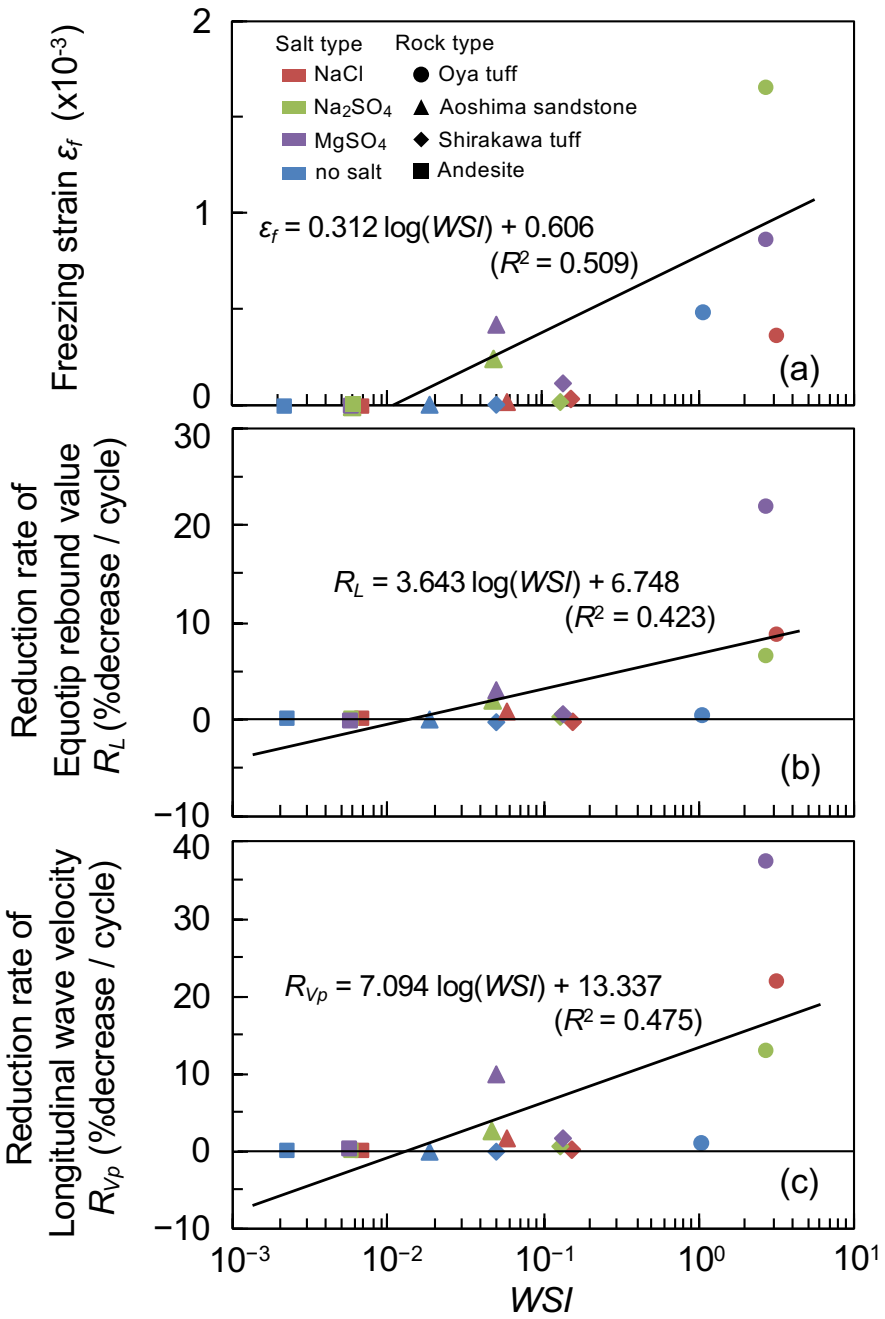

Figure 4.4 Relationship between *WSI* and freezing strain (a), reduction rate of Equotip rebound value (b) and longitudinal wave velocity (c) in freeze-thaw experiment

WSI is a Weathering Susceptibility Index defined by Matsukura and Matsuoka (1996) and calculated based upon surface tension at 20˚C. The reduction rates were calculated by dividing the final value by both the cycle-0 value and the number of freeze-thaw cycles.

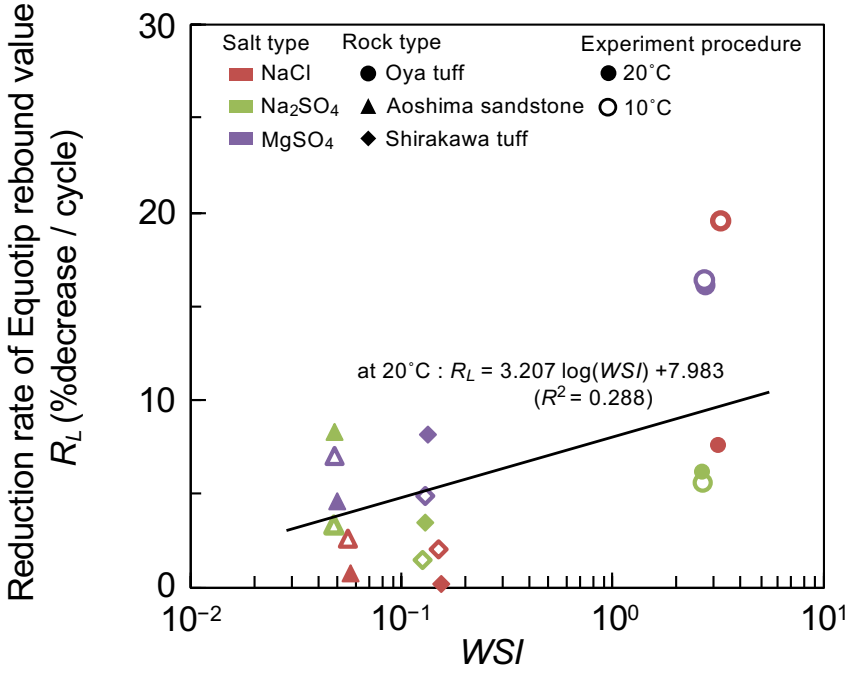

Figure 4.5 Relationship between *WSI* and reduction rate of Equotip rebound value in total immersion experiment

WSI is a Weathering Susceptibility Index defined by Matsukura and Matsuoka (1996) and calculated based upon surface tension at 20˚C. The reduction rate of Equotip rebound value was calculated by dividing the final value by both the cycle-0 value and the number of freeze-thaw cycles.

(a) Environment where liquid water is supplied to rock

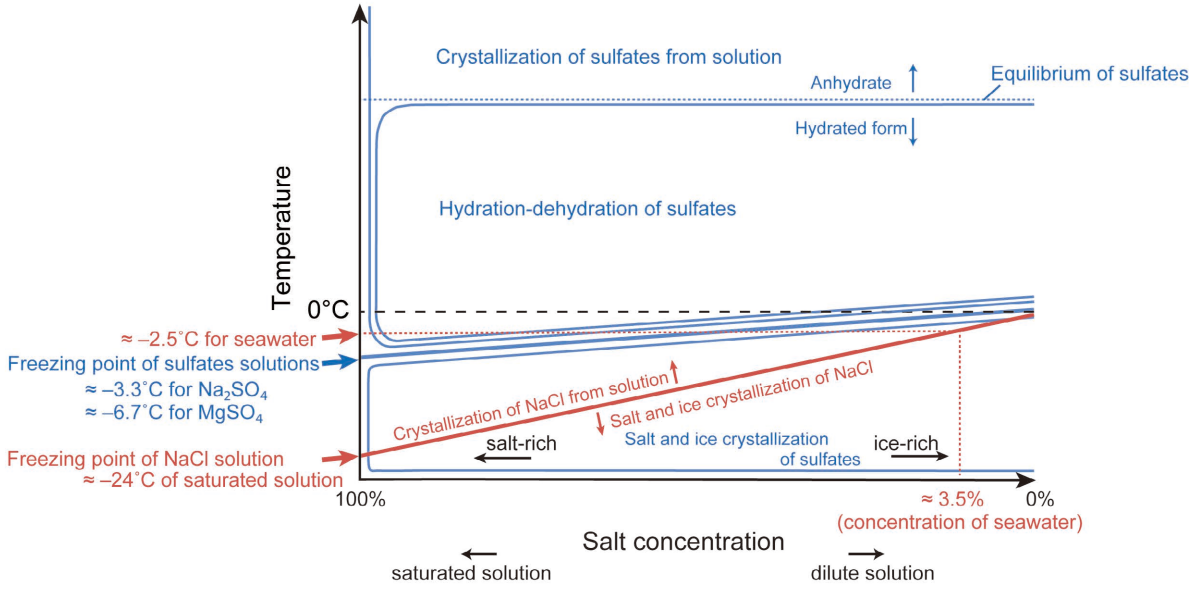

(b) Environment where liquid water is not directly supplied to rock surface

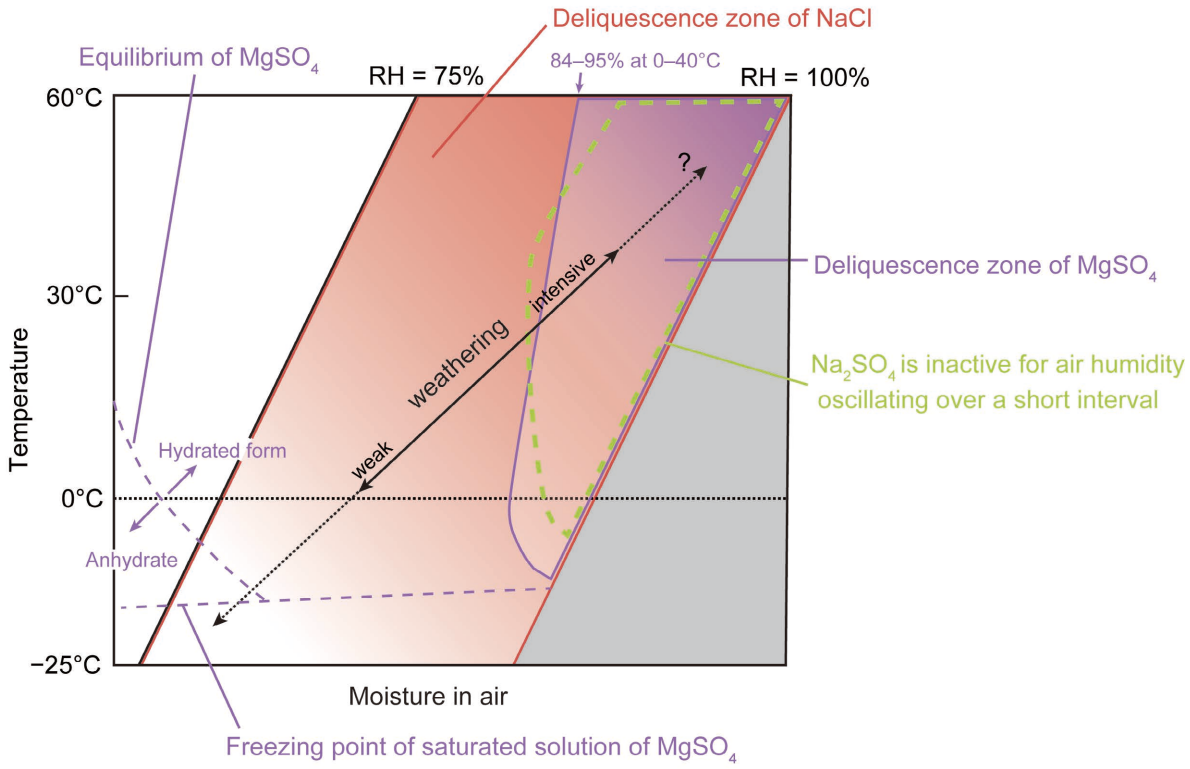

Figure 4.6 Schematic diagrams of the dominant weathering processes under variable temperature and moisture conditions

Schematic effective zone of (a) salt crystallization processes where a large amount of a large amount of liquid water is supplied, and (b) salt deliquescence and hydration processes where air humidity fluctuates in short period.